Detecting optical transients and variables with MeerLICHT

Thesis Presented for the Degree of
DOCTOR OF PHILOSOPHY
in the Department of Astronomy

UNIVERSITY OF CAPE TOWN

Kerry Paterson

Supervisors: Prof. P. A. Woudt, Em. Prof. B. Warner and Prof P. J. Groot

March 2019

Figure 1: Colour-composite image of the Fornax Cluster (field 16023, see 4.1) taken with MeerLICHT and created by Charl Cater. All 6 filters (see 1.1) were used with the following colour assignment: u = blue; g = green; r = red; i = dark red; z = magenta; q = orange.

Abstract

For a long time, the discovery of a transient in a one wavelength triggered observations in other wavelengths. Due to various constraints such as telescope access, scheduling and availability, and the need for human intervention, follow up observations of the transient event could take place long after the initial discovery. Due to the time-critical nature of some transients, with prompt emission that can fade rapidly, this delay in follow up observations can result in important information about the event being missed. Thus, the concept of MeerLICHT was born.

MeerLICHT is an fully robotic, optical telescope whose main goal is the detection of transients in real-time. In collaboration with two legacy-style large survey projects (ThunderKAT and MeerTRAP) on MeerKAT (South Africa's precursor to the Square Kilometre Array), MeerLICHT is the first fully dedicated telescope to follow another telescope in a different wavelength. Through linked-pointing, MeerLICHT and MeerKAT will provide simultaneous optical and radio data of the transient sky. This will provide invaluable information on emission at both wavelengths, including: the relation and evolution of emission from both wavelength windows, the discovery of optical counterparts of radio transients, the characterization of radio transients, and an early warning of radio transients using optical transients.

This thesis contains the work on the development and implementation of the data processing pipeline for MeerLICHT. This data processing pipeline was developed for the automatic processing of data from MeerLICHT/BlackGEM for transient detection in real time.

Plagiarism Declaration

I, Kerry Paterson, hereby declare that the work on which this thesis is based is my original work (except where acknowledgements indicate otherwise) and that neither the whole work nor any part of it has been, is being, or is to be submitted for another degree in this or any other university. I authorise the University to reproduce for the purpose of research either the whole or any portion of the contents in any manner.

Signature: Signed by candidate Date: ......13/03/2019......

I confirm that I have been granted permission by the University of Cape Town's Doctoral Degrees Board to include the following publication in my thesis, and where co-authorships are involved, my co-authors have agreed that I may include the publication:

High-speed photometry of faint cataclysmic variables - IX. Targets from multiple transient surveys by Paterson et al. (submitted and under review with MNRAS)

Acknowlegdement

This thesis was made possible through funding by the National Research Foundation of South Africa (NRF) through a South African Radio Astronomy Observatory (SARAO) bursary, funding from the University of Cape Town (UCT) and funding from the Erasmus+ funding programme provided by the EU through Radboud University.

The MeerLICHT consortium consists of Radboud University, the University of Amsterdam, the Netherlands Organisation for Scientific Research (NWO), the Netherlands Research School for Astronomy (NOVA), the University of Oxford, the University of Manchester, SAAO, the South African Radio Observatory (SARAO) and the University of Cape Town (UCT). This research has made use of the KMTNet system operated by the Korea Astronomy and Space Science Institute (KASI) and the data were obtained at three host sites of CTIO in Chile, SAAO in South Africa, and SSO in Australia. We should like to thank the SkyMapper team for sharing the SkyMapper Transient Survey pipeline to begin development for the MeerLICHT pipeline.

Thank you to everyone who took part in this journey with me. To my father, thank you for encouraging me to follow my dreams. I miss you greatly. To my mother and sister, thank you for always supporting me throughout my studies. To my family and friends, thank you for all the support and encouragement. To my friends and colleagues, having your accompany throughout this journey has been a wonderful experience. Through both the good and difficult times, it was always reassuring to know I could talk to those around me. To my supervisors, Patrick, Brian and Paul, thank you for all your help, the wonderful experiences and interesting conversations.

Contents

Chapter 1

Introduction

This thesis contains the work on the development and implementation of the data processing pipeline for MeerLICHT, developed for the automatic processing of data from MeerLICHT/BlackGEM for transient detection in real time. After an introduction to time domain astronomy, I describe MeerLICHT and its associated projects, BlackGEM as well as ThunderKAT and TRAPUM on MeerKAT, in Sections 1.2 and 1.3 respectively. In Section 1.4, I briefly discuss the MeerLICHT data volume and data base in the context of big data, and describe the platform we used for the processing of MeerLICHT data. I provide an introduction to CCD reductions and photometry in Sections 1.5 and 1.6 respectively, followed by an overview of this thesis.

1.1 Time Domain Astronomy

Time domain astronomy involves the study of astronomical objects which vary in time. These variations can be extrinsic, such as the object's movement or obscuration, or caused by intrinsic changes in the system, such as stellar pulsations or cataclysmic explosions. Figure 1.1 shows a diagram taken from Eyer & Mowlavi (2008), summarizing the types of variability grouped by the physical phenomena displayed by the source. The time scale of variability ranges from time scales as short as milliseconds to time scales as long as several decades. At the very short time scales, objects such as millisecond pulsars (rapidly spinning, highly magnetized neutron stars; see Lorimer 2008) exist, while at the longer time scales, dwarf novae (a subset of cataclysmic variables) can undergo repeated outbursts (resulting in a brightening on the order of a few magnitudes) on time

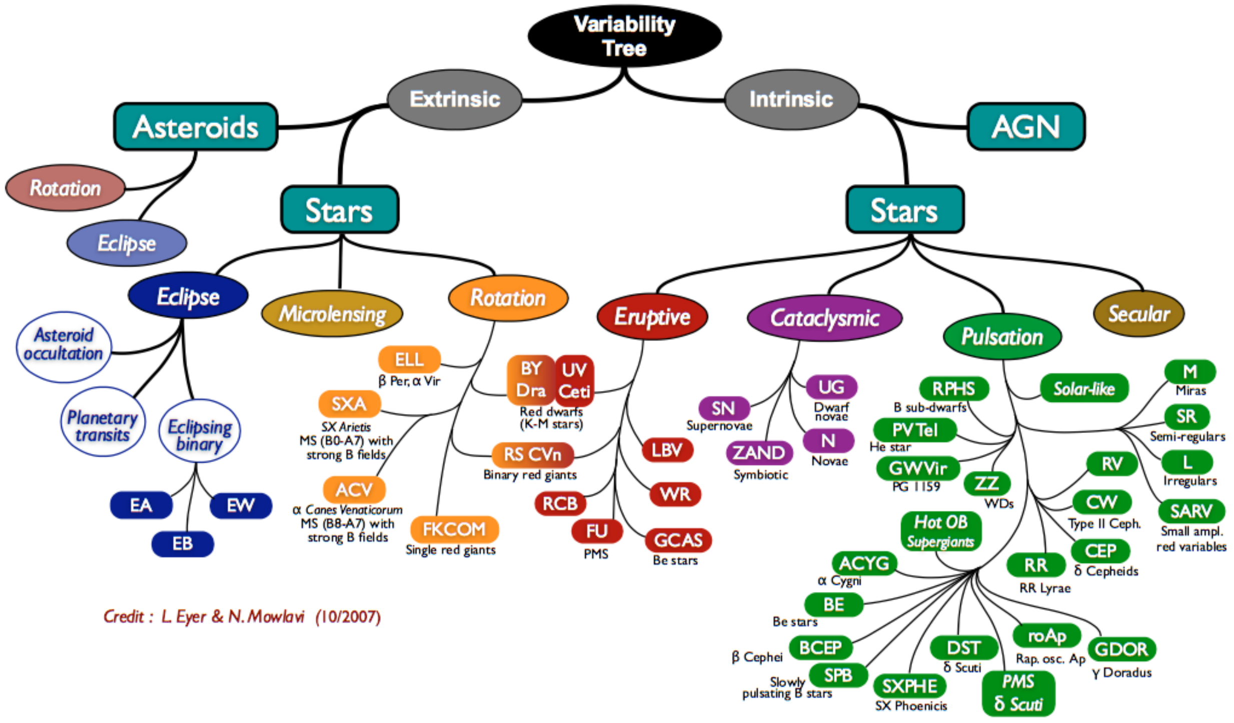

Figure 1.1: Types of variability, grouped by the physical phenomena displayed by the source. Taken from Eyer & Mowlavi (2008).

scales ranging between a few days to centuries (see figure 9, Coppejans et al. 2016). Recent work in the time-domain has led to many notable discoveries, including a better understanding of the population of cataclysmic variables, increasing the sample of AM CVn stars, the rapid evolution of transients, the first observation of a kilonova, and the detection of electromagnetic counterparts of gravitational waves. MeerLICHT, along with MeerKAT, will contribute greatly to the field of time-domain astronomy, especially in the areas of providing rapid response to unusual transients, to optical counterparts of radio transients such as fast radio bursts, and to study the relative delays between optical and radio emission in astrophysical transients. In the context of this thesis, I focus on some of the variable stars and transients expected for MeerLICHT.

Cataclysmic variables (CVs; see Warner 1995 for a review on CVs) are short-period semi-detached binary star systems consisting of a white dwarf accreting matter from a companion star. The matter flows from the companion star through the inner Lagrangian point towards the white dwarf, forming an accretion disc. This accretion disc can be truncated at the inner edge, or be completely non-existent, depending on the magnetic field strength of the white dwarf and the extent of its magnetosphere (see Wickramasinghe 2014 for a review on magnetic accretion). Due to the transfer of matter onto the white dwarf, the system can undergo explosive changes. Build up of matter on the white dwarf itself can ignite in a runaway thermonuclear detonation, rapidly converting the surface layer of accumulated hydrogen to helium. This occurs when this layer reaches the critical temperature and density needed for the nuclear reactions. Nuclear fusion ignites within the layer, resulting in a runaway reaction throughout the entire layer, rapidly burning the layer resulting in a brightening of the star; this is commonly referred to as a classical nova (see Bode & Evans 2008 for a review). For white dwarfs close to the Chandrasekhar limit of $\sim 1.4\ M_{\odot}$ (Chandrasekhar, 1931), this can perhaps result in the triggering of carbon fusion on the star, leading to the detonation of the entire star in a cataclysmic explosion known as a supernova Ia (Hillebrandt & Niemeyer 2000; Kato & Hachisu 2012).

For systems with an accretion disc, matter can build up within the disc. A thermal-viscous instability (see Osaki 1996 for a discussion on the outburst mechanisms, and Dubus et al. 2018 for recent work on testing the disc instability model) in the accretion disc can result in a brightening of the accretion disc, during which material stored in the disc accretes at high rates onto the white dwarf; this is known as a dwarf nova. The time scale on which these outbursts occur, the brightness, and the length of these outbursts depends on the physical parameters of the system. Outbursts can occur with periods ranging from days to decades and longer, durations (the time it takes for the system to return to quiescence) on the order of days, and a brightness increase of a few magnitudes (see Coppejans et al. 2016 for a overview of the statistical properties of dwarf novae).

AM CVn stars (see Solheim 2010 for a review) are ultracompact binary systems in which the companion star is helium-rich. This helium-rich companion star can either be an evolved main-sequence star, or another white dwarf. These systems are important for studying the late-stage evolution of binary systems and are quite rare, with only around 50 known (see Breedt 2015 and Ramsay et al. 2018 for the most recent published count). Of these, only 7 have orbital periods less than 20 minutes (see figure 1 of Green et al. 2018 for the distribution of AM CVn stars with published orbital periods). These short period systems are characterized by high mass transfer rates.

This occurs for systems where the accretion disc is permanently in a high state, or where there is direct impact accretion (Marsh et al., 2004). Analogous to the classical novae seen in CVs, AM CVn stars can undergo a helium nova explosion in which the helium-rich surface layer undergoes nuclear fusion in a runaway conversion to carbon and oxygen. To date only one helium nova is known, namely V445 Puppis (Woudt et al., 2009). For a white dwarf nearing critical mass, carbon fusion could be triggered resulting in a supernova Ia (Bildsten et al., 2007). Short period AM CVn stars are preferentially found in high cadence synoptic surveys (with sampling timescales of minutes) such as PTF (Levitan et al., 2013), OmegaWhite (Macfarlane et al. 2015, Kupfer et al. 2017) and MeerLICHT. These ultracompact systems are strong sources of gravitational wave emission (Nelemans et al. 2001; Kupfer et al. 2018).

Stellar pulsations, caused by oscillations within the interior of the star (see Catelan & Smith 2015 for a review), are important objects for the study of asteroseismology, and provide a means to study the interiors of stars. These pulsations cause the radius of the star, and thus the brightness, to vary with different frequencies. Radial pulsations involve the entire star shrinking and expanding as one, while non-radial pulsations result in different parts of the star to pulsate on different frequencies. The location of the pulsation within the star, as well as the modes/frequencies of the pulsation, affect the observables, such as the period and amplitude of brightness changes, of the star. There are many classes of pulsating stars, classified by these observables. Cepheid and cepheid-like variables (Breger, 1979) pulsate with very regular periods. They have a well defined period-luminosity relation, making them useful for distance determination (Bhardwaj et al., 2017). δ Scuti variables (Breger & Montgomery, 2000) have low amplitude pulsations, with shorter periods compared to Cepheids. They often display pulsations from multiple pulsational modes, resulting in complex light curves composed of many periods superimposed. High amplitude δ Scuti stars (Rodríguez et al., 1996) show pulsations dominated by the fundamental radial mode, making them good distance indicators (Petersen & Christensen-Dalsgaard, 1999). Compact stars, such as white dwarfs, can also display pulsations, with non-radial pulsational periods as short as 100s of seconds and extremely small amplitudes (as small as 0.001 mag) observed (see Winget & Kepler 2008; Althaus et al. 2010 for properties of pulsating white dwarfs).

There are many large variability surveys, past, present and future, spanning a broad range of the electromagnetic spectrum. Given the focus on optical transient and variability surveys in the context of MeerLICHT, I provide a brief overview on the following most recent and relevant surveys: the Catalina Real-time Transient Survey, OmegaWhite, PanSTARRS, ASAS-SN, ZTF, and the Large Synoptic Survey Telescope.

The Catalina Real-time Transient Survey (CRTS; see Drake et al. 2009) is a synoptic astronomical survey whose goal is the discovery of rare and interesting transients in the optical. CRTS makes use of images from the Catalina Sky Survey (CSS), whose aims was the detection of potentially hazardous asteroids (PHAs) and Near-Earth Objects (NEOs), and consisted of 3 telescopes situated at Mt Lemmon Observatory (Arizona, USA), Steward Observatory Catalina Station (Arizon, USA), and Siding Spring Observatory (Australia). Each telescope uses a 4k x 4k CCD, observing the night sky using a V-band filter. CRTS has covered 33 000 square degrees of the sky, ranging from –80° to +70° in declination, while avoiding 10° on either side of the Galactic plane (i.e. at $|b| < 10°$), and the Magellanic Clouds, due to star crowding. Each field is visited up to four times a month, with each visit consisting of a series of 4 observations 10 minutes apart (Djorgovski et al., 2011) to look for moving sources. CRTS examines these images, providing alerts for variations ≥ 2 magnitudes. All alerts are made public through VOEventNet and SkyAlert, allowing rapid follow up of newly discovered sources by the community. Archival data are also publicly accessible through their website[1] (Drake et al., 2014), making CRTS ideal for studying the long-term behaviour of transients. CRTS-II (Drake et al., 2016), using only the telescopes at Mt Lemmon Observatory and Steward Observatory Catalina Station, continued the search for transients and variables after an upgrade to the telescope at Mt Lemmon Observatory (increasing the field of view to ~ 5 square degrees). CRTS-II continues the legacy of CRTS, providing public access to all detections.

The OmegaWhite Survey (Macfarlane et al. 2015; Toma et al. 2016; Macfarlane et al. 2017) is an optical variability survey aimed at detecting sources with orbital periods between 5 and 60 minutes. It forms a part of the European Galactic Plane Survey (EGAPS) and covers 400 square degrees of the sky, following the Galactic plane ($|b| < 5$ degrees) and Galactic bulge ($|b| < 10$

---

[1] http://crts.caltech.edu

degrees). OmegaWhite makes use of the wide-field camera OmegaCam (Kuijken, 2011) on the Very Large Telescope (VLT) Survey Telescope (VST; Capaccioli & Schipani 2011). The observing strategy for OmegaWhite was designed to optimize both cadence and sky coverage. As such, two neighbouring fields were alternately observed using a g-band filter with a 39 second exposure time for a duration of 2 hours. Thus, each field has a mean cadence of 3.5 minutes, and allows observations to reach a magnitude limit of $g \approx 21.5$ mag. The survey area of OmegaWhite was chosen to overlap with the VST Photometric Hα Survey of the Southern Galactic Plane (Drew et al., 2014) and the Galactic Bulge Survey (Jonker et al., 2011) to provide complimentary colour information and photometric zeropoints. Understanding the Galactic population of short-period white dwarf binaries is crucial for many astrophysical questions such as: the physics of common-envelope evolution; the progenitors of supernovae of type Ia; the Galactic background for the gravitational wave detector LISA (Nelemans, 2013); and the physics of ultra-low mass transfer rate accretion discs. The short-period white dwarf binary populations detectable in OmegaWhite include: AM CVn stars, CVs, detached red-dwarf white dwarf binaries, and detached double white dwarfs. From the OmegaWhite data, Kupfer et al. (2017) discovered an ultracompact hot subdwarf binary, with a white dwarf companion in a 44 min orbit. With high signal-to-noise ratio (SNR) photometry and phase-resolved spectroscopy follow-up they were able to constrain the nature and evolution of the system. Using evolutionary models, they were able to predict the future evolution of the binary, concluding it would not result in a supernova Ia.

The Panoramic Survey Telescope and Rapid Response System (PanSTARRS; Kaiser et al. 2002) currently consists on two 1.8 m telescopes situated at Haleakala in Hawaii, USA. Like CSS, PanSTARRS' primary goal is the detection of NEOs that pose an impact threat for the Earth. PanSTARRS's largest survey, the 3pi Steradian Survey (Chambers & Pan-STARRS Team, 2016), covers 30000 square degrees of sky. Using difference imaging to detect changes in the night sky, PanSTARRS has discovered many photometric variables and transients besides the NEOs. Archival data are available through the PanSTARRS website[2] (Flewelling et al., 2016).

The All Sky Automated Search for Super-Novae (ASAS-SN; see Shappee et al. 2014) survey is

---

[2] https://panstarrs.stsci.edu

a dedicated all-sky survey focusing on the search for supernovae. However, besides the focus on supernovae, ASAS-SN has discovered a broad range of unusual transients including many cataclysmic variables. It is made up of five units, each consisting of four 14-cm robotic telescopes, located at the Haleakala, Cerro Tololo, the South African Astronomical Observatory (SAAO) and McDonald stations of the Las Cumbres Observatory Global Telescope (LCOGT) Network. Together, these telescopes are able to observe the entire night sky every 2-3 days. ASAS-SN provides alerts to the community through their website[3] (Shappee et al., 2014).

The Zwicky Transient Factory (ZTF; Bellm 2014) is a new time-domain survey that began operations in 2018. ZTF makes use of a mosaic camera, consisting of 16 6k x 6k CCDs, offering a 47 square degree field of view. This camera is mounted on the Samuel Oschin 48-inch Schmidt telescope at Palomar Observatory. ZTF follows the highly successful Palomar Transient Factory (PTF; Rau et al. 2009), and scans $\sim$ 3750 square degrees of the sky every hour. ZTF aims to search for and catalogue rare and exotic transients, with supernovae, variable stars, binaries, AGN, and asteroids being the main science cases to come out of the data.

The Large Synoptic Survey Telescope (LSST; LSST Science Collaboration et al. 2009) is a 8.4 m wide-field survey telescope currently under construction in Chille, South America. It will be equipped with a mosaic camera, made up of 189 16-megapixel CCDs. Using a special 3 mirror design, LSST will achieve a 3.5 square degree field of view, enabling it to image 30 000 square degrees of the southern sky in three nights. With such high cadence, and its planned project length of 10 years, LSST will revolutionize our understanding of the variable night sky, providing an unprecedented catalogue, both in size and depth. The survey was designed to address four main science areas: dark matter and dark energy; hazardous asteroids; the formation and structure of the Milky Way; and the transient sky. LSST will use image subtraction to perform real-time processing of data, in order to provide rapid transient alerts to the community. With such large amounts of data each night ($\sim$ 15 TB; Jenness et al. 2016), producing $\sim 10^4$ transient alerts, LSST represents the challenge of the Era of Big Data in optical surveys.

---

[3] `http://www.astronomy.ohio-state.edu/~assassin/transients.html`

In addition to the electromagnetic spectrum, a new window of astronomy is now assessable through Gravitational Waves (GWs; see Cai et al. 2017 for a review on the sources and physics of GWs). In general relativity, the acceleration of a massive object will produce a change in the surrounding curvature of spacetime (Einstein, 1916). For two objects in orbit around a common centre of mass, the continuous acceleration experienced by the objects results in ripples that propagate outwards. These ripples in spacetime are known as GWs. The amplitude and frequency of these GWs are related to the masses of the objects and the orbital period of the system. Thus, the study of such GWs can tell us about the mass, and therefore probably identification, of the objects before merger. This is important for the study of population synthesis, binary evolution, and to understand the structure of spacetime in the relativistic ('strong') limit. Compact binary systems composed of white dwarfs, neutron stars, and black holes produce the strongest GWs. The first detection of a GW event, a binary black hole merger (Abbott et al., 2016), was announced in 2016 by the Advanced Laser Interferometer Gravitational-wave Observatory (LIGO, see Singer et al. 2014) and Virgo (Acernese et al., 2015) collaboration. Since then, a total of 6 GW events from merging black holes has been detected, with the first detection of GWs from a binary neutron star merger observed in 2017 (Abbott et al., 2017).

A major achievement in time-domain astronomy in recent years is the filling of the luminosity-time phase space for transients. Compared to 10 years ago, our knowledge of the transients phase space of has greatly improved, along with our understanding of transients in general. The impact of this is best illustrated by figure 1 from Rau et al. (2009) and figure 1 from van Roestel et al. (2019) (shown in Figure 1.2), which shows the same luminosity-time phase space 10 years apart. Recent work in the time-domain has pushed this phase space to faster and fainter transients (an area which is still largely unexplored), and increased our understanding of the populations of unusual transients, e.g. kilonovae (GW170817; Abbott et al. 2017), superluminous supernovae (e.g. ASASSN-15lh; Dong et al. 2016) and tidal disruption events (e.g. ASASSN-14li; Krolik et al. 2016, ASASSN-15oi; Holoien et al. 2016). MeerLICHT will probe the phase space on the minutes-to-hours-to-days-to-weeks time scales, further improving our understanding of these fast transients, as well as longer time scales (months to years) after extended operation on selected MeerKAT fields.

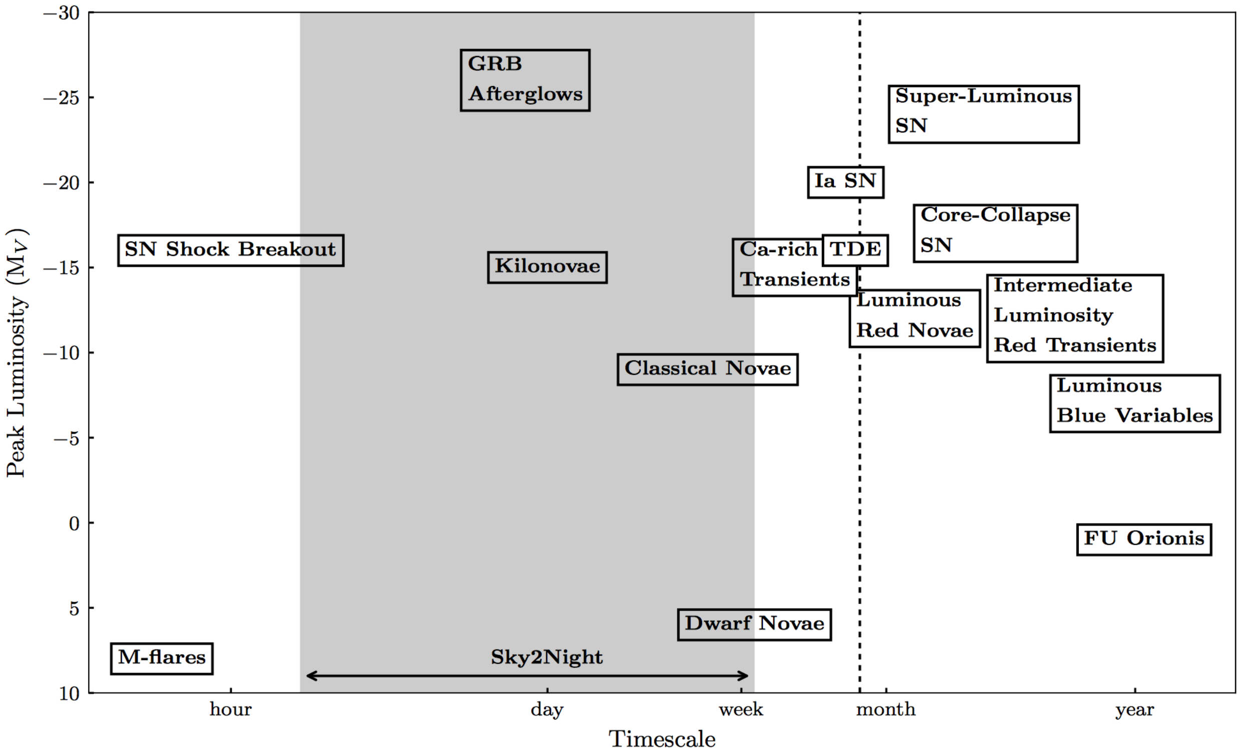

Figure 1.2: Most recent plot of the transient luminosity-time phase space, reproduced from van Roestel et al. (2019).

1.2 MeerLICHT and BlackGEM

MeerLICHT (Bloemen et al., 2016) is a fully robotic, wide-field optical telescope situated at the South African Astronomical Observatory (SAAO) site in Sutherland. The telescope's design is shown in Figure 1.3 and is comprised of a carbon fibre frame housing a modified Dall-Kirkham Cassegrain optical system on a FORNAX 200 equatorial mount. The primary mirror is parabolic with a diameter of 65 cm. The primary mirror is oversized for the 60 cm photometric aperture and 330 cm focal length of the telescope in order to reduce vignetting. The pupil of the telescope is located on the secondary mirror which is spherical in shape. A triple set of lenses acts as field corrector to produce a flat 9.5 by 9.5 cm focal plane at the position of the CCD. The third lens in this system acts as a first-order atmospheric dispersion corrector (ADC) by slightly decentering the lens and produces no loss of light (Ter Horst et al., 2016).

MeerLICHT makes use of a shutter wheel and filter wheel encased inside the camera housing. There are 6 available filters; see Table 1.1 for filter names and corresponding wavelength range, and Figure 1.4 for the transmission curves. These filters are derived from the Sloan (SDSS) set, with an additional wide filter, q, roughly equivalent to $g+r$. The secondary mirror contains actively controlled piezo actuators for active focusing and guiding. Three guide cameras provide accurate guiding across the wide field. The camera is fitted with a single large STA1600 chip (Bredthauer et al., 2012), offering 10560 by 10560 pixels each 9 x 9 μm large. This results in a 2.7 square degrees field of view (FoV) with a 0.564 arcsec/pixel scale. The CCD is read out over 16 ports at 1 MHz, resulting in a 7 sec read-out time. The CCD is housed inside a cryostat operated at 170 K for the reduction of thermal noise. The electronics are housed in the counterweight, which is glycol-cooled to reduce heat load on the telescope environment. Operation is to be robotic, with minimal human intervention. As such, low-maintenance, robustness and reliability have been the main drivers in the design of the telescope and its controls.

MeerLICHT is the prototype for the BlackGEM array (Bloemen et al., 2015), an array of wide-field synoptic survey telescopes. The first three will be installed at La Silla, Chile, towards the end of 2018. These telescopes aim to detect and characterize the optical counterparts of GW events detected by the Advanced LIGO and Virgo interferometers. The BlackGEM array is well suited for searching the large error boxes associated with GW events reported by Advanced LIGO/Virgo and detecting the faint optical counterparts, as it is able to reach faint magnitudes (see Table 1 in Bloemen et al. 2016 for expected depths in 1 and 5 minutes) and cover a large area of the sky. Building an array of smaller telescopes, versus a single large telescope with a large FoV, allows efficient scanning of the, often oblong, sky localization of the GW event, with flexible operations in terms of individual telescope pointing and multi-filter observing. An additional advantage is the extension of the array with more telescopes when new partners join and extra funds become available.

BlackGEM will have 5 main observing programmes:

1) BlackGEM Southern Sky Survey: BlackGEM will spend 50% of the first year of operations (namely the 2 weeks around each new moon) building up a reference catalogue of the southern sky in all filters. This will provide deep reference images for transient detection and a complete multi-filtered catalogue of the entire southern sky.

2) BlackGEM Fast Synoptic Survey: For 2 weeks around each full moon for the first year

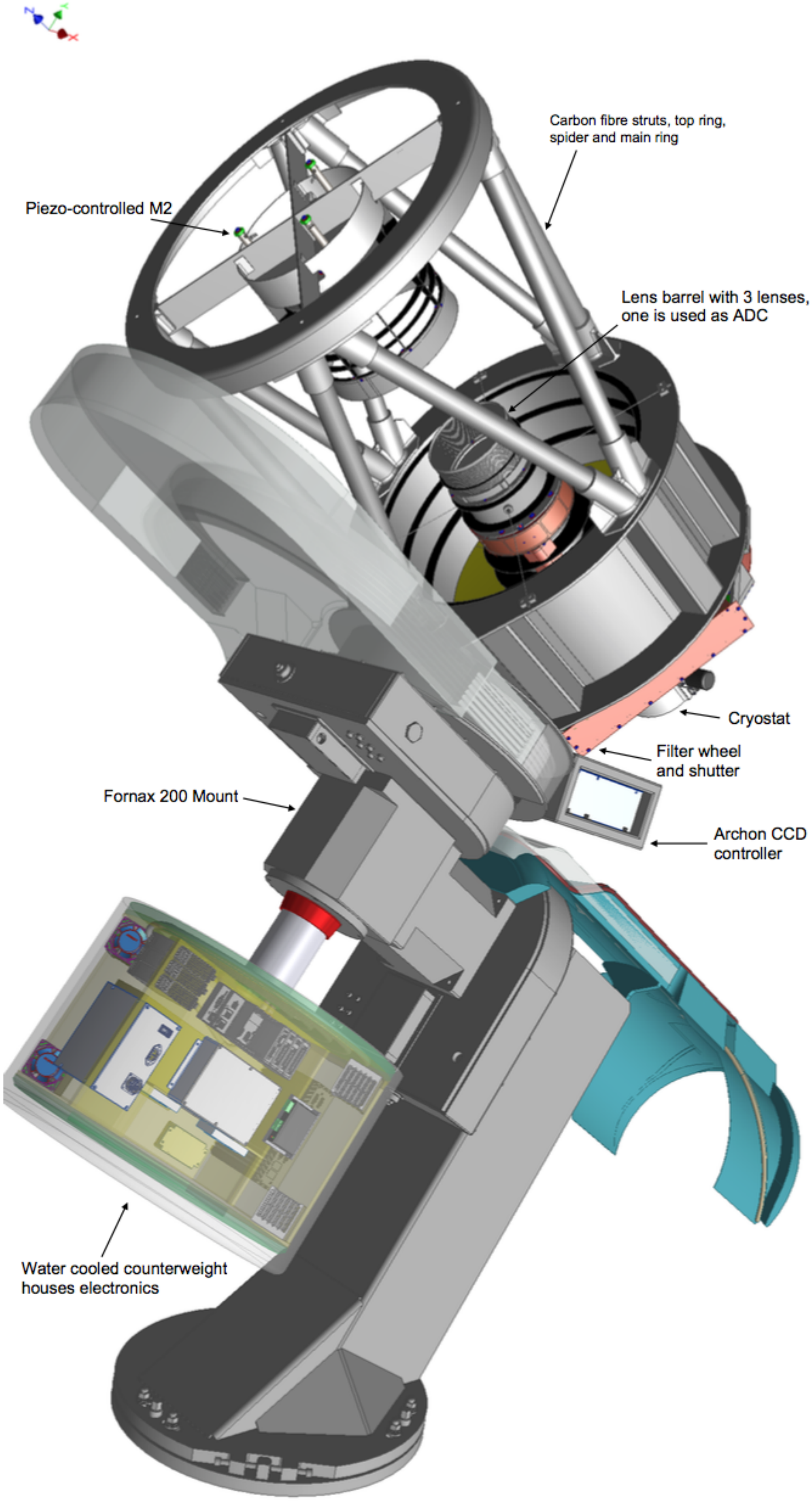

Figure 1.3: MeerLICHT/BlackGEM telescope design reproduced from Bloemen et al. (2016).

Table 1.1: Filters for MeerLICHT/BlackGEM.

Filter	Wavelength range (nm)
u	350 - 410
g	410 - 550
r	563 - 690
i	690 - 840
z	840 - 990
q	440 - 720

of operations and most of the time after the first year, BlackGEM will perform a high cadence (at 1 minute) synoptic survey of a number of fields, including the Chandra Deep Field South, the Hubble Deep Field South, the LMC, the SMC, and a number of galaxy clusters. The goal will be to improve our understanding of transients and variables on the short time scales (minutes to hours). This will be critical in distinguishing GW events from other transients.

3) BlackGEM GW Trigger Follow-Up: This is the highest priority programme for BlackGEM and involves the follow-up of gravitational wave triggers from Advanced LIGO and Virgo. The sky localization of the GW event, along with other parameters such as field visibility and probability of the event in an area, will be used to tile the area in search of the optical counterpart (see Ghosh et al. 2016 for more details).

4) BlackGEM Twilight Program: Every twilight, for 30 minutes, BlackGEM will monitor a set of nearby (< 30 Mpc) large galaxies in u and r to monitor massive luminous binaries and detect low-luminosity transients events.

5) BlackGEM Local Universe Survey: Every three hours the main galaxy clusters in the local Universe (< 100 Mpc) will be imaged in u, q and i.

1.3 MeerLICHT and MeerKAT

MeerKAT (Booth & Jonas 2012; Jonas et al. 2016), is a radio telescope recently inaugurated near Carnarvon in the Northern Cape in South Africa. MeerKAT is South Africa's precursor to the Square Kilometre Array (SKA; see Bourke et al. 2015), and will form the core of the mid-frequency component of SKA Phase 1. The array consists of 64 13.5 m diameter radio antenna, with an offset Gregorian design. MeerKAT will have 3 receivers operating between 580 - 1015 MHz (UHF-band),

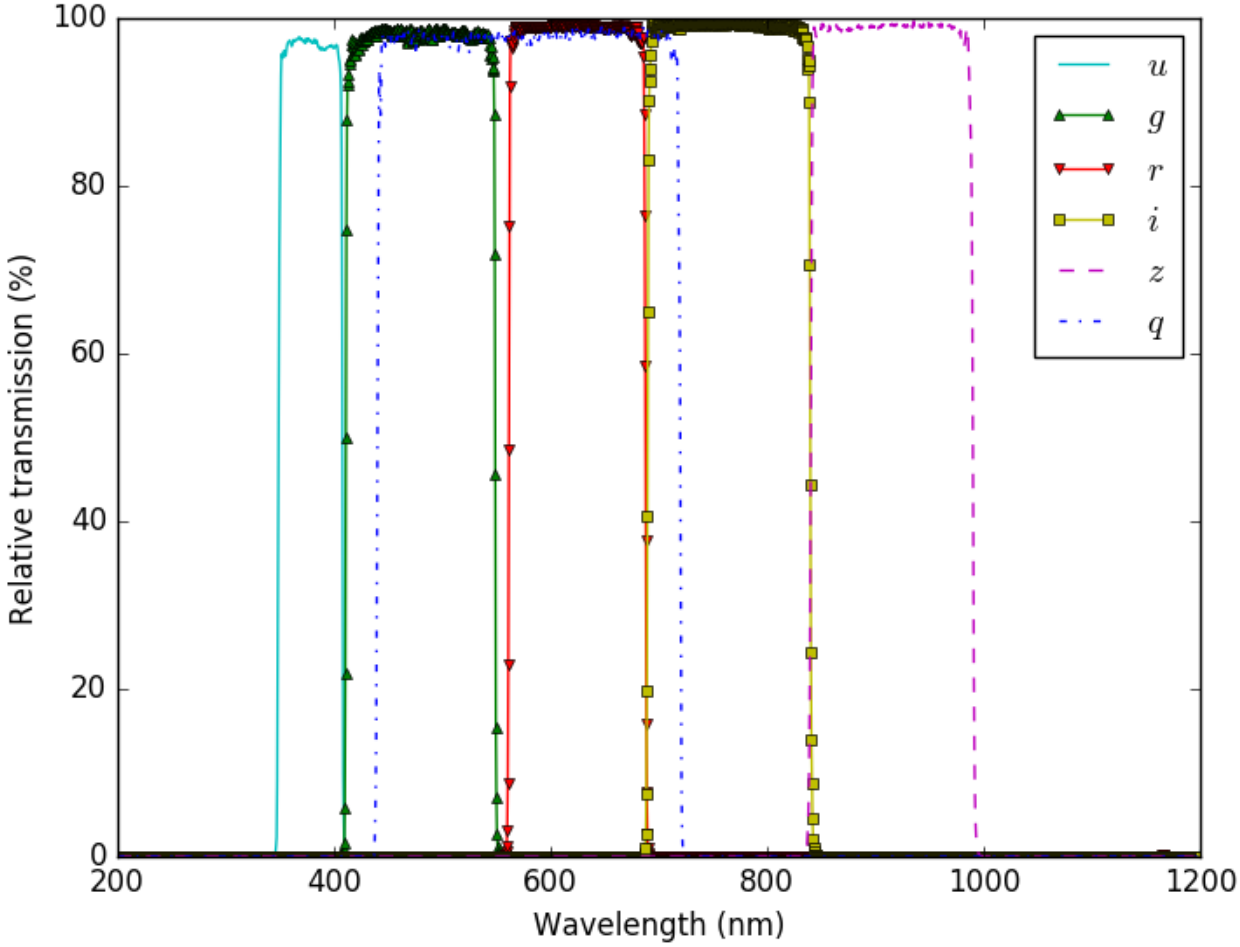

Figure 1.4: MeerLICHT/BlackGEM filter transmission curves obtained from Astrodon. These filters are derived from the Sloan (SDSS) set, with an additional wide filter, q, roughly equivalent to g+r.

900 - 1670 MHz (L-band) and 1750 - 3440 MHz (S-band). The UHF and L bands are currently installed, with the S-band to be installed later. The wide field of view (1.69 square degrees at 1 GHz), wide frequency coverage, and excellent sensitivity make MeerKAT ideal for studying the transient sky.

MeerKAT has allocated two-thirds of its 5 years of observations to 8 Large Survey Projects (LSPs; see Taylor et al. 2018). The LSPs are:

- **LADUMA**: Looking at the Distant Universe with the MeerKAT Array; see Blyth et al. (2016)

- **MALS**: The MeerKAT Absorption Line Survey; see Gupta et al. (2016)
- **MeerKAT Fornax Survey**; see Serra et al. (2016)
- **MeerTIME**: The MeerKAT Key Science Project on Pulsar Timing; see Bailes et al. (2016)
- **MHONGOOSE**: MeerKAT HI Observations of Nearby Galactic Objects: Observing Southern Emitters; see De Blok et al. (2016)
- **MIGHTEE**: The MeerKAT International GHz Tuned Extragalactic Exploration Survey; see Jarvis et al. (2016)
- **ThunderKAT**: The Hunt for Dynamic and Explosive Radio Transients with MeerKAT; see Woudt et al. (2016)
- **TRAPUM**: Transients and Pulsars with MeerKAT; see Stappers & Kramer (2016)

The LADUMA survey will observe neutral hydrogen in galaxies out to redshifts ≈ 1, resulting in the deepest neutral hydrogen survey. MALS will search for HI and OH absorption lines over the redshift range $0 < z < 2$ to probe the evolution of galaxies. Observing the Fornax cluster, the MeerKAT Fornax Survey will study the interaction of galaxies in clusters. MeerTIME will observe pulsars, using precise timing to probe fundamental physics. The MHONGOOSE survey will observe the neutral hydrogen in 30 nearby galaxies to probe the conditions, such as the evolution of gas to stars and the process of feedback, within the disc of local galaxies. Unlike the other LSPs, MIGHTEE is an extragalactic continuum survey, probing the faintest most distant galaxies. ThunderKAT and TRAPUM will focus on the discovery and study of transients. The remaining time (one-third) has been reserved for open time proposals, allowing the community to apply for time on MeerKAT.

ThunderKAT is one of the 8 LSPs on MeerKAT, focusing on time-domain radio transients. Patrick Woudt and Rob Fender are the Principal Investigators (PIs) of ThunderKAT, with over 70 researchers from 11 countries forming the research team[4]. As an LSP, ThunderKAT has been awarded time for pointed observations over the 5 years of MeerKAT operation, and is also fully

---

[4] http://www.thunderkat.uct.ac.za

commensal with all other LSPs. Commensal access to data allows the search for radio transients in real-time, increasing the discovery-space for rare transients by a factor of ~ 10. The main science goals of ThunderKAT include accretion and outflow processes in compact object binaries (black hole, neutron star and white dwarf binaries); Gamma-Ray Bursts (GRBs) and Supernovae (SNe); and Gravitational Wave (GW) sources. The extreme conditions experienced in these transients are beyond anything reproducible in a laboratory, and allow ThunderKAT researchers to probe the laws of physics in these extreme conditions. Most of these event produce transient radio emission, tracing the acceleration of particles and their interaction with the local magnetic field. This radio emission can be used to pinpoint the source of the explosive event, probe relativistic accretion and study the energy released into the surroundings.

TRAPUM is another of the LSPs on MeerKAT, with a focus on pulsars and Fast Radio Bursts (FRBs). The PIs of TRAPUM are Ben Stappers and Michael Kramer. TRAPUM includes over 38 researchers from 8 countries as part of the research team[5]. The primary science goals of TRAPUM include the discovery of new pulsars within the Milky Way; studying globular clusters using pulsars; probing the Galactic Centre using pulsars interacting with Sgr A*; studying gravity using relativistic binaries and millisecond pulsars; and cosmological studies using high redshift fast radio bursts. MeerTRAP (Stappers, 2016), funded by the European Commission, is a project to search MeerKAT data commensally for pulsars and fast transients in the time domain, allowing rapid, accurate localization of these sources within the data.

Due to the time-critical nature of most transients, the concept of MeerLICHT was born: a dedicated optical telescope linked in real-time to the pointing of MeerKAT in order to provide simultaneous multi-filter optical data when possible. MeerLICHT is the first of its kind, a dedicated telescope following another telescope observing in a different wavelength. The concept of MeerLICHT is tied to the commensal nature of both ThunderKAT and MeerTRAP. With the commensal search of radio transients with these projects, a true view of the transient sky in both the optical and radio can be achieved. With a number of the LSPs focusing on selected fields, such as the LADUMA Survey observing the Extended Chandra Deep Field South for over 3000 hrs, a

---

[5] `http://www.trapum.org`

complete study of transients within these fields can be achieved.

The default observing schedule for MeerLICHT will be 1 minute exposures, looping through the 6 available filters. Although the sequence of filters can be adapted for each MeerKAT programme or sky position, the default will be a higher cadence in the wide filter (q) with lower cadence colour information i.e. g, q, r, q, i, q, u, q, z, q, etc.

1.4 MeerLICHT and Data-Intensive Astronomy

We are now in the era of Big Data. Research facilities are starting to produce large volumes of data, at a rate at which manual processing by humans is impossible. MeerLICHT aims to provide a stream of optical data, along with transient alerts, every minute, resulting in ~ 50 TB of raw data per year. Consisting of 3 such telescopes, the BlackGEM array will provide 3 times the data rate of MeerLICHT, while large optical transient surveys, like LSST, will produce ~ 15 TB per night (Jenness et al., 2016). In the radio, MeerKAT will provide vast amounts of data, on the order of GBs per second, with the SKA producing over 10 TB of raw data per second (Grainge et al., 2017). These large data volumes, with the need to process, store and visualize the data, have led to the development of large data centres. With the most important aspect of MeerLICHT being the link to ThunderKAT and MeerTRAP, and the discovery of transients in real-time, having adequate computing power to process the large amounts of the data in real-time is especially important.

The Inter-university Institute for Data Intensive Astronomy (IDIA) is a partnership between 3 South African universities (University of Cape Town, University of the Western Cape and University of Pretoria), and provides a cloud environment for data storage, processing and visualization for data intensive projects such as the MeerKAT LSPs. The data storage, processing and visualization for LADUMA, MIGHTEE, MONGHOOSE, MeerKAT Fornax Survey, ThunderKAT and MeerLICHT will all be based at IDIA.

The African Research Cloud[6] (ARC), a partnership between North-West University and the

---

[6] http://idia.ac.za/research-and-projects/african-research-cloud

University of Cape Town, provided a cloud-based computing infrastructure to the partner institutes. One of the pilot projects hosted on the ARC was the Astronomy Proof of Concept. This project allowed the development of data processing pipelines associated with MeerKAT before deployment at IDIA, and is where testing for MeerLICHT and ThunderKAT began.

1.5 Basic primer to CCD reductions

Before scienctific analysis can be performed on a science image, a number of basic reductions need to be applied. These reductions include: crosstalk correction, gain correction, bias correction, overscan correction, and flat field correction (see Howell 1992 for more details). These are needed to correct for effects such as electrical interference, controller conversions and offsets, temperature noise, and the quality of the CCD. A more detailed description of these reductions, focusing on photometry, is given below.

The first reduction step is the gain correction. As photons fall onto the CCD, the photons knock electrons out of the silicon layer within the CCD, building up a charge (Einstein, 1905). When the CCD reads out the charge built-up in each pixel, the electrons are converted to digital units in the Analog-to-Digital-Convertor (ADC) using a set gain. The digital counts are called Analog Digital Units (ADU). Thus, the counts in the raw image are in ADU, and a gain correction needs to be applied to revert this back to electrons. Although the gain is a set parameter of the CCD, set by the operator, the true gain is affected by camera electronics and is thus different for each channel. To determine the gain for each channel, a pair of flat frames (having the same count level) and a pair of bias frames is needed. The gain can then be determined as described by Howell et al. (2006). Using a series of flat frame pairs, with the count level for the pairs spanning the full count range, a better determination of the gain can be found by fitting a straight line to

$$\sigma_{\mathrm{f_{A_i}-f_{B_i}}} - \sigma_{\mathrm{b_{A_i}-b_{B_i}}} = \frac{1}{\mathrm{gain}}[\mathrm{mean(f_{A_i}) + mean(f_{B_i}) - mean(b_A) - mean(b_B)}] \tag{1.1}$$

where $\mathrm{f_{A_i}}$ and $\mathrm{f_{B_i}}$ are the i_{th} flat frame pair, $\mathrm{b_A}$ and $\mathrm{b_B}$ are the bias frame pair, and $\sigma_{f_{A_i}-f_{B_i}}$ and $\sigma_{b_{A_i}-b_{B_i}}$ is the standard deviation of the difference between the flat and bias pairs. Ideally, these flat frame pairs should be taken with a dome screen and variable lamp to control the count levels. At the time of these tests, MeerLICHT did not have access to a dome screen and made use of sky flats for calibrations. Since then, a dome lamp and screen has been installed. For initial gain determination, the use of sky flats was sufficient as it is the relative correction between the channels that is more important. This determination should be redone with dome flats to confirm these values.

The second reduction step is the bias correction. The bias level is a positive charge-offset applied at readout to prevent negative counts. Since random Gaussian fluctuations in the counting of the charge in each pixel is centred around the mean value, a CCD with zero charge in a pixel could read out as having negative counts due to these fluctuations. As the controller is unable to interpret these negative counts while reading out, a positive offset is applied at readout to prevent this fluctuation around zero. Thus, as this bias level is not from an astronomical source, it needs to be subtracted before science analysis can be done in the image. This is done by subtracting a master bias. A bias frame is created by taking a zero-second exposure, creating a snapshot of the CCD without any light. A master bias is created using multiple bias frames in order to probe the true bias level and remove the random Poisson noise produced during the read out.

Additional charge, known as dark current, can be generated when electrons become excited due to temperature and not photons. This occurs because any object above 0 K will emit radiation. As the temperature of the CCD is above 0 K, this results in the thermal generation of electrons in the CCD. This effect is dependent on temperature and can be greatly reduced by cooling the CCD to very low temperatures. Thus, this effect can be negligible for short exposures taken with a well cooled CCD. To correct for this effect, an image with the same exposure time as the science image, but with the shutter closed (such that only the bias level and dark current is present) must be used. Since a dark frame only contains the bias level and dark current, subtracting a master dark (created using multiple dark frames) corrects for both the bias and dark current correction, provided of course that the science image has the same exposure time and the dark has not been bias corrected.

Although the bias level of the CCD is set by the operator, it can be affected by the tempera-

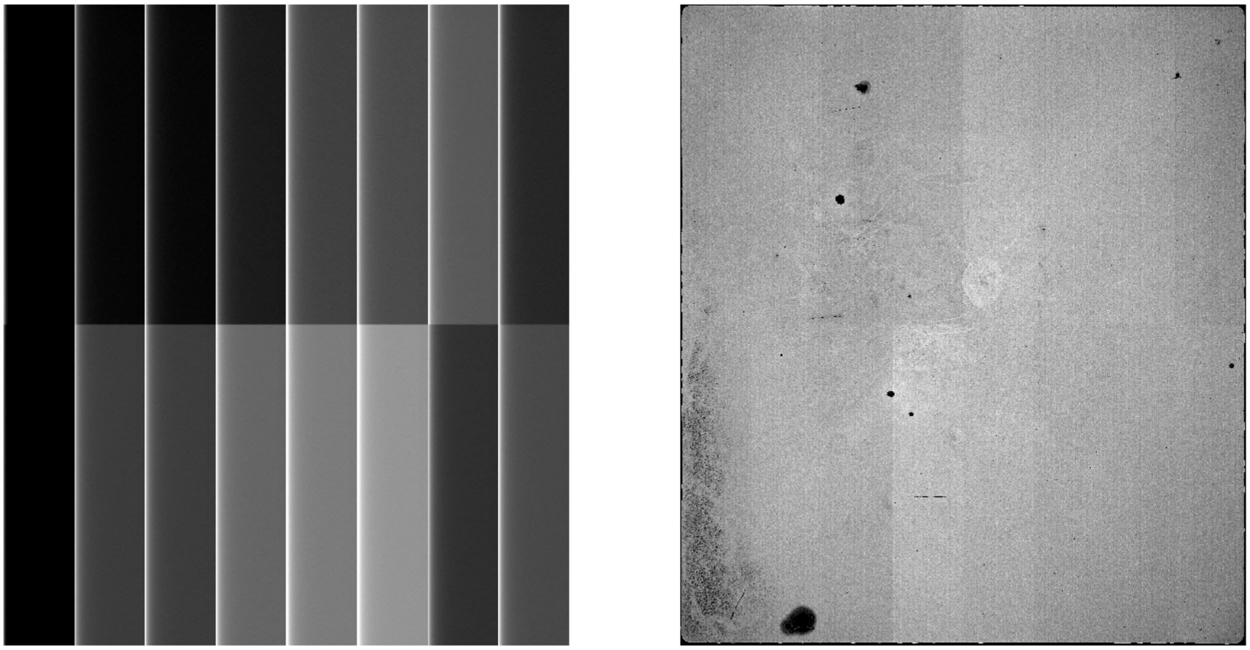

Figure 1.5: Left: A bias frame from MeerLICHT. As seen in the image, each readout channel has a slightly different bias level. Right: A flat from MeerLICHT. Dark spots, caused by defects on the CCD, and imperfections, caused by dust or scratches on the filter, can be seen clearly.

ture at the time of exposure, if the signal from the CCD is digitized outside of the cryostat. Raw images usually contain multiple read-out channels, where each channel contains a data section and an overscan/bias section. The data sections contain the part of the chip which is exposed to light when the shutter of the camera is open. The bias and/or overscan sections are not physical sections on the chip, and are added by the software to represent the bias level at the time of exposure. The bias and/or overscan sections only contain the bias level. Thus, after the subtraction of the master bias, any residual signal in these sections results from the temperature dependences of the bias level. To correct for this, the median within the overscan needs to be subtracted.

The third reduction step is the crosstalk correction (Freyhammer et al., 2001). As the signal from the CCD is read from multiple readout channels, electrical interference occurs across the readout channels. This interference is different for each channel, but proportional to the signal being read out i.e. the higher the signal in a readout channel, the higher the interference it causes

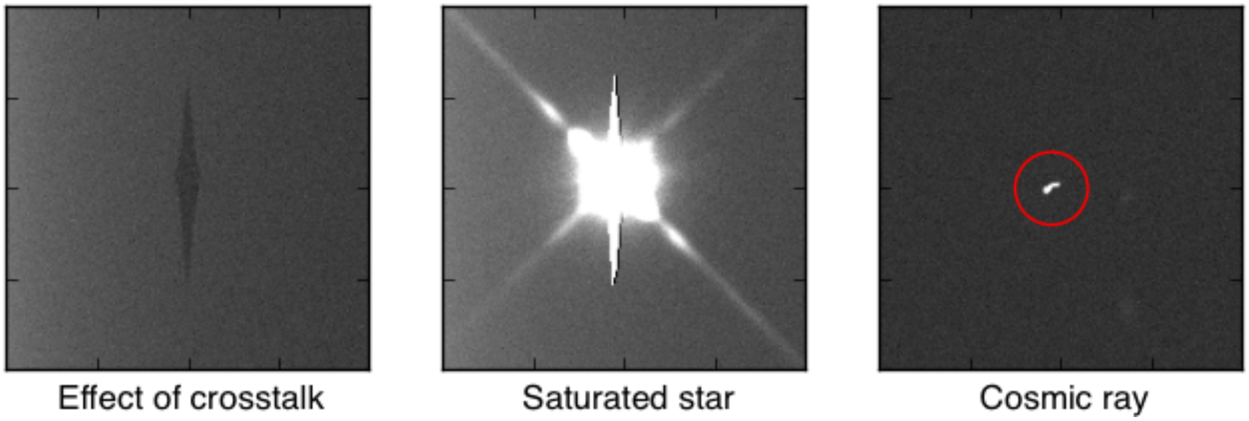

Figure 1.6: Sections of an image from MeerLICHT showing various effects. Left: The effect of crosstalk. A saturated star in another channel results in the measured signal deviating from the true signal. Middle: A saturated star. The potential wells in which the charge collects in the CCD have a maximum capacity. This maximum capacity results in pixels becoming saturated for stars exceeding this value during the exposure. When saturation of a pixel occurs, the charge bleeds out, usually along the read out direction, resulting in stripes. Right: A cosmic ray. The cosmic ray is shown inside the red circle. The shape of the cosmic ray is very different to the shape of a star.

in the other readout channels. The measured signal in a readout channel is given by

$$\mathrm{C}_{\mathrm{i_m}} = \mathrm{C}_{\mathrm{i_t}} + \sum_{k,k\neq i} X_{ik} C_k \tag{1.2}$$

where $\mathrm{C}_{\mathrm{i_m}}$ is the measured signal, $\mathrm{C}_{\mathrm{i_t}}$ is the true signal, X_{ik} is the crosstalk correction coefficient between the i_{th} readout channel and the k_{th} readout channel, and C_k is the true signal in the k_{th} readout channel. A first order correction can be determined rather simply, by assuming the signal in the k_{th} readout channels is the true signal from that readout channel i.e. $C_k = \mathrm{C}_{\mathrm{k_t}}$.

The fourth reduction step is the flat field correction. “All pixels are equal, but some pixels are more equal than others.”[7] When a CCD is created, every pixel has a slightly different sensitivity. This results in pixel-to-pixel differences regarding the charge measured by pixels when exposed to the same intensity of light. Defects on the CCD, known as ‘bad’ pixels, have very different responses compared to the other pixels. This response can either be a highly reduced sensitivity, or completely dead (i.e. the pixel measures no charge). Imperfections on the CCD window or filters, such as dust or scratches, also affect the pixel’s ability to measure photons. To correct these

---

[7] Adapted quote from George Orwell’s *Animal Farm.*

effects, a master flat is needed. A flat field is obtained by taking exposures of a uniformly bright surface. This surface can be a uniformly illuminated surface within the telescope dome, such as a screen illuminated by a bright light (called a dome flat), or the twilight sky (called a sky flat). Sky flats are taken after sunset to prevent saturation, but while the sky is still bright enough to observe high levels of counts (normally the aim is to observe a median count level between 20000 and 30000 per pixel). For large areas across the sky, the sky is not uniform. This thus affects wide-field instruments such as MeerLICHT and must be taken into consideration when taking sky flats. Factor such as the telescope pointing with regards to the Sun can play a major role in the uniformity of the counts. Each filter only allows light through within a range of wavelengths, so each filter is different in terms of brightness. As pixel sensitivity also depends on the wavelength of light, it is important to apply the flat correction on a filter by filter basis. A master flat for a particular filter is then created using multiple flats in that filter.

As light may not fall uniformly on the CCD, a flat field (assumed to be uniformly illuminated) also corrects for this illumination effect. This non-uniformity is caused by the aperture of telescope/camera i.e. light is concentrated at the centre of the CCD and falls off towards the edges (vignetting). These effects are thus corrected for by dividing science images by a normalized master flat.

An additional reduction step, not caused by the properties of the CCD, is cosmic ray correction. Cosmic rays are highly energetic particles that pass through us every day. When a cosmic ray falls on (and is absorbed by) the CCD, the result is a sharp, high count signal. Due to this unique feature, cosmic rays can be detected and corrected for (by replacing the affected pixels with the mean value of the surrounding, unaffected pixels) using algorithms such as Laplacian Cosmic Ray Identification (Van Dokkum et al., 2012).

1.6 Basic primer to CCD photometry

After these corrections have been applied, science analysis on the image can begin. For photometry, we wish to determine the flux or magnitude of the star. A description of the various types of

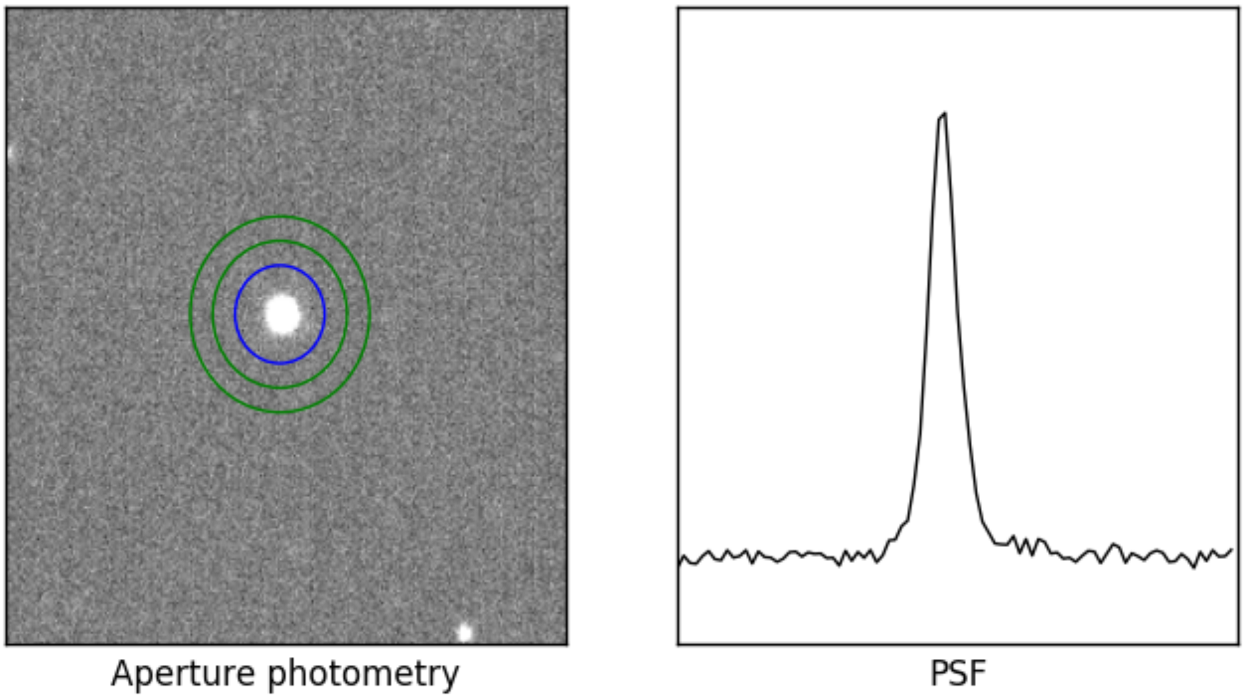

Figure 1.7: Left: An example of aperture photometry of a star within MeerLICHT field 16023. The signal within the inner radius (blue) minus the background determined from the annulus (green) is used to determine the flux of the source. Right: An example of the 1-dimensional PSF of a star, taken from the cross-section of the star in the left plot. It is the 2-dimensional PSF that is used to model the shape of the star in PSF and optimal photometry.

photometry, focusing on photometry of point sources, as well as the calibration, is given below.

Aperture photometry (see Howell et al. 2006 for more details) involves extracting the flux from an aperture around the source. The radius of this aperture is important and affects the flux determination. A too small radius will not include all the flux from a source, resulting in an underestimation of the flux. A too large radius will start to add unnecessary background, and hence noise, to the flux determination, as well as possibly including nearby sources in the aperture (see Figure 1.7, left panel). To determine the background contribution an annulus around the source is used, which allows a correction for the background included in the aperture. Since the optimal aperture depends on the source size, an aperture depending on the Full Width Half Maximum (FWHM) of the source is usually used. Mighell (1999) suggests that the optimum aperture, which provides the best SNR (see Figure 1.8, right panel) has a radius of 0.68 times the FWHM.

Aperture-corrected photometry involves the extra step of correcting the source flux based on the size of the aperture used. When determining the flux within an aperture, the size of the aperture affects the amount of flux from the source included within the aperture, and hence the flux determined. Except when very large apertures are used, not all of the source flux will fall within the aperture. This needs to be corrected for, especially when using smaller apertures. To do this, a curve of growth, which gives the total as a function of radius, is used. A curve of growth is created by determining the total flux within concentric apertures of increasing size (see Figure 1.8, left panel). As the aperture increases, more of the source's flux is included in the aperture. Initially, the amount of flux within the aperture increases rapidly as the aperture is increased in size, as more of the source is included within the aperture. At some large aperture, when all the source's flux is included, the total amount of flux within the aperture flattens off. As the aperture increases however, the noise, which is related to the number of pixels, increases as well. Thus, the SNR for the source increases to a maximum value before dropping again. This drop is caused by the flattening of the flux, but continual increase of noise to larger apertures. The radius at which this maximum SNR occurs is smaller than the source (see Figure 1.8), therefore does not include all the source's flux, but gives higher precision. It is this measurement that is then corrected to a very large aperture to determine the source's flux.

PSF photometry (see Mighell 2005 for more details) involves extracting the flux from a source, based on the measured point-spread-function (PSF). The PSF is the measured 2-dimensional shape of a point source. The shape of the PSF (see Figure 1.7, right panel) is affected by the image quality. This includes sky conditions i.e. the seeing, as well as telescope effects such as focus and drifting. The average PSF for the image, or sections of the image (as the PSF can vary across the image), is used to determine the flux of the source by fitting the amplitude of the average PSF to the counts of the source. PSF photometry allows a more accurate determination of the flux in crowed fields, since the flux is fitted to the counts and is not strongly affected by nearby sources, and for sources in which artifacts such as cosmic rays land on the source, affecting the measured flux. PSF photometry is however, more computational expensive as the PSF needs to be fitted to each source across the entire image. Fitting the PSF as a function of position on the CCD is especially important if the PSF varies greatly across the image.

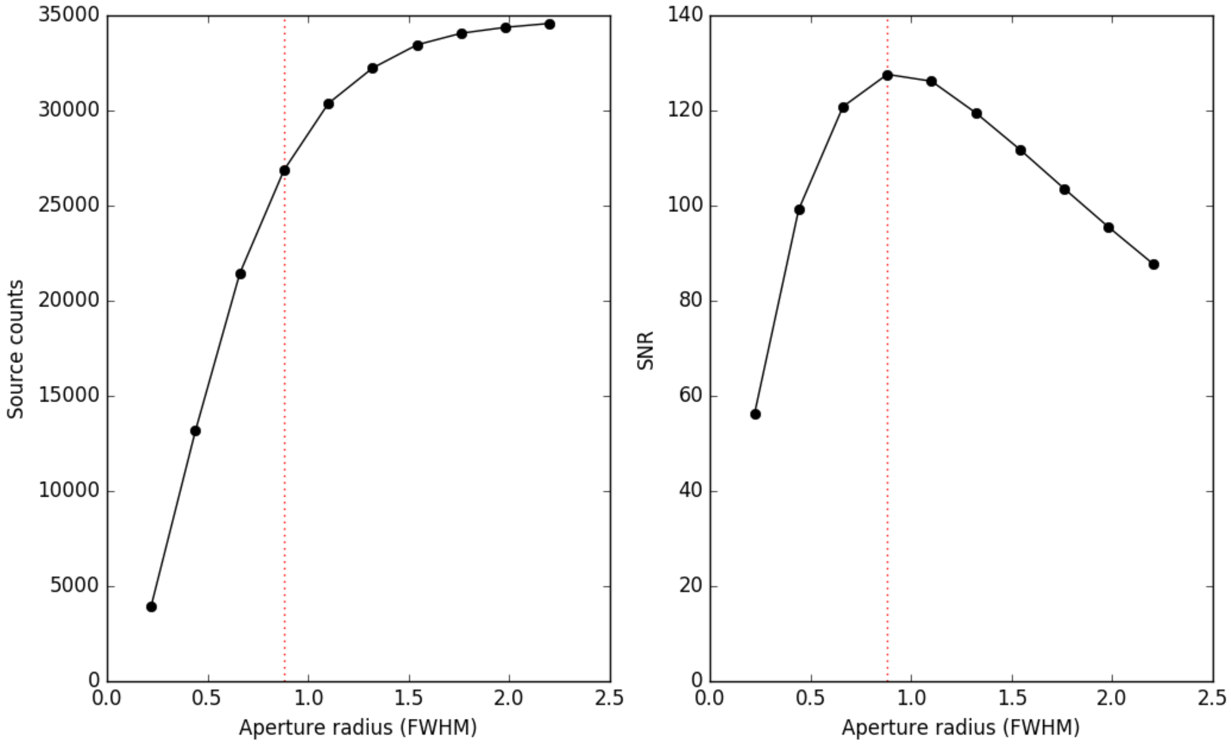

Figure 1.8: An example of a curve of growth for a star within MeerLICHT field 16023. Left: The source counts (source-sky counts) within an aperture as a function of aperture size. Initially, the amount of flux within the aperture increases rapidly as the aperture is increased in size, as more of the source is included within the aperture. At some large aperture, when all the source's flux is included, the total amount of flux within the aperture flattens off. Right: The SNR within an aperture as a function of aperture size. The SNR for the source increases to a maximum value (shown by the dotted red line) before dropping again. This drop is caused by the flattening of the flux, but continual increase of noise to larger apertures. The dotted red line shows the radius at which the maximum SNR occurs for this source.

Optimal photometry (Horne 1986, Naylor 1998) involves the use of the measured PSF and a weight mask to estimate the flux. Like with PSF photometry, the average PSF for the image, or sections of the image, is determined using bright, isolated, non-saturated stars. This PSF is then used to calculate the weighted sum of the pixels, centred on the source. Since no fitting is done when performing optimal photometry, the speed of determining the flux/magnitude over an image is much faster when compared to PSF photometry.

Once the flux from a source has been determined, it can be converted to an instrumental magnitude using

$$m_i = -2.5\log(f) + C \tag{1.3}$$

where m_i is the instrumental magnitude, f is the flux of the source per unit time and C is a calibration constant (often $C = 0$ for instrumental magnitudes). The extent of the calibration then depends on the number of standard/calibration stars available.

Filters allow light within narrow wavelength ranges to pass through them. Unless the exact same filters and CCDs are used, the wavelength range of each filter and the response (i.e. the percentage of light at each wavelength that passes through the filter) can differ from one system to another i.e. a v filter on one system may be different from a v filter on another system. Thus, the filter response needs to be corrected for when comparing magnitudes from different filters. An example of such transformations can be see in Jordi et al. (2006).

Differential photometry is the simplest method to determine the change in magnitude over a time span with multiple exposures taken (i.e. a light curve). This involves using multiple nearby stars to determine the change in the target star's magnitude. The comparison stars should be non-variable and close in brightness and colour to the target star. It is preferable to use brighter stars, as the associated errors are smaller for brighter stars. As light travels through the atmosphere, extinction caused by scattering and absorption affects the amount of light reaching the telescope. This extinction is lowest directly above the observer, the zenith, and increases towards the horizon. Since this extinction is wavelength dependent, stars with different colours are affected differently, making it important to use comparison stars with similar colours. If the comparison stars have a distinctly different colour than the target, differential reddening might occur at high airmass, and thus will need to be corrected for. In general, since the comparison stars are observed at the same time, with the same filter, and the same optical path as the target star, no additional corrections such as filter transformations and airmass corrections are needed. Exceptions occur for large fields of view, where small CCD separation can equate to large sky separation. The differential magnitude is thus simply $\Delta m = m_{i_c} - m_{i_t}$, where m_{i_c} is the average instrumental magnitude of the comparison stars and m_{i_t} is the instrumental magnitude of the target star. The error on this magnitude is then given by $\sigma_{\Delta m} = \sqrt{\sigma_c^2 + \sigma_t^2}$, where $\sigma_c^2 \ll \sigma_t^2$ for multiple, brighter comparison stars.

Relative photometry involves using a star of known magnitude to calibrate the target star. The comparison star is used to determine the offset between the instrumental magnitude of the telescope and the true magnitude of the star. This calibration is known as the zero point (zp) and replaces the constant C given in Equation 1.3, transforming m_i to m_t. Unlike with differential photometry, the comparison star does not need to be on the same part of the sky, or observed simultaneously. In this case, atmospheric extinction needs to be corrected for. Including the atmospheric correction, we arrive at

$$m_t = m_i + zp - kX \tag{1.4}$$

where k is the extinction coefficient and X is the airmass. k is filter dependent and can be calculated from the slope of the instrumental magnitude versus the airmass since $m_i = m_0 + kX$, where m_0 is the instrumental magnitude above the atmosphere. As discussed earlier, atmospheric extinction is wavelength dependent, and therefore an additional colour correction is needed for accurate photometry. This colour correction takes the form $k_c XC$, where k_c is the secondary extinction coefficient and C is the colour index. As the name suggests, the colour index is a term describing the colour of the star and is formed from the difference between 2 filters e.g. $C = B - V$ when correcting a V magnitude for extinction. When comparing magnitudes from different photometric systems, a correction to account for the difference in filters needs to be included. This correction is known as the colour term and is calculated from

$$cC = m_t - m_0 - zp \tag{1.5}$$

where c is the colour term. If the optical system (telescope, instrument, filter) was exactly the same as the photometric system being compared to, this colour term would be zero. If the comparison star is nearby and observed simultaneous however, the discussed corrections for effects such atmospheric extinction do not need to be done.

Absolute photometry involves converting the star's flux or magnitude into flux units such as

$ergs/s/cm^2/Hz$. This involves calibrating the star on the absolute photometry of Vega (Hayes & Latham 1975; Hayes 1985)). In this system, the magnitude, as well as the colour of Vega is set to be zero. Vega is used as the comparison star to calibrate the target as discuss above under relative photometry, and has to include all the discussed corrections. The zero points here depend on the flux of Vega over the filter's wavelength range, and thus require you to know the spectrum of Vega for this range. These measurements are then converted to $ergs/s/cm^2/Hz$ units for absolute photometry. This direct conversion is hardly ever done though, replaced with using secondary or tertiary photometric standard stars to calibrate the target star. These photometric standard stars have been calibrated directly, or on another star which has been calibrated in this way, on the absolute photometry of Vega. Once these corrections are known, stars with known magnitudes within the observing field can be used to calibrate all sources in the field. Another magnitude system often used is the AB magnitude system (Oke, 1974). This system makes use of flux measurements calibrated in units of spectral flux density. In $ergs/s/cm^2/Hz$, this equates to

$$m_{AB} = -2.5\log(f) - 48.60 \tag{1.6}$$

where m_{AB} is the monochromatic magnitude and f is the spectral flux density of the source. Conversion between the magnitude systems is often non-trivial due to differences in the bandbass of the observations, but many have published conversions between standard systems and filters (see Blanton & Roweis 2007 for an example of the conversion between Vega and AB magnitude systems).

Other than using the direct photometric measures of sources to look for variables and transients i.e. looking for variability in the extracted photometric flux, a key tool in transient astronomy is difference images (Alard & Lupton 1998; see Zackay et al. 2016 for an updated method for image subtraction as well as Sections 2.2.2 and 2.3.2 for further discussions). Difference imaging involves subtracting two images, which have been aligned and convolved to each other, and extracting the flux from any residuals. The main difference in this approach is that the comparison of the star's brightness is done on the pixel level and not on the extracted flux from e.g. aperture or PSF photometry. The images are aligned using their astrometry, while the convolution of the images is needed to account for the different image qualities (which changes the shape of the sources).

Since difference imaging allows the detection of variability at the pixel level, it is especially useful for sources with low amplitude variations and in crowded fields. For a full description on the methods and equations used in image subtraction, relevant to the MeerLICHT pipeline, see Zackay et al. (2016). When detecting transients with difference imaging, a real-bogus machine learning algorithm, such as Gieseke et al. (2017), is usually used to distinguish between true transients and artifacts caused by the image subtraction (bogus detections). A mask, masking out bad pixels and objects such as saturated stars, can also be applied to avoid having to run any artifacts resulting from these known issues through the real-bogus algorithm.

When performing wide-field photometry, a number of difficulties can be experienced due to the large observing area. When observing over small areas of the sky (on the order of a few arcminutes), the curvature of the focal plane can be approximated as flat. As the area of the FoV becomes larger however, the curvature of the focal plane becomes more apparent. Projecting the curved focal plane onto the flat CCD results in the focus not being uniform across the entire image. This results in a PSF that varies across the image, which is important when performing photometry that depends on the PSF of the image, such as PSF photometry, optimal photometry and difference imaging. The curvature of the focal plane also affects the pixel scale across the image. This can affect the accuracy of the astrometry if not enough stars across the entire image or the incorrect projection is used to determine the astrometric solution. Another problem to take into account when observing over a large area is the range of airmass that can be experienced across the image. This results in a range of atmospheric extinctions, including diffraction (secondary extinction coefficient) as a function of source colour, across the image. The large FoV also results in the non-uniformity of the sky in flat fields.

The calculation and propagation of errors is of vital important if one wishes to report reliable results. For MeerLICHT, these errors are calculated and propagated within the pipeline. ZOGY performs optimal photometry (described above) to extract fluxes. This is calculated using equation 8 from Horne (1986)

$$F_{opt} = \frac{\Sigma\{P * (D - S)/V\}}{\Sigma\{P^2/V\}} \tag{1.7}$$

where P is the PSF of the star, D is the data, S is the sky background, and V is the variance (calculated from equation 12 from Horne (1986) in the form $V = D + RON^2$, where RON is the read noise). The error on this is then calculated using equation 9 from Horne (1986) via

$$\sigma_{F_{opt}} = \frac{1}{\sqrt{\Sigma\{P^2/V\}}} \tag{1.8}$$

Since the magnitude is calculated using the log of the flux, the error on the magnitude is related to the ratio of the flux and the error on the flux. Following propagation of errors, we get the error on the magnitude to be

$$\sigma_m = \sqrt{\left(\frac{2.5}{\log(10)} * \frac{\sigma_{F_{opt}}}{F_{opt}}\right)^2 + {\sigma_{zp}}^2} \tag{1.9}$$

where ${\sigma_{zp}}^2$ is the error of the zero point. Another important value associated with the detection of transients is the signal-to-noise (S/N). This parameter provides an estimate on the reliability of a detection, and as the name suggests gives the ratio of signal from the source over the noise. For transients detected the difference imaging method described by Zackay et al. (2016), and also discussed later in Sections 2.2.2 and 2.3.2, the pipeline calculates the S/N based on equation 51 from Zackay & Ofek (2017) via

$$S/N = \sqrt{\Sigma\left\{\frac{(\Sigma\{D - S\} * P^2}{V}\right\}} \tag{1.10}$$

1.7 Overview of thesis

The overall aim of this thesis is the development and implementation of the data processing pipeline for MeerLICHT, in order to process data from MeerLICHT/BlackGEM automatically, in an effort to perform the detection of transients in real-time. Above, I have outlined the relevant aspects of time domain astronomy, and introduced MeerLICHT and its associated projects. I have also provided a basic introduction to CCD reductions and photometry to prepare the reader for the later chapters.

In Chapter 2, I describe the development and implementation of the pipeline in detail with emphasis on the adaption of the SkyMapper Transient Search pipeline for wide-field photometry and transient detection through proper image subtraction using an implementation of the ZOGY algorithm. In Chapter 3, I present quantitative results on the performance of the pipeline with respects to astrometry, photometry, and transient detection. This is followed by the scientific results obtained with test data from MeerLICHT in Chapter 4. In Chapter 5, I present a more in-depth study on a number of cataclysmic variables with multiple larger telescope facilities, followed by the conclusions of the thesis, and future outlooks.

The pipeline manual can be found in the Appendix A, and the full observation log for Chapter 5 in Appendix B.

Chapter 2

Pipeline development

The development of the MeerLICHT pipeline can be divided into two parts. First is the development of the mainframe of the pipeline, controlling the data flow and processing the raw data for further analysis. The main developments into this component were the pipeline mainframe, allowing processing of data in real-time, and applying basic CCD corrections. The second part is the adaption of the SkyMapper Transient Survey pipeline, hence forth called *subpipe*, for MeerLICHT and BlackGEM. The main developments into this component were the generalization of *subpipe* to analyze MeerLICHT data, transient detection using an implementation of the ZOGY algorithm, and the incorporation of *subpipe* into the main pipeline flow.

The development of the pipeline began on a mid-2014 MacBook Pro with a 2.6 GHz Intel i5 core, 4 CPUs, and 8 GB of RAM. The development then moved to a virtual machine on the African Research Cloud (ARC) with 2.5 GHz Intel Core Processors (Haswell, no Transactional Synchronization Extensions), 8 CPUs, and 32 GB of RAM. The ARC provided the ideal environment for the development and testing of the pipeline, as the final pipeline for MeerLICHT will run on a virtual machine at the Inter-university Institute for Data Intensive Astronomy (IDIA).

In Section 2.1, I introduce SkyMapper and *subpipe*, followed by a detailed description of *subpipe*. In Sections 2.2 and 2.3, I discuss how the pipeline was developed using real data from the Korean Micro-lensing Telescope Network and MeerLICHT, respectively.

2.1 Our starting point - SkyMapper

SkyMapper (Keller et al., 2007) is a 1.35-m robotic telescope situated at the Siding Spring Observatory (SSO) in Australia. The main objective of SkyMapper is the creation of a deep multi-epoch, multi-colour catalogue of the Southern Sky. One of the science projects making use of SkyMapper data is the SkyMapper Transient Survey (STS; see Scalzo et al. 2017). The STS pipeline, *subpipe*, was developed with the main aim of discovering supernovae using difference imaging. *subpipe* is written in Python and calls a number of external programs such as SWarp (a program for remapping images based on their astrometry; see Bertin 2010), SExtractor (Source-Extractor; see Bertin & Arnouts 2010), and HOTPANTS (High Order Transform of PSF ANd Template Subtraction; see Becker 2015). *Subpipe* is available on GitHub[1] and was made available to us for the purpose of identifying transients and variables in the MeerLICHT data stream, and thus became the starting point of the MeerLICHT pipeline. The choice of *subpipe* over other transient pipelines was due to the pipeline infrastructure in place (field based registration, reference image searching, and transient search via difference imaging) and the uniform programming (Python and C). A flow diagram summarising the steps within *subpipe* is shown in Figure 2.1.

Once *subpipe* is called using the `subpipe_master.py` script, it checks for new files for the specified date (either input by the user or defaulted to the current date). For new files, *subpipe* first checks the field ID and seeing in the file header. If the field ID in the header is 0000, indicating a problem with the WCS (World Coordinate System; Greisen & Calabretta 2002) header keywords, the file will be skipped by *subpipe*. The seeing is used for basic quality control as well as for finding a suitable reference frame for difference imaging. A file with unknown or very bad seeing or elongation will be skipped. A suitable reference frame needs to be older than two weeks (a particular setting aimed for the discovery of SNe) and have a seeing that is better than the new file. For images with seeing > 6 arcsec, the reference image seeing needs to be within ~ 0.5 arcsec of the new image seeing. If no suitable reference is found, *subpipe* will submit the new file as a reference job. If a suitable reference is found, *subpipe* will submit the file as a subtraction job.

---

[1] `https://github.com/rscalzo/subpipe`

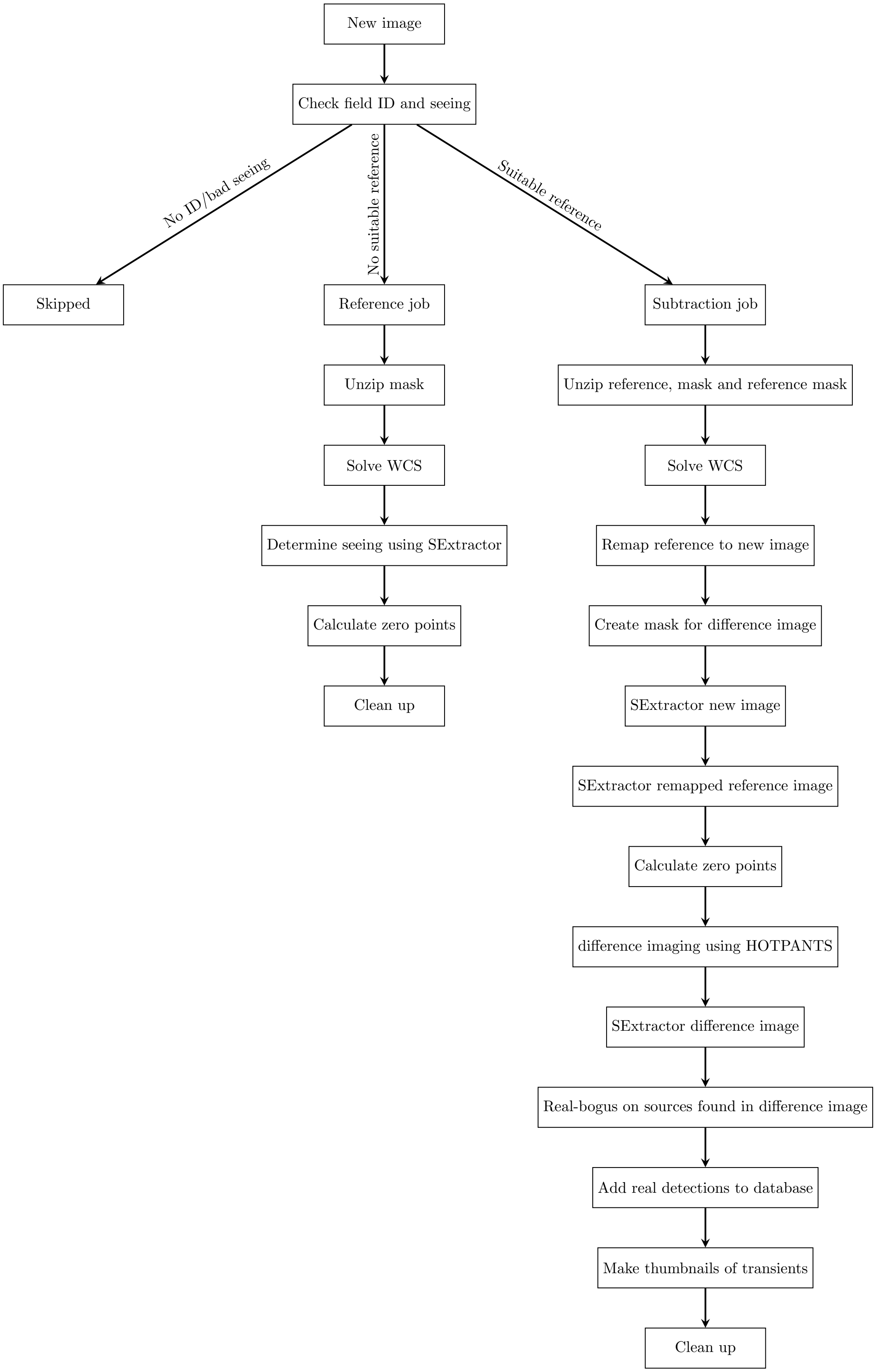

Figure 2.1: The basic flow diagram of the SkyMapper Transient Search pipeline (*subpipe*) before the adaption for MeerLICHT/BlackGEM.

For reference jobs, *subpipe*:

- unzips the corresponding mask (the default for SkyMapper is to have a zipped mask, which masks out bad pixels, accompanying each image),
- solves the astrometry for the new file,
- determines the seeing for the new file using SExtractor,
- calculates the zero points for the new file,
- and finally cleans up (i.e. zips and moves the pipeline products to the correct output directory.).

For subtraction jobs, *subpipe*:

- unzips the reference file, reference mask and new file mask,
- solves the astrometry for the new file,
- remaps the reference file to the new file using SWarp; creates a combined mask for the difference file,
- runs SExtractor on the new file and the remapped reference file,
- calculates the zero points for the new file,
- performs the difference imaging using HOTPANTS,
- runs SExtractor on the difference image,
- performs a real-bogus on the sources detected in the difference image,
- adds the real detections to the database,
- makes thumbnails of these detections,
- and finally cleans up.

Although *subpipe* has the option to use `Astrometry.net` (see Lang et al. 2010) to solve the astrometry, the default is to use an external perl script written by Brian Schmidt, followed by the use of the `ccmap` (under `images.imcoords`) command in `IRAF` (Tody, 1986). A sanity check on the astrometric solution found is done internally to ensure the solution makes sense, i.e. check that the plate scale is correct, the axes are orthogonal, and the position angle makes sense (if `Astrometry.net` was not used). *Subpipe* assumes an estimate of the seeing is in the header of new files - added by SkyMapper when the file was taken. As this seeing may not be accurate, *subpipe* determines the seeing for each new file using SExtractor, updating the header with this more accurate seeing estimate. For the calculation of zero points *subpipe* will first attempt to calculate zero points for a new file on a pre-existing SkyMapper frame calibrated with the AAVSO Photometric All Sky Survey (APASS, Henden & Munari 2014) Data Release 6 (DR6). If a previous calibration does not exist, *subpipe* will attempt to query a APASS DR7 catalogue for calibrations. If this fails, *subpipe* will auto-calibrate with default zero point values for each filter.

The image subtraction performed by HOTPANTS (Becker, 2015) is based on the 1999 Alard image subtraction algorithm (Alard, 1999). HOTPANTS uses a Gaussian-like convolution kernel to align images photometrically. This convolution kernel is determined for multiple sections of the image, allowing different convolution kernels to be determined for each section. The reference image is then convolved using these kernels and subtracted from the new image. Although HOTPANTS can use a reference image of a worse quality than the new image, this results in larger residuals, so it is recommended to use a reference image of better quality. Due to the way the convolution is performed by HOTPANTS, some noise terms are lost in the off-diagonal covariance terms. This results in the noise of the difference image being underestimated. Because of this, the error on detections within the difference image cannot be reported accurately.

The real-bogus algorithm used in *subpipe* makes use of a random forest machine learning classifier (an example of such an implementation is seen in Díaz et al. 2016). The classifier has been trained on SkyMapper data to identify sources more likely to be astronomical transients (real) versus artifacts caused by the image subtraction (bogus). *Subpipe* then adds any real detections to a database built with `Django`, an open source web framework in `Python`, allowing access to the thumbnail and light curve through a web browser.

In its original form, *subpipe* provided the benefit of a pipeline capable of transient detection through difference imaging. Three main points however, were identified at the start of the project for adaptation. These are:

- The generalization of *subpipe* i.e. moving hard-coded settings to a telescope specific constants file, making the code itself telescope independent.
- Adapting the way *subpipe* solves the astrometry to allow accurate solutions across large fields (see Section 2.2.2).
- Minimizing the artifacts produced by the image subtraction method.

2.2 Development of the main pipeline - KMTNet

The Korean Micro-lensing Telescope Network (KMTNet; see Kim et al. 2016) is a network of telescopes situated at the South African Astronomical Observatory (SAAO) site in Sutherland (South Africa), the Siding Spring Observatory (SSO) site in Australia and the Cerro Tololo Inter-American Observatory (CTIO) site in Chile. These 2.0-m class telescopes are equipped with a mosaic CCD camera optimised for wide-field photometric surveys. The primary science goal of KMTNet is the discovery of extrasolar planets towards the Galactic bulge using microlensing (see Paczynski 1986; see Schneider et al. 1992 for more details on gravitational lenses in general). When the Galactic bulge is not observable, the telescope is open to the host country for use, allowing us to obtain data from the SAAO site.

The primary reason why KMTNet observations were chosen as a pilot project to start the development of the MeerLICHT pipeline is the similarities between the CCDs. These features include the large field of view (FoV), the pixel scale, the large CCD size, and multiple readout channels. A comparison between KMTNet and MeerLICHT is given in Table 2.1. Known fields from 3 Large Survey Projects (LSPs) on MeerKAT, see Section 1.3, as well as a field from the OmegaWhite Survey (Macfarlane et al., 2015), were observed during the 2015/2016 KMTNet open

Table 2.1: A comparison between KMTNet and MeerLICHT.

Telescope	MeerLICHT	KMTNet
Mirror (m)	0.65	1.6
Camera (Mpixel)	110	340
Total FoV (deg^2)	2.7	4.0
# of CCDs	1	4
CCD Size	10k by 10k	9k by 9k
Plate scale (”/pixel)	0.564	0.400
Readout time (s)	7	30
Channels	16	32

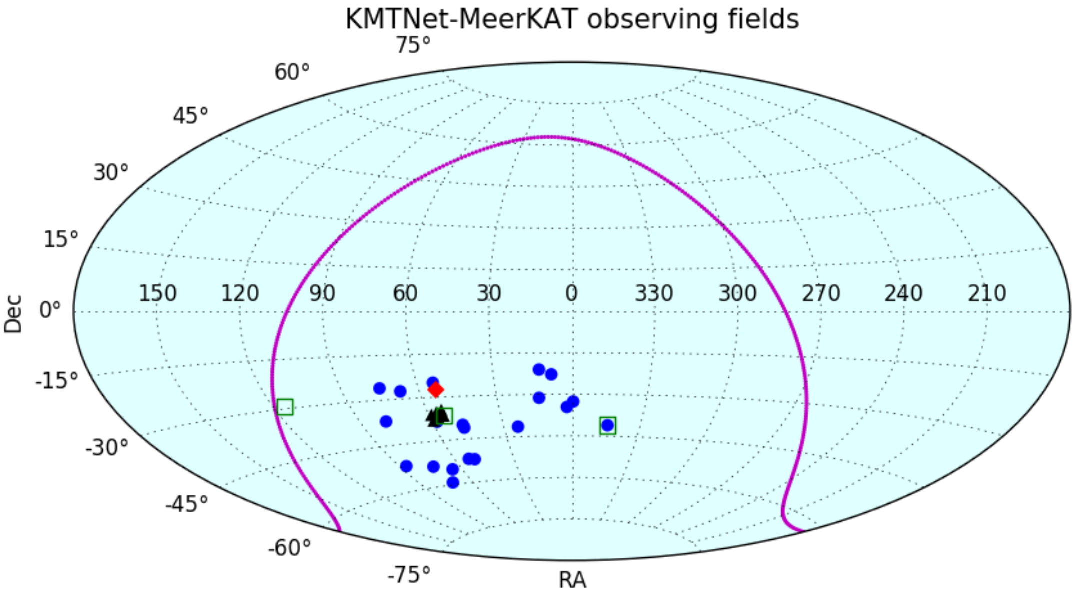

Figure 2.2: The fields observed with KMTNet. The magenta line shows the Galactic Plane, the solid markers represent multi-filter snapshot data, while the open squares represent time-series data. The blue circles are fields belonging to the MHONGOOSE Survey (De Blok et al., 2016); the black triangles are fields belonging to the MeerKAT Fornax Survey (Serra et al., 2016); and the red diamond is the field belonging to the LADUMA Survey (Blyth et al., 2016). The green squares overlap with a selected MHONGOOSE and Fornax field, while the empty square near the Galactic Plane is a field belonging to the OmegaWhite Survey (Macfarlane et al., 2015).

semester. Figure 2.2 shows a sky map of the fields observed.

2.2.1 Pre-processing based on KMTNet data

The use of KMTNet data was the starting point for the development of the MeerLICHT pipeline. This includes creating the mainframe for the pipeline, controlling the data flow and performing the basic corrections discuss in Section 1.5. I used KMTNet data to create the first version of the main MeerLICHT pipeline, as the format of the data was similar to that of MeerLICHT's. This part of the pipeline is written in Python and was developed as the main pipeline script, which submits images to *subpipe* for science analysis. Figure 2.3 shows a basic flow diagram summarizing the flow within the pipeline after using KMTNet data.

For a more detailed description of the pipeline (including installation, usage, parameters and functions), see Appendix A. The main developments I worked on with the use of KMTNet data include:

- Creating the overall structure of the pipeline.
- Including user definable parameters.
- Performing gain correction on all images.
- Creation of a master bias.
- Creation of a master flat.
- Performing the bias, overscan and flat field correction on science images.
- Constructing the data array for images.
- Cleaning cosmic rays.
- Creating a mask for each science image.
- Submission of the reduced science image to *subpipe* for science analysis.
- Allowing the processing of both single and multi-extension filts files.
- Allowing processing of files compressed via fpack.
- Including an option to compress output files.
- Implementing multi-processing.
- Including standard logging.

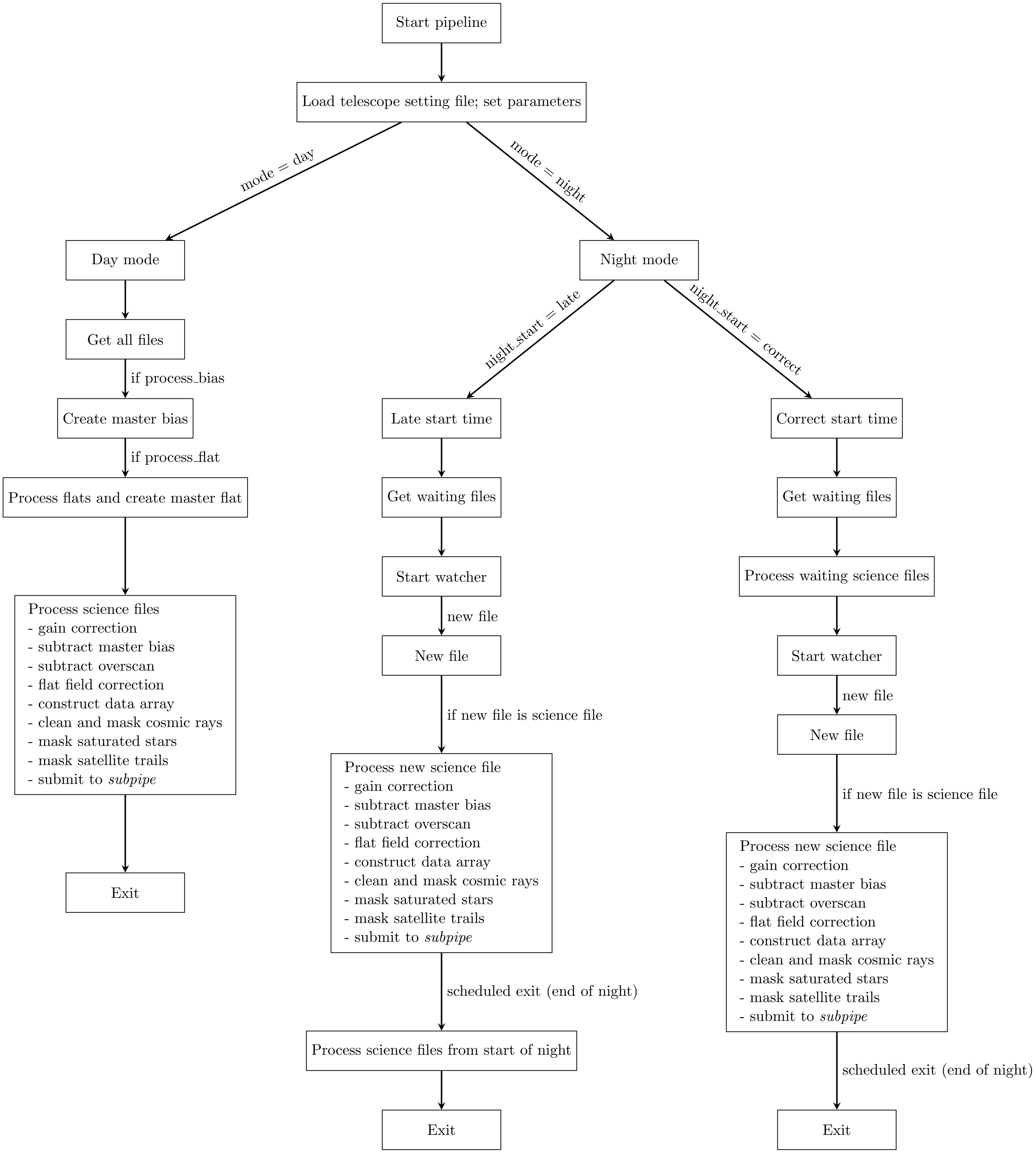

Figure 2.3: The basic flow diagram of the main pipeline after development with KMTNet data.

- Including option to upload logs to slack.
- Including a scheduled exit time.

The overall structure of the pipeline controls the data flow within the pipeline. A number of parameters, either loaded from a file or inputed by the user, defines how the data are treated and which functions are performed on the data. The pipeline can perform both bulk processing, using the day mode, or real-time processing, using the night mode. The night mode of the pipeline makes use of a watcher to 'watch' for new files.

The gain for KMTNet was determined using the `biasgain_determination_kmtnet.py` script written by Paul Vreeswijk - see Figure 2.4. The mask covers bad pixels, edge pixels, cleaned cosmic rays, saturated stars, and satellite trails present in the science image. For KMTNet, the bad/edge pixels were determined manually using the raw data.

Since KMTNet data contained each readout channel in a separate extension - forming a Multi-Extention Fits (MEF) file, I developed the pipeline to process both single fits and MEF files. Due to the large size of each file, it was decided that both input and output files would be compressed using NASA's HEASARC software: fpack[2]. Thus, I developed the pipeline to read both uncompressed and fpacked raw files, with the option to compress output files via fpack.

With the main objective of this pipeline being the real-time processing of files, I implemented multiprocessing with the purpose of speeding up processing time. I included standard logging within the pipeline, printing the pipeline status to screen, as well as writing the pipeline status to a log file. To allow the status of the pipeline to be monitored, I also included the option to upload the night mode log messages, including the normal running of the pipeline as well as errors, to `slack`. `Slack` is a cloud-based messaging tools that allows users to subscribe to different channels within the workspace. As such, I set up a MeerLICHT workspace, with different channels reporting different levels of the pipeline status e.g. a critical channel reports all critical errors for immediate attention.

---

[2] `https://heasarc.gsfc.nasa.gov/fitsio/fpack/`

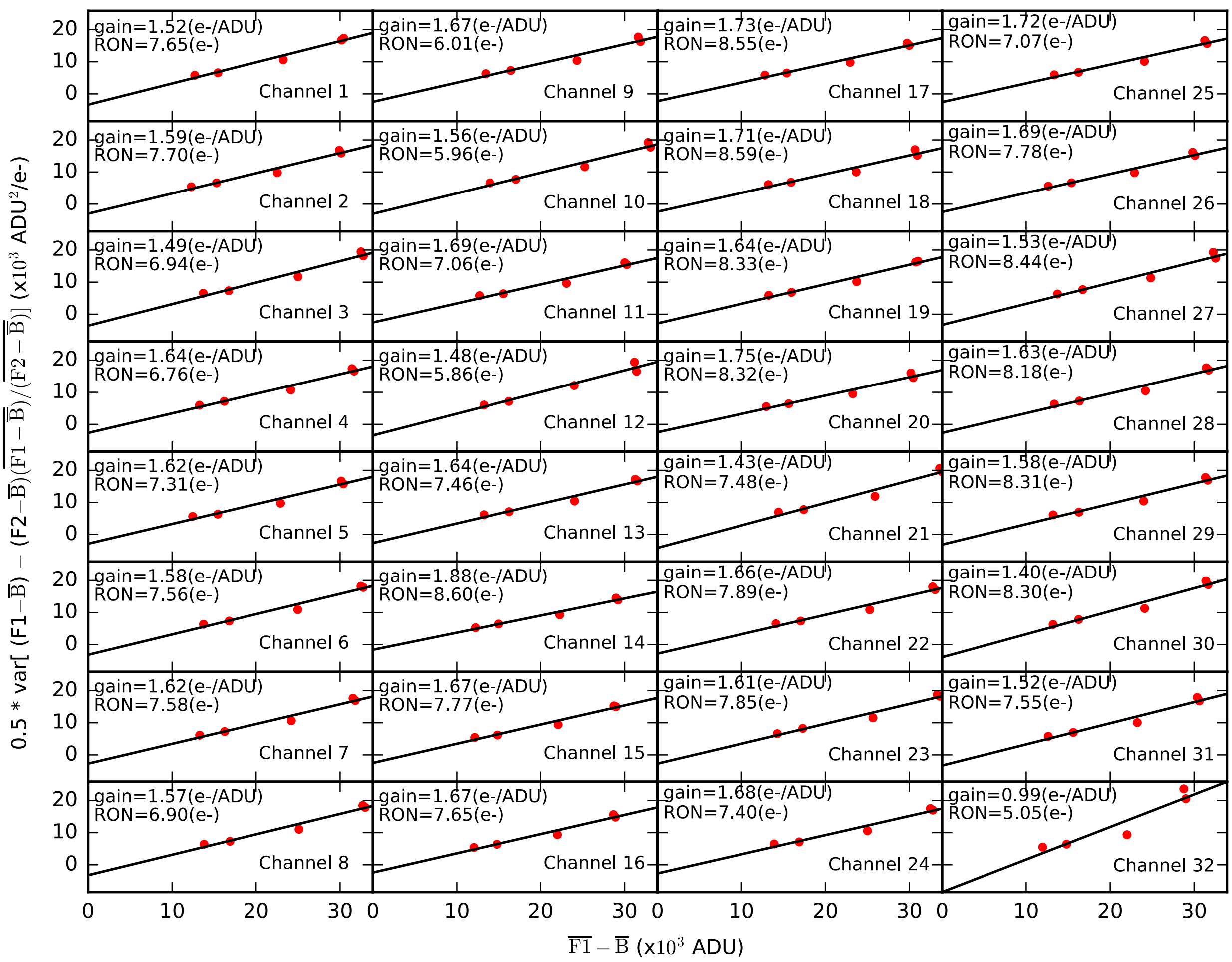

Figure 2.4: The gain and readnoise for KMTNet determined using Paul Vreeswijk's script using method 2 from http://www.mirametrics.com/tech_note_ccdgain.php. The channel number corresponds to the extension in the KMTNet MEF i.e. channel 1 is extension 1 etc.. The mean gain and readnoise of 1.6 e^-/ADU and 7.5 e^-, respectively, are close to the reported values of 1.4 e^-/ADU and 7 e^- (Atwood et al., 2012).

I included two options for the night mode of the pipeline (correct or late), with slightly different data flows (see Figure 2.3), depending on when the pipeline is started. This was done to ensure no files were missed during the night mode of the pipeline, while focusing on real-time processing. I included a scheduled exit time for the night mode of the pipeline, allowing the pipeline to finish up any waiting files and exit once the night is over.

2.2.2 Adaption of *subpipe* with KMTNet

KMTNet data were also used to begin the adaption of *subpipe*. The main developments to *subpipe* I implemented using KMTNet data include the following:

- Generalizing *subpipe* by moving all settings to a constant file to be loaded in for each telescope/instrument.
- Making *subpipe* callable by other python scripts and linking it to the pre-processing.
- Moving to standard python logging within *subpipe*.
- Changing the criteria for the reference used.
- Replacing the astrometry solver purely to `Astrometry.net`.
- Replacing HOTPANTS with ZOGY.
- Restructuring the data flow within *subpipe*.

As *subpipe* was originally written for SkyMapper use only, many settings were hard coded and not kept in the settings file (named as `Constant.py`). In order to make *subpipe* a part of a generalized pipeline, able to process data from multiple telescopes, I moved all telescope specific settings within the code to the constants file, each telescope having its own constants file (named as `Constant_telescope.py`, where `telescope` is the name of the particular telescope). I also adapted *subpipe* to be callable by another script, while still keeping its ability to be run independently, to be integrated into the MeerLICHT pipeline. I moved all logging within *subpipe* to standard python logging, with links between the main pipeline log file and each *subpipe* log file for a complete record of the pipeline run. Since the main focus of the MeerLICHT pipeline is the detection of transients in general, I removed the constraint that the reference used must be older than two weeks.

With different FoV and WCS projection types for different telescopes, I replaced the use of Brian Schmidt's WCS code and `IRAF` with `Astrometry.net` in order to solve the astrometry over large FoVs accurately. Without corrective lenses to flatten the focal plane for the large FoV of KMTNet, the focus of KMTNet lies in the centre of the 4 frames (see Figure 2.5). The use of

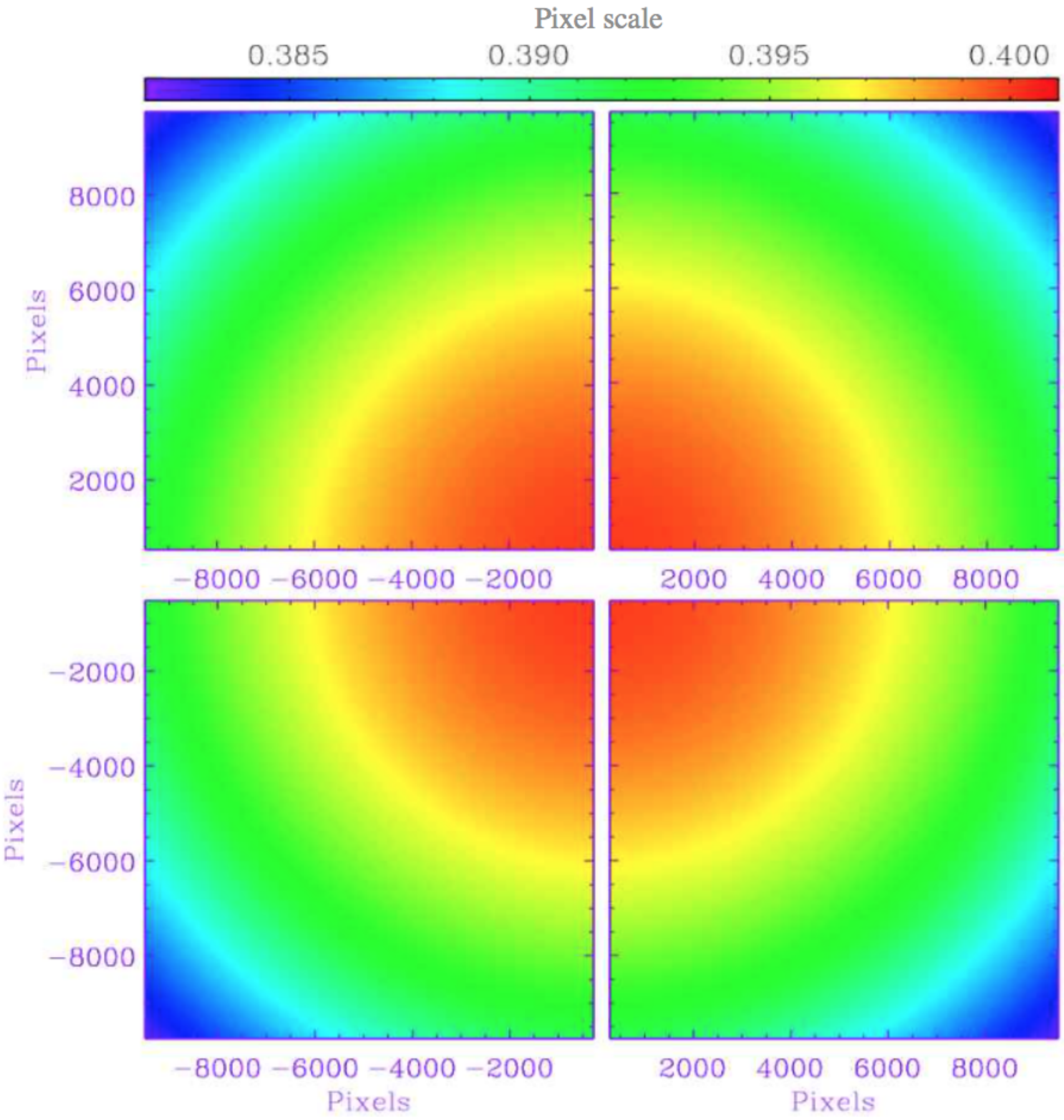

Figure 2.5: A plot from the KMTNet website (`http://kmtnet.kasi.re.kr/kmtnet-eng/astrometric-calibration-for-kmtnet-data/`) displaying the pixel scale (whose value is given by the colourbar at the top) across the four KMTNet chips. Since the focus point lies off image for all frames, using too few stars across the entire field does not allow an accurate determination of the astrometry.

`Astrometry.net` greatly improved the astrometry over the large FoV, but still with a noticeable increase in offset towards the outer corners of the frame due to the curved focal plane and the fact that `Astrometry.net` only uses a minimum number of star to determine the astrometric solution. By providing `Astrometry.net` a list of all the detected stars in the image to use in the astrometric

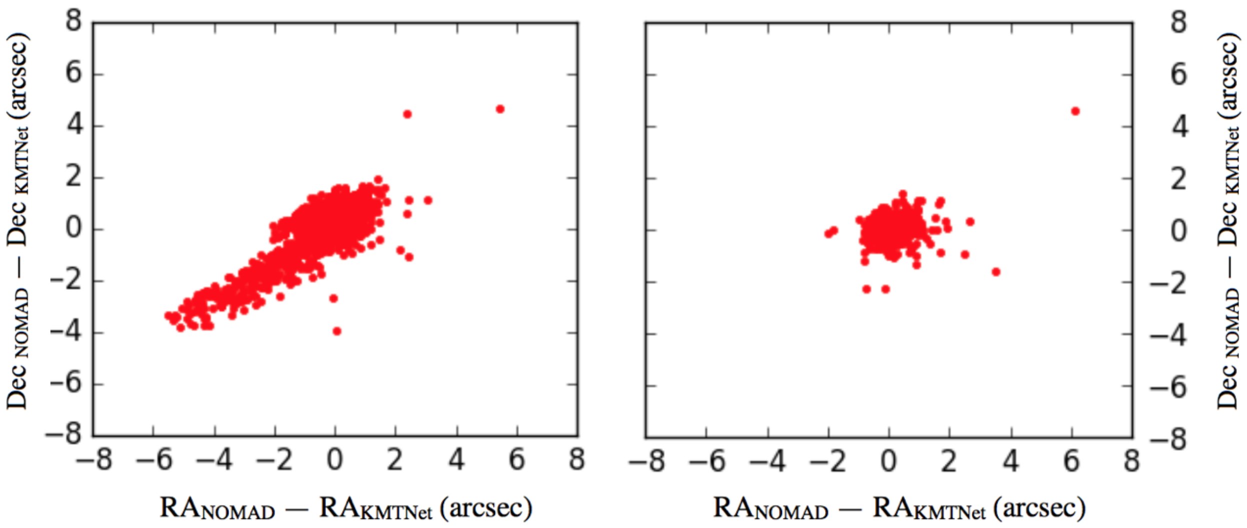

Figure 2.6: Plots showing the offset of the astrometry compared to the NOMAD catalogue for a single KMTNet image. Left: astrometry from the NOMAD catalogue compared to the solution found by `Astrometry.net`, using the built-in source extractor without the extra verify step. Right: Astrometry from the NOMAD catalogue compared to the solution found by `Astrometry.net` with the extra verify step.

solution, this corner effect was removed. This was initially achieved by running `Astrometry.net` a second time with the **- - verify** parameter. This parameter makes `Astrometry.net` use all the stars in the list originally produced by `Astrometry.net`'s built-in source extractor. Figure 2.6 shows the astrometric offset, compared to the NOMAD catalogue (Zacharias et al., 2005), using `Astrometry.net`'s built-in source extractor without and with running this extra step. By replacing `Astrometry.net`'s built-in source extractor with SExtractor (by using the **- - sex** parameter when running `Astrometry.net`), the SExtractor catalogue is used to determine the astrometric solution, producing the same effect as the extra verify step.

Using `Astrometry.net` to solve the astrometry did, however, resulted in an issue caused by WCS projection types. This issue is due to the fact that the output WCS projection type from `Astrometry.net` is set to SIP (Simple Imaging Polynomial), but SWarp, which is used to remap the reference image to the new image, does not understand the SIP projection. This issue was solved by converting the WCS projection type from the SIP projection to the TPV projection, a TAN (tangent plane) projection with a general polynomial distortion correction, using the `sip_to_pv.py` script obtained from the Palomar Transient Factory (PTF) team (Shupe et al., 2012) after running

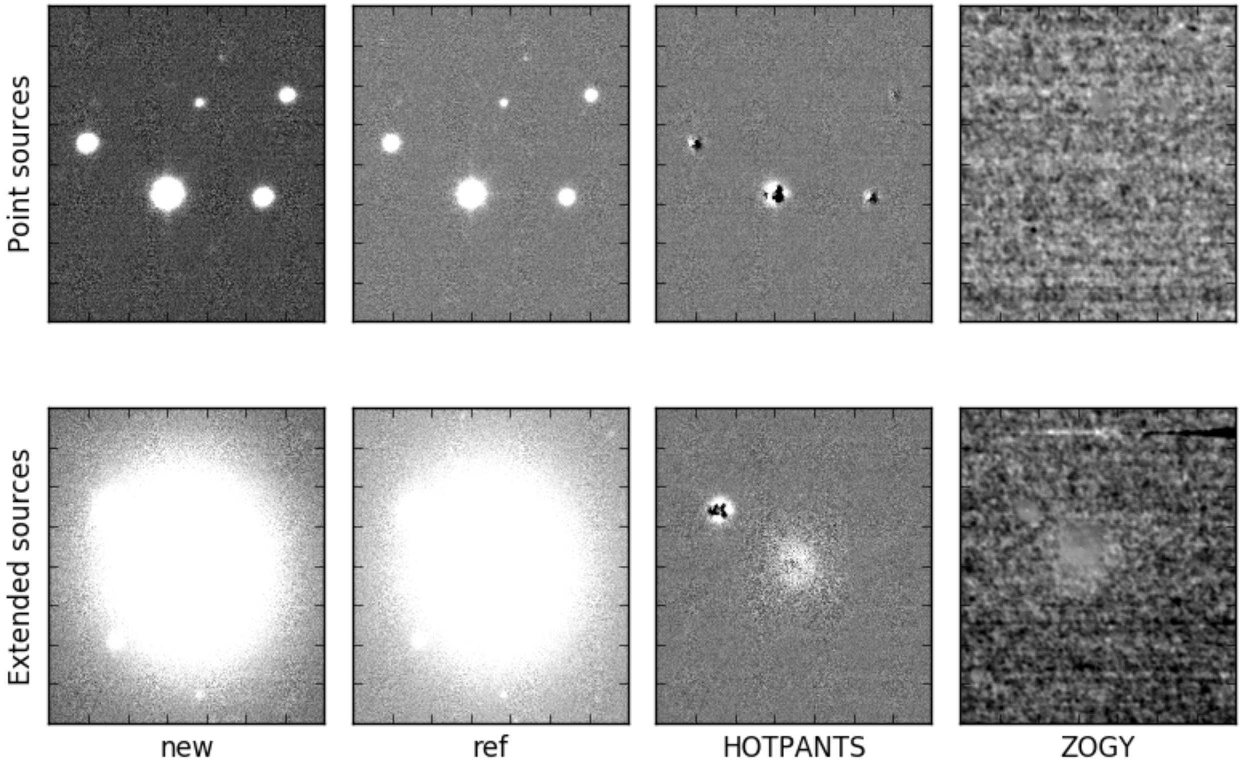

Figure 2.7: Comparing the results that are used in transient detection produced by HOTPANTS and ZOGY for point sources (top) and extended sources (bottom), respectively. Top (from left to right): New image, reference image, difference image produced by HOTPANTS, S_corr image produced by ZOGY. Bottom (from left to right): New image, reference image, difference image produced by HOTPANTS, S_corr image produced by ZOGY. Each image is zscaled to its own limits in order to highlight the structure present in the image (since the structure present in S_corr can not be seen if scaled to the same values as the difference image produced by HOTPANTS). Due to the accuracy of the PSF fitting in ZOGY, the artifacts produced in the difference image are far less.

`Astrometry.net`.

The development of a proper image subtraction method by Zackay, Ofek and Gal-Yam (ZOGY; see Zackay et al. 2016) provided an alternative method to HOTPANTS. ZOGY uses statistical principles to derive the optimal statistic for transient detection, correctly taking into account all errors. Instead of a convolution kernel, ZOGY uses the PSF across the reference and new images during the photometric alignment, providing a much more accurate representation of the sources in the image compared to the convolution kernel fitted by HOTPANTS. This is especially true for extended objects such as galaxies (see Figure 2.7). ZOGY uses the derived PSFs, along with an

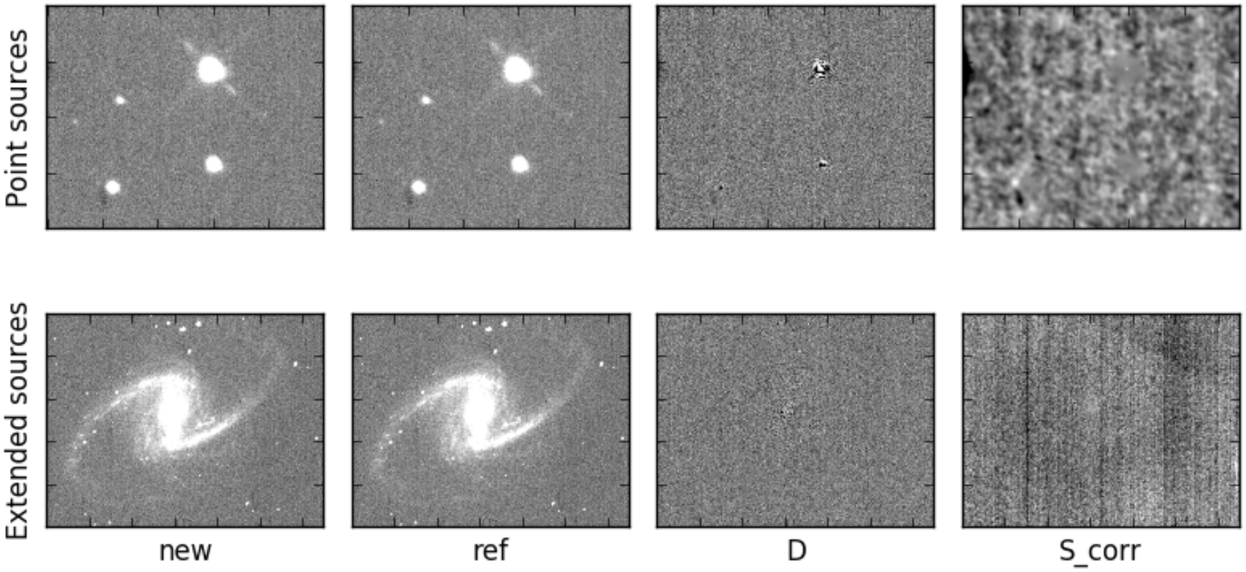

Figure 2.8: Outputs from ZOGY for point sources (top) and extended sources (bottom), respectively. Top and bottom (from left to right): New image, ref image, difference image, corrected significance image. Each image is zscaled to its own limits in order to highlight the structure present in the image (since the structure present in S_corr can not be seen if scaled to the same values as the difference image). It is the corrected significance image (right panel) that is used for transient detection.

estimate of the background standard deviation and flux ratios, to perform the image subtraction by using Fast Fourier Transforms (FFTs). The difference image is then used to create a significance and a corrected significance image (see Figure 2.8).

It goes beyond the scope of this thesis to quantify the difference in performance of HOTPANTS versus ZOGY, as we are not developing a new image subtraction technique, but merely implementing the best possible image subtraction algorithm available. The improved performance of ZOGY over e.g. the algorithms by Alard & Lupton (1998) has been demonstrated most convincingly by Zackay et al. (2016) in Section 6 of their paper. Our comparison in Figure 2.7 supports the main findings of Zackay et al. (2016), in the sense that for images that are accurately registered and adequately sampled, ZOGY does not leave any subtraction residuals or deconvolution artifacts. I do, however, test the computational performance of ZOGY in the MeerLICHT pipeline and refer to Section 3.4 for more details.

As the name suggests, the significance image represents the significance of all pixels in the difference image, with the corrected significance image including corrections for source noise and astrometric error. It is the corrected significance image that is used by *subpipe* to look for transients. There are three main advantages of ZOGY (Zackay et al., 2016) that are in use in its implementation in the MeerLICHT pipeline. First, it is mathematically proven to be the optimal transient detection statistic in the limit of background-limit noise. Second, it provides credible detection significance directly from the output image. It is symmetric between the reference and new image, so the reference image does not need to be of better quality than the new image. And thirdly, it is roughly an order of magnitude faster than other methods.

With the implementation of ZOGY in Python by Paul Vreeswijk, I added the option to perform difference imaging with ZOGY to *subpipe*. The method used by *subpipe* is determined by the `subtraction` variable defined in the constants file. This implementation of ZOGY uses the external program, PSFex (Bertin, 2013), to determine the PSF across the reference and new image. Comparing the results that are used for transient detection from HOTPANTS (difference image) and ZOGY for both point sources and extended sources, see Figure 2.7, we see ZOGY produces much cleaner images.

To simplify the flow, I rearranged the overall structure of *subpipe* to perform common steps first, before submitting the image as a reference or subtraction job. A flow diagram showing the adapted steps is shown in Figure 2.9. The new data flow at this point evolved to:

- unzipping the image mask,
- solving the astrometry,
- calculating the zero points for photometric calibration,
- and then proceeding to submit the image as a reference or subtraction job.

Since ZOGY does not require the reference to be within a margin, or of better quality, to the new image, I removed the constraints on the seeing of the reference. If no reference is found, *subpipe* will submit the image as a reference job: only needing to clean-up (compressing outputs and moving them to their final write path). If a reference is found, *subpipe* will submit the image as a subtraction job:

- unzipping the reference and the corresponding mask,
- remapping the reference image to the new image using SWarp,
- creating a mask for the difference image,
- performing the difference imaging using ZOGY,
- running SExtractor on the difference image,
- performing a real-bogus on sources detected,
- making thumbnails of the transients,
- and cleaning-up.

Solving the astrometry with `Astrometry.net` using SExtractor, instead of the built-in source extractor, I could remove the additional steps to perform SExtractor on each image, as this was already done by `Astrometry.net`. Because *subpipe*'s real-bogus algorithm was only trained on SkyMapper data, I removed the real-bogus step at this point as it could not provide an accurate classification of real transients for KMTNet data. I also removed the database step as the final MeerLICHT pipeline will not make use of the SkyMapper database.

The major lesson learnt from the use of KMTNet data is the need for accurate astrometric and photometric alignment in order to perform reliable difference imaging. If the astrometry is not accurately determined across the image, the result is dipole residuals in the difference image. ZOGY has the advantage of taking the astrometric errors into account, allowing it to correct for small astrometric offsets and removing this effect. If the photometry is not accurately aligned, the result can be ring-like structures in the difference image (caused by the over/under estimation of the source's centre/wings). Since ZOGY uses the PSF determined for each image and the flux ratios to align images photometrically, the shape of each source is accurately represented.

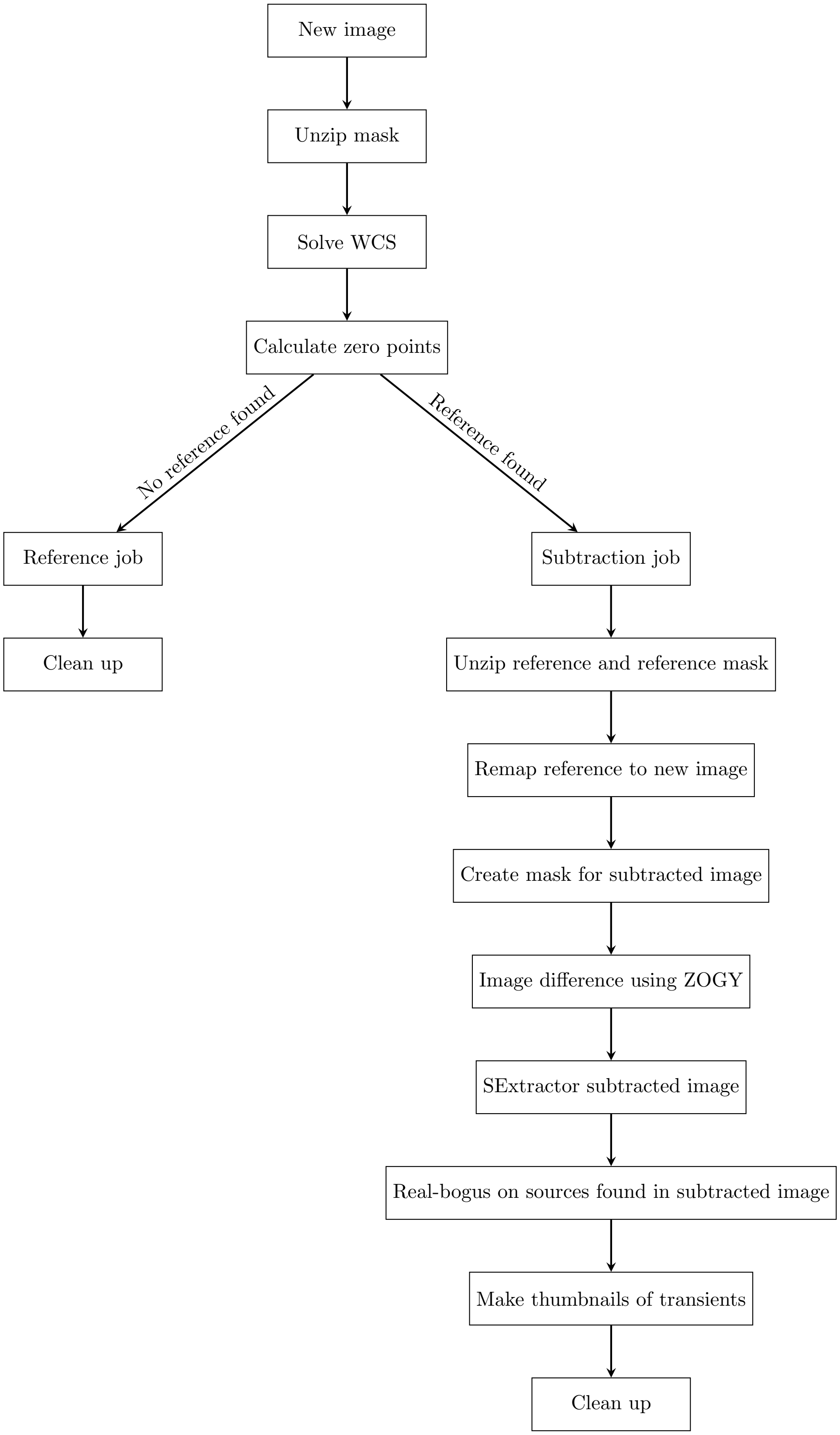

Figure 2.9: The basic flow diagram of *subpipe* after the adaption using KMTNet data.

During the development of the pipeline, the pre-processing pipeline was used to reduce KMTNet data by a group at the South African Astronomical Observatory (SAAO) interested in asteroid photometry in wide field surveys. The pipeline played a crucial role in obtaining the quality needed to obtain their results. These results have been submitted as a paper (Erasmus et al., 2019) and is currently under review after minor changes.

2.3 A real-time transient pipeline for MeerLICHT

MeerLICHT was installed in Sutherland on 7 July 2017 and test observations were obtained in the following weeks and months to continue the development of the MeerLICHT pipeline. The changes described below where implemented on top of the adaptions previously described. A basic flow diagram of the main pipeline after development with MeerLICHT data is shown in Figure 2.10.

Unlike KMTNet, raw MeerLICHT files contain all readout channels as a single array within a single extension. Due to the compression of files via `fpack`, I found that the primary header of the file (containing the header keywords) appears in the compressed extension alongside the data. This is different compared to compressed MEF files (as was the case with KMTNet), where the primary header appears in the uncompressed extension. Thus, I changed which header the pipeline will read from, depending on whether the file is compressed or not, and the number of extensions present in the file. Since the amount of compression can also be defined by the user, I included additional settings to set the dithering and quantization parameters of `fpack`.

2.3.1 Characterisation of the MeerLICHT CCD properties for the main script pipeline

Using a series of exposures where a bright isolated star was placed on each readout channel, I determined the crosstalk correction for each channel by looking at the effect the bright star had on the background level in all other channels (see Section 1.5). To determine the crosstalk correction, I used the same method implemented by `IRAF`'s `xtcoeff` in Python. Using this method, we get

$$\text{crosstalk correction for a single channel pair} = \frac{\text{victim} - \text{median}_{\text{victim}}}{\text{source} - \text{median}_{\text{source}}} \tag{2.1}$$

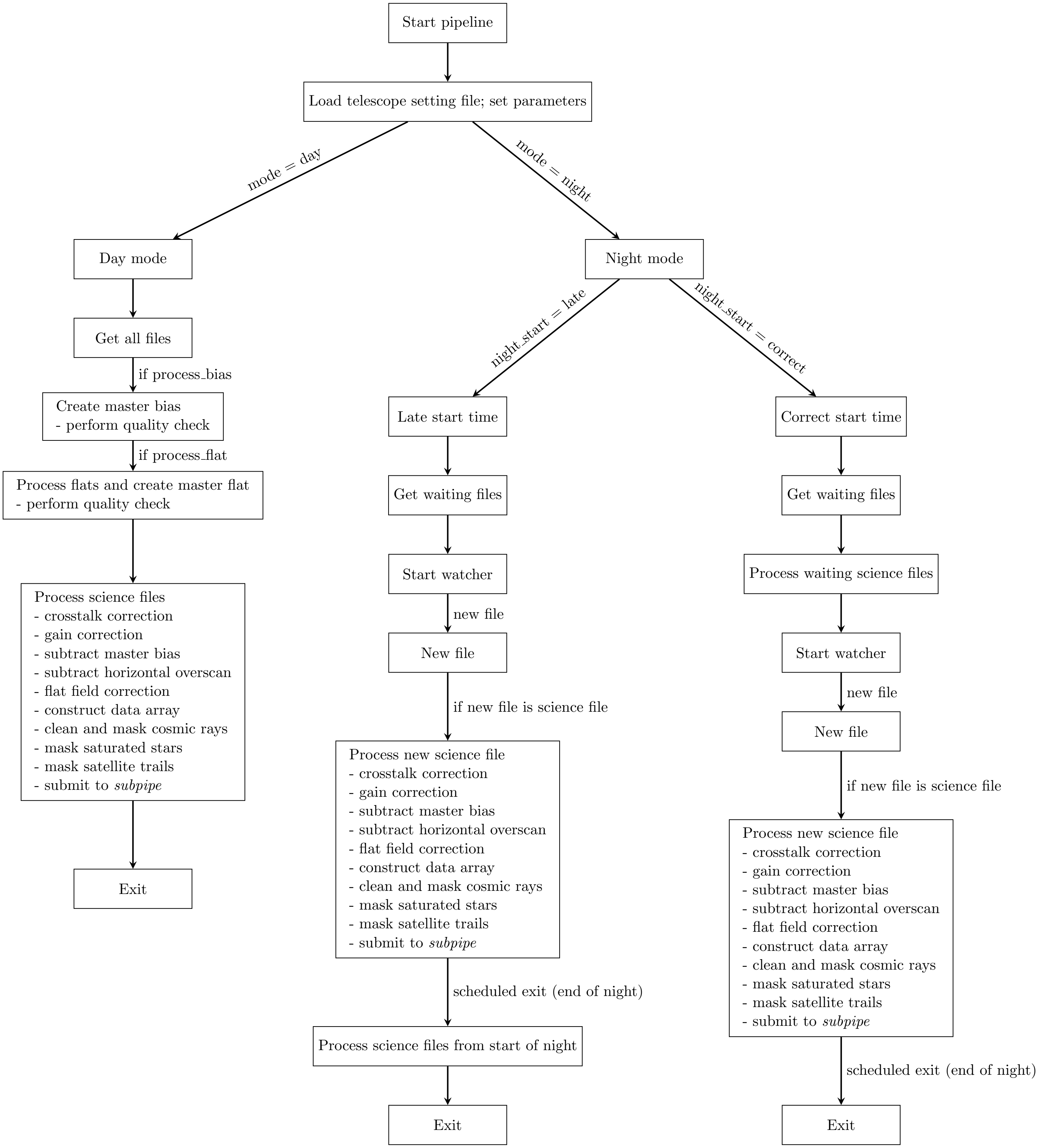

Figure 2.10: The basic flow diagram of the main pipeline after development with MeerLICHT data. The main differences are the implementation of the quality checks and crosstalk correction.

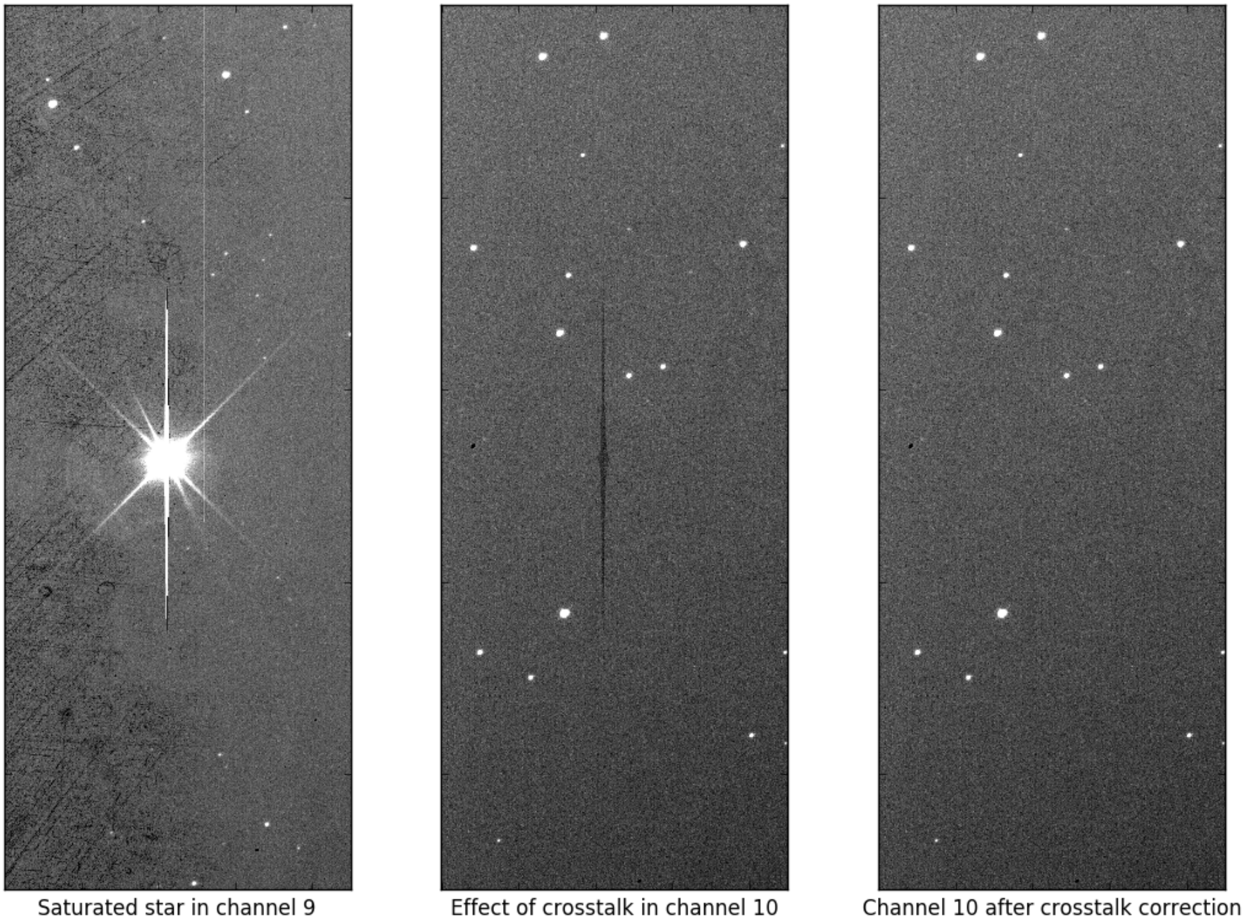

Figure 2.11: A section of an image before and after crosstalk correction (see Figure 2.16 for how channels are defined). Left: Section in channel 9, showing a saturated star. Middle: The same section as the left, but in channel 10, showing the effect of the saturated star. Right: The same section as the middle. but after the crosstalk correction. The previously seen effect is gone.

where ‘victim’ is the counts in the channel effected by the crosstalk and ‘source’ is the counts in the channel containing the bright star. A visual presentation of the effect of crosstalk on the image, as well as the correction, is shown in Figure 2.11. The crosstalk correction implemented on MeerLICHT is only to first order, as the source channel is assumed to have no crosstalk when making these calculations. This correction is adequate, but to achieve higher orders of crosstalk correction, a more complex calculation including initial crosstalk terms needs to be done.

To ensure proper bias subtraction and flat field correction, I included quality checks for the master bias and master flats in the pipeline. These checks were put in place to ensure that the calibration files are within the expected values, since, if an error occurred during the creation of the master files, certain statistical values would be affected. I performed a series of tests to determine the optimal noise levels of the master files.

For bias frames, the noise is determined by the read noise plus Poisson noise. Thus, the expected noise level for master biases follows the characteristic $1/\sqrt{N}$ expected by Poisson statistics, where N is simply the counts. This is shown in Figure 2.12. The measured noise, given by the solid points, closely follows the expected $1/\sqrt{N}$ trend given by the red dashed line. The dot-dashed horizontal line shows the read noise determined by an adapted version of Paul Vreeswijk's script, while the dotted horizontal line shows where the improvement between consecutive measurements reached 10%. The optimal noise is determined when the noise in the master file is below the read noise and improvements to the noise are below 10%. Thus, the optimal noise for master bias files is ~ 3.3 electrons. It is at this level that we start probing the actual read noise of the CCD.

For the master flat, the quality depends on the total signal per pixel used to create the master flat, instead of simply the number of files. This is because the median signal in a flat is not constant (since the median counts is determined by the exposure time and the time of day each flat was taken). Because of this, extra parameters such as weighting and scaling are used during the creation of the master flat. Since flat frames have different levels, a scaling factor needs to be applied before combining them to place the flats on the same level. However, since a flat with higher signal will be more significant, weighting also needs to be taken into account when creating the master flat. The standard deviation within the normalization section of the normalized master flat is shown in Figure 2.13 as a function of the median signal per pixel, for each filter. We note this standard deviation flattens out for all filters around 150 000 electrons ($\sim$ 65 000 counts). It is at these levels, that the true pixel-to-pixel sensitivity is being probed. We also see a clear wavelength dependence, with the redder filters showing smaller standard deviations.

MeerLICHT's CCD is housed inside a cryostat, which is cooled to a constant temperature to reduce thermal noise. The signal from the CCD, however, is digitized outside of the cryostat in the CCD controller (see Figure 1.3). Because of this, thermal noise is introduced as the signal travels along the cables. This noise also differs from image to image. This effect can be determined using

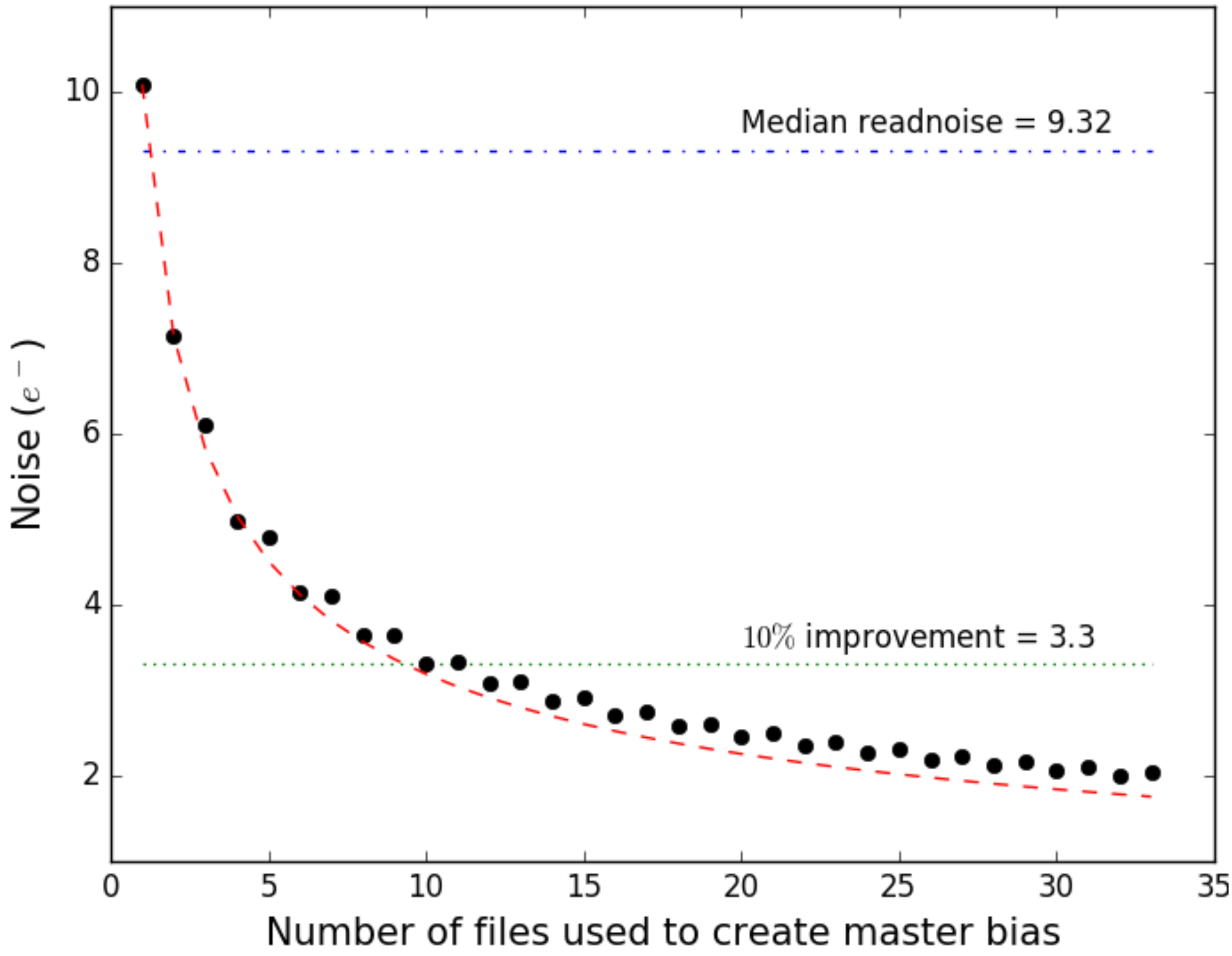

Figure 2.12: The measured and expected noise from a master bias created with increasing number of bias files. The solid circles represent the measured noise, measured from the bias region in the channel. The red dashed line is the expected noise of $\frac{1}{\sqrt{N}}$. The dot-dashed horizontal line is the median measured readnoise, determined by the adapted version of Paul Vreeswijk's script (see Figure 2.17), for all channels. The dotted line shows the level at which the measured noise improves from the previous measurement by 10%.

the residual in the overscan regions of the CCD. As these regions only contain the signal from the bias level (a set parameter), the residuals present after subtracting the master bias, are purely due to this effect. Normally, this is then corrected by subtracting the median of the overscan region after the master bias correction. MeerLICHT has two overscan regions per readout channel, see Figure 2.14. A vertical region running alongside the right of the readout channel, and a horizontal region running alongside the readout end of the channel (this is defined by the direction is which the channel is read out i.e. this is the bottom of the channel for the top channels, and the top of the channel for the bottom channels). However, the bias level across the channel contains a slope,

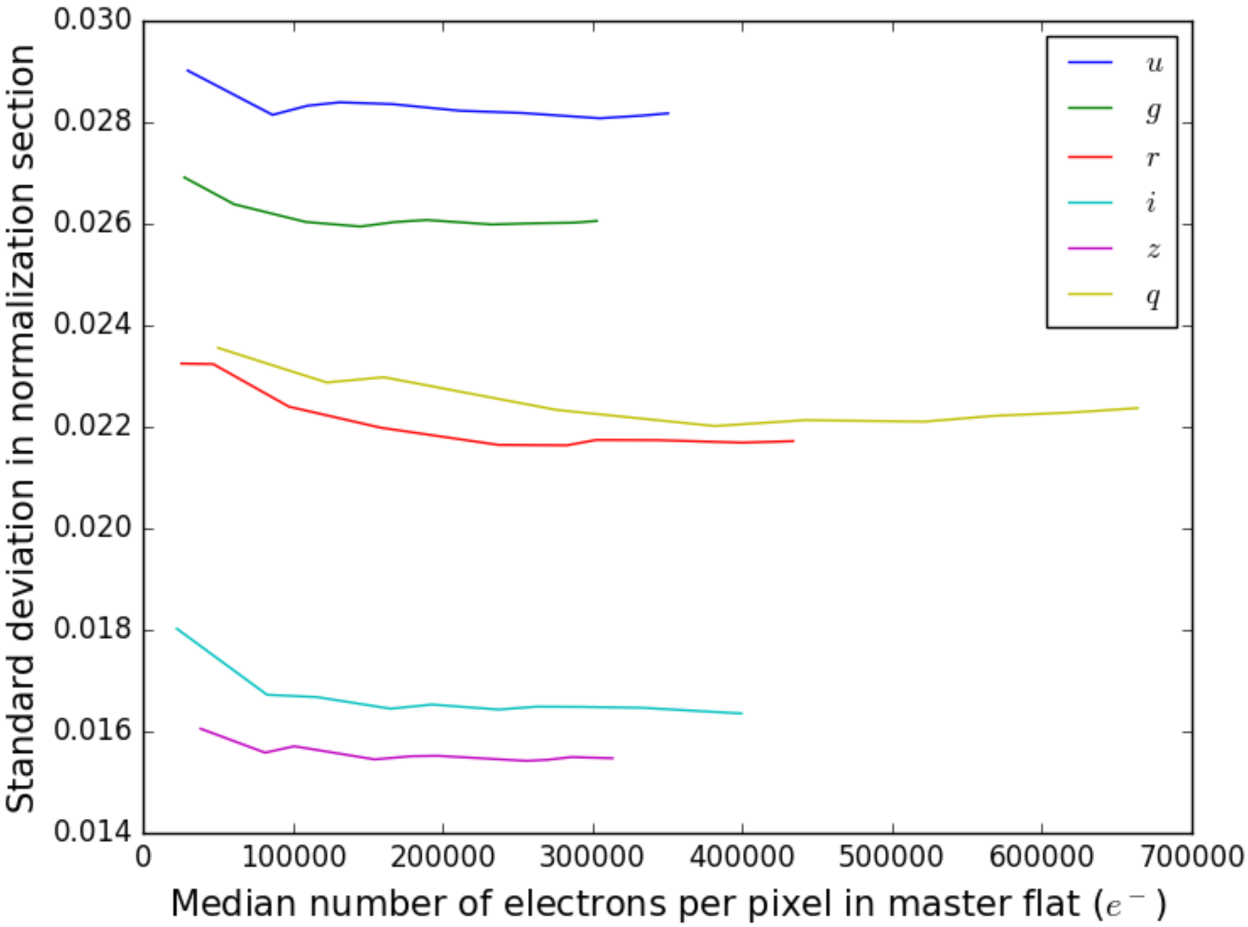

Figure 2.13: The standard deviation within the normalization section of the normalized master flat for each filter as a function of the median electrons per pixel. The true pixel-to-pixel sensitivity is probed at the levels where the standard deviation levels off. A clear wavelength dependence, with the redder filters showing smaller standard deviations is seen.

see Figure 2.15, and thus, the residual after subtracting the master bias is not constant across the channel. Therefore, I implemented the use of the horizontal overscan region for MeerLICHT, subtracting the column-wise median instead of the usual overall median (see Figure 2.15) in the pipeline.

I incorporated the addition of multiple new keywords, describing the processing and parameters used by the pipeline, to the headers of both calibration and science files. A summary of these header keywords is shown in Table 2.3. The gain determined for MeerLICHT, using an adapted version of Paul Vreeswijk's script, is shown in Figure 2.17, and summarized in Table 2.2. A full frame image from MeerLICHT, showing the channel numbers in shown in Figure 2.16. For MeerLICHT,

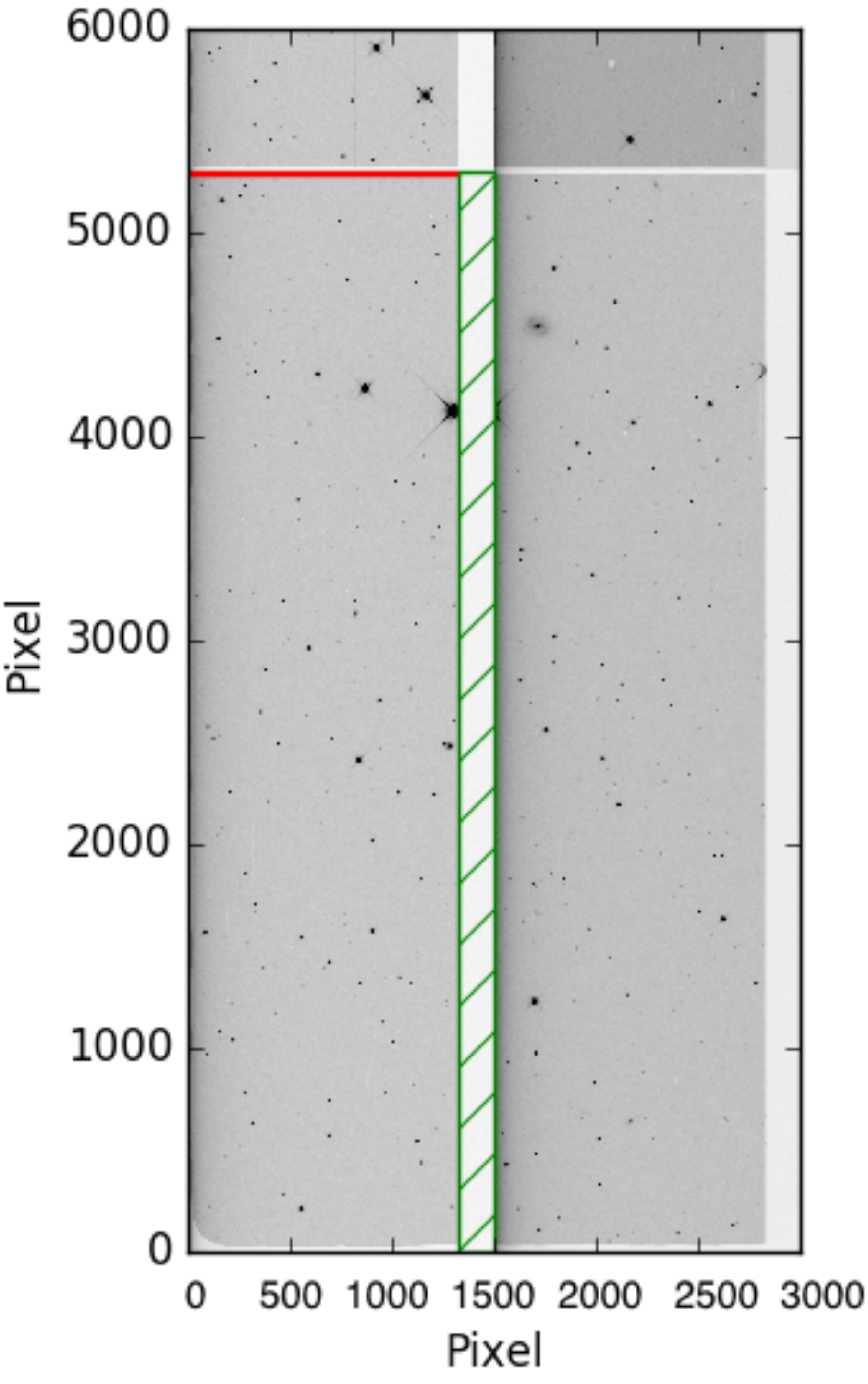

Figure 2.14: The bottom left corner (3000 x 6000 pixels) of a raw science image. The overscan regions for the bottom left channel are highlighted by the coloured rectangles. The green, striped rectangle shows the overscan region to the right of the channel, while the red solid rectangle shows the overscan region used to fit the temperature dependent signal. This region is at the top of the channel for the bottom row of channels and at the bottom of the channel for the top row of channels.

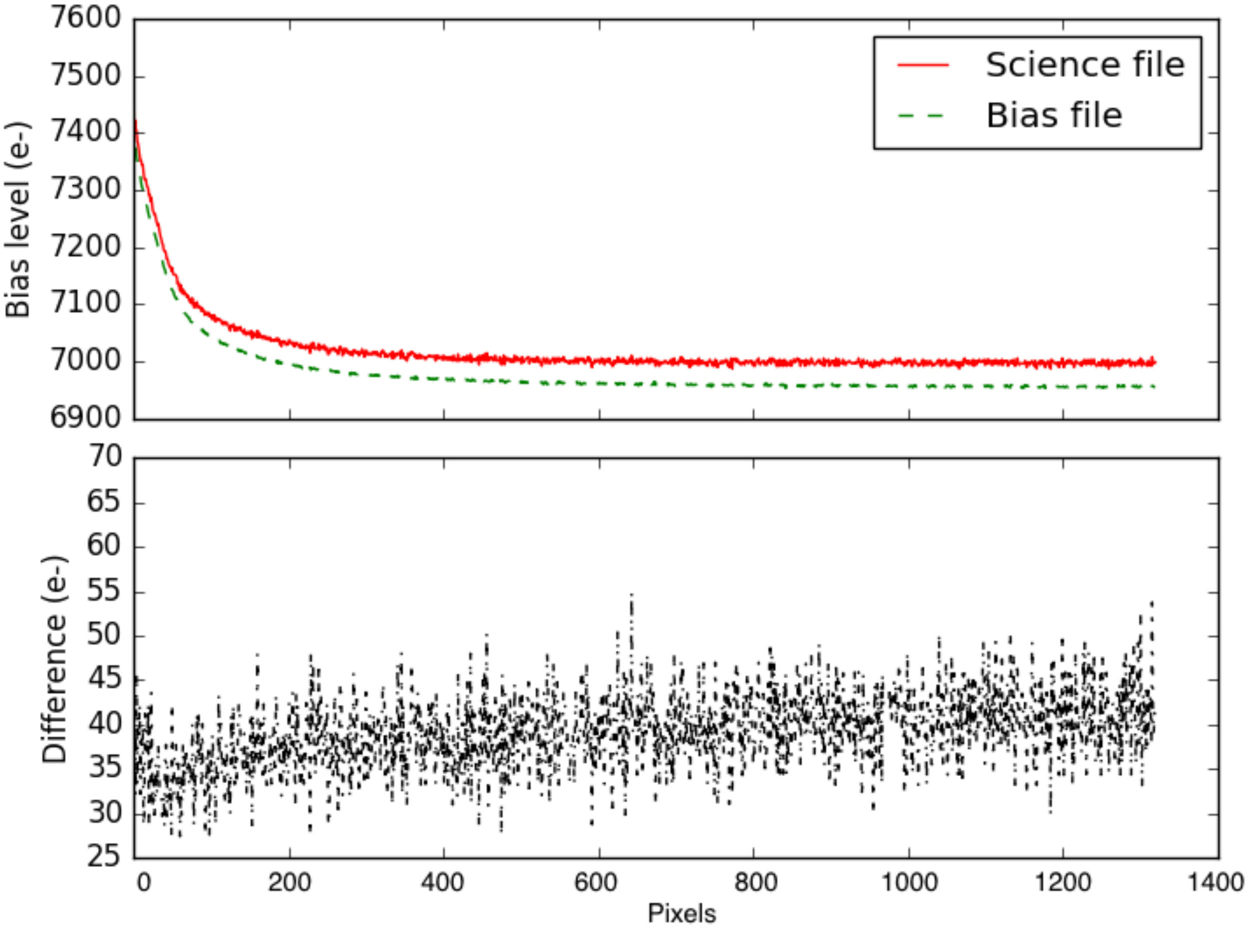

Figure 2.15: Top: The shape of the bias level, in the overscan region, across a single channel for a science image and a master bias. The solid red line is the bias level for a science image taken on 21 October 2017, while the dashed green line is the bias level for a master bias created on 20 October 2017. Bottom: The difference between the two bias levels in the overscan region. As this difference is not flat, a column-wise median is used to correct for this effect, instead of the usual overall median.

a bad pixel mask, shown in Figure 2.18, is loaded in from file. This mask was determined using the test data and separately masks bad and edge pixels. These masked pixels make up 1.3% of the entire image. With MeerLICHT's large FoV, the possibility of observing multiple satellite trails in a single image increases. Therefore, I adjusted the settings for the satellite trail fitting, including a loop to look for multiple trails.

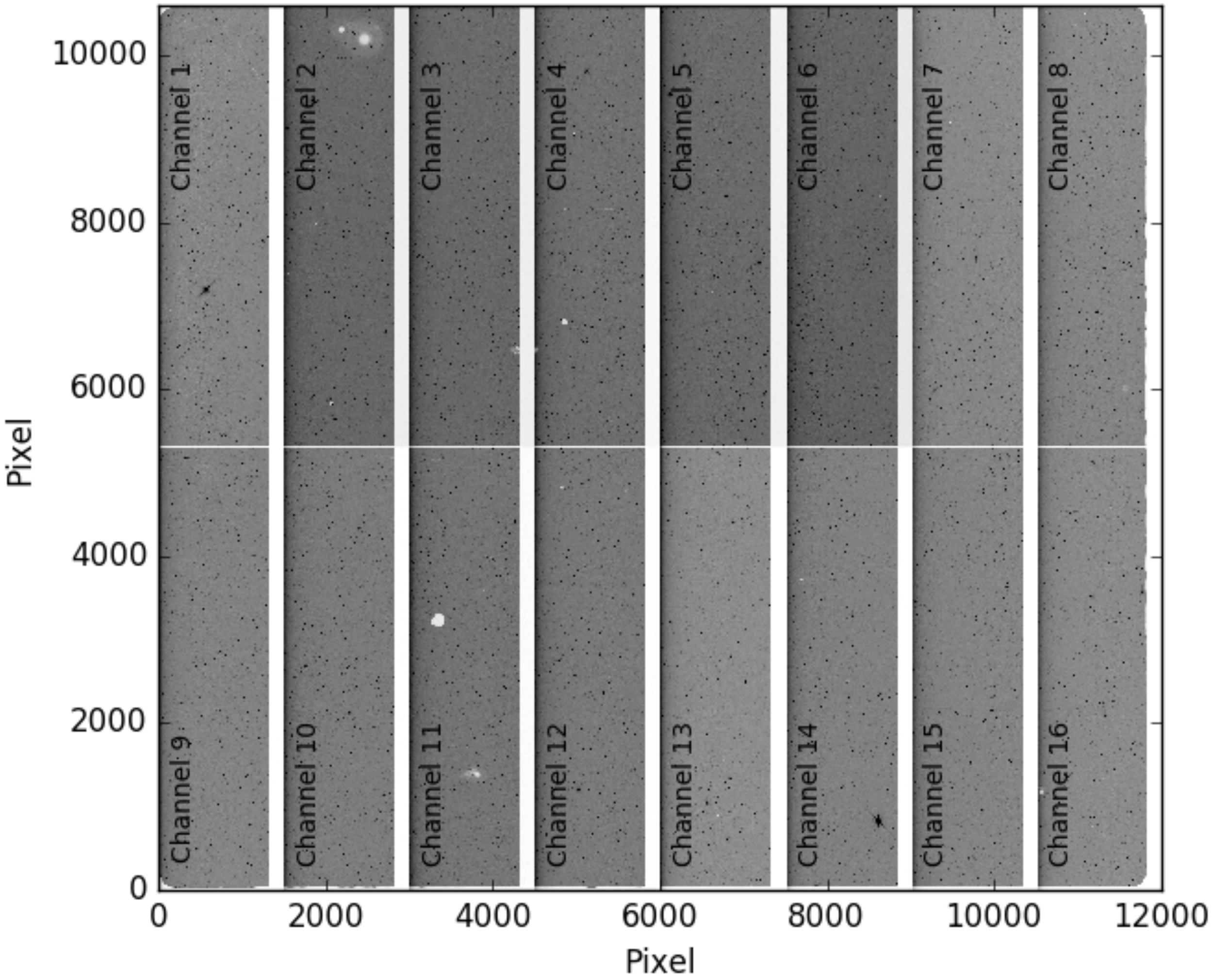

Figure 2.16: A full frame image from MeerLICHT, showing the channel numbers.

Table 2.3: MeerLICHT header keywords added by the pipeline.

Added to	Keyword	Value	Description
Master bias	BIAS#	str	Name of bias frame used in master bias creation. # depends on the number used.
	BIASMED	flt16	Median level of master bias.
	BIASSTD	flt16	Standard deviation of master bias.
	BIASM$_{\#}$	flt16	Median level of master bias in channel #.
Master flat	FLAT#	str	Name of flat frame used in master bias creation. # depends on the number used.

Table 2.3: - *continued*

Added to	Keyword	Value	Description
	FLATMED	flt16	Median level of master flat.
	FLATSTD	flt16	Standard deviation of master flat.
	STATSEC	str	Section of master flat used to normalize flats and determine statistics.
	SECMED	flt16	Median level of master flat in STATSEC.
	SECSTD	flt16	Standard deviation of master flat in STATSEC.
Science image	IPS-VERS	str	Version of the pipeline used.
	SET-VERS	str	Version of the setting file used.
	SUB-VERS	str	Version of *subpipe* used.
	ZGY-VERS	str	Version of ZOGY used.
	LOG	str	Name of the log file.
	SUB-LOG	str	Name of the *subpipe* log file.
	XTALK-P	bool	Corrected for crosstalk?
	XTALK-F	str	Name of crosstalk correction file.
	NONLIN-P	bool	Corrected for non-linearity?
	GAIN-P	bool	Corrected for gain?
	GAIN	flt16	Gain used for channel .
	OS-P	bool	Corrected for overscan?
	MBIAS-P	bool	Corrected for master bias?
	MBIAS	str	Name of master bias used.
	MFLAT-P	bool	Corrected with master flat?
	MFLAT	str	Name of master flat used.
	COSMIC-P	bool	Corrected for cosmic rays?
	SAT-P	bool	Processed for satellite trails?
Mask	M-BP	bool	Bad pixels included in mask?
	M-BPVAL	int8	Value of masked bad pixels.
	M-BPNUM	int	Number of bad pixels.

Table 2.3: - *continued*

Added to	Keyword	Value	Description
	M-EP	bool	Edge pixels included in mask?
	M-EPVAL	int8	Value of masked edge pixels.
	M-EPNUM	int	Number of edge pixels.
	SATURATE	int16	Saturation level.
	M-SP	bool	Saturated pixels included in mask?
	M-SPVAL	int8	Value of masked saturated pixels.
	M-SPNUM	int	Number of saturated pixels.
	M-SCP	bool	Saturated-connected pixels included in mask?
	M-SCPVAL	int8	Value of masked saturated-connected pixels.
	M-SCPNUM	int	Number of saturated-connected pixels.
	M-SAT	bool	Satellite trail pixels included in mask?
	M-SATVAL	int8	Value of masked satellite trail pixels.
	M-SATNUM	int	Number of satellite trail pixels.
	M-CR	bool	Cosmic rays included in mask?
	M-CRVAL	int8	Value of masked cosmic ray pixels.
	M-CRNUM	int	Number of pixels affected by cosmic rays.

2.3.2 Optimizing transient detection for MeerLICHT using ZOGY

Within *subpipe*, I added a reference building lock and field lock. These locks are responsible for queuing or skipping certain fields. The reference building lock is created whenever a reference building job is submitted. This stops the pipeline from processing more images from the same field, until the reference building job is complete. This ensures that only one reference image is created for a particular field. As soon as the pipeline has finished creating the reference images, the reference lock will be removed and the pipeline will continue to process images for that field (as subtraction jobs). If a field has been waiting for a reference building job to complete for more than 30 minutes, however, an error is assumed to have occurred and a field lock will be created. With a field lock in place, any image for that field will be skipped. The field lock needs to be

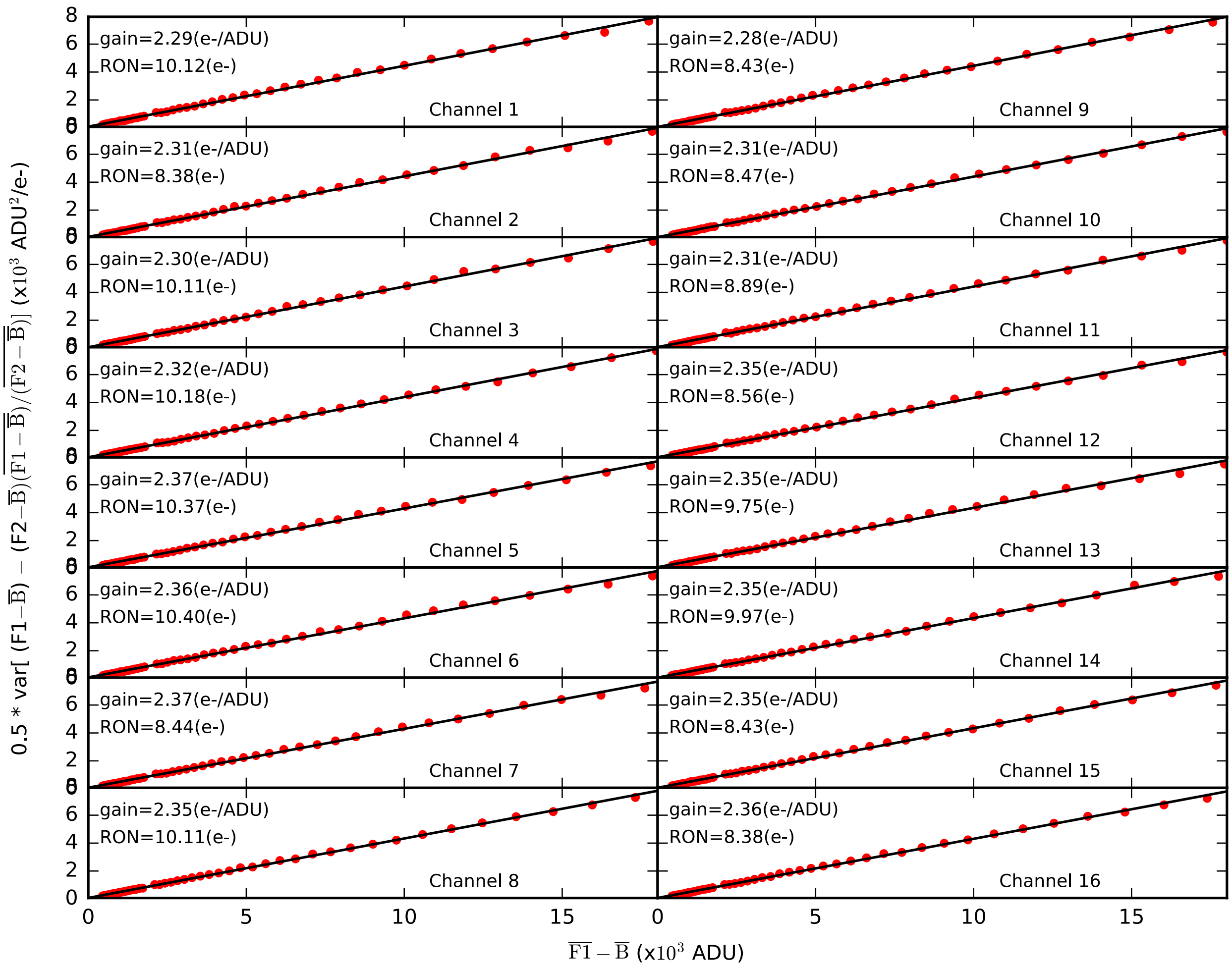

Figure 2.17: The gain and readnoise of MeerLICHT determined using an adapted version of Paul Vreeswijk's script using method 2 from http://www.mirametrics.com/tech_note_ccdgain.php.

manually removed after the issue has been resolved. If *subpipe* successfully completes a job, the unique temporary working directory will be removed. If *subpipe* does not successfully complete a job, the unique temporary working directory will not be removed. This is to clean up unneeded files as the pipeline runs, and to keep all files related to a failed job for further manual inspection.

The following steps (including the various improvements already discussed) were then included in ZOGY:

- solving the astrometry,
- performing optimal photometry (including calculating the zero points for photometric calibration),

Table 2.2: A summary of the gain and readnoise determined for MeerLICHT.

Channel	Gain (e^-/ADU)	Readnoise e^-
1	2.29	10.12
2	2.31	8.38
3	2.30	10.11
4	2.32	10.18
5	2.37	10.37
6	2.36	10.40
7	2.37	8.44
8	2.35	10.11
9	2.28	8.43
10	2.31	8.47
11	2.31	8.89
12	2.35	8.56
13	2.35	9.75
14	2.35	9.97
15	2.35	8.43
16	2.36	8.38
Median	2.33	9.32

- transient detection,
- creating the catalogues, metadata and thumbnails for the database.

With all the required steps for the pipeline contained inside ZOGY, I removed the individual steps within *subpipe* and replaced them with the full use of ZOGY. A flow diagram showing the resulting structure is shown in Figure 2.20. Now, *subpipe* controls the flow of images, such as finding the reference images and cleaning up, while ZOGY handles all science processing. A flow diagram of ZOGY in shown in Figure 2.21.

When submitting images to ZOGY, images are tagged with `new_fits` and `ref_fits`. If a single image tagged as `ref_fits` is submitted, ZOGY will run as a reference job. First, an estimate of the seeing will be determined by running SExtractor on a fraction of the image. This estimate is then used as an input when solving the astrometry with `Astometry.net` (see Section 3.1 for more details on the astrometry) and using SExtractor for source detection. The image is then prepared for the proper image subtraction method described by Zackay et al. (2016). This preparation includes: using PSFex to determine the PSF of the image, determining optimal fluxes using these PSFs, and

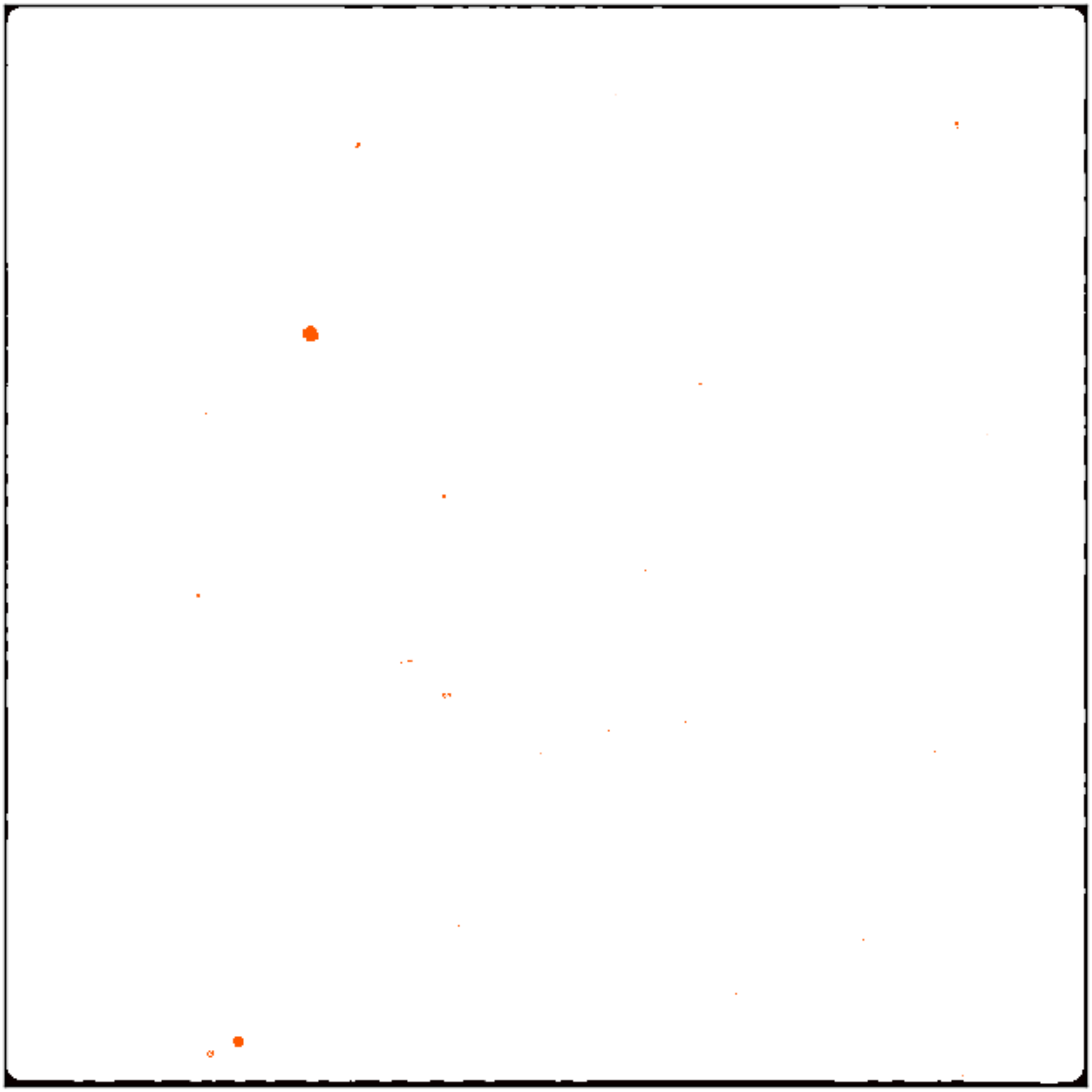

Figure 2.18: The bad pixel mask for MeerLICHT. The red shows bad pixels, while the black shows edge pixels. These masked pixels make up 1.3% of the entire image.

performing photometric calibration if a photometric catalogue is available. Finally, the full source catalogue is written to file.

If both a reference and new image is submitted, ZOGY will run as a subtraction job. When running a subtraction job, if the reference outputs are present (from a previous run through ZOGY), the reference image is not processed again and the present reference outputs are used. If the ref-

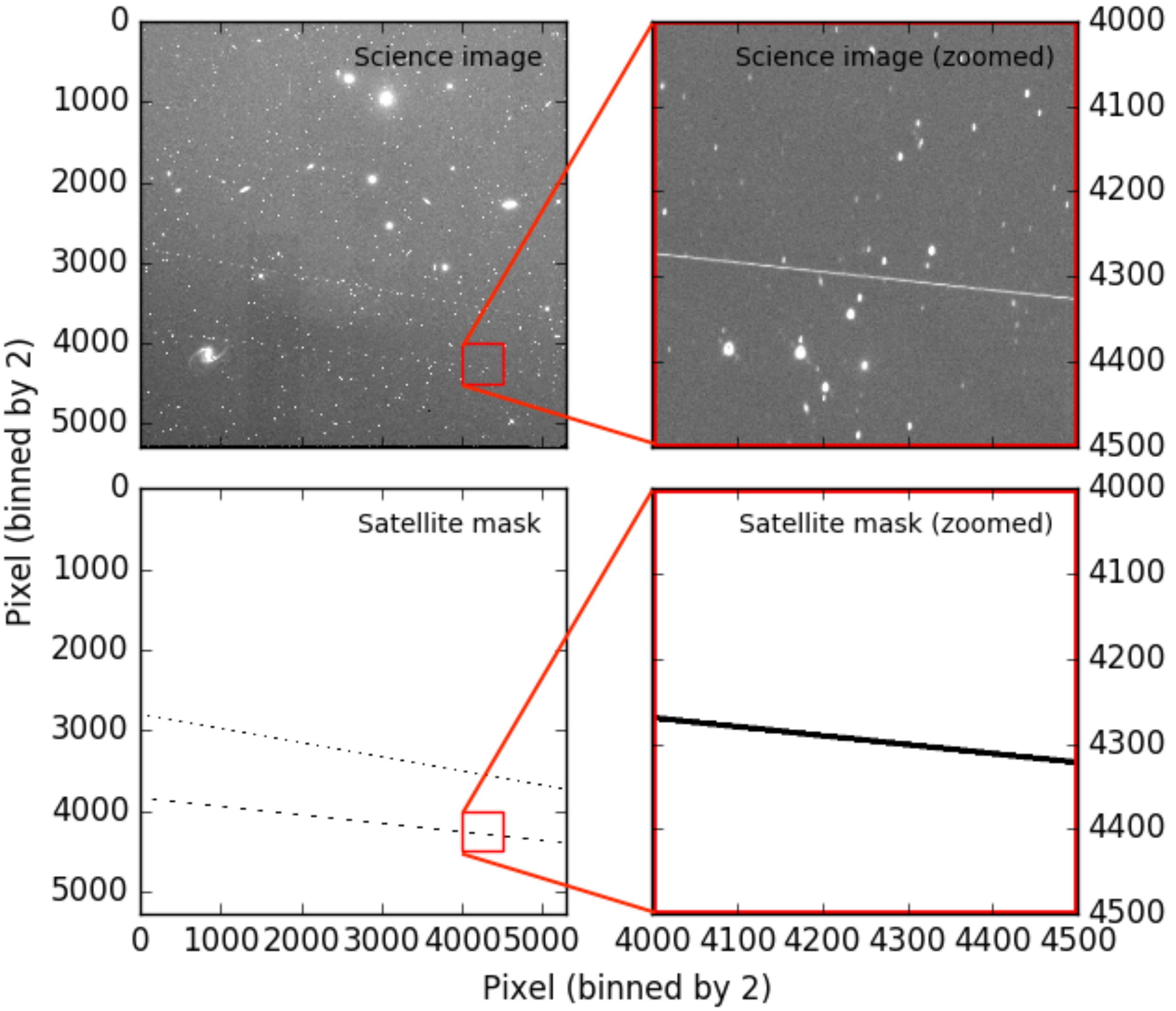

Figure 2.19: A binned science image containing 2 satellite trails and the corresponding satellite trail mask below. The right shows a zoomed view of the red box on the left image.

erence outputs are not present, the subtraction job will complete the previously described steps in the reference job alongside the subtraction job steps. As with the reference job, first, an estimate of the seeing is determined and then used when solving the astrometry for the new image. The reference image is then remapped to the new image. The new image is then prepared for the image subtraction with the same steps as with the reference image. The flux ratio between the new and reference images are then determined for use during the image subtraction method of Zackay et al. (2016). The number of transients, determined by a threshold cut on the S_corr image, is reported to the log. Both the positive and negative (occurring when a transient is present in the reference image) transients are then extracted directly from the S_corr image based off this threshold cut. ZOGY uses the transient's peak significance from the S_corr image along with the PSF determined for that position to calculate PSF photometry for the transient. As the positioning and flux is determined form the S_corr image, transients like supernova which are often embedded in galaxies are easily recovered. The full source catalogue for the new image, as well as the transient catalogue, including thumbnails of the transients, are written to file.

The ingestion of the catalogues to the database and linkage to the web interface has been developed by collaborators (Bart Scheers) and runs independently from the pipeline. The only step originally in *subpipe* but currently missing, is the real-bogus algorithm on the transients detected. A neural network machine learning algorithm has been developed for implementation on MeerLICHT/BlackGEM (Gieseke et al., 2017), but testing on MeerLICHT data is not part of this PhD project, and is deferred to a future study. Once the algorithm has been trained on MeerLICHT data, the real-bogus algorithm will be implemented on the SExtracted transients, before adding them to the transient catalogue.

The final pipeline (see Appendix A) is now ready to run on MeerLICHT data. In the subsequent chapters (3 and 4) I will describe the performance of the pipeline on science commissioning data.

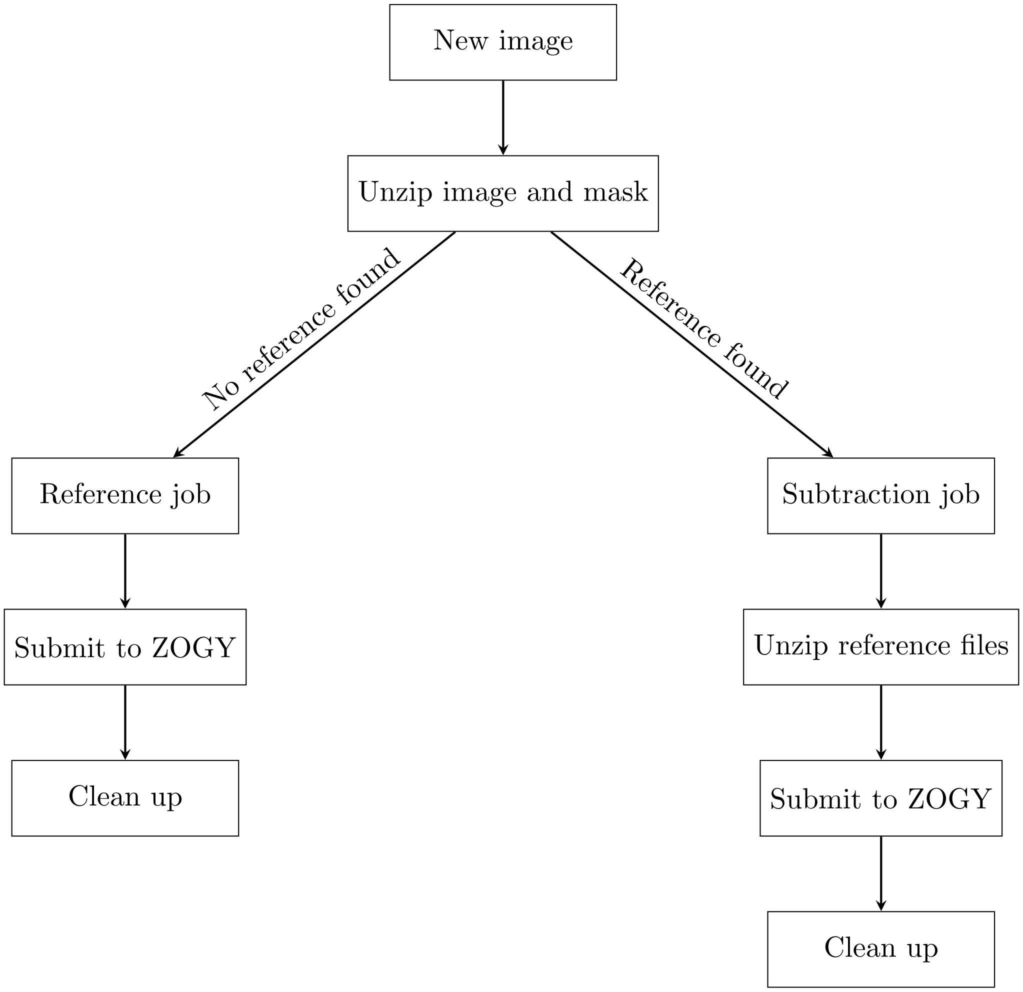

Figure 2.20: The basic flow diagram of *subpipe* after the adaption, and inclusion of ZOGY, using MeerLICHT data.

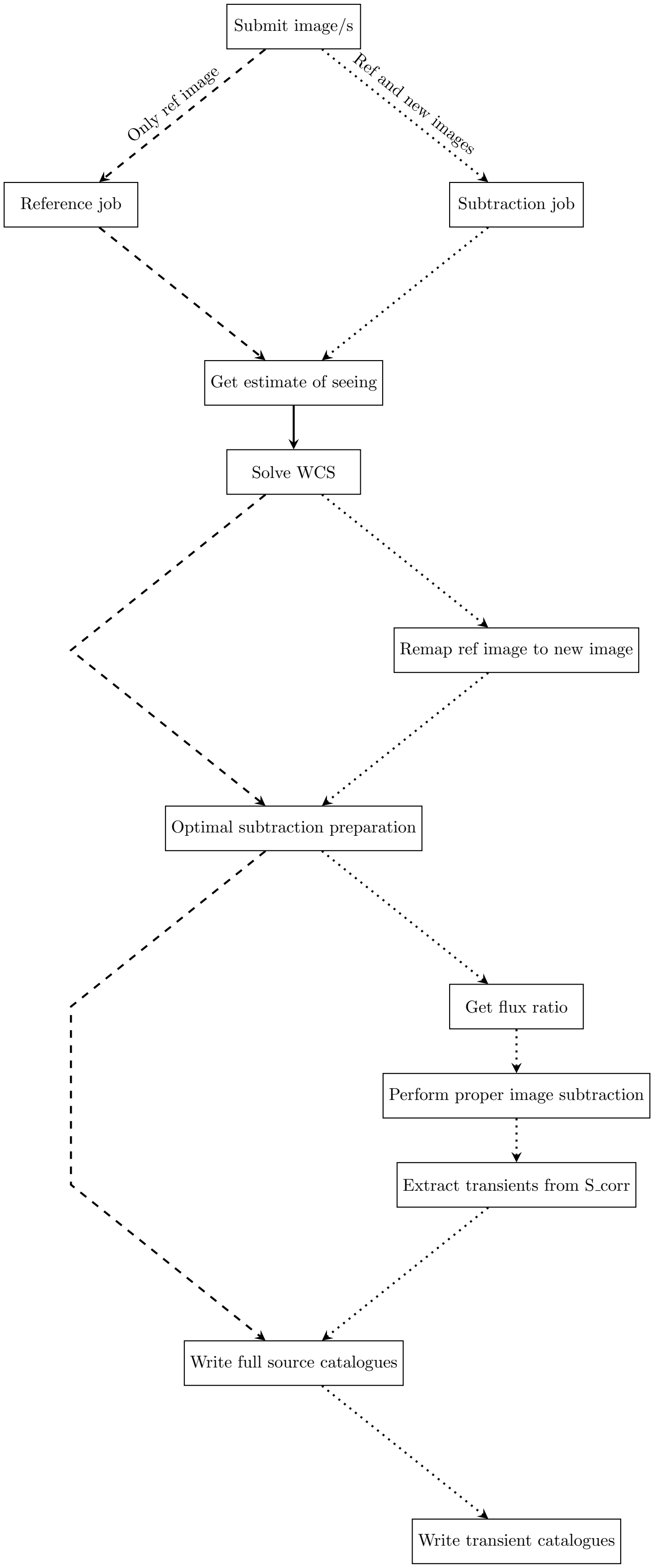

Figure 2.21: The basic flow diagram of ZOGY.

Chapter 3

Pipeline Performance

After the installation of MeerLICHT in July 2017, commissioning of MeerLICHT began. Testing and calibrating the individual components, such as setting mount speed, setting the telescope limits, checking mirror alignment, performing vibration tests, performing polar alignment, and ADC calibrations, were vital steps before any commissioning observations could be taken. In October 2017, after these tests were completed, a number of commissioning observations were carried out by a group of MeerLICHT members, including myself. These observations included known fields from the MeerKAT LSPs and the MeerLICHT twilight program. The purpose of these observations were to begin building up reference images for the known MeerLICHT fields before operations, to test the quality of the data, and to test the performance of the MeerLICHT pipeline.

Table 4.1 shows the 14 fields from the commissioning observations I used for the purpose of quantifying the performance of MeerLICHT and the pipeline. These observations were taken on 21 and 22 October 2017. To represent the expected data from MeerLICHT, fields were observed in all filters and with an exposure time of 60 sec. An exception to this was field 90013, which had an exposure time of 20 sec, for time series testing.

The tests performed on these data cover 4 main themes: astrometry, photometry, transient detection and timing. They are described in more detail in Sections 3.1, 3.2, 3.3 and 3.4, respectively.

Table 3.1: Fourteen fields from the MeerLICHT commissioning used for testing.

Field ID	Object	RA (2000.0)	DEC (2000.0)	Date of observation	Used for
90013	V2008-1753	20:08:16	-17:53:11	2017/10/21	A
90015	MKDeep8	03:49:57	-80:59:51	2017/10/21	A
90016	MKDeep5	04:16:56	-80:59:53	2017/10/21	A
90017	MKDeep8	03:49:57	-80:59:51	2017/10/21	A, TD
90018	MKDeep10	03:57:57	-79:59:52	2017/10/21	A
16015	NGC300	00:54:53	-37:41:04	2017/10/22	A
16016	NGC55	00:14:54	-39:11:48	2017/10/22	A
16017	NGC247	00:47:09	-20:45:37	2017/10/22	A, TD
16020	M74	01:36:42	15:46:59	2017/10/22	A
16023	Fornax1	03:36:51	-35:30:25	2017/10/22	A, T
16024	Fornax2	03:24:17	-36:51:56	2017/10/22	A
16038	NGC6822	19:44:56	-14:47:51	2017/10/21	A, TD
16061	CDFS	03:32:28	-27:48:30	2017/10/22	A, P
16079	NGC7793	23:57:50	-32:35:28	2017/10/22	A

Notes: A: astrometry; P: photometry; TD: transient detection; T: timing.

3.1 Astrometry

As discussed in Section 2.2.2, an accurate astrometric solution is important when doing difference imaging in order to minimize alignment errors. To verify the accuracy of the astrometric solution, I compared the astrometry in the commissioning observations to available catalogues. `Astrometry.net` makes use of index files built from a catalogue, using the positions of the matched stars in the index file, to solve for the astrometry. At the time of testing, the pipeline used index files built from 2MASS, along with a 3rd order polynomial distortion correction. By default, Astromety.net makes use of a 3rd order polynomial distortion correction. This correction is indeed needed, as the standard deviation in both RA and Dec improved significantly between using a 2nd order and 3rd order polynomial distortion correction (by over 30%). Tests were conducted using higher order polynomial distortion corrections (4th and 5th order), but improvement to the standard deviation was less than 2% in Dec and 0.1% in RA. As such, the default of using a 3rd order polynomial distortion correction provides sufficient corrections to the astrometric solution. This is also in-line with the MeerLICHT optical design which aimed for uniformity over the full field and therefore would require a low-order fit if high-quality optics were used. In order to determine how well the pipeline solved the astrometry using the 2MASS index files, I compared the astrometry to 2MASS. Since GAIA provides a higher accuracy on the astrometry of sources, I also compared the astrometry of the same field to GAIA. In Figure 3.1, I compared the astrometry of all sources, including stars and galaxies, in a single field (16024) in the q filter to both the Two Micron All-Sky Survey (2MASS; see Skrutskie et al. 2006) and GAIA (GAIA Collaboration et al., 2016). We see the median difference in position, for sources identified in field 16024 on the comparison with 2MASS, show a small offset of 0.051 arcsec in RA, in the sense of $\mathrm{RA_{REF}} - \mathrm{RA_{ML}}$ where REF refers to 2MASS in this case. Similarly, a small positional offset of 0.040 arcsec is seen in Dec. The standard deviation is 0.281 and 0.284 arcsec for RA and Dec, respectively compared to (2MASS) and 0.246 and 0.251 arcsec for RA and Dec, respectively compared to (GAIA). This error mostly represents the internal error of 2MASS which is 0.2 arcsec in both RA and Dec.

Figure 3.1 showed the accuracy of the astrometry compared to 2MASS and GAIA for a single filter. To test the astrometry in all filters, I compared the astrometry for field 16024 in all filters to GAIA. This is shown in Figure 3.2. We note no large difference in the median difference and standard deviation between filters. In order to determine if the astrometric differences have any trends in terms of position on the CCD and magnitude of the sources, I looked at the differences as a function of x (position horizontally across the image), y (position vertically across the image), R (distance from the centre of the image), and magnitude. These are shown in Figures 3.3, 3.4, 3.5, and 3.6, respectively. A linear fit to the data was done, the results of which are shown in Table 3.2. From these fits, we see no significant trends in the data. We do note the larger differences towards fainter sources. This is due to the fact that it is more difficult to determine the positions of fainter sources.

Table 3.3 shows the median difference, as well as the standard deviation, in the astrometry for all the commissioning test fields in the q filter. The larger difference in RA is thought to be due to the fact that these observations had no auto-guiding (as the guide cameras had not been commissioned), introducing additional error in the determination of the RA position of sources. In order to determine if there are any trends in the astrometry when comparing MeerLICHT to GAIA astrometry, I looked at the differences as a function of the number of sources in the field, the hour angle of the telescope, and the declination pointing of the telescope. The results are

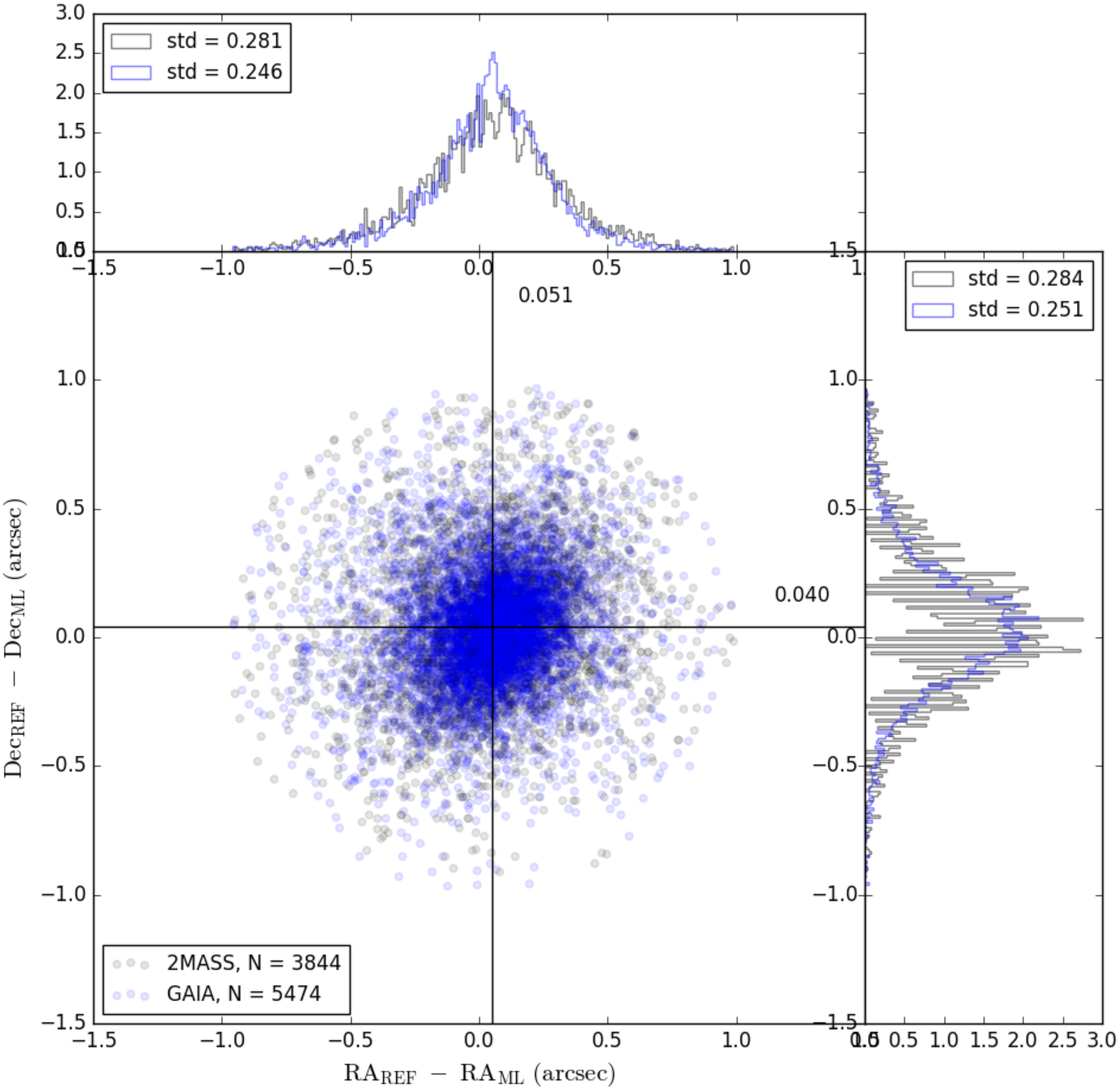

Figure 3.1: Difference in the astrometry compared to 2MASS (used to solve the astrometry) and GAIA for field 16024 in the q filter. A 1 arcsec search radius was used for the crossmatching. The median difference compared to 2MASS is 0.051 arsec in RA and 0.040 arcsec in Dec. The standard deviation is 0.281 and 0.284 arcsec for RA and Dec, respectively compared to (2MASS) and 0.246 and 0.251 arcsec for RA and Dec, respectively compared to (GAIA). This error mostly represents the internal error of 2MASS which is 0.2 arcsec in both RA and Dec. We note no large difference between the median difference for 2MASS and GAIA, while GAIA shows a smaller standard deviation for both RA and Dec.

shown in Figure 3.7. No obvious trends are seen in the astrometry when comparing MeerLICHT to GAIA astrometry as a function of sources or hour angle. While there appears to be some evidence of a trend as a function of declination, without adequate coverage over MeerLICHT's observable

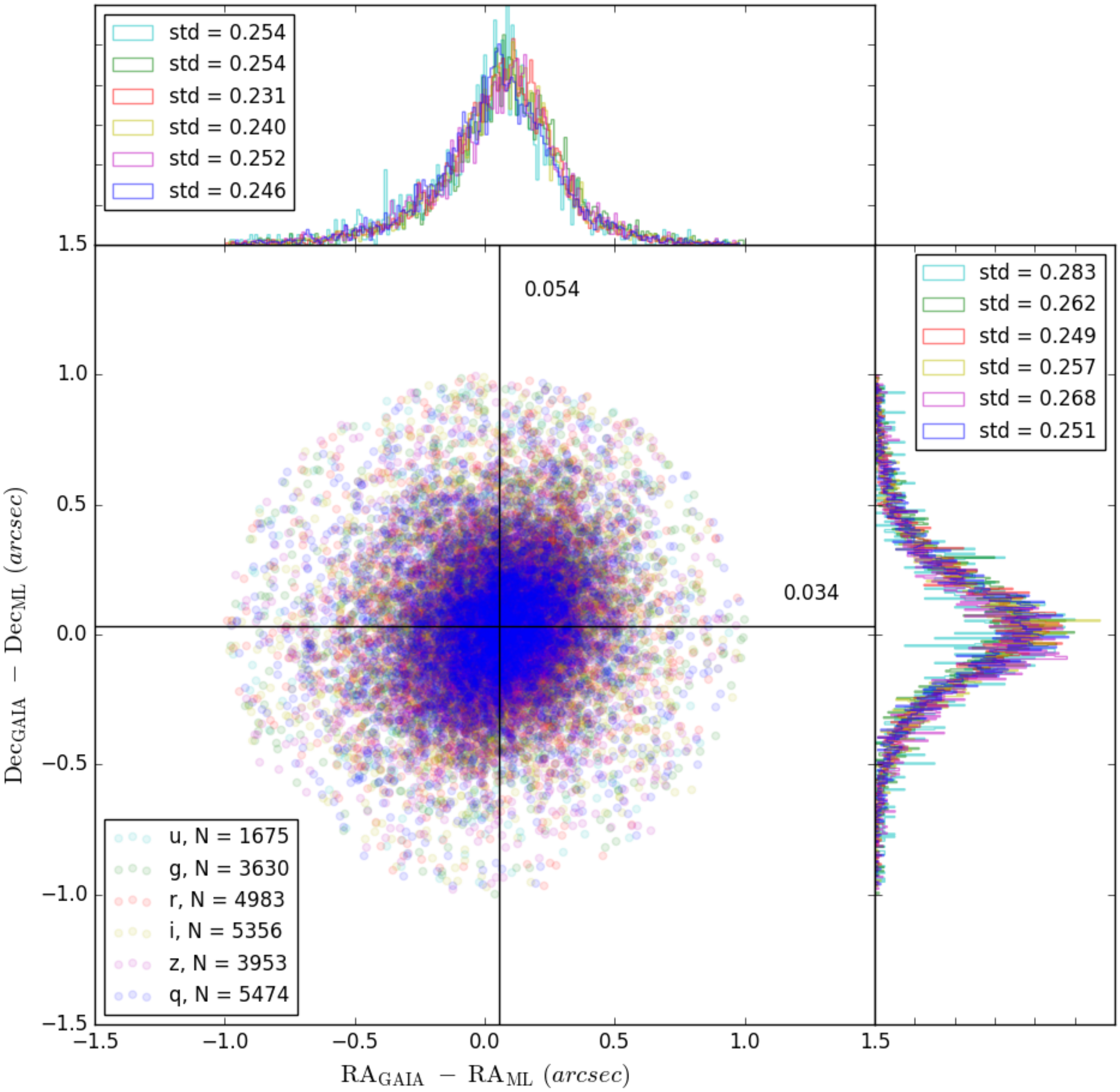

Figure 3.2: Difference in the astrometry when comparing MeerLICHT to GAIA astrometry for field 16024 in all filters. A 1 arcsec search radius was used for the crossmatching. The median difference compared is 0.054 arsec in RA and 0.034 arcsec in Dec for the q filter. The standard deviation is 0.246 and 0.251 arcsec for RA and Dec, respectively for the q filter. We note no large differences in the median offset and standard deviation between filters.

declination range ($-90^\circ - \sim 30^\circ$), it is difficult to make any concrete claims.

Subsequent to this analysis, and prompted by these results, a set of index files built from GAIA DR2 (Hobbs et al., 2018) have been implemented in the pipeline, with initial results of 0.005 arcsec median difference in both RA and Dec when compared to GAIA, and a standard deviation of 0.024 arcsec in RA and 0.035 arcsec in Dec. With the large improvement on the astrometry when comparing MeerLICHT to GAIA astrometry using GAIA as the reference catalogue within the pipeline, I suggest observing a set of fields spanning the entire observable range in both hour angle and declination to confirm the present or absence of trends. These observations should be carried out once guiding has been enable to ensure the elimination of additional sources of error on the astrometry.

3.2 Photometry

ZOGY performs calibrated optimal photometry (see Section 1.6) to determine the flux and magnitude of sources. Unless otherwise stated, magnitudes given here are on the MeerLICHT system. The reference catalogue used to perform the photometric calibration was built by Paul Vreeswijk and contains stars from SDSS and SkyMapper transformed to the MeerLICHT filters. The filter transmission curves for SDSS and SkyMapper (see Bessell et al. 2011) are shown in Figure 3.8. First, I compared the magnitudes of stars (defined as sources with a `CLASS_STAR` > 0.8 produced by SExtractor) determined by ZOGY against the photometric calibration reference catalogue. The difference between the magnitudes obtained from optimal flux through ZOGY and the reference catalogue, as a function of reference catalogue magnitudes, for all filters is shown in Figures 3.9 and 3.10 for field 16061. Since this catalogue was used to calibrate the magnitudes, we would expect no offset, and very little scatter between the two magnitudes. This is indeed the case, with the standard deviation less than 0.08 magnitudes for all filters. The largest scatter is seen in the u filter. This is expected as the reference filters are shifted more towards the blue compared to MeerLICHT's u filter and u is intrinsically difficult to calibrate. Outliers are also expected, as any variable star included in the reference catalogue would have a different brightness each time it is observed.

I then compared the magnitudes determined by ZOGY for the same field to the PanSTARRS catalogue. The difference between the magnitudes obtained from optimal flux through ZOGY and

Table 3.2: The slope and intercept obtained from performing a linear fit to the differences in astrometry between MeerLICHT and GAIA astrometry as a function of x, y, R (distance from centre) and magnitude for field 16024.

Function of	Filter	RA slope (arcsec)	RA intercept (arcsec)	Dec slope (arcsec)	Dec intercept (arcsec)
x	u	−0.2(2) x 10^{-7}	0.04(1)	−2.0(2) x 10^{-5}	0.14(1)
	g	−0.4(1) x 10^{-7}	0.099(9)	−2.3(1) x 10^{-5}	0.175(8)
	r	−0.7(1) x 10^{-7}	0.093(7)	−2.0(1) x 10^{-5}	0.150(7)
	i	−0.7(1) x 10^{-7}	0.096(8)	−1.4(1) x 10^{-5}	0.102(7)
	z	−0.6(1) x 10^{-7}	0.087(8)	−0.7(1) x 10^{-7}	0.040(9)
	q	−0.9(1) x 10^{-7}	0.090(6)	−2.1(1) x 10^{-5}	0.152(7)
y	u	1.7(2) x 10^{-5}	−0.06(1)	−0.0(2) x 10^{-6}	0.04(1)
	g	2.0(1) x 10^{-5}	−0.022(8)	0.5(1) x 10^{-7}	0.024(9)
	r	1.1(1) x 10^{-5}	−0.003(6)	0.4(1) x 10^{-7}	0.024(7)
	i	0.7(1) x 10^{-7}	0.026(6)	0.5(1) x 10^{-7}	−0.00(7)
	z	0.2(1) x 10^{-7}	0.042(8)	0.3(1) x 10^{-7}	−0.010(9)
	q	−0.9(1) x 10^{-7}	0.09(7)	0.3(1) x 10^{-7}	0.022(7)
R	u	−0.5(4) x 10^{-7}	0.05(2)	2.0(5) x 10^{-5}	−0.04(2)
	g	0.5(3) x 10^{-7}	0.06(1)	2.6(3) x 10^{-5}	−0.05(1)
	r	0.5(2) x 10^{-7}	0.037(9)	1.7(2) x 10^{-5}	−0.02(1)
	i	0.5(2) x 10^{-7}	0.039(9)	0.05(2) x 10^{-7}	0.01(1)
	z	0.3(3) x 10^{-7}	0.04(1)	1.7(3) x 10^{-5}	−0.07(1)
	q	0.3(2) x 10^{-7}	0.029(9)	$1.2(2)^{-5}$	−0.01(1)
magnitude	u	0.006(3)	−0.07(6)	0.007(4)	−0.09(6)
	g	0.008(2	−0.07(4)	0.002(2)	0.02(4)
	r	0.007(2)	−0.07(3)	0.005(2)	−0.05(3)
	i	0.009(2)	−0.09(3)	0.004(2)	−0.05(3)
	z	0.007(2)	−0.07(4)	0.001(3)	−0.01(4)
	q	0.006(2)	−0.06(3)	0.004(2)	−0.04(3)

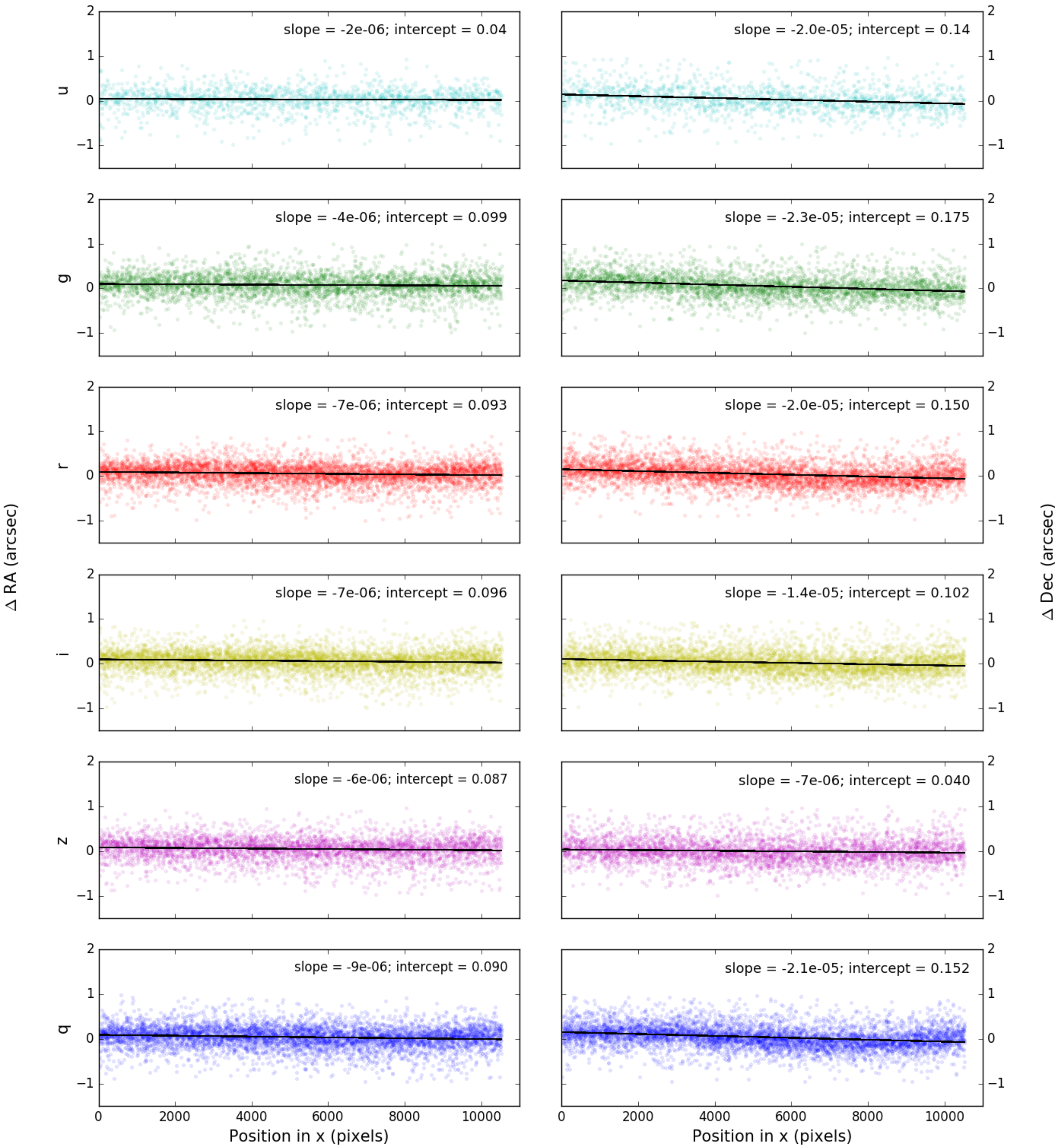

Figure 3.3: Difference in the astrometry when comparing MeerLICHT and GAIA astrometry as a function of x (position horizontally across the image) for all filters. Top to bottom: u, g, r, i, z, q. Left column: Difference in RA. Right column: Difference in Dec. A straight line has been fitted to all plots.

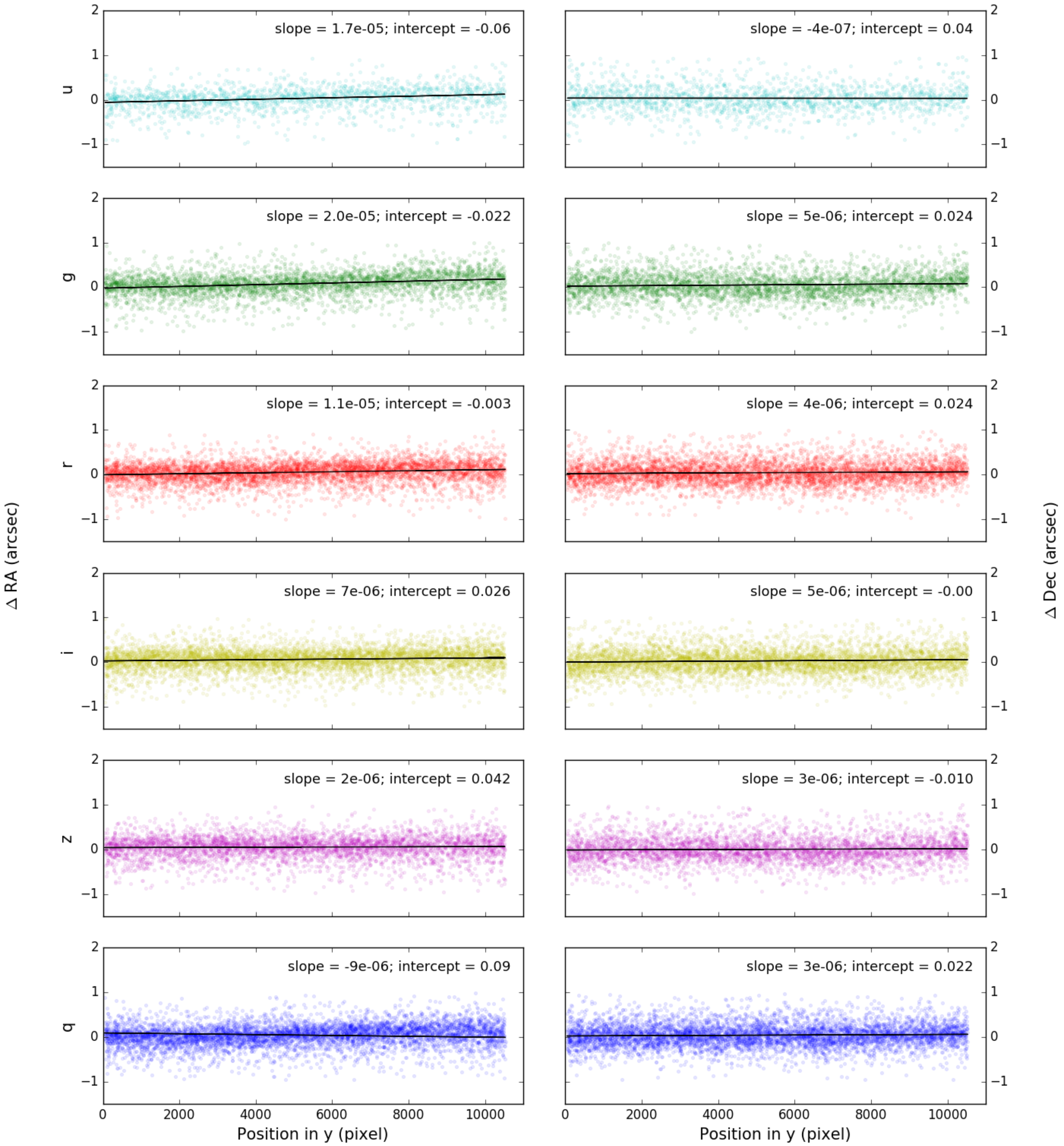

Figure 3.4: Difference in the astrometry when comparing MeerLICHT and GAIA astrometry as a function of y (position vertically across the image) for all filters. Top to bottom: u, g, r, i, z, q. Left column: Difference in RA. Right column: Difference in Dec. A straight line has been fitted to all plots.

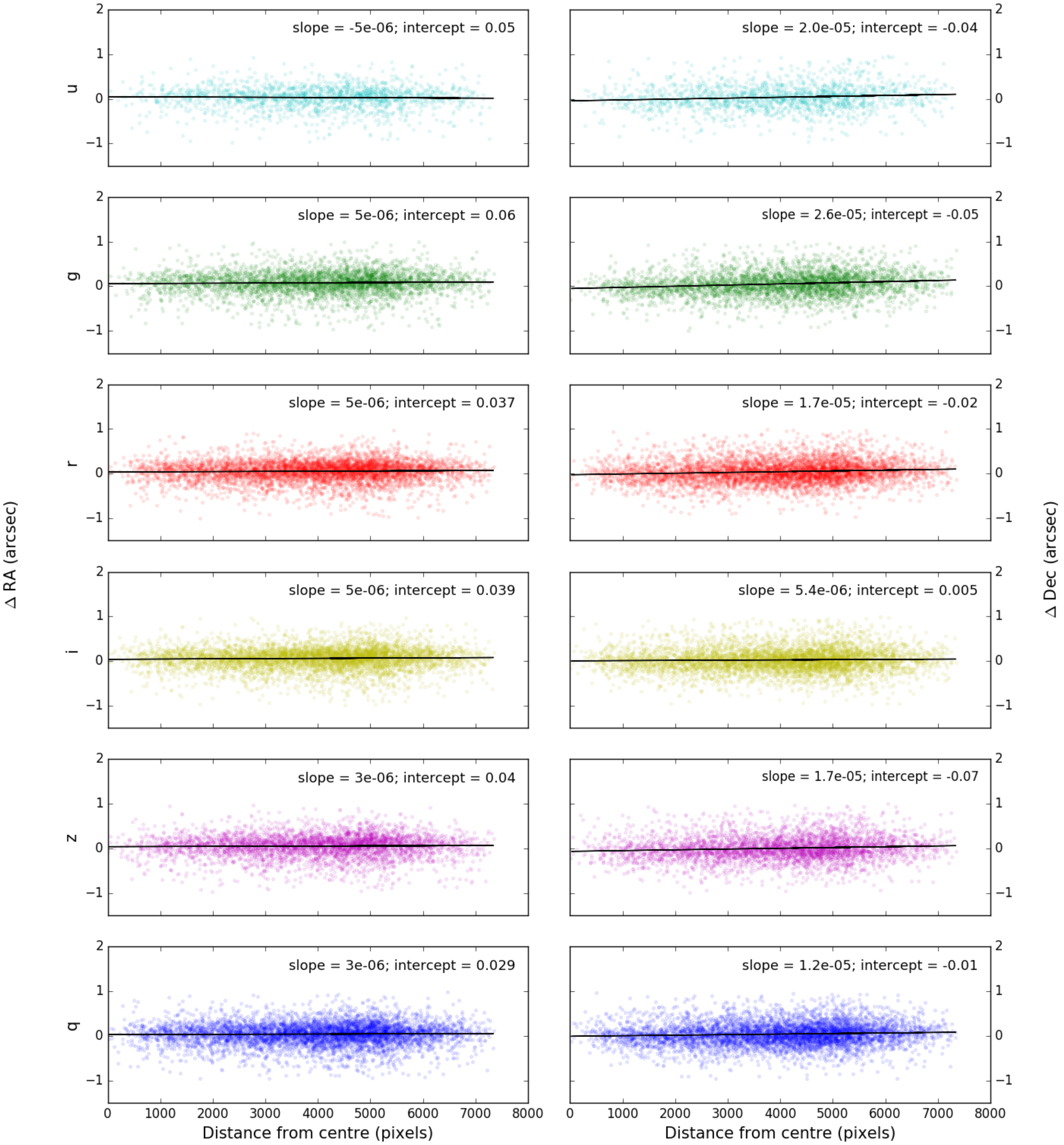

Figure 3.5: Difference in the astrometry when comparing MeerLICHT and GAIA astrometry as a function of R (distance away from the centre of the image) for all filters. Top to bottom: u, g, r, i, z, q. Left column: Difference in RA. Right column: Difference in Dec. A straight line has been fitted to all plots.

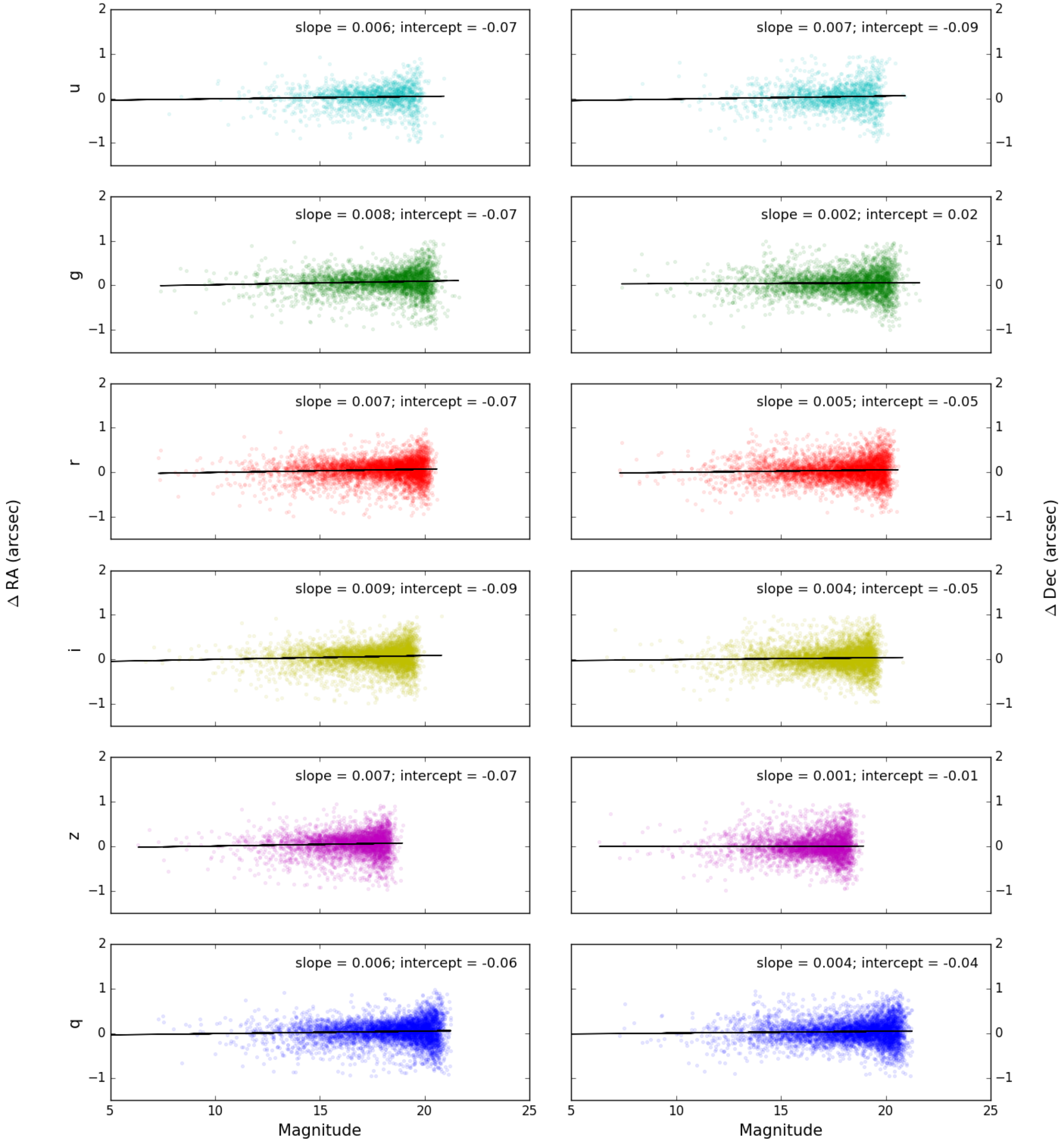

Figure 3.6: Difference in the astrometry when comparing MeerLICHT and GAIA astrometry as a function of magnitude for all filters. Top to bottom: u, g, r, i, z, q. Left column: Difference in RA. Right column: Difference in Dec. A straight line has been fitted to all plots. We see larger scatter for fainter magnitudes.

Table 3.3: Median difference in astrometry when comparing MeerLICHT and GAIA astrometry for all fields. The median difference in RA and Dec, as well as the standard deviation for all fields in the q filter.

Field ID	Δ RA (arcsec)	Δ Dec (arcsec)	σ_{RA} (arcsec)	σ_{Dec} (arcsec)
90013	0.137	0.023	0.209	0.222
90015	0.102	0.120	0.194	0.224
90016	0.100	0.180	0.231	0.226
90017	0.112	0.188	0.203	0.221
90018	0.099	0.188	0.207	0.229
16015	0.170	-0.018	0.286	0.257
16016	0.130	0.016	0.258	0.230
16017	0.117	-0.058	0.269	0.236
16020	0.186	-0.218	0.307	0.284
16023	0.125	0.055	0.228	0.244
16024	0.054	0.034	0.246	0.250
16038	0.099	0.022	0.235	0.213
16061	0.123	0.014	0.230	0.220
16079	0.106	-0.022	0.269	0.225
median	0.114	0.023	0.233	0.228

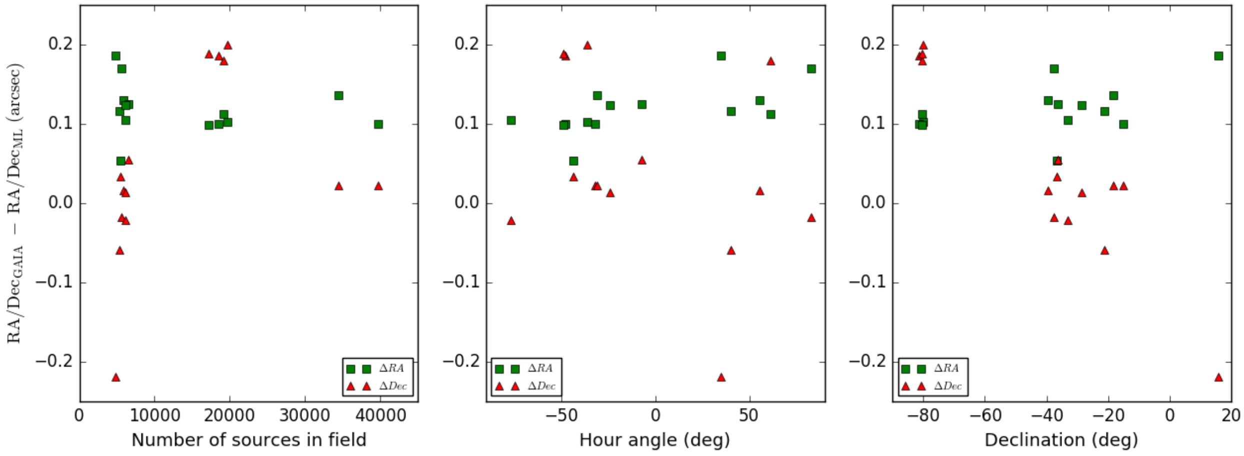

Figure 3.7: Median difference in the astrometry when comparing MeerLICHT and GAIA astrometry for all fields. Left: Median difference plotted against the number of sources in the image. Middle: Median difference plotted against the hour angle of the telescope. Right: Median difference plotted against the declination of the telescope. No obvious trends are seen in the astrometric errors as a function of sources and hour angle. There may be trends present in the astrometric errors as a function of declination, but without adequate coverage over the observable declination range, it is difficult to make any concrete claims.

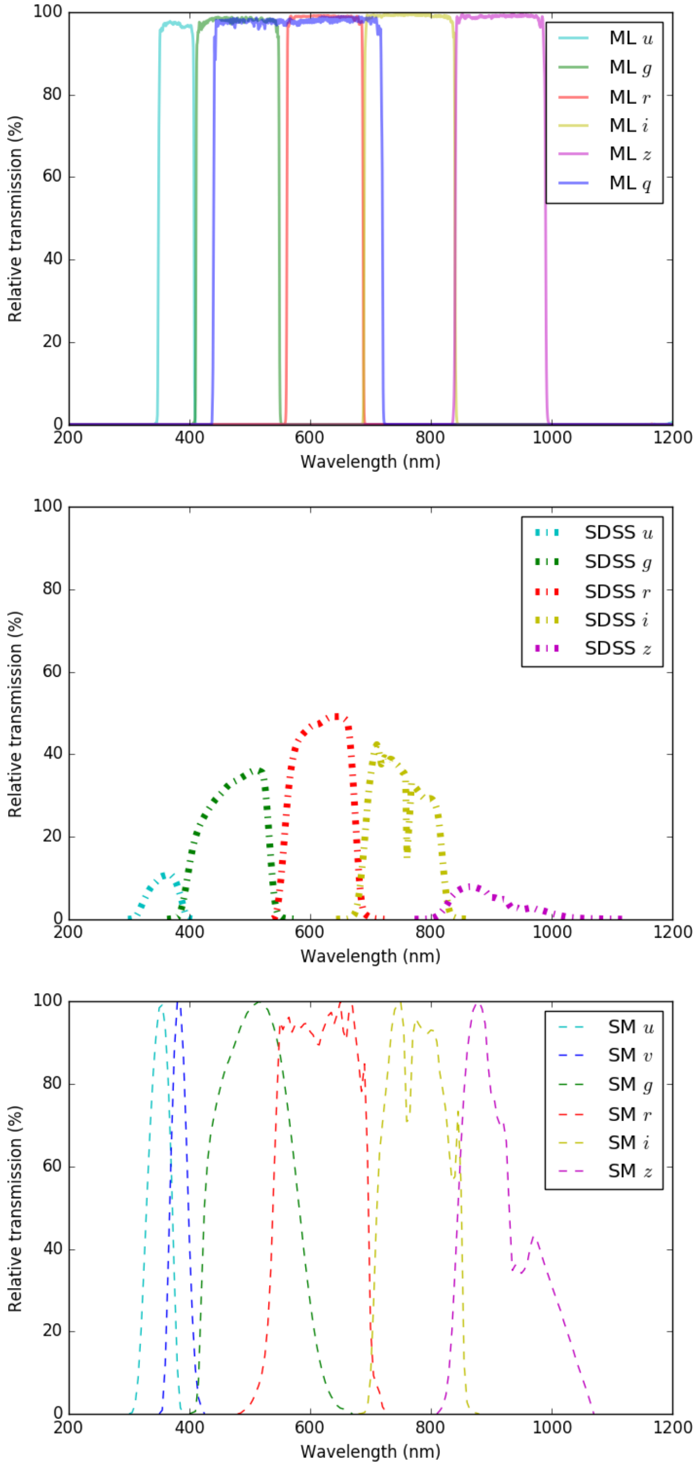

Figure 3.8: The filter transmission curves for SDSS and SkyMapper (see Bessell et al. 2011), compared to MeerLICHT. Top: The MeerLICHT curves only show the filters. Middle: The SDSS curves show the transmission through the entire optical system as well and the atmosphere. Bottom: The SkyMapper curves also show the transmission through the entire optical system and atmosphere, but have been normalized such that the peak is 1.

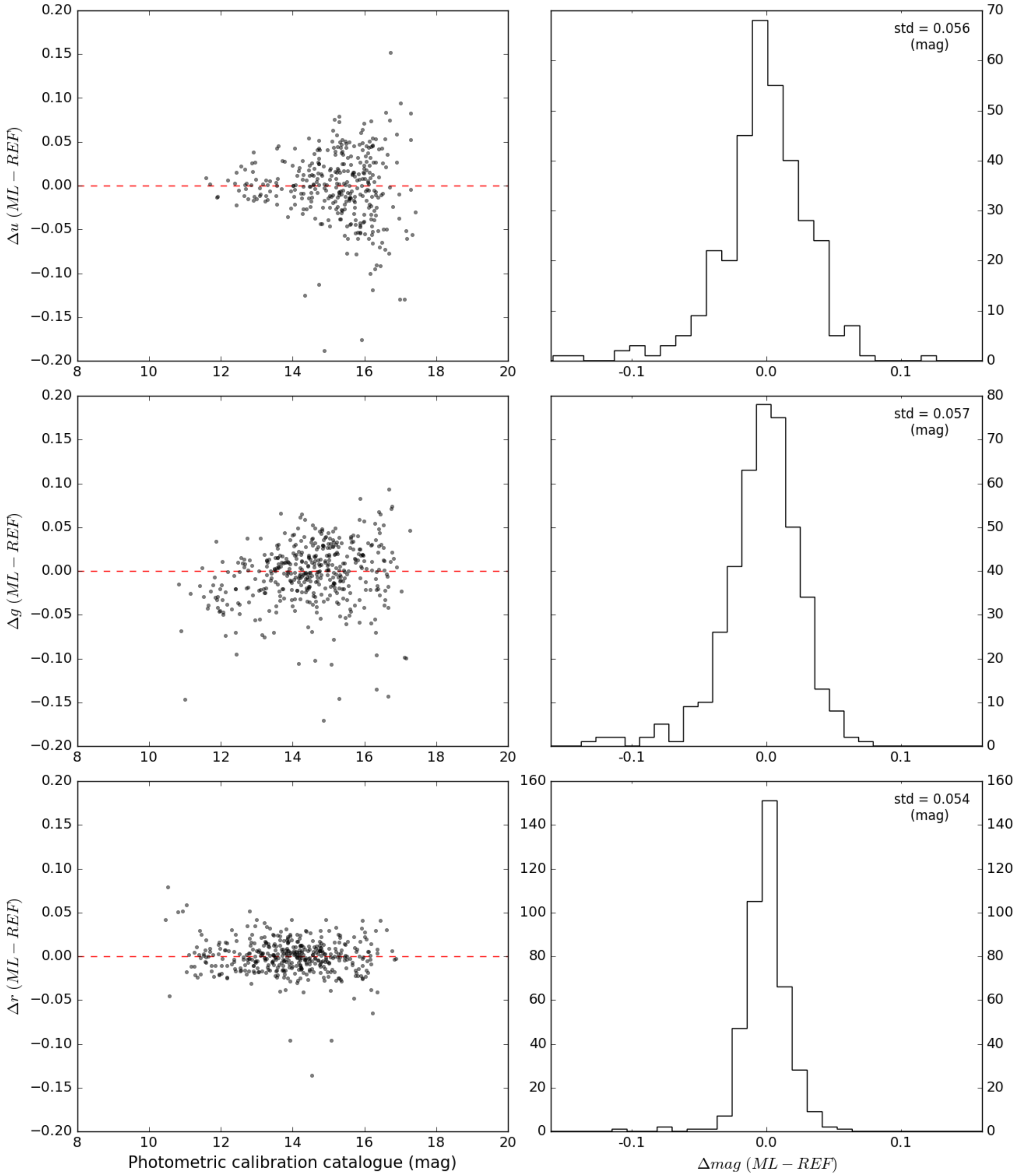

Figure 3.9: Photometry for the u, g and r filters compared to the reference catalogue (built from SDSS and SkyMapper) used to perform the photometric calibration within ZOGY for field 16061. This reference catalogue contains data from SDSS and SkyMapper. The dashed horizontal line shows $\Delta m = 0$. Left column: The difference between the magnitudes obtained from optimal flux through ZOGY (ML) and the reference catalogue (REF), as a function of reference catalogue magnitudes. Right column: A histogram of the difference between the magnitudes.

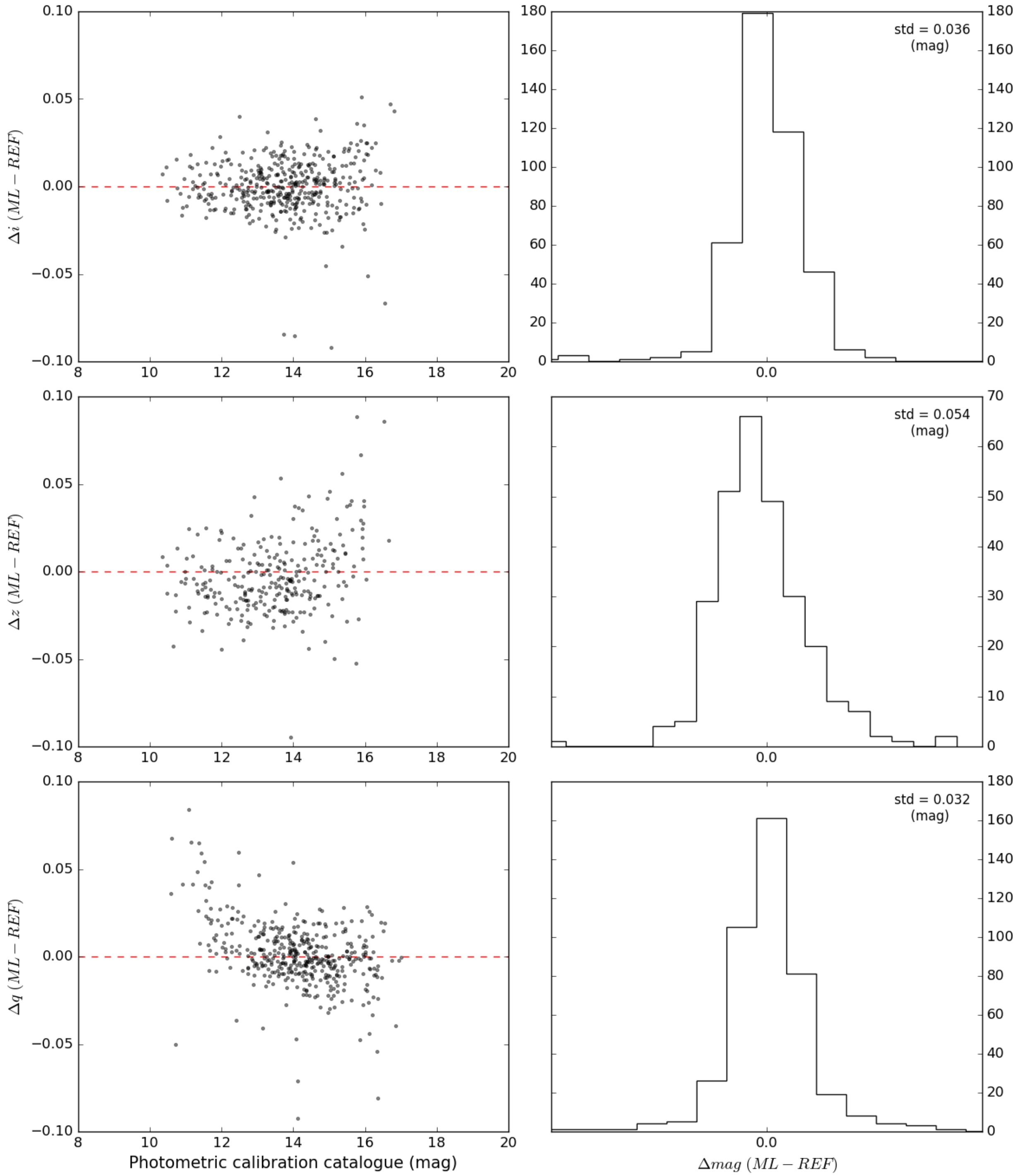

Figure 3.10: Photometry for the i, z and q filters compared to the reference catalogue (built from SDSS and SkyMapper) used to perform the photometric calibration within ZOGY for field 16061. This reference catalogue contains data from SDSS and SkyMapper. The dashed horizontal line shows $\Delta m = 0$. Left column: The difference between the magnitudes obtained from optimal flux through ZOGY (ML) and the reference catalogue (REF), as a function of reference catalogue magnitudes. Right column: A histogram of the difference between the magnitudes.

PanSTARRS, as a function of PanSTARRS magnitudes, for all filters, except u and q, is shown in Figures 3.11. The comparison for u and q is not shown as PanSTARRS has no equivalent filters. From these figures we see large scatter at the brighter magnitudes, close to saturation, and increasing scatter towards fainter magnitudes. The increase in scatter towards the fainter magnitudes is due to the different filter responses and shows the importance of transforming magnitudes if one wishes to compare magnitudes from different filters. Comparing the magnitudes (for magnitudes between 13 and 17) between MeerLICHT and PanSTARRS, r is the most comparable, followed by i and z. g has the largest offset, $(g_{\mathrm{ML}} - g_{\mathrm{PS}}) = –0.15$ mag, showing a significant difference between the two filters.

To highlight the need for transformations between photometric systems, a colour-colour diagram is shown in Figure 3.12. An offset of 0.2 in g and 0.55 in u is needed to align the main sequence track from Drew et al. (2014) to the MeerLICHT magnitudes. These offsets are a natural consequence of the calibration to the MeerLICHT filter system. An additional complication here is that the Drew et al. (2014) curve is based on colours in the Vega system for VPHAS+ photometry, while MeerLICHT photometry is based on the AB system.

The saturation magnitude and the magnitude at which a signal-to-noise ratio (SNR) of 5 is reached for each filter is shown in Figure 3.13. Table 3.4 summarizes these results. These values were obtained in photometric conditions with 2.63 arcsec seeing and no moon for field 16061. These values are within 0.1 mag of the expected values for these conditions (obtained using a SNR calculator). This indicates that MeerLICHT/BlackGEM will be able to achieve the predicted photometry (shown alongside in Table 3.4) in optimal conditions.

The small scatter between the MeerLICHT photometry and the reference catalogue photometry, seen in figures 3.9 and 3.10, shows that the MeerLICHT magnitudes are self consistent, while the offsets required in Figure 3.12 highlight the need for further calibrations, especially towards the blue, in order to make MeerLICHT magnitudes consistent with other surveys. To achieve this, simultaneous photometric and spectroscopic observations are needed to calibrate the MeerLICHT filters. These data were taken in January 2018 using the South African Astronomial Observatory

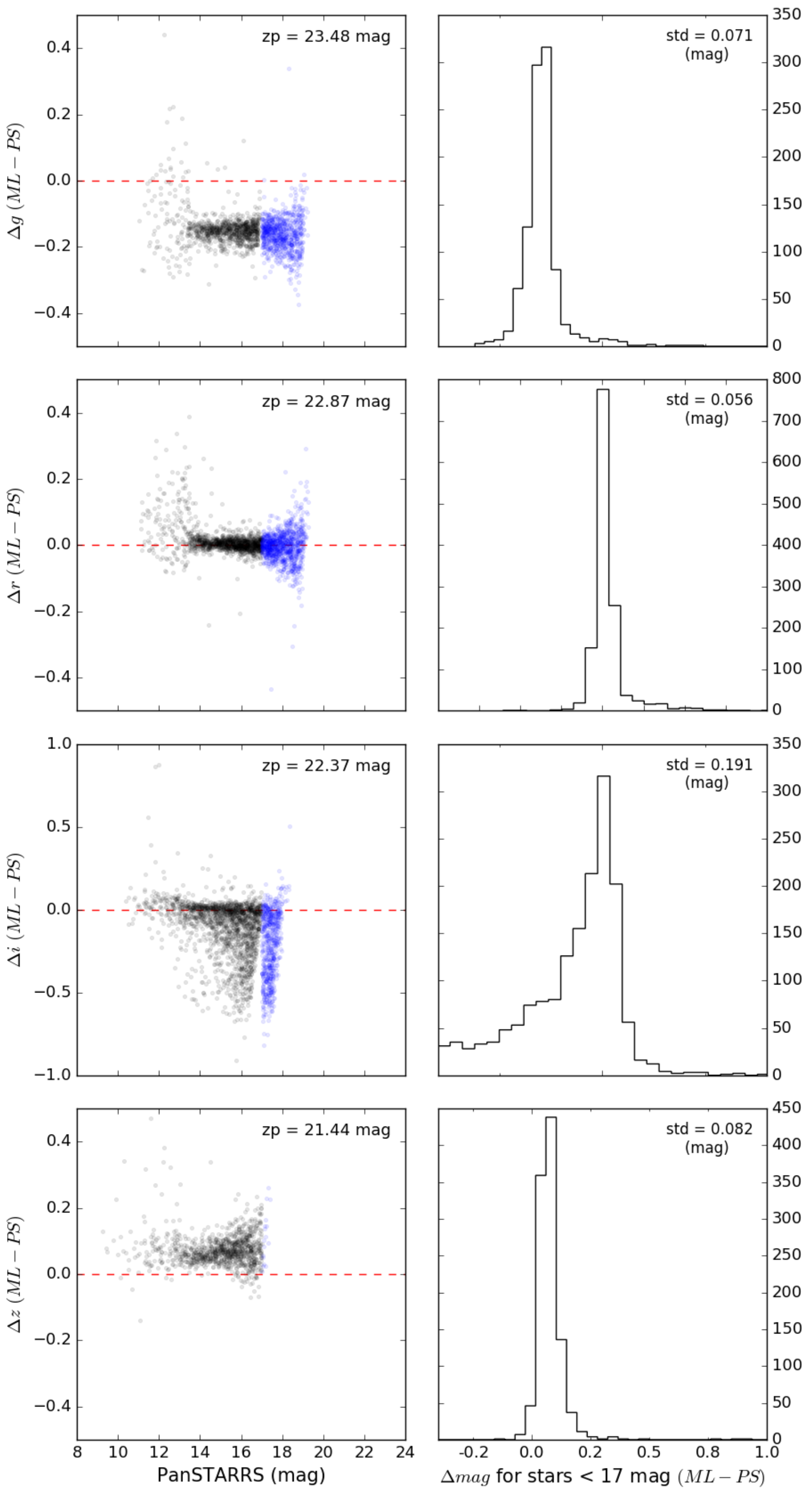

Figure 3.11: Photometry for the g, r, i and z filters compared to PanSTARRS. Left column: the difference between the magnitudes obtained from optimal flux through ZOGY (ML) and the PanSTARRS catalogue (PS), as a function of PanSTARRS magnitudes for field 16061. The zero point used for the photometric calibration is shown in the top right. Right column: a histogram of the difference between the magnitudes, for magnitude 17. Since MeerLICHT's u and q filters are unique with no easily related filters in PanSTARRS, the comparison for u and q is not shown.

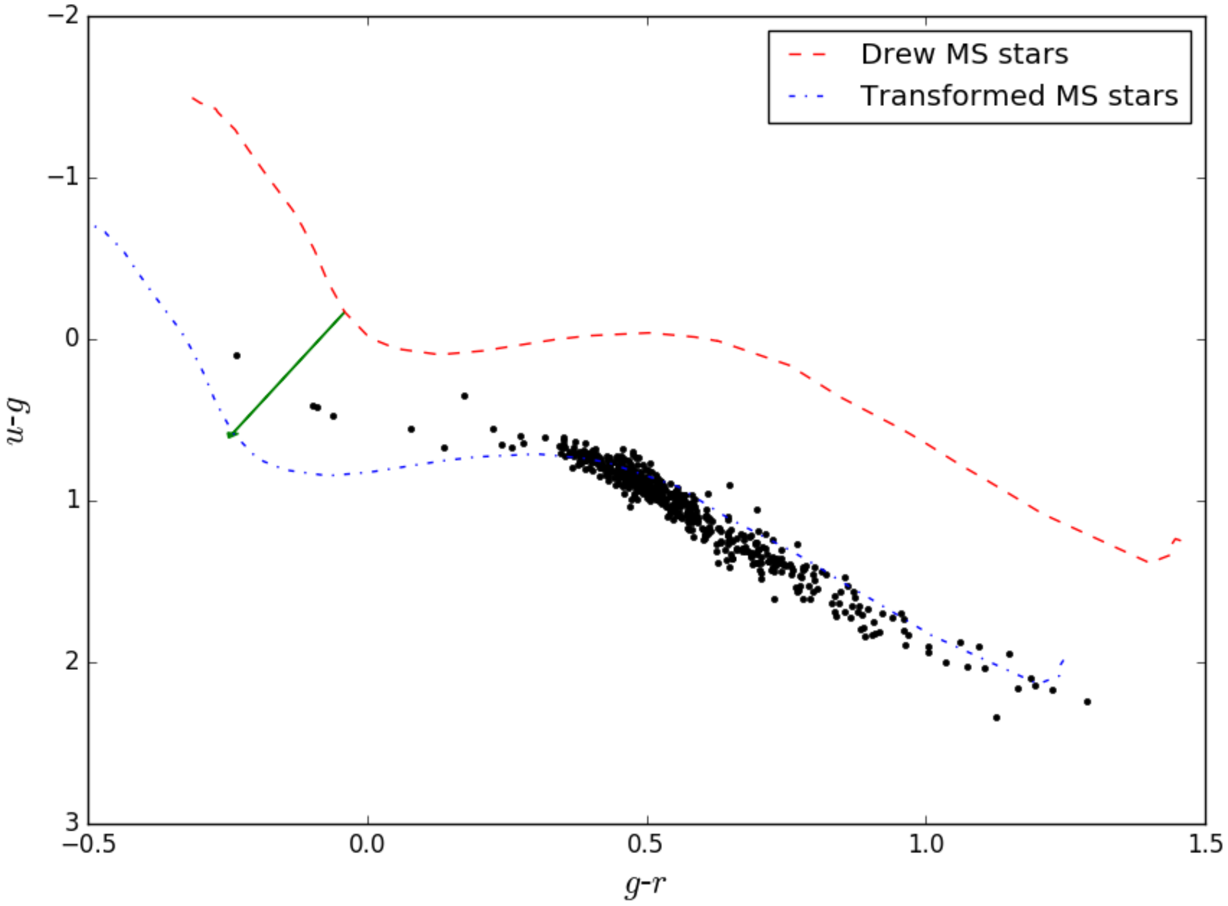

Figure 3.12: The colour-colour diagram for stars in field 16061. The dashed red line shows the Drew et al. (2014) main sequence (MS) track, while the blue dot-dashed line shows the same MS track, but offset by 0.2 in g and 0.55 in u. The need for these offsets illustrates the difference in photometric systems. The Drew et al. (2014) track makes use of photometry from the VPHAS+ filter system (based on the Vega system), while MeerLICHT data is based on the AB system.

Table 3.4: Saturation limit and magnitude at which a SNR of 5 is reached in 2.63 arcsec seeing, as well as the expected depth taken from Bloemen et al. (2016) for 0.95 arcsec seeing. For field 16061 taken in photometric conditions and no moon.

Filter	Saturation (mag)	SNR = 5 achieved in 2.63 arcsec seeing (mag)	Expected depth for 0.95 seeing (mag)
u	8.7(1)	19.3(2)	19.8
g	11.2(1)	20.9(2)	21.9
r	11.0(1)	20.5(2)	21.3
i	10.3(1)	19.7(2)	20.7
z	9.1(1)	18.6(2)	20.4
q	11.7(1)	21.2(2)	22.2

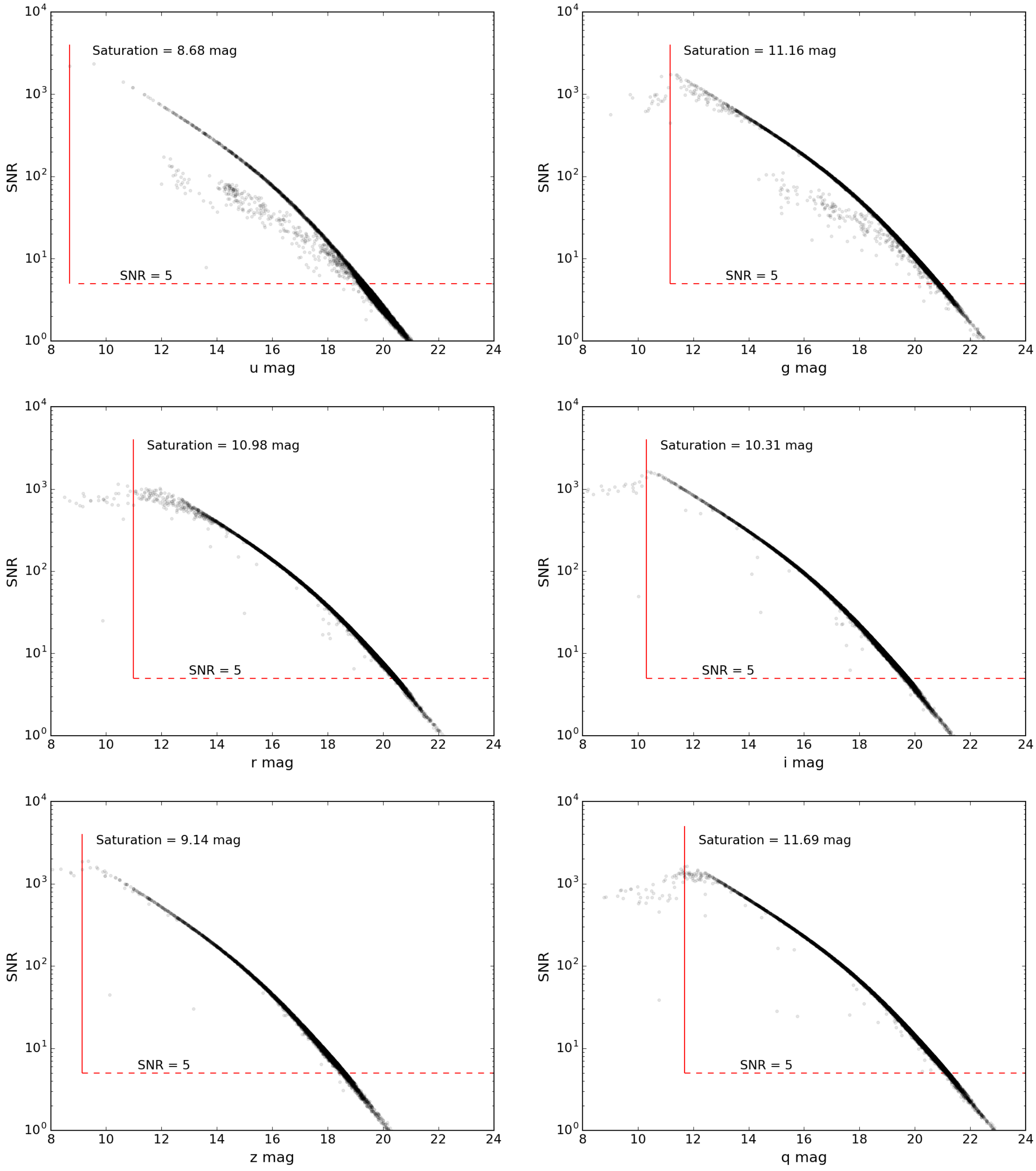

Figure 3.13: SNR for a 1 minute exposure in photometric conditions with 2.63 arcsec seeing and no Moon for field 16061 with an exposure time for these conditions. The dashed horizontal line highlights where $SNR = 5$. The solid vertical line shows the magnitude at which saturation for each filter occurs.

(SAAO) 74-inch reflector telescope and the Spectrograph Upgrade - Newly Improved Cassegrain (SpUpNIC; Crause et al. 2016). This calibration is not part of this PhD project, and is being worked on by Danielle L.A. Pieterse, a student at Radboud University. In light of the results produced here, the reference catalogue used to perform the photometric calibration was expanded to include GALEX (Bianchi et al., 2018), GAIA, PanStarrs and 2MASS to increase the accuracy of the calibration while the simultaneous spectroscopic observations are being analysed. With over 75 million stars over the whole sky, this has improved the photometric calibrations to better than 0.5% due to the large number of stars in each field.

3.3 Transients

ZOGY has the option to add a number of fake transients in each subimage, set by the `nfakestar` and `fakestar_s2n` parameters in the settings file. `nfakestar` sets the number of fake transients added to each subimage. If set to 1, a fake transient is added to the centre of each subimage. If greater than 1, the first is added to the centre of each subimage, with the remaining distributed randomly. `fakestar_s2n` sets the SNR of the fake transient. With the given SNR, the pipeline calculates the flux each transient should have in order to get to achieve the stipulated SNR, and adds a fake transient with the corresponding flux and a PSF determined from the image by ZOGY.

In order to determine how well the pipeline can recover transients, I ran a single image, from fields 16017 and 16038, through the pipeline multiple times, each time adding 1 fake transient to each subimage with different SNRs. The percentage of transients recovered is shown in Figure 3.14. One hundred and twenty one (121) fake transients were added to each image, resulting in 1 transient making up 0.83% of the total transients added. Out of the 121 fake transients added to the image in field 16017, the pipeline was able to recover over 96% of the fake transients for the entire SNR range, while recovering over 99% of the fake transients for SNRs of 13 and above. For field 16038, the pipeline was able to recover over 95% of the fake transients for the entire SNR range, with 100% of fake transients recovered for SNRs of 11 and above. In this test, photometry was performed at the known position of the fake transients, in order to compared the input flux and the recovered flux. A transient was considered recovered if the photometry measured at the known position of the transient was positive. If a negative flux was measured at the known position, I classified this as the pipeline failing to recover the transient. Figure 3.15 shows three

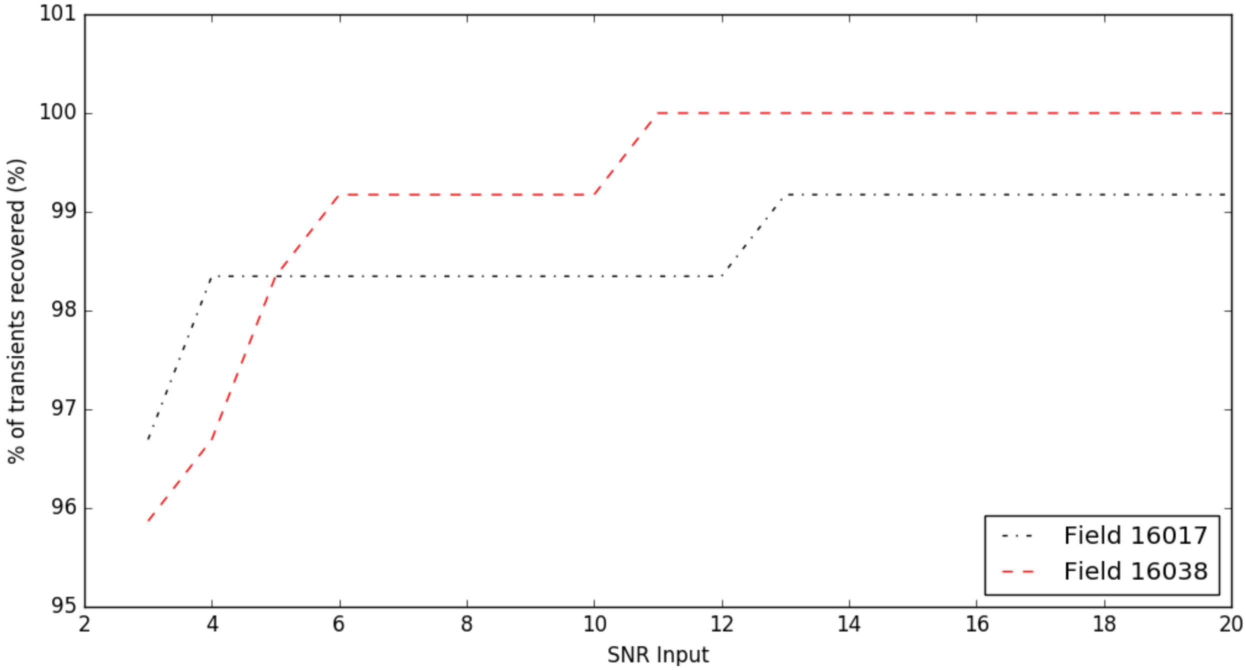

Figure 3.14: The percentage of transients recovered as a function of the SNR for fields 16017 and 16038. 121 fake transients were added during the test, resulting in 1 transient making up 0.83% of the total transients added.

examples where the pipeline failed to recover the fake transient. The fake transient is not shown in the images, but the red circle highlights the position where the fake transient was added. This test allows a check on the reliability of the pipeline to recover a transient as the flux of the fake transients is known. For a true test of the pipeline's ability to detect transients, a blind search should be carried out on an image. The number of transients found can then be compared to the number of real transients found, the number of false positives, and the number of transients missed.

The reason a transient with an adequate SNR could fail to be detected is related to the random noise governed by Poisson statistics. A histogram of the values in S_corr (the image showing the corrected significance of each pixel) produced by the pipeline is shown in Figure 3.16. As seen from the histogram, the distribution of S_corr is given by a Gaussian distribution centred around zero. Given this distribution, there is a 0.3% chance that a pixel has a value either above 3σ, or below -3σ. This equates to roughly 3x10^5 pixels with values above or below $|3\sigma|$. Since this image is used to detect transients using a significance threshold, i.e. any pixel above the set threshold is detected as a transient, the noise can significantly shift the significance value. Therefore, a normal

An example where recovery failed for a transient with high SNR (> 13)

An example where recovery failed for a transient with medium SNR (4<SNR<13)

An example where recovery failed for a transient with low SNR (< 4)

Figure 3.15: Three examples of where the pipeline failed to recover the fake transient. Each image is 100 by 100 pixels in size and is taken from a clean image (i.e. before the transient was added). The red circle shows the position where the fake transient was added to. Transients which failed recovery were classified by a negative recovered flux. Left: An example where the pipeline failed to recover a transient with high SNR. Middle: An example where the pipeline failed to recover a transient with medium SNR. Right: An example where the pipeline failed to recover a transient with low SNR.

pixel could be seen as a transient (depending on the threshold set for transient detection) purely due to noise, while a pixel containing a transient could be missed if the noise shifted the significance value below the detection threshold. As such, the pipeline was set to use a slightly higher detection threshold of 6σ to eliminate these noisy pixels.

The median recovered flux for the fake transients in fields 16017 and 16038, with SNRs ranging between 3 and 20, is shown in Figure 3.17. At low SNRs, the median recovered flux is within ~15% of the input flux, but the error on this determination is almost 50% of the value. As you would expect however, the recovered flux converges to the input flux for higher SNRs, with the error on this determination decreasing below 10% of the value for SNRs of 15 and higher.

In order to determine how well the pipeline can recover transients in terms of the position across the image and the field density, I ran images from 3 different fields with different field densities (16017 containing 5337 extracted sources; 90017 containing 19109 extracted sources; and 16038 containing 39744 extracted sources) through the pipeline with `nfakestar` set to 1 and `fakestar_s2n` set to 10. A histogram of the recovered flux compared to the input flux for all fake transients is shown in Figure 3.18. Plotting the recovered flux compared to the input flux for each field as a

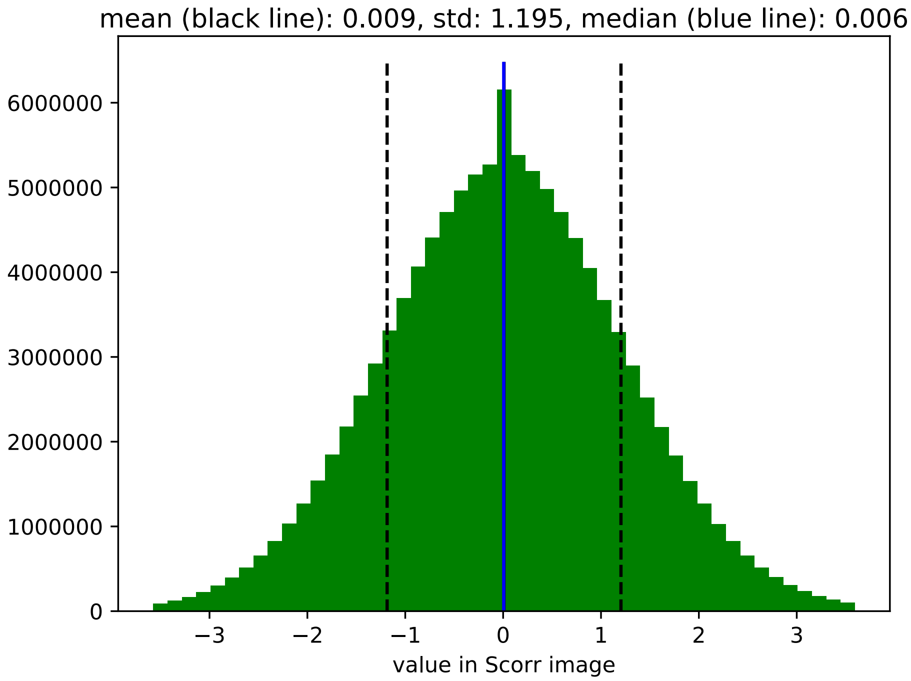

Figure 3.16: A histogram of the pixel values in S_corr produced by the pipeline. The distribution of the values is a Gaussian distribution centred on zero. This is expected as the significance of the majority of the pixels should be zero (as they do not contain a transient) with some level of noise.

function of x, y, R and flux is shown in Figures 3.19 and 3.20. The recovered flux fluctuates around the true flux of the transient, with no significant trends seen.

The majority of transients observed with MeerLICHT should thus be successfully detected with the pipeline. Although some low SNR transients can be missed by setting the detection threshold higher, the higher detection threshold can eliminate a large number of false detections that would require real-bogus vetting.

3.4 Timing

As the main objective of the pipeline is the detection of transients in real-time, it is important to test the time it takes to run each image from start to finish. The pipeline was designed with the ability to process multiple image at once, so each image does not need to be processed within the 1 minute cadence to ensure real-time reporting of the result. This is because, given enough resources (CPUs and RAM), the pipeline can ingest a new image each minute by assigning the new image to

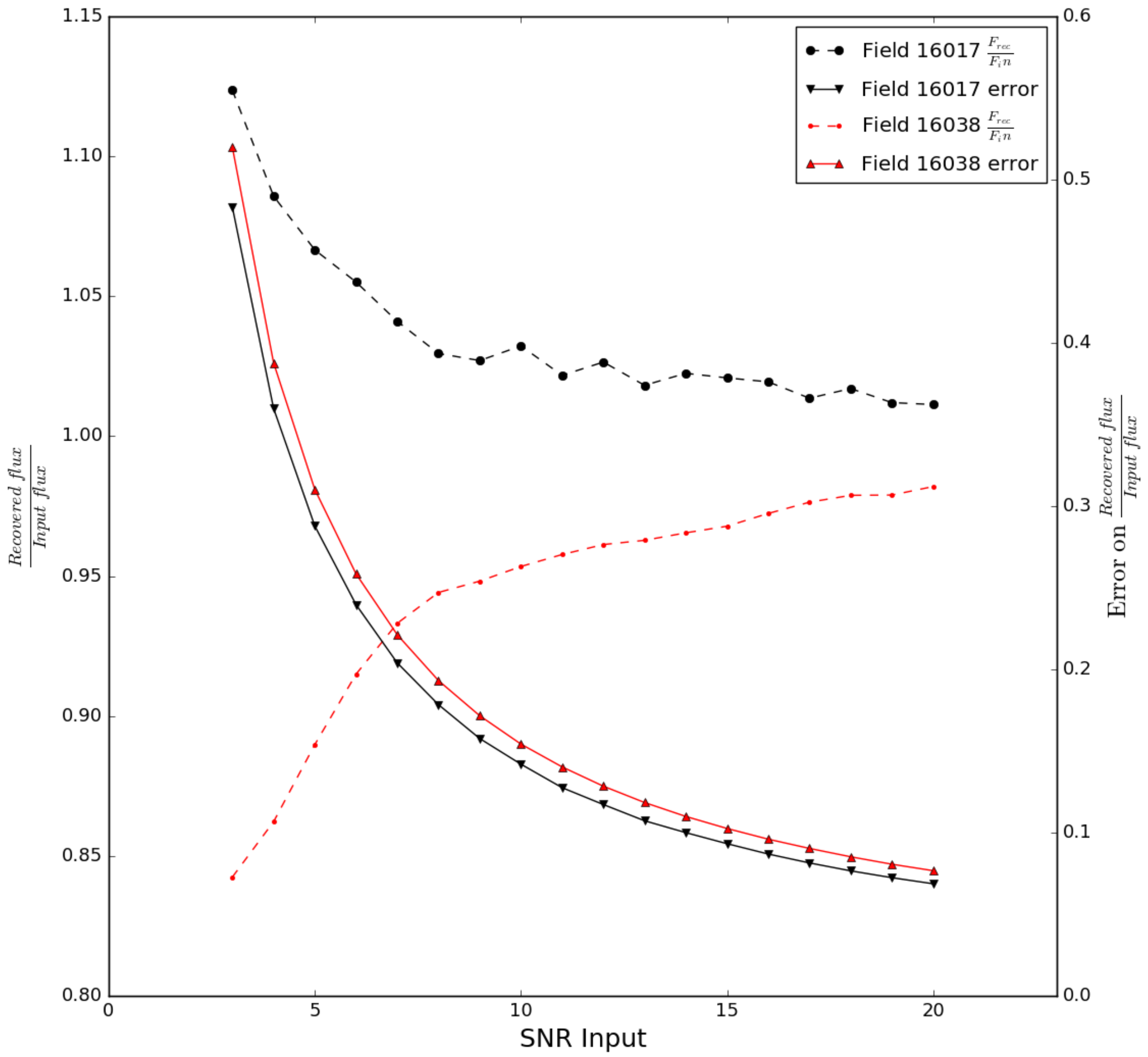

Figure 3.17: Median recovered flux, as well as the median error on the recovered flux, for fields 16017 and 16038, compared to the input flux as a function of the SNR. The black markers show the results for field 16017. The circles and dotted line show the recovered flux over the input flux, while the downward triangles and solid line show the error of the recovered flux over the input flux. The red markers show the results for field 16038. The dots and dashed line show the recovered flux over the input flux, while the upward triangles and solid line show the error of the recover flux over the input flux.

a new CPU. Thus, the processing of images will not get held up, and results will be produced in real-time, with a delay between the start and end of image being the time it takes to process the image.

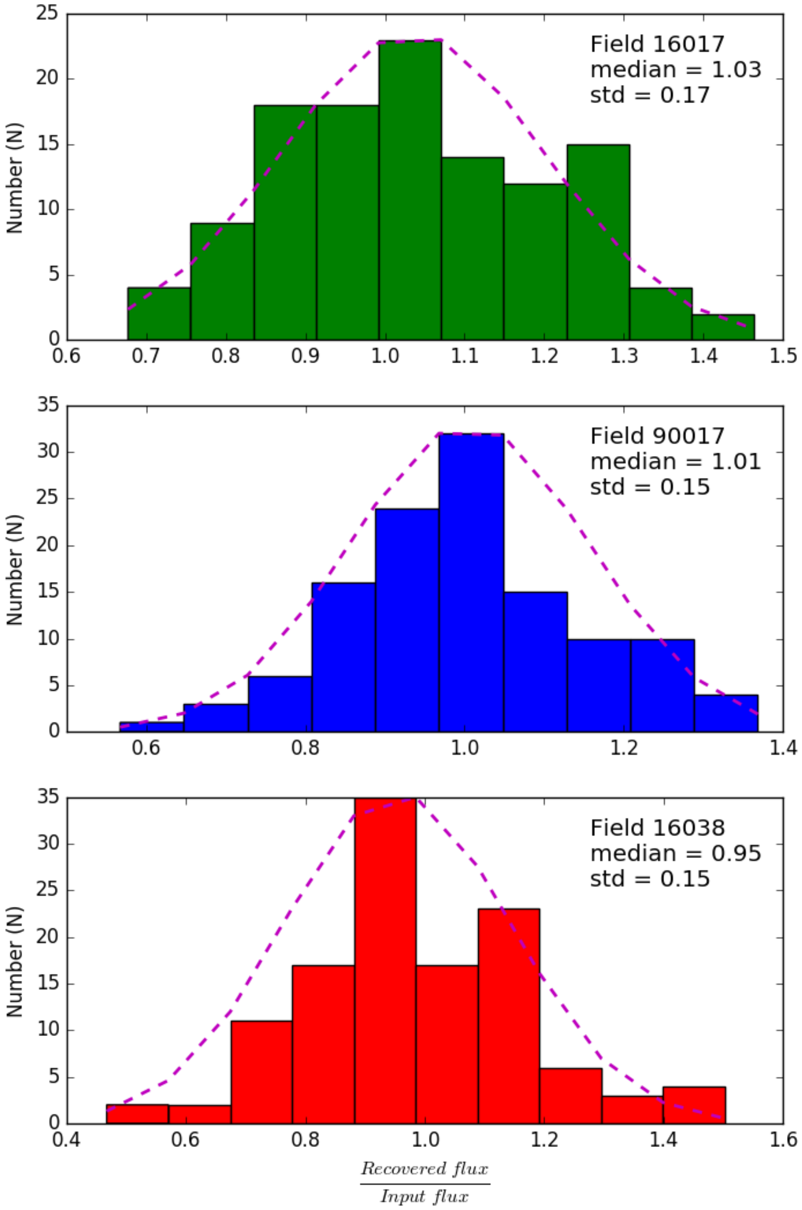

Figure 3.18: Histogram of the recovered flux compared to the input flux for transients with SNR = 10, for fields 16017, 90017 and 16038, and the corresponding Gaussian fit.

The main pipeline log contains the time stamps of when each science image was successfully reduced with the pre-processing part of the pipeline, as well as when each science image successfully ran through `subpipe`. I plotted the time it took (in minutes) for each image, for a series of images from field 16023 (in the q filter), to successfully run through the reduction part of the pipeline and through `subpipe` in Figure 3.21. The median time an image took to run through the reduction part of the pipeline is 1.27 minutes, while through `subpipe` is 9.30 minutes. These

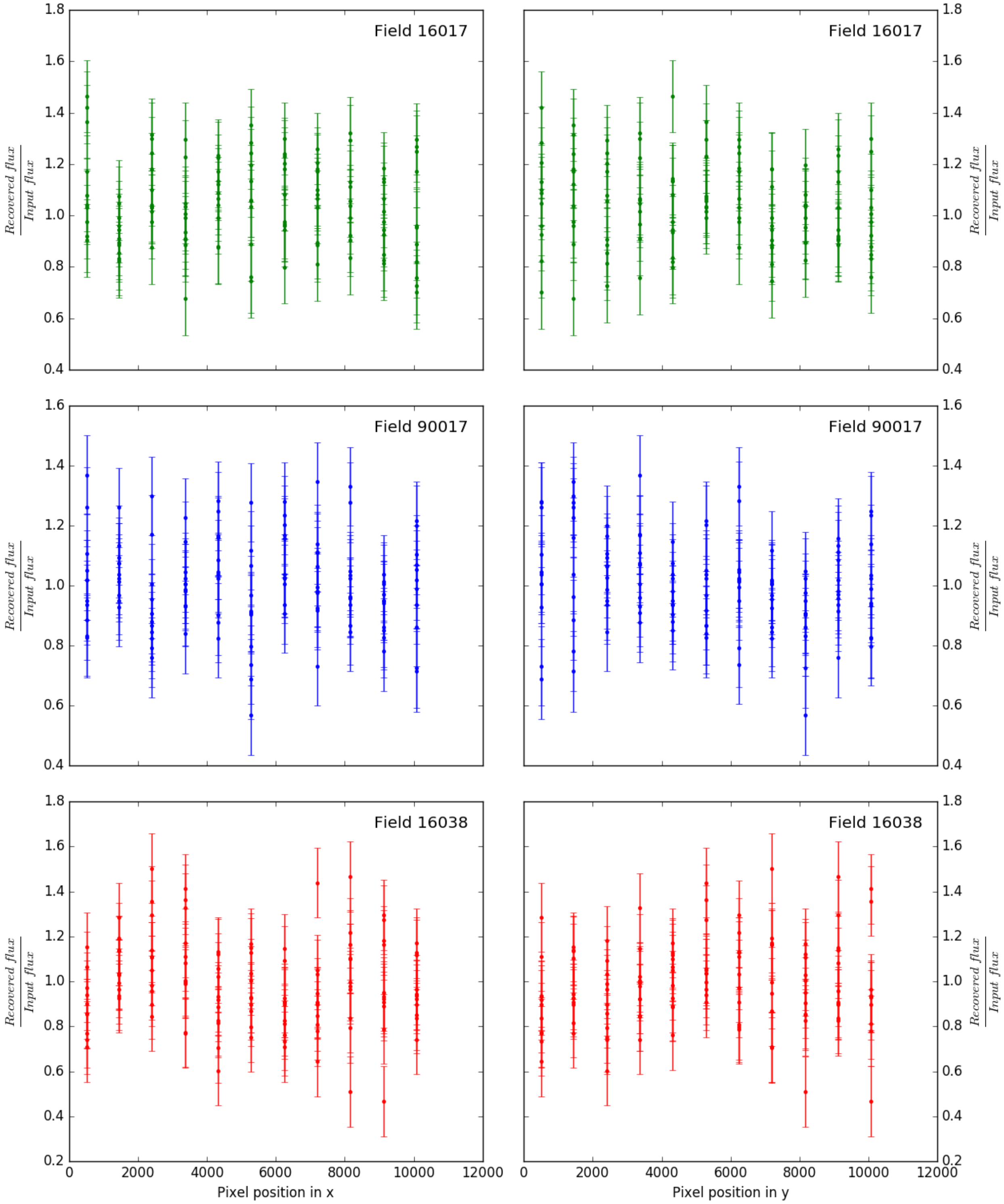

Figure 3.19: Recovered flux compared to the input flux for transients with SNR = 10, for fields 16017, 90017 and 16038 as a function x (left) and y (right).

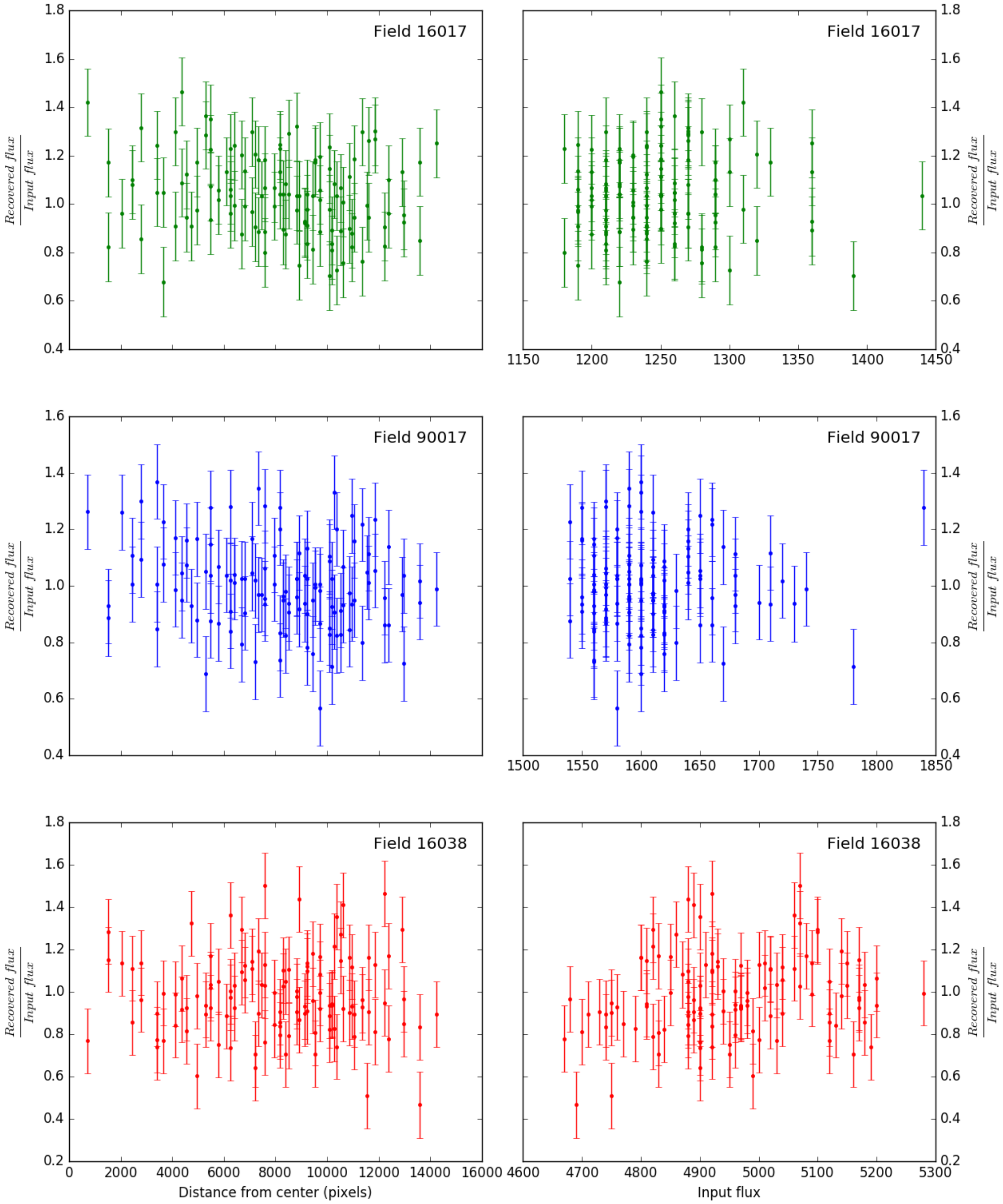

Figure 3.20: Recovered flux compared to the input flux for transients with SNR = 10, for fields 16017, 90017 and 16038 as a function R (left) and input flux (right).

Table 3.5: Median time in minutes to complete each step of the pipeline for field 16023.

Step	Median time (min)
Reduction	1.27
`Subpipe`	9.30

Function in ZOGY	Median time (min)
`Run_wcs`	0.20
`Run_remap`	0.16
`Prep_optimal_subtraction`	3.10
`Get_psf`	1.39
`Get_psfoptflux_xycoords`	0.49
`Deriving_optimal_subtraction`	0.49
`Get_fratio_radec`	0.01
`Run_ZOGY`	1.06

results mean that the pipeline will process an image from start to finish with a median time of 10.57 minutes. A slight increase in the run time for `subpipe` is seen towards the end of the series of images.

To investigate the run time of `subpipe` in greater detail, I plotted the time it took (in minutes) for individual functions inside ZOGY to complete in Figure 3.22. From the plot, we see that all functions, except `prep_optimal_subtraction`, are mostly consistent in run time. The function `prep_optimal_subtraction`, which includes `get_psf`, `get_psfoptfluxxycoords`, and `deriving optimal fluxes`, shows an increase in run time as the series of images is processed. Since the above mentioned functions within `prep_optimal_subtraction` are consistent in run time, the increased run time observed may be a cumulative effect which could be linked to memory leakage in the pipeline.

After this, the results need to be ingested into the database to check whether transients found are new, and thus need reporting, or previously found. Independent work has been done on the database and web interface for MeerLICHT/BlackGEM, with a focus on reducing the time of ingesting the data points to report new sources.

While a delay of 10 minutes is already good, work is still in progress to minimize the time it takes to process each image in order alert the community of new transients as soon as possible.

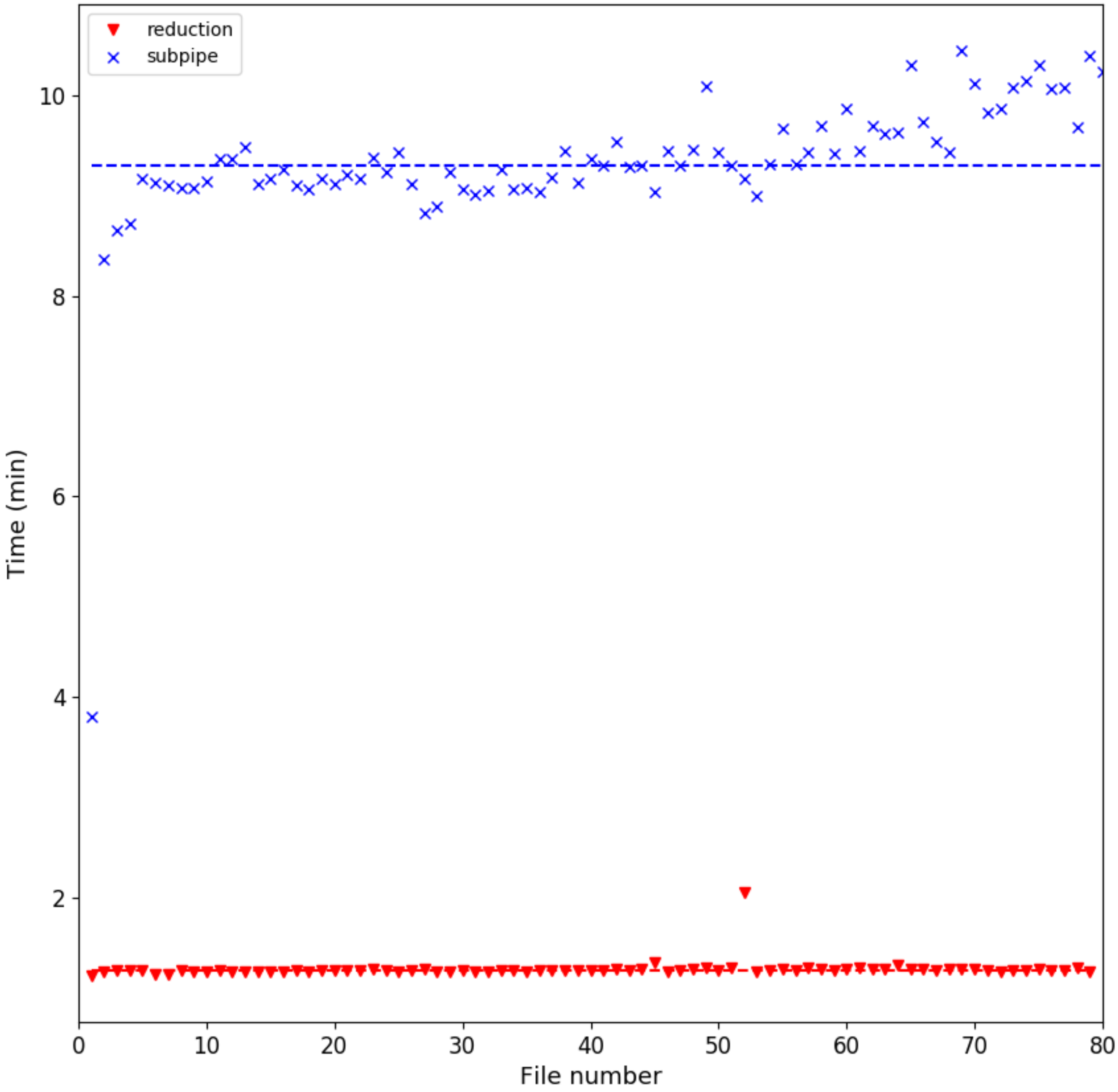

Figure 3.21: Time (in minutes) it took a series of images from the same field (16023) in the q filter to successfully run through the reduction part of the pipeline, and through `subpipe`. The points show the time for individual images, while the dotted line show the median time it took to run through the corresponding part of the pipeline. The first image in the series ran as a reference job, and therefore required less time to complete in subpipe.

One of the options being looked at to achieve this is the multi-processing of a single image i.e. processing a single image over multiple CPUs, in order to speed up the individual processing time. Extensive testing on memory usage within the pipeline is also needed to optimize run times and ensure no memory leakage is present.

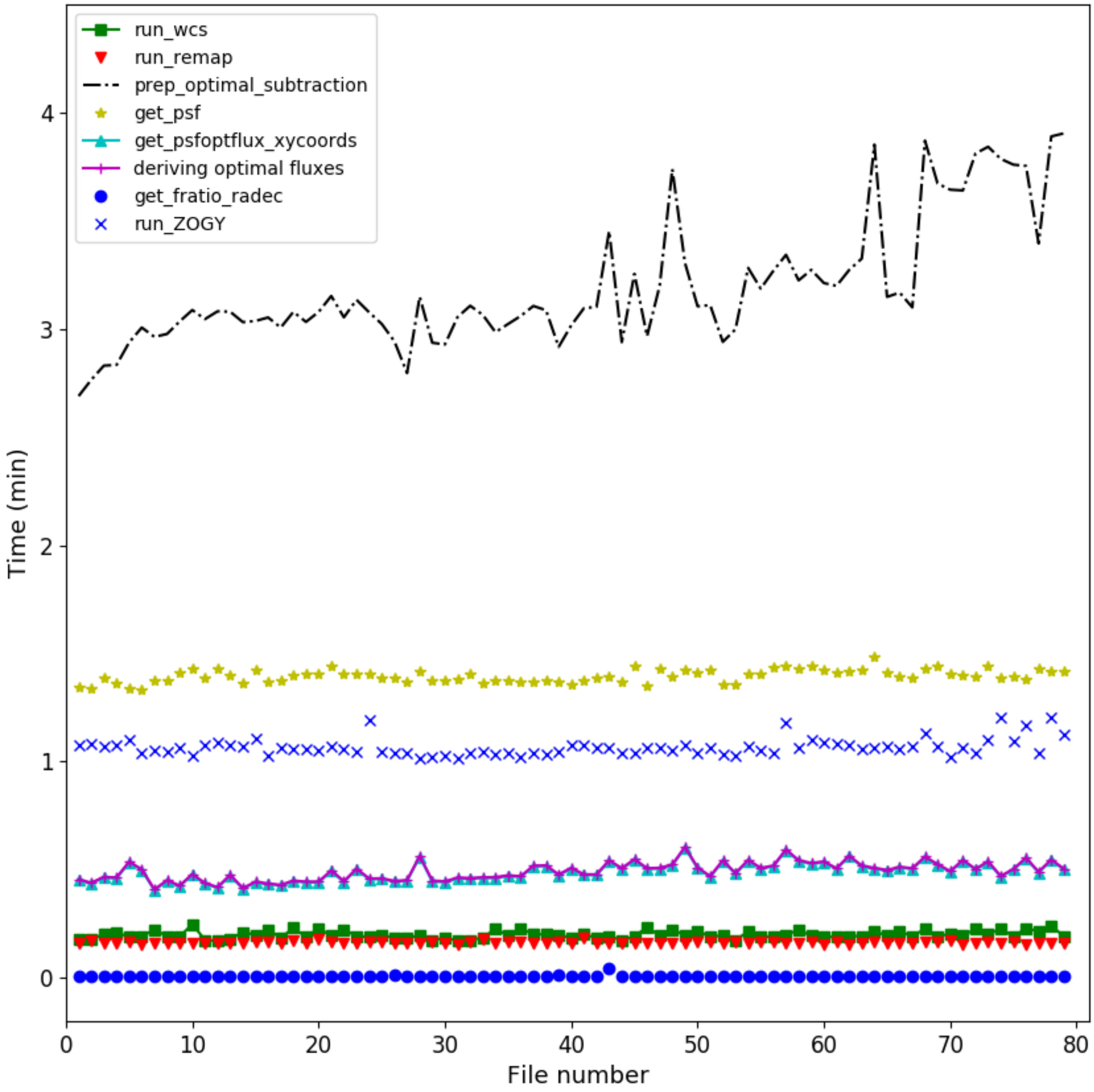

Figure 3.22: Time (in minutes) it took multiple functions inside ZOGY to complete for a series of images from the same field (16023) in the q filter.

3.5 Overall performance

Overall, the pipeline has shown promising results in all four performance tests. With the use of GAIA data, the pipeline will be able to obtain 0.005 arcsec astrometric accuracy in both RA and Dec. With regards to photometry, although some improvement can be done, and is underway, to the photometric calibration, initial results are promising with the measured limits within the expected range. Transient detection based purely on the significance of pixels shows a 100 % recovery rate for higher SNR transients, and above 95 % for lower SNR transients. Although a time delay, from the ingestion of an image to the production of the catalogues, of 10 minutes is the current limit of the pipeline and a reasonable time for transients alerts, further work is underway to reduce this time.

Chapter 4

Variability

To study the variable sky three main things are required: reliable photometry, accurate timing, and adequate cadence. In Section 3.2, I provided an indication of the reliability of MeerLICHT's photometry. For example, good agreement was found with PanSTARRS in r for non-saturated sources < 17 mag, while a magnitude of 21.2 could be reached in 60 seconds in q for sources with SNR $= 5$. For accurate timing, MeerLICHT will make use of GPS timing to time stamp each image. As MeerLICHT will be linked in real-time to MeerKAT, the fields observed during the night directly depend on the MeerKAT schedule. As such, the cadence will vary for different fields. Fields from the LSPs, such as the LADUMA field which has been allocated over 3000 hrs, as well as the calibration fields (which are a limited number), will provide the longest baseline for variability studies at both short and long timescales, from minutes to years.

Table 4.1 shows the 5 fields from the commissioning observations I used for the purpose of this variability study. These observations were taken on 1 and 2 September, and 21 October 2017. For the purpose of studying variability, these fields were observed as a time series in the wide filter, q, as this filter will have the highest cadence during normal operations. Observations in all filters were obtained for one of these fields.

In Section 4.1, I discuss a number of ways in which variables can be found. In Section 4.2, I implement a number of tests on a set of commissioning data to identify sources which show significant variability, and discuss the results and implications for future operation in Sections 4.3

Table 4.1: MeerLICHT test fields used in this section.

Field ID	Object	RA	DEC	Date	Filter	Exposure time (sec)	Number of exposures
16023	Fornax1	03:38:00	-35:27:00	2017/09/01	q	120	1
					r	120	1
					i	120	1
					g	120	1
					u	120	1
					z	120	1
					q	60	80
				2017/09/02	q	60	60
				2017/10/22	q	60	5
					r	60	5
					i	60	5
					g	60	5
					u	60	5
					z	60	5
16089	NGC7424	22:57:18	-41:04:14	2017/09/02	q	60	120
90004	OGLE-BLAP-014	18:14:33	-31:19:56	2017/09/01	q	60	120
90006	QU Tel	20:09:40	-52:25:17	2017/09/01	q	60	60
90013	V2008-1753	20:08:16	-17:53:11	2017/10/21	q	20	215

and 4.4 respectively.

4.1 Characterising variability

There are a number of different statistical tests thats can be used to find variables. Graham et al. (2013) and Ramsay et al. (2014) outlined how the various tests are able to identify different classes of variable stars better than others. The Lomb Scargle test (LS; Lomb 1976; Scargle 1982) is more suited to finding shorter period pulsating sources in data that are irregularly spaced. The alarm test (Tamuz et al., 2006) and Analysis of Variance periodogram (Schwarzenberg-Czerny, 1989) are best for finding eclipsing binaries and flare stars, while the Stetson J statistic (Stetson, 1996) was designed to identify Cepheid variables (and thus is suited for high amplitude variables such as contact binaries, flare stars and long period pulsators). For this chapter, the discussed light curves are extracted from the full source catalogue produced by ZOGY. These catalogues make use of SExtractor to identify sources in the field, after which ZOGY performs optimal photometry for each source.

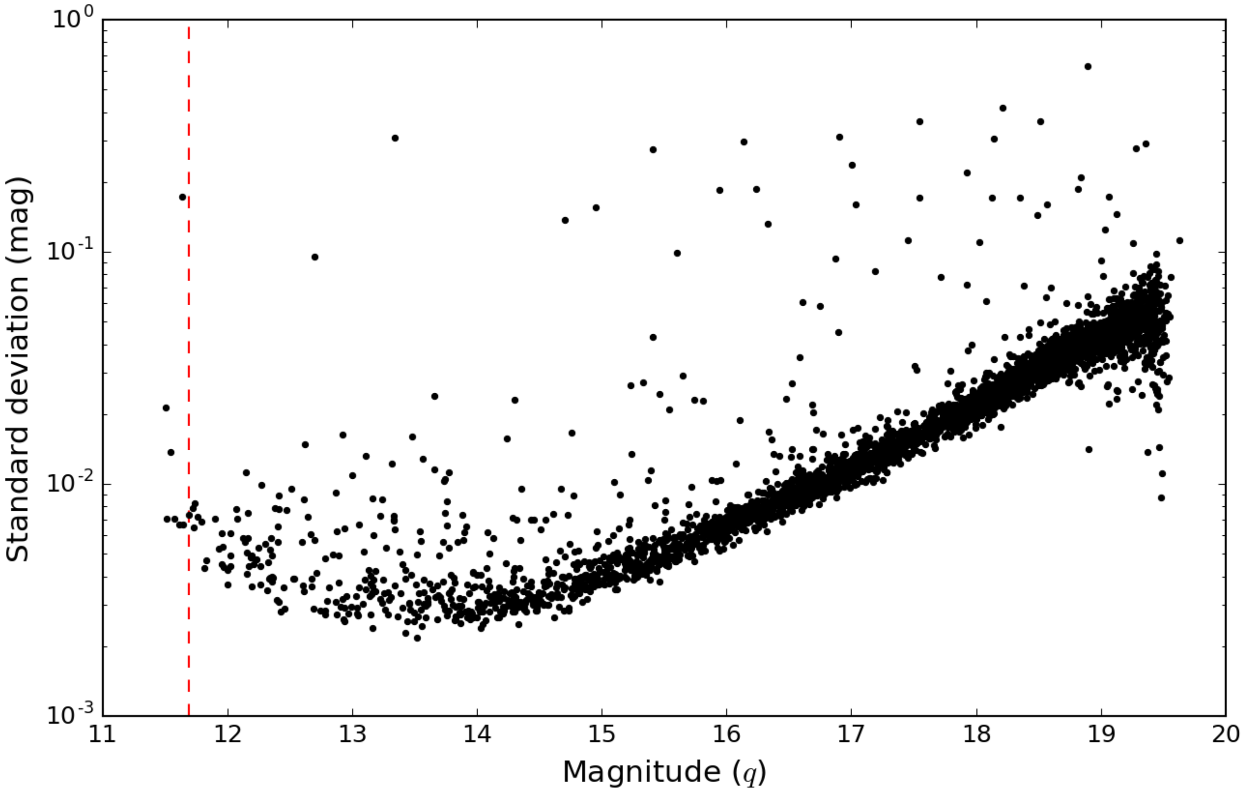

Figure 4.1: Standard deviation of the light curves for stars (defined as having a CLASS_STAR > 0.8) in field 16023. The dashed red line show the previously determined saturation limit for q. We obtain variation on the level of a few mmag towards bright sources.

4.1.1 Minimum variations

To investigate the minimum photometric variation MeerLICHT can accurately be detected in a light curve, I show the standard deviation against the average magnitude for light curves of stars (defined as having a `CLASS_STAR` > 0.8) extracted from field 16023 in Figure 4.1. The increase towards the fainter range is due to larger errors associated with smaller count rates. We also see an increase in error towards saturation, as the determination of the star's flux/magnitude becomes unreliable due to saturation and non-linearity effects. For the bright, non-saturated stars, we obtain variation on the level of a few mmag.

4.1.2 Lomb-Scargle test

With typical data lengths (T_{len}) between 1 and 2 hours for each field, and a cadence, $t_{cad} \sim 67$ sec for most fields, I focused on the detection of variability on timescales ($2t_{cad} < \tau < \frac{1}{3}T_{len}$). Focusing on variability with $2t_{cad} < \tau < \frac{1}{3}T_{len}$ ensures that there is a minimum of 3 period cycles within the light curve. As such, I made use of the LS test to identify variability. I ran the LS test on each light curve using `VARTOOLS` (a program containing statistical analysis tools for period finding in time series data; Hartman & Bakos 2016). This test produces a variability timescale (τ_{LS}), along with a false alarm probability (FAP) for the peak with the highest statistical significance in the power spectrum. The FAP gives the probability that this peak is caused by random noise. In log space, the more negative log(FAP) is, the higher the probability that the light curve has variability on those timescales. Theoretically, a light curve with log(FAP) = –2.5 has a probability of being variable with a 3σ confidence level. Due to systematic effects such as red noise however, the threshold for true variability can be lower. Additional routines such as detrending were not used during the handling of the light curves as no large trends were found across most of the data, given the short data lengths and the limited range of airmass over which the data were taken. However, for future long (all-night) MeerLICHT observations of a single MeerKAT field, the effects of differential atmospheric extinction might become important, and a future upgrade of the variability analysis should include a light curve detrending algorithm.

4.1.3 MAD statistic

To determine which stars show variability within the noise, I used the median absolute deviation (MAD) from the median to find outliers in the log(FAP) - period plane, as done by Macfarlane et al. (2015). The MAD statistic allows an estimation of the deviation from the median within a bin of values. This is important as the number of data points per bin may vary greatly, changing both the median and the standard deviation from the median from bin to bin. Using period bins of 0.5 minutes, I computed the median and MAD of the log(FAP) values within the bin, where the MAD is calculated using

$$\mathrm{MAD} = median(|x_i - median(x_i)|) \tag{4.1}$$

where x_i is the log(FAP) value. Variables are then identified as stars which satisfy:

$$\log_{10}(\mathrm{FAP}) < \mathrm{median}(\mathrm{logFAP}) + (n \text{ x } \mathrm{MAD}_{\mathrm{logFAP}}) \tag{4.2}$$

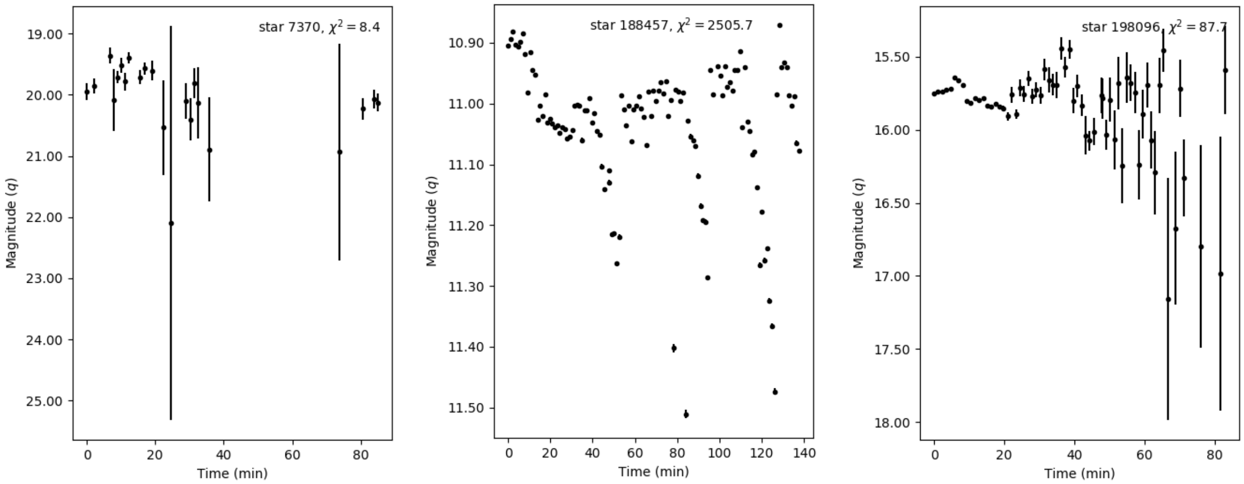

Figure 4.2: Three examples of light curves which originally passed the MAD statistic and reduced χ^2 cut-offs, but failed the manual inspection when no CLASS_STAR > 0.8 cut was made. Left: A light curve with less than 25 data points, as well as single bad data points. Middle: Spurious variability caused by variable seeing for a star close to saturation. Right: A light curve made from poor quality data.

where n is an integer defining how far a source is from the local median. For each field I plot τ_{LS} and the corresponding log(FAP) of each star. I show the various cut-offs using $n = 1, 3, 5, 10$. As this exercise is to highlight MeerLICHT's ability to find variables, I chose to focus on stars with a higher probability of being variable, using a cut-off of $n = 10$ i.e. stars with $\log(\text{FAP}) < 10\text{MAD}_{\text{logFAP}}$.

4.1.4 Chi2

Another statistical test used to determine if the variability seen is significant is a reduced χ^2 fit with respects to the mean magnitude. Fitting a straight line, I use $N - 1$ degrees of freedom when calculating the χ^2. Here, a $\chi^2 \approx 1$ indicates a light curve consistent with being constant. The higher the χ^2, the more likely the variability seen is real and not caused by systematic errors. After computing the MAD, I calculate the reduced χ^2 of the stars satisfying $\log(\text{FAP}) < 10\text{MAD}_{\text{logFAP}}$. Focusing on the light curves showing higher variability, I restrict the results to light curves with $\chi^2 > 5$.

4.1.5 Manual inspection of light curves

After filtering the results with the MAD statistics and reduced χ^2, I performed a manual inspection of the remaining light curves. Using the Faint Sky Variability Survey (Groot et al., 2003), Morales-

Rueda et al. (2006) found that ~ 25 data points are needed in order to provide reliable variability detection. Thus light curves with less than 25 measurements were discarded for this purpose. The seeing determines how narrow/spread-out the PSF of the star is. The better the seeing, the narrower the PSF, with the star's flux concentrated towards the centre. For stars close to saturation, the flux extracted can vary as the centre of the star becomes saturated with better seeing. As such, stars close to saturation were flagged during the manual inspection for spuriously variability. Light curves containing artifacts, such as single bad data point, were also flagged for causing spurious variability. Figure 4.2 shows 3 examples of light curves which failed the manual inspection. Originally, variability tests were run on all sources within the field (i.e. not using `CLASS_STAR` to restrict the results to only stars). This resulted in a large number (order tens) of sources passing the MAD statistic and reduced χ^2 cut-off, only to fail the manual inspection due to the above mentioned points. After implementing the `CLASS_STAR` > 0.8 cut, the number of stars which passed the variability tests, but failed the manual inspection greatly reduced, with only two fields requiring manual inspection of the passed light curves. This shows the importance of stricter criteria if we wish to restrict the need for human intervention.

4.1.6 Colour

To identify certain classes of variable stars, one can look at where they lie in colour-colour space. Sources such as Cataclysmic Variables (CVs) are known to the bluer in colour, due to the contribution of light from the white dwarf and the accretion disc. AM CVn stars, a subclass of CVs with shorter periods (and thus more likely to be detected in this data set), are very blue sources and occupy a particular region in the $u - g$ vs $g - r$ colour plane (Carter et al., 2013). Only one field (16023) in this data set has colour information. For field 16023, I investigated the $u - g$ vs $g - r$ colour plane to highlight any blue sources in the field.

4.2 MeerLICHT commissioning fields

Using the set of commissioning data summarized in Table 4.1, I looked at identifying variability from light curves created by the pipeline. These fields were chosen as they contain a known variable, and in some cases overlap with known MeerKAT LSP fields e.g. the Fornax cluster (16023) and MHONGOOSE (16089). This allows us to determine how well the pipeline can extract these variables, as well as provide an indicated of the reliability of new variables found. Except for field 90013 which has an exposure time of 20 s, all other fields have an exposure time of 60 s, and each field was observed for 1 - 2 hours. No guiding was available during this time, and noticeable drifting was observed during observations. Dome tracking was also not available during this time. As the dome had to be manually controlled to follow the tracking of the telescope, observations are at risk of being vignetted by the dome if the dome is not moved in sync with the telescope. This vignetting by the dome results in a decrease of light from sources and can be mistaken as variability. During the early commissioning of MeerLICHT, the telescope software was incomplete and basic keywords such as start and end of exposure were not written to the header of each image. Thus, the start time for the first image (in a series of images) is only accurate to the manually recorded start time. The start time of each consecutive image contains additional uncertainty because the exact readout time of the camera was not know due to the absence of timing. Without GPS timing recorded in the header of each image, the accuracy of the timing is limited. The start time of each observations is accurate to the minute, while each consecutive exposure has an error of 0.05 min. Sources were extracted from the pipeline catalogues and cross matched with a 1.5 arcsec radius in `Python` to produce the light curves. Data points which where saturated, as well as images with a large zero point error (indicating bad quality) where not included in the light curves for quality control. Stars were defined as sources with a `CLASS_STAR` (produced by SExtractor) value of > 0.8.

4.2.1 16023 - The Fornax Cluster

Centred on the Fornax Cluster, Field 16023 contains a bright high-amplitude δ Scuti star with a period of 77.92272 mins (ASAS J033219-3539.3, Pojmanski 2002). Field 16023 was observed for $\sim$ 1.3 hours on two consecutive nights, and is the only field in this test data set that has colour information for all the MeerLICHT filters. As discussed earlier, some classes of variable stars, such as CVs, are intrinsically blue. Thus, colour information can be used to help distinguish the type of system. Plotting the 1317 stars for which we have colour information in u, g, and r, in the $u-g$ vs $g-r$ MeerLICHT photometric system colour plane (see Figure 4.3), we see 2 (0.15%) of these stars have $u-g<0$ (within the errors). The main sequence (MS) track by Drew et al. (2014) is shown

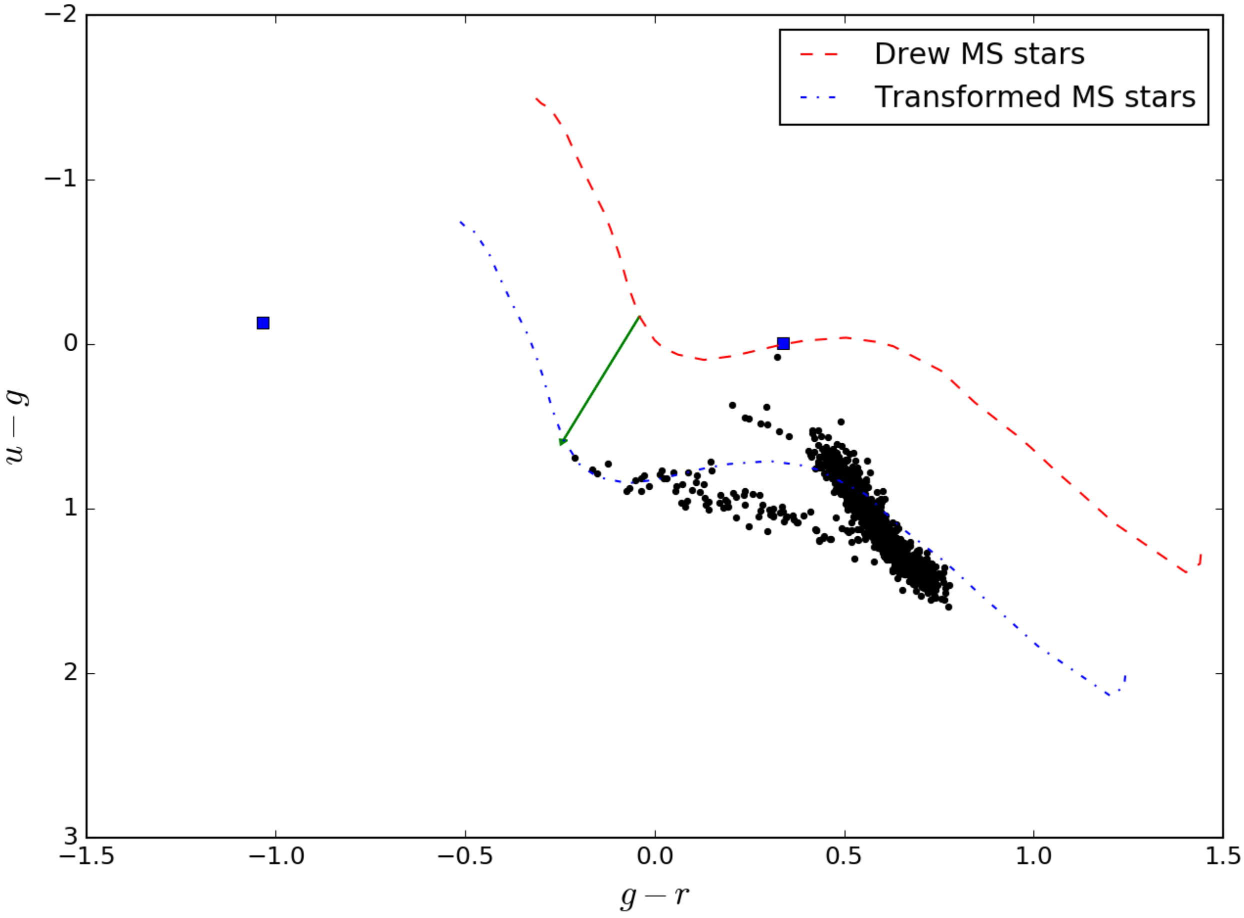

Figure 4.3: The $u - g$ vs $g - r$ colour plane of field 16023. Stars with $u - g < 0$, within the errors, are highlighted by the blue squares. Out of the 1317 stars which had colour information in u, g, and r, 2 (0.15%) were found have $u - g < 0$. The dashed red line shows the Drew et al. (2014) main sequence (MS) track, while the blue dot-dashed line shows the same MS track, but offset by 0.2 in g and 0.55 in u.

overlaid on the data. The resulting shift and tilt of the MS track with regards to the data is due to the combined effect of different u-passbands and the conversion between the AB and Vega magnitude systems. Although the stars within this field do not fit the MS track as well as the previously shown colour-colour diagram (Figure 3.12), scatter around the track is expected (see Verbeek et al. 2012). The large branch below the MS is most likely due to extragalactic contamination as this field is centered around a cluster of galaxies. Although a star/galaxy cut was made on the data using SExtractor's `CLASS_STAR`, this is not always a reliable cut between stars and galaxies (see discussion around Figure 4.11 later). These objects should not make the task of using colours to identify objects more difficult as they do not interfere with the colour determination of sources.

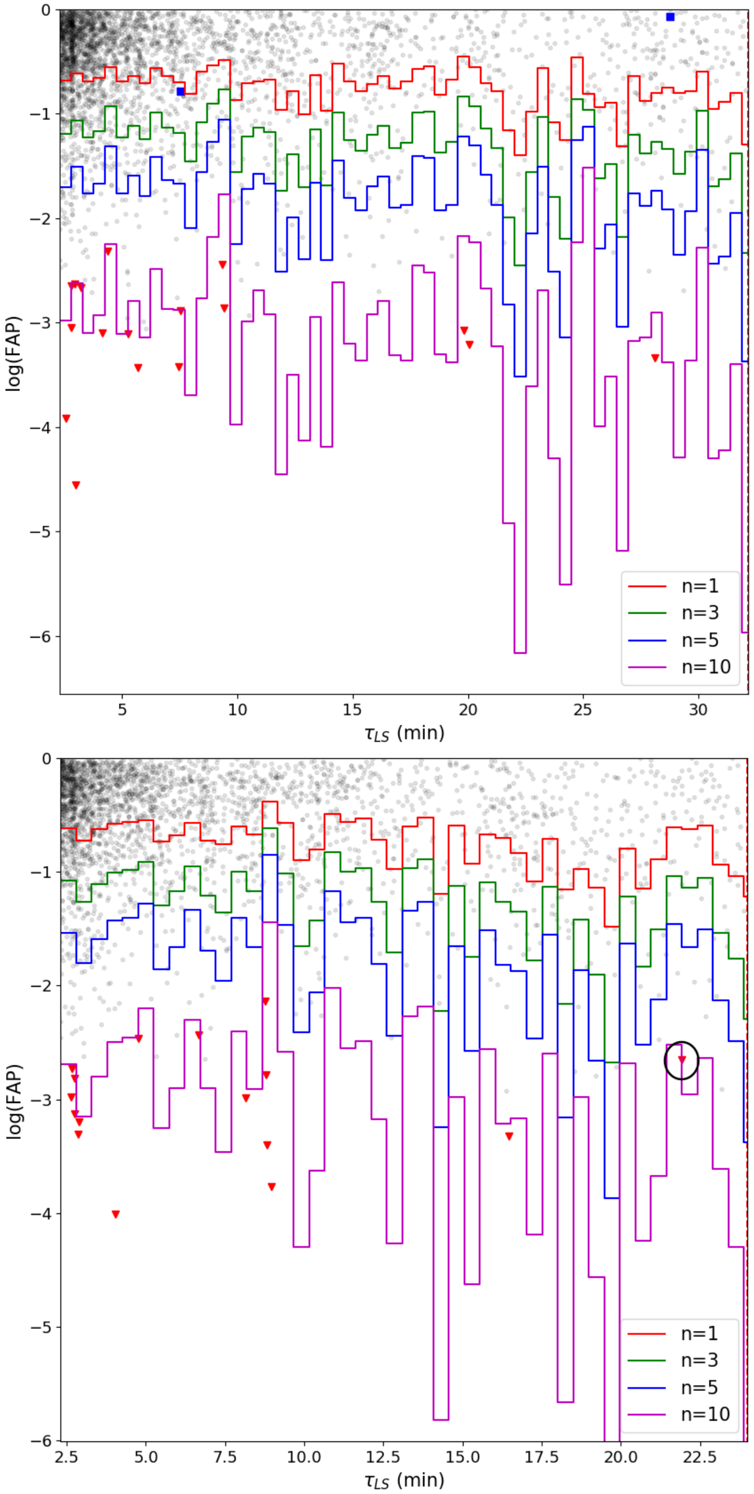

Figure 4.4: The log(FAP) - period planes for field 16023. Stars with log(FAP) $< 10\mathrm{MAD}_{\mathrm{logFAP}}$ are represented with by the red triangles. The stars with $u - g < 0$ are shown by the blue squares. Top: The log(FAP) - period plane for the first night. Bottom: The log(FAP) - period plane for the second night. The single stars which satisfied $\chi^2 > 5$ and passed the manual inspections is highlighted within the black circle. n is the integer used in the MAD statistics.

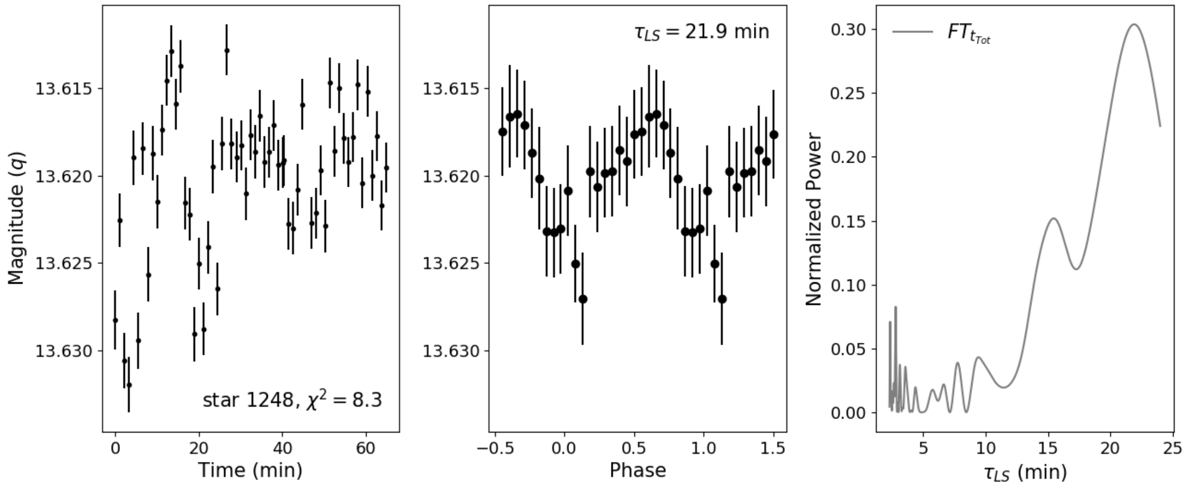

Figure 4.5: The single star within field 16023, from the second night, which shows variability. Left: light curve of star. Middle: Average light curve, folded on the found τ_{LS}, across 2 phases. Right: FT of the light curve.

For the LS test, each night was treated independently. The log(FAP) - period planes for field 16023 are shown in Figure 4.4. The stars with $u - g < 0$ are shown by the blue squares. No blue sources were found above the $n = 3$ cut-off. Out of the 17 stars found to satisfy log(FAP) $< 10\mathrm{MAD}_{\mathrm{logFAP}}$ during the first night, and the 16 stars found to satisfy log(FAP) $< 10\mathrm{MAD}_{\mathrm{logFAP}}$ during the second night, only 1 star showed a $\chi^2 > 5$ on the second night. The light curve and FT for this star is shown in Figure 4.5, while the details are summarized in Table 4.2. With a magnitude of 10.550 mag in V, ASAS J033219-3539.3 was saturated within the 1 minute exposure and its light curve could not be extracted.

4.2.2 16089 - A MHONGOOSE galaxy field

Field 16089 contains SSS_J225854.2-410856, a high-amplitude δ Scuti star with a period of 3.6 hrs (Watson et al., 2006). Field 16089 was observed for ~ 2 hours, shorter than the pulsation period of SSS_J225854.2-410856. The log(FAP) - period plane for field 16089 is shown in Figure 4.6. 14 stars were found to satisfy log(FAP) $< 10\mathrm{MAD}_{\mathrm{logFAP}}$, with only 1 of these satisfying $\chi^2 > 5$. The light curve and FT for this star is shown in Figure 4.7, while the details are summarized in Table 4.2. The light curve in Figure 4.7 shows possible signs of differential atmospheric extinction (upwards rising trend). We think this is unlikely as observations were taken at low airmass (mean airmass

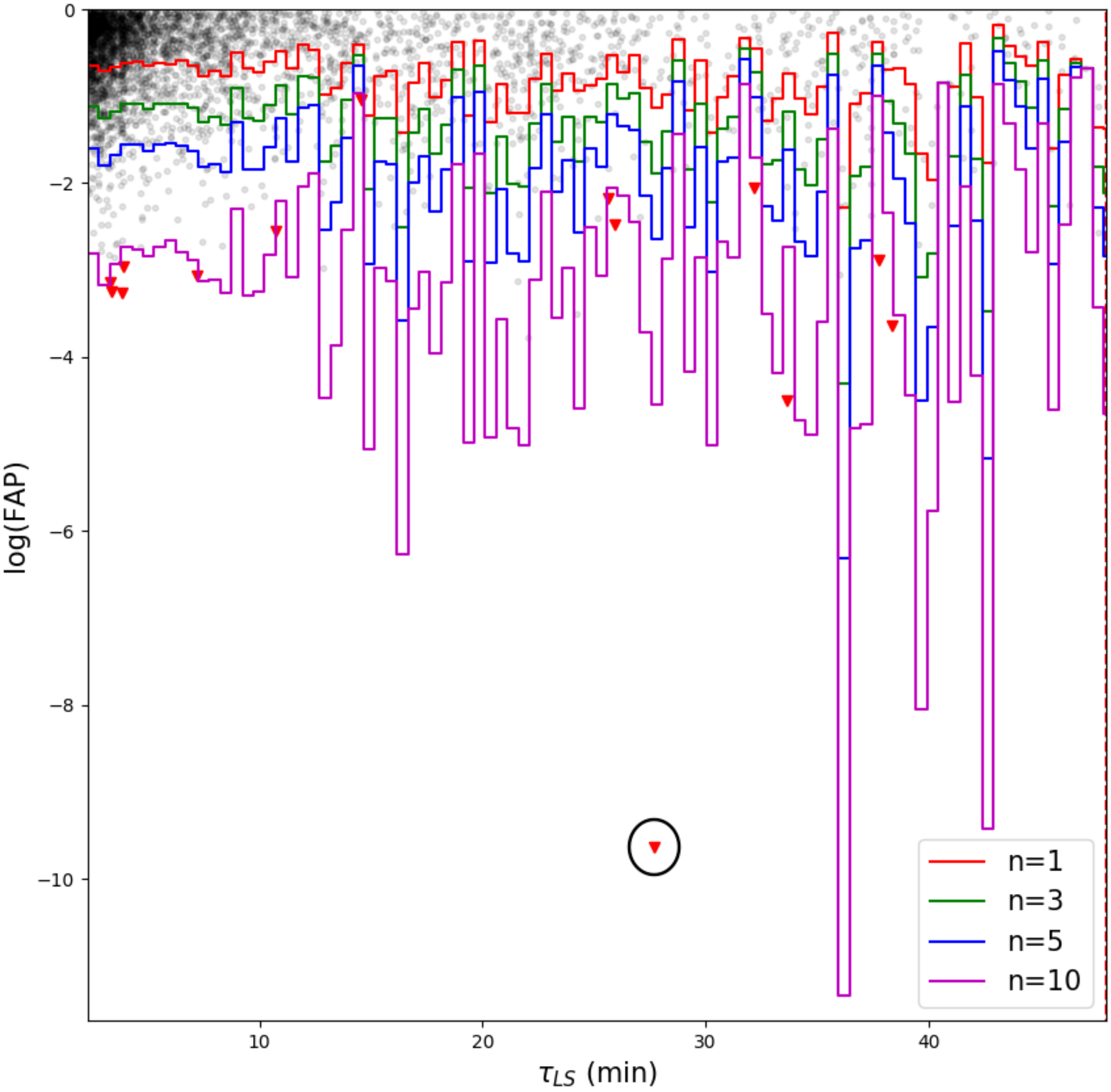

Figure 4.6: The log(FAP) - period planes for field 16089. Stars with log(FAP) $<$ 10MAD$_{\mathrm{logFAP}}$ are represented with by the red triangles. The single stars which satisfied $\chi^2 > 5$ and passed the manual inspections is highlighted within the black circle. n is the integer used in the MAD statistics.

of 1.05 throughout the observation). Although atmospheric extinction is corrected for during the photometric calibration within ZOGY, this emphasizes the possible need for the additional calibrations mentioned in Section 3.2, especially for long all-night observations of a single field over a large range of airmass. Although the timescale of variability could not be correctly recovered for SSS_J225854.2-410856 due to the data length, the LS test was able to detect longer variability with a log(FAP) = –110.7. The light curve of SSS_J225854.2-410856 is shown in Figure 4.8.

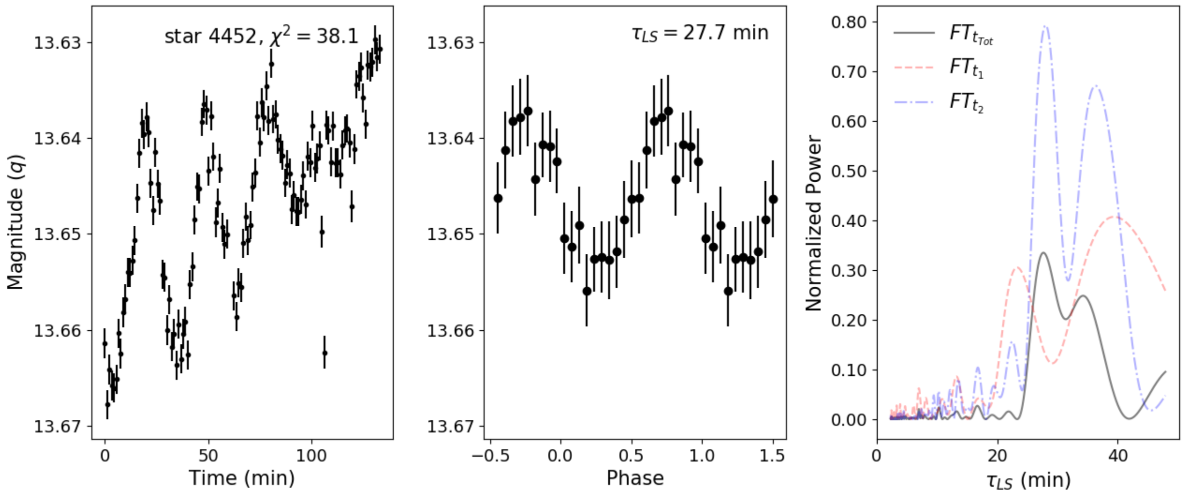

Figure 4.7: The single star within field 16089 which shows variability. Left: light curve of star. Middle: Average light curve, folded on the found τ_{LS}, across 2 phases. Right: FT of the light curve, FT_{tot} is the FT produced by the total light curve, and FT_{t1} and FT_{t2} are the FTs produced by the first and second half of the light curve.

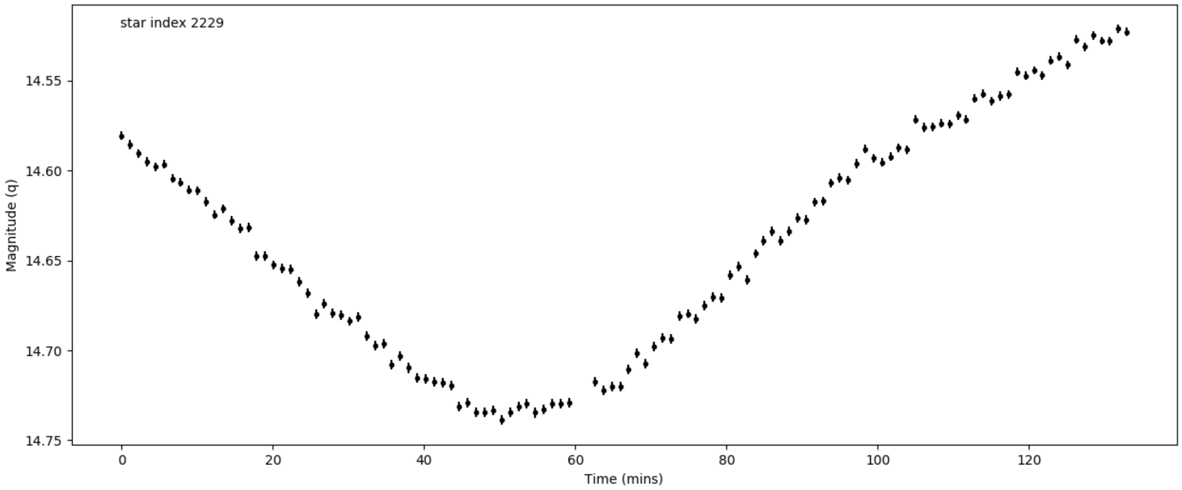

Figure 4.8: Light curve of SSS_J225854.2-410856.

4.2.3 90004 - The Galactic Centre

Towards the Galactic Centre, field 90004 contains a Blue Large-Amplitude Pulsator (BLAP) discovered by the Optical Gravitational Lensing Experiment (OGLE; Pietrukowicz et al. 2017) Survey. OGLE-BLAP-014 has a period of 33.62 mins with an amplitude of 0.339 mag in V and 0.264 mag in I. Field 90004 was observed for ∼ 2 hours. The log(FAP) - period plane for stars in field 90004 is shown in the top panel of Figure 4.9. The unusual density structures seen in Figure 4.9 (cf Figure 4.9 or Figure 4.6) are artifacts caused by the poor dome tracking during this sequence. Five stars

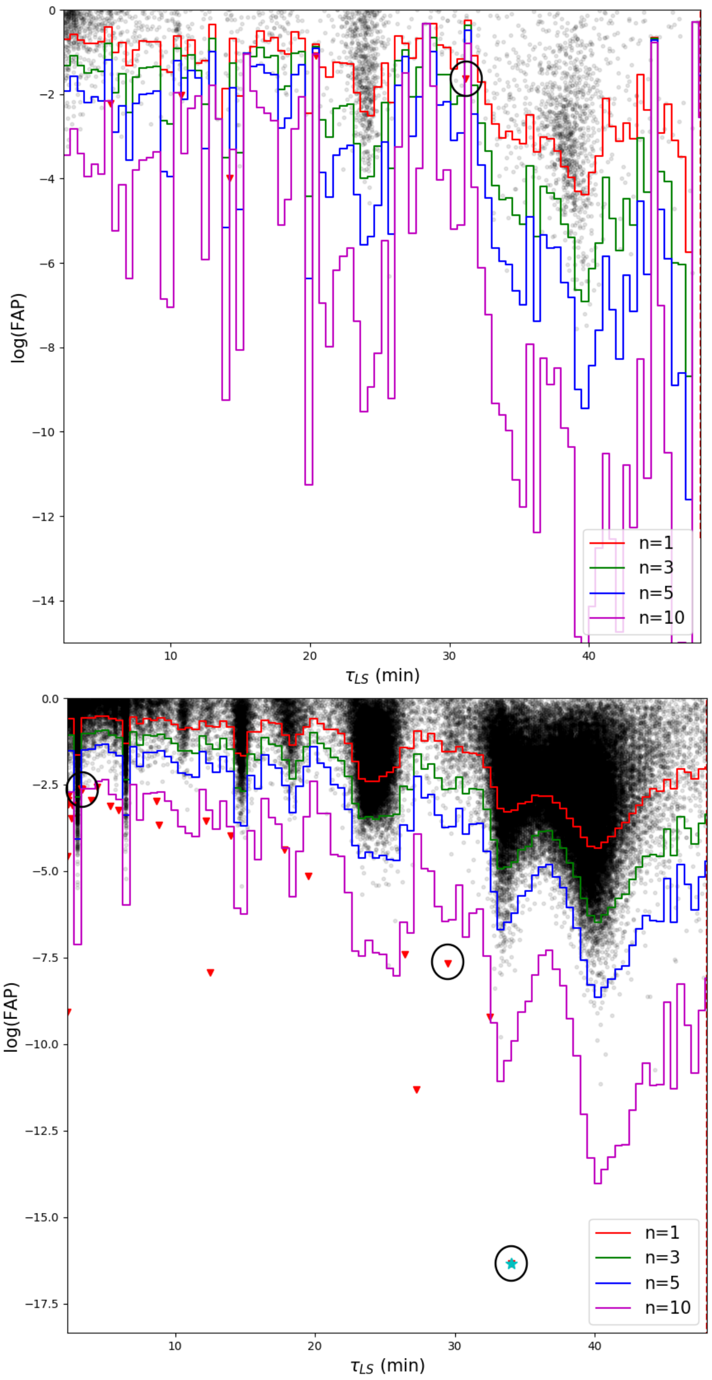

Figure 4.9: The log(FAP) - period planes for field 90004. Top: The log(FAP) - period planes for stars (CLASS_STAR > 0.8) within field 90004. Stars with log(FAP) < 10MAD$_{\mathrm{logFAP}}$ are represented with by the red triangles. The single star which satisfied $\chi^2 > 5$ and passed the manual inspections is highlighted within the black circle. Bottom: The log(FAP) - period planes all sources within field 90004. Sources with log(FAP) < 10MAD$_{\mathrm{logFAP}}$ are represented with by the red triangles. The 3 sources which satisfied $\chi^2 > 5$ and passed the manual inspections are highlighted within the black circles. n is the integer used in the MAD statistics.

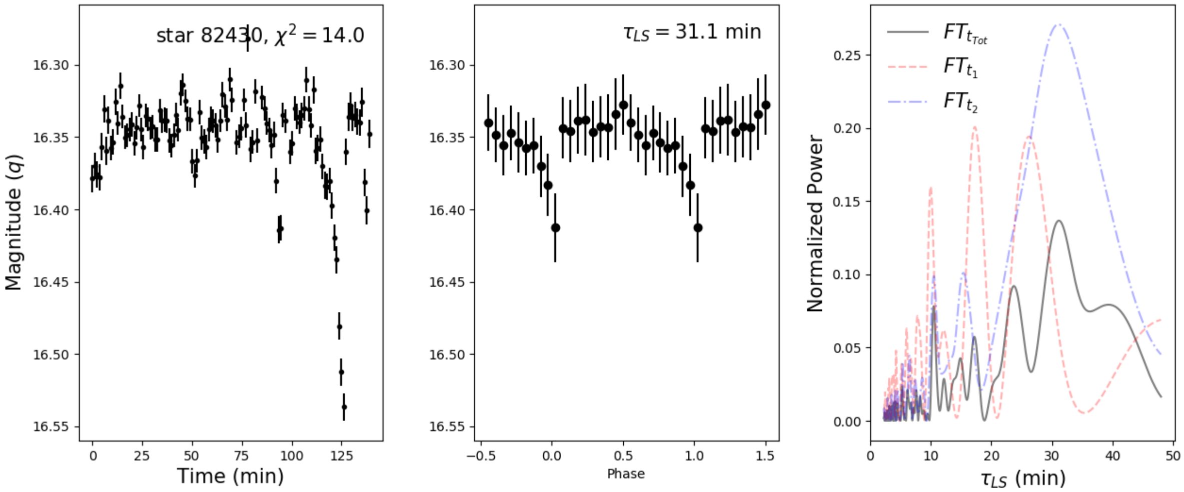

Figure 4.10: The single star within field 90004 which shows variability. Left: light curve of star. Middle: Average light curve, folded on the found τ_{LS}, across 2 phases. Right: FT of the light curve, FT_{tot} is the FT produced by the total light curve, and FT_{t1} and FT_{t2} are the FTs produced by the first and second half of the light curve.

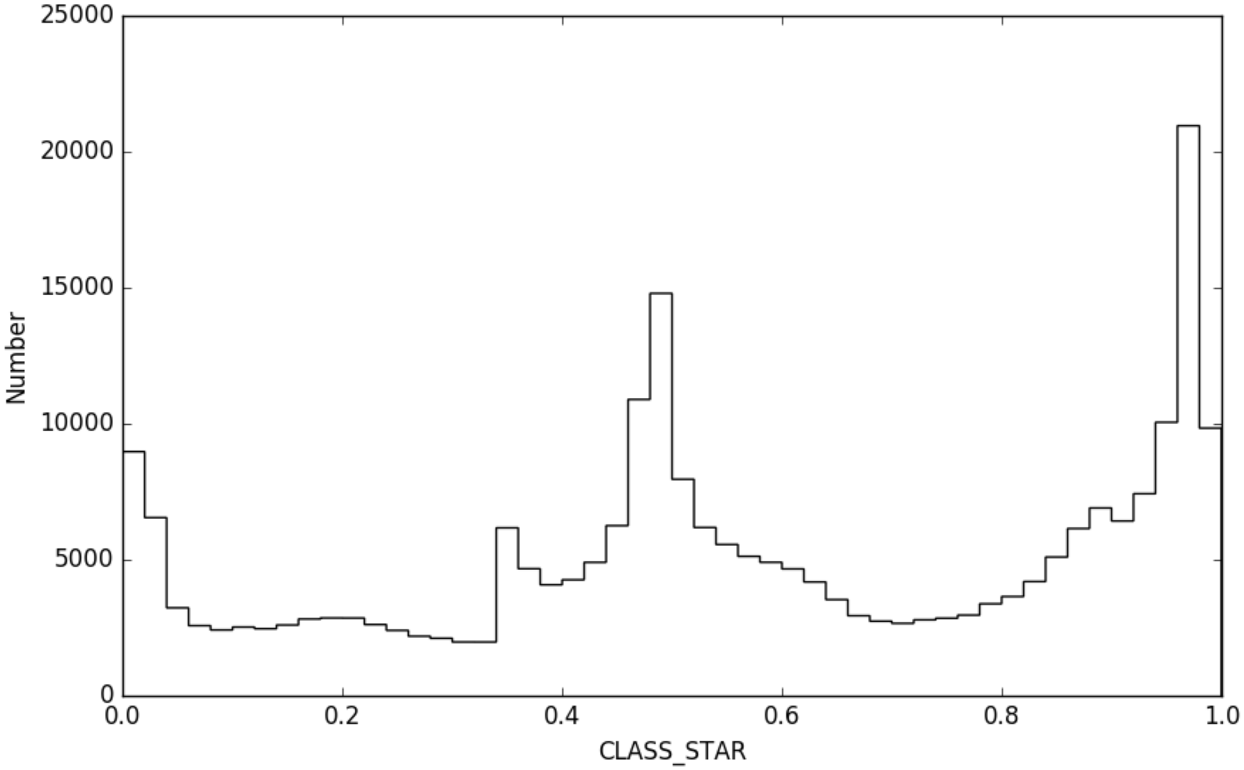

Figure 4.11: Histogram of CLASS_STAR from SExtarctor. A large portion of sources lie around 0.5, showing SExtractor's difficulty in correctly classifying sources as stars (CLASS_STAR = 1) or galaxies (CLASS_STAR = 0) in crowded fields.

were found to satisfy log(FAP) $< 10\mathrm{MAD}_{\mathrm{logFAP}}$, with only 2 of these satisfying $\chi^2 > 5$. Out of these two stars, one failed the manual inspection of its light curve as it contained less than 25 data points. The remaining light curve and FT is shown in Figure 4.10. From the figure, the effect of the poor dome tracking is seen by the dips around 50, 95 and 125 mins after the start of the observation. With the main variability in the light curve seen at this times and the disconnect in the average light, it is unlikely that this is a real variable.

With a well defined period, and amplitude above the minimum amplitude detectable (Figure 4.1), we expected to recover OGLE-BLAP-014. This, however, was not the case. We also noted very few stars in the log(FAP) - period plane in Figure 4.9. This should not be so, as 90004 is pointed towards the Galactic Centre, and has a high stellar density. Figure 4.11 shows the distribution of `CLASS_STAR` for all sources within field 90004. From the figure, we see that although there are well defined stars (`CLASS_STAR` > 0.8) and galaxies (`CLASS_STAR` < 0.1), there are a large number of sources centered around 0.5. This shows SExtractor's difficulty in correctly classifying sources in crowded fields. As such, I re-did the variability tests on all sources (i.e. no `CLASS_STAR` cut). The log(FAP) - period plane for all sources in field 90004 is shown in the bottom panel of Figure 4.9. With many more sources in the log(FAP) - period plane, the clumping effect at particular periods is more pronounced. As mentioned before, this is caused by poor dome tracking, and is discussed later in Section 4.3. With the unrestricted `CLASS_STAR` cut, 25 stars were found to satisfy log(FAP) $< 10\mathrm{MAD}_{\mathrm{logFAP}}$, with only 12 of these satisfying $\chi^2 > 5$. Out of these, 9 failed the manual inspection of their light curves. Three of the light curves were close to saturation, 1 light curve contained a single bad data point, and 2 light curves had poor data quality.

The light curves and FTs of the remaining three candidates are shown in Figure 4.12. One of these sources (210668, Figure 4.12, top) displayed a highly variable light curve (~ 1 mag amplitude) with a very short timescale of variability ($\tau_{LS} = 3.3$ mins). Further investigation showed that the variability was caused by the shifting extraction position from SExtractor. Figure 4.13 shows 2 cut outs from different images during the observation with the SExtractor positions for sources within 1.5 arcsec of the target overlaid. On the left, we see that SExtractor has determined the position of the source off-centre, skewed by a nearby faint neighbour. On the right, SExtractor correctly

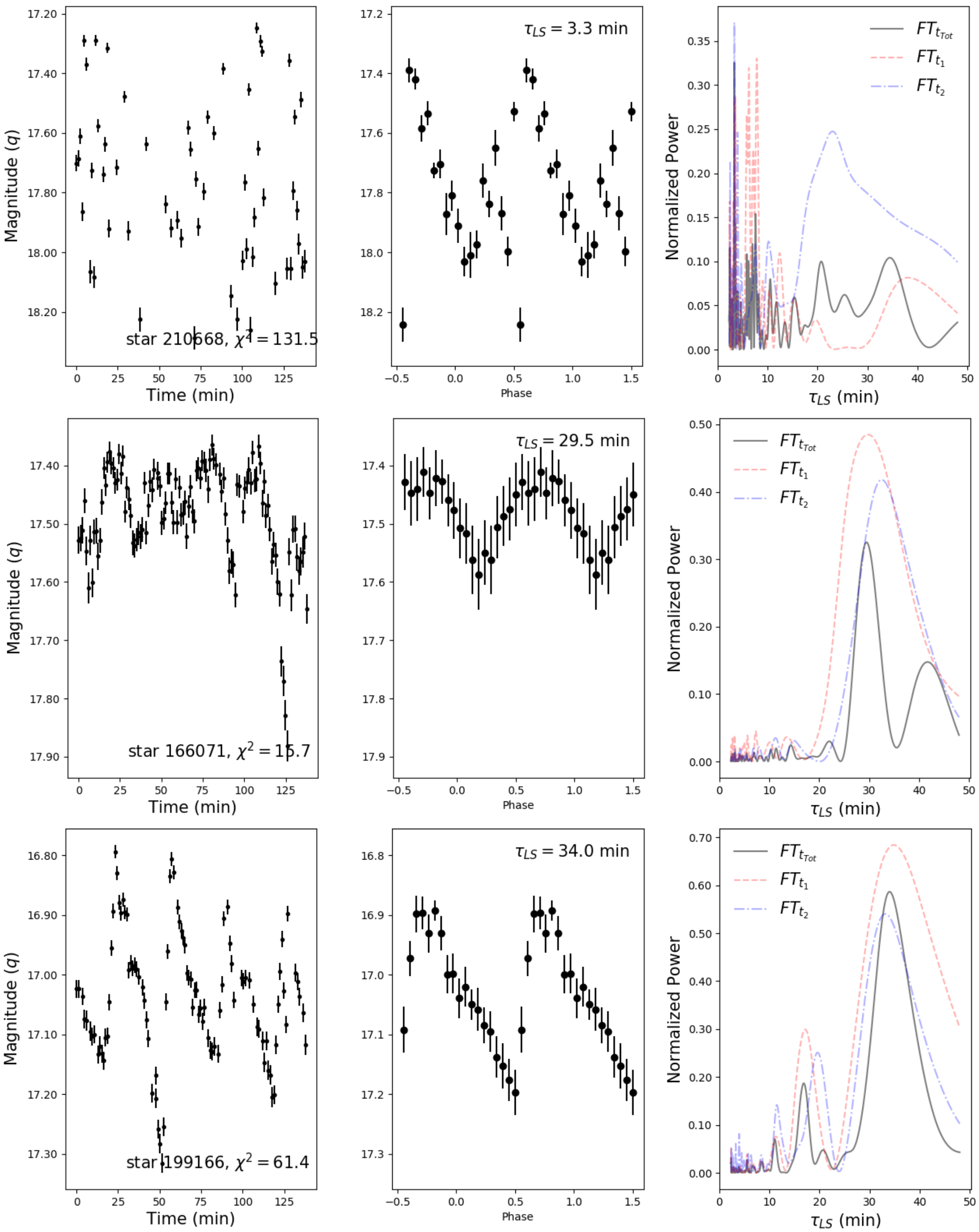

Figure 4.12: The 3 sources, including OGLE-BLAP-014 (at the bottom), within field 90004 which shows variability. Left: Light curve of the star. Middle: Average light curve, folded on the found τ_{LS}, across 2 phases. Right: FT of the light curve, FT_{tot} is the FT produced by the total light curve, and FT_{t1} and FT_{t2} are the FTs produced by the first and second half of the light curve. n is the integer used in the MAD statistics.

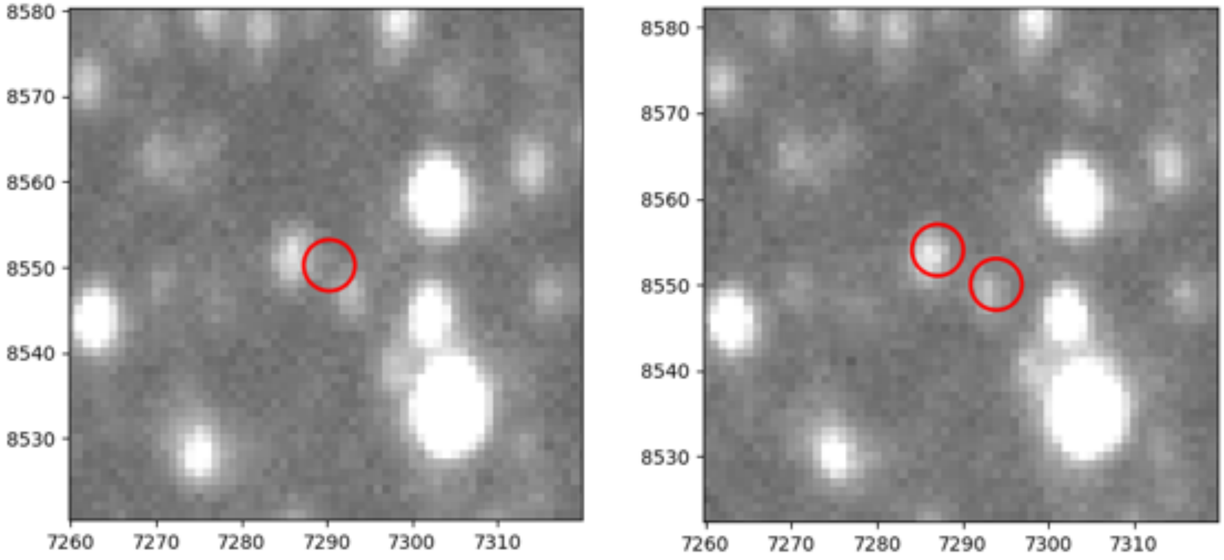

Figure 4.13: Two cut outs from different images during the observation of field 90004 with the SExtractor positions for sources within 1.5 arcsec of source 210668 overlaid. Left: SExtractor has determined the position of the source off-centre, skewed by a nearby faint neighbour. Right: SExtractor correctly detects the two sources individually.

detects the two sources individually. Thus, the light curve is highly variable as the position on which SExtractor extracts a magnitude shifts between the two states. These data were taken in poor seeing conditions (3 arcsec seeing), which could be the cause of SExtractor's confusion with the source position. The details of the remaining 2 stars are summarized in Table 4.2. Here, OGLE-BLAP-014 was recovered with a log(FAP) of -16.3, a $\chi^2 = 61.4$ and a timescale of variability of 34.0 mins. This variability is close to the known period, while the found amplitude of 0.32 mag is between the known V and I period amplitudes. OGLE-BLAP-014 is shown in the bottom panel of Figure 4.9 by the cyan star.

4.2.4 90006 - QU Tel

Field 90006 contains EC20058–5234 (also known as QU Tel), a pulsating white dwarf with multiple low-amplitude, short periods (Koen et al., 1995). The most prominent of these occur at 281 and 257 s. Field 90006 was observed for $\sim$ 1 hour. The log(FAP) - period plane for field 90006 is shown in Figure 4.14. Thirty nine stars were found to satisfy log(FAP) $< 10\text{MAD}_{\text{logFAP}}$, with only 1 of these satisfying $\chi^2 > 5$. This star failed the manual inspection due to saturation effects. Without guiding, EC20058–5234 was often blended with a nearby neighbouring star during the observation.

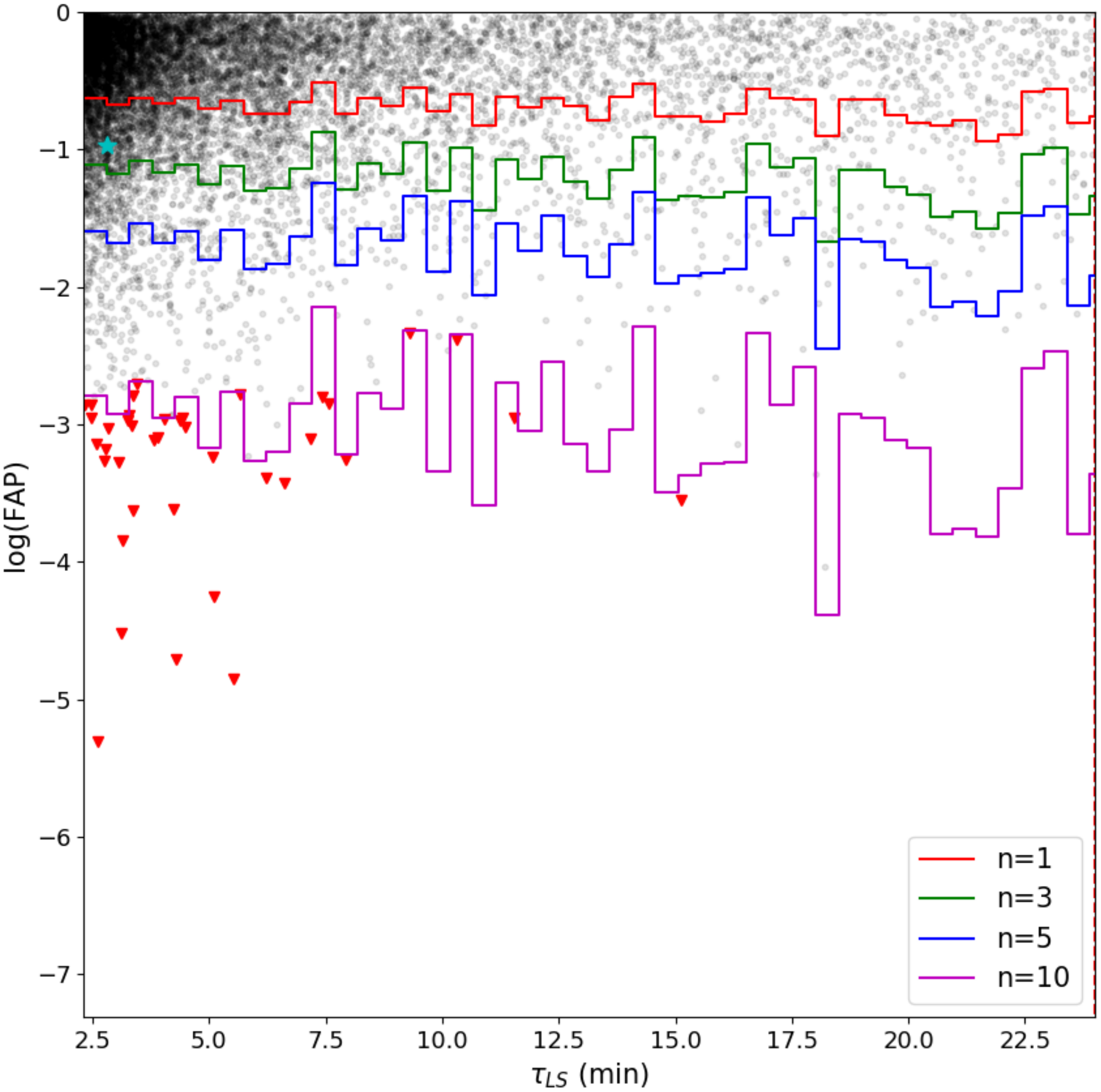

Figure 4.14: The log(FAP) - period planes for field 90006. Stars with log(FAP) $<$ 10MAD$_{\mathrm{logFAP}}$ are represented with by the red triangles. EC20058-5234 is shown by the cyan star. n is the integer used in the MAD statistics.

Although the LS test was able to detect variability with a log(FAP) $= -0.96$, this is below the $n = 3$ cut off and the timescale of variability was 2.8 mins (see cyan star in Figure 4.14). This shows the importance of having stable guiding, especially in crowded fields, if we wish to extract reliable light curves.

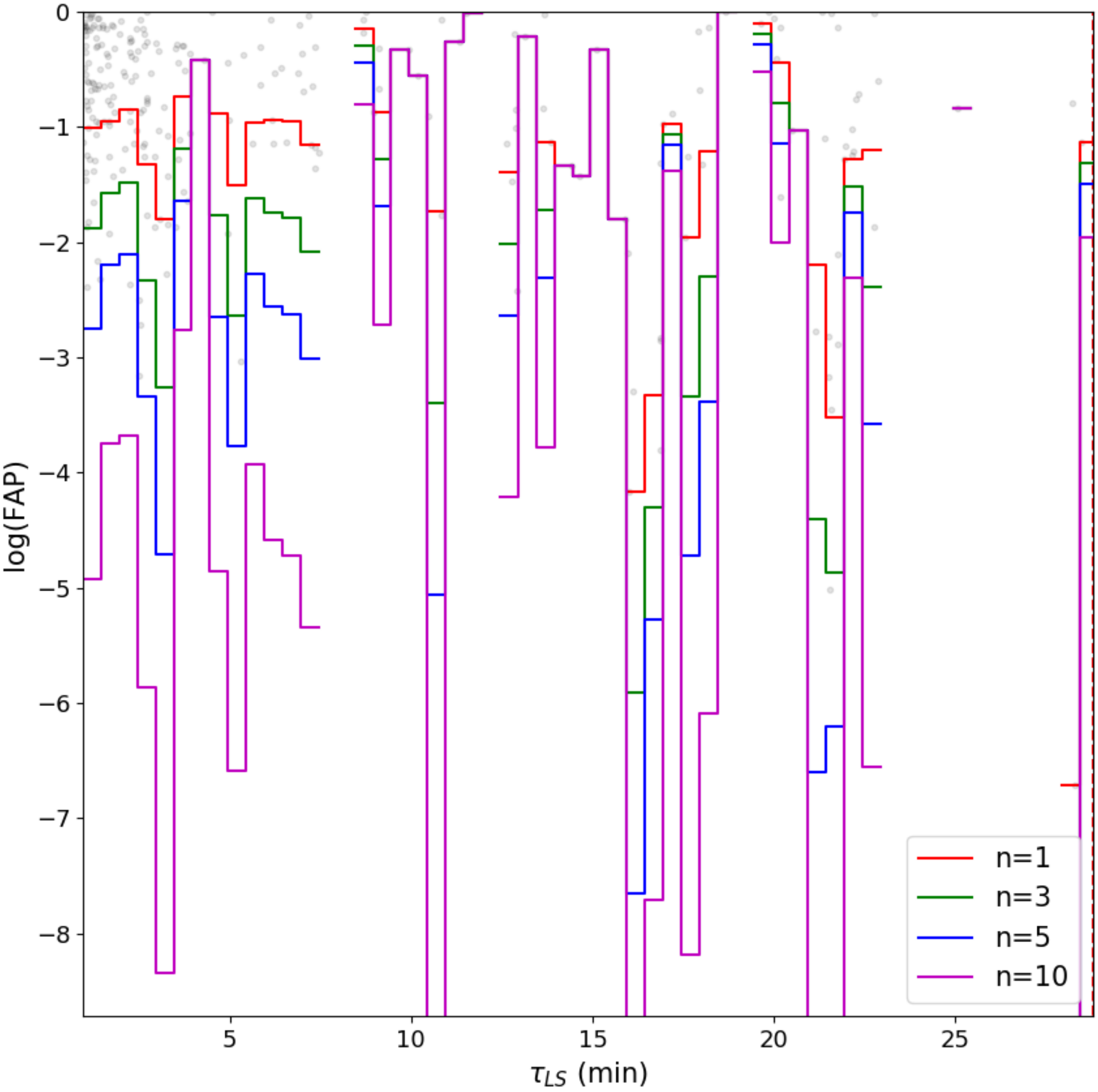

Figure 4.15: The log(FAP) - period planes for field 90013. No stars satisfied log(FAP) < $10\mathrm{MAD}_{\mathrm{logFAP}}$. n is the integer used in the MAD statistics.

4.2.5 90013 - V2008–1753

Field 90013 contains V2008–1753, an eclipsing post common-envelope binary system consisting of a pulsating hot subdwarf B star (Schaffenroth et al., 2015). V2008-1753 has an orbital period of 1.5796280 ± 0.0000002 hrs, above the observation length of ∼ 1.2 hours. Compared to the other observations, field 90013 has a shorter exposure time of 20s. Poor observing conditions during this observation resulted in large gaps in the light curves and poor coverage in the log(FAP) - period

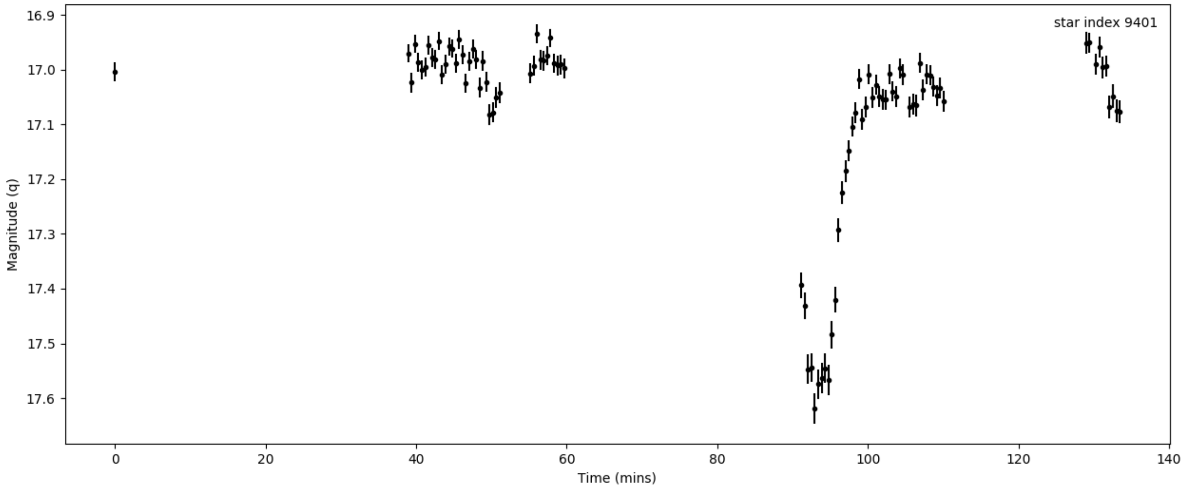

Figure 4.16: Light curve of V2008-1753, showing a single eclipse.

plane. The log(FAP) - period plane for field 90013 is shown in Figure 4.15. No stars were found to satisfy log(FAP) $< 10\mathrm{MAD}_{\mathrm{logFAP}}$. V2008–1753 was not found to be variable using this test. The light curve of V2008–1753 is shown in Figure 4.16.

4.3 Discussion of variables discovered

From the 5 commissioning fields observed for this test, 4 sources showing significant variability were found with timescales of variability ranging between 21.9 and 34.0 mins. The details of these are summarized in Table 4.2. Out of these four, only one was known to be variable upon observing the field (star 199166 from field 90004 was known to be OGLE-BLAP-014). Although the accuracy of the data is limited by a number of factors, the LS test was able to recover a timescale of variability and amplitude close to the known parameters of OGLE-BLAP-014. This provides a good indication on the reliability of the variability found in the other sources.

One star (1248 from field 16023) showed variability with an amplitude of 10 mmag (Figure 4.5). Although this is of the order of what we can detect, the data for this field was spread over 2 nights, with only the light curve from the second night passing the variability tests. The τ_{LS} found from the light curve from the first night was ~ 0.5 of the τ_{LS} found in the second night. An obvious disconnect is also seen in the average light curve of 1248 (Figure 4.5), pointing to the actual variability being slightly different to the τ_{LS} found. Another star (4452 from field 16089) showed

Table 4.2: Sources with log(FAP) $< 10\mathrm{MAD}_{\mathrm{logFAP}}$ and $\chi^2 > 5$ which passed the manual inspection.

Field	Star #	RA	DEC	Magnitude (q mag)	τ_{LS} (min)	log(FAP)	χ^2	Comments
16023	1248	03:38:52.6	-35:57:45.72	13.62	21.9	-2.6	8.3	Small amplitude, only from second night, disconnect in average light curve.
16089	4452	22:56:55.6	-41:59:15.98	13.65	27.7	-9.6	38.1	Mean magnitude on the rise.
90004	166071*	18:13:38.6	-32:19:50.52	17.50	29.5	-7.7	15.7	Caution due to data quality (poor dome tracking).
	199166*	18:12:41.8	-31:12:07.81	17.00	34.0	-16.3	61.4	OGLE-BLAP-014

*source extracted with no CLASS_STAR cut.

an increase in the mean magnitude during the observation (Figure 4.7). Whether this increase was intrinsic to the star, or caused by external factors, such as dome eclipsing can not be confirmed. Sources from the 90004 field showed dips around 50, 95 and 125 mins in their light curve (example Figure 4.10), pointing to external factors (such as dome vignetting due to poor dome tracking) affecting the data from this field. The effect of this is also seen in the log(FAP) - period plane for field 90004 (Figure 4.9) by the clumping of sources at particular periods. Thus, caution should be taken when interpreting the results from this field. The variability seen in the light curve of 82430 is mostly only due to this effect and thus unlikely a real variable. For another source from this field (166071), larger variability is seen at different times (Figure 4.12, middle), pointing to real variability, although uncertainty on the amplitude and period of this variability is introduced by the poor dome tracking. Another source (210668) from field 90004 showed a highly variable light curve (Figure 4.12, top) caused by inaccurate source position (Figure 4.13). This is most likely due to poor seeing conditions. As such, caution should be taken when dealing with fainter sources in poorer ($\sim$ 3 arcsec seeing) conditions. The LS test was able to detect significant variability in two of the other known variables, but their periods are beyond the scope of this tests to make any significant comments. The remaining two known variables could not be recovered as one saturated within the 1 min exposure time, while the other was affected by blending due to no guiding within a crowded field.

4.4 Looking ahead

The tests presented in this chapter have shown that MeerLICHT, and the pipeline, is able to produce reliable light curves. Even when experiencing several limitation on the data quality, I was able to recover a timescale of variability and amplitude close to the known parameters of OGLE-BLAP-014. This provides a good validation on MeerLICHT's ability to produce light curves. This shows promising potential for future operation, when data are not expected to be limited by various factors (e.g. guiding, dome tracking, etc.). These results show the importance of reliable telescope operation. Without fully functioning dome tracking, the quality and reliability of the data can be severely degraded. Additional operations such as guiding play a vital role in extracting sources in crowded fields. Another very important aspect is accurate timing. As a telescope aimed to find variable objects in the time-domain, accurate timing is of vital importance. Once these elements have been fully commissioned, a number of these test should be carried out on new data to validate the accuracy with which MeerLICHT can find these objects. Moving forward to variability detection, these tests have shown that multiple parameters are needed to correct identify variables. In this case, a combination of LS, MAD statistics and χ^2 were used. Once normal operation of MeerLICHT starts, I propose a detailed study on the detection of variability be conducted to determine the best variability tests for the MeerLICHT data. As MeerLICHT starts to build up its database, the detection of longer period variables will be possible. With more data, the variability found within the light curves will also become more reliable. Manual inspection of individual light curves will be longer be feasible with the expected volume of data. With links to MeerKAT, MeerLICHT also has the additional information in the radio. Motivated by this and larger surveys such as LSST and SKA, work on the classification of transients in multiple wavelengths with machine learning has begun (Sooknunan et al. 2019, submitted). As operations start, MeerLICHT will be able to provide a wealth of information about the variable sky.

Chapter 5

High-speed photometry of faint cataclysmic variables.

This chapter is based on the paper **High-speed photometry of faint cataclysmic variables - IX. Targets from multiple transient surveys** by Paterson et al. (submitted and under review with MNRAS). I took over 75% of the observations presented in this chapter (making up 352 hrs over 15 weeks of observing time), was responsible for the reduction of the photometric observations, and led the write-up of this paper. This chapter highlights the in-depth investigation into cataclysmic variables found in optical transient surveys, the kind of science that MeerLICHT enables. We present high-speed photometric observations of 25 cataclysmic variables detected by the All Sky Automated Search for Super-Novae (ASAS-SN), the Mobile Astronomical System of the TElescope-Robot (MASTER) and the Catalina Real-Time Transient Survey (CRTS). From these observations we determine 16 new orbital periods and 1 new superhump period. Two systems (ASASSN-14ik and ASASSN-14ka) have outburst periods of approximately 1 month, with a third (ASASSN-14hv) having outbursts approximately every 2 months. Included in the sample are 11 eclipsing systems, one probable intermediate polar (ASASSN-15fm), 1 SW Sex-type star (MLS 0720+17), 1 WZ Sge-type star (ASASSN-17fz) and one system showing different photometric and spectroscopic periods (ASASSN-15kw).

5.1 Introduction

We present the latest results of photometric follow-up of faint cataclysmic variables (CVs; see Warner 1995 for a review on CVs) that are accessible from the southern hemisphere. This work is the last in series of papers (see Coppejans et al. 2014 and references therein) aimed at the characterisation of newly discovered CVs, including the determination of their orbital periods, a search for sub-orbital periodicities and the discovery of interesting targets for possible in-depth studies. Previous papers in the series focused on faint nova remnants and CVs identified by the Sloan Digital Sky Survey (SDSS; see Szkody et al. 2002, Szkody et al. 2003), attention then shifted to CVs discovered by the Catalina Real-Time Transient Survey (CRTS; see Drake et al. 2009).

In this chapter we present observations of 25 faint CVs identified in the All Sky Automated Search for Super-Novae (ASAS-SN; see Shappee et al. 2014), the Mobile Astronomical System of the TElescope-Robots (MASTER) node situated in Sutherland (MASTER-SAAO; see Lipunov et al. 2010), as well as from CRTS. The ASAS-SN survey is a dedicated all-sky survey focusing on the search for supernovae. It is made up of five units, each consisting of four 14-cm robotic telescopes, located at the Haleakala, Cerro Tololo, South African Astronomical Observatory (SAAO) and McDonald stations of the Las Cumbres Observatory (LCO[1]); and in Chile. Together, these telescopes are able to observe the entire night sky. The MASTER GLOBAL Robotic Net is a Russian collaboration of robotic telescopes distributed across the globe whose goal is the observation of the entire sky each night up to 20-21 mag with the aim of answering questions about Gamma Ray Bursts (GRBs), dark energy and exoplanets. CRTS is a transient survey, covering 33,000 square degrees of the sky between -80and 70 declination, whose main goal is the discovery of rare and interesting transients. With all data being publically accessible, CRTS provides valuable long-term light curves for many sources.

In this chapter Section 5.2 summarises the observations and data reduction. Sections 5.3 - 5.6 contain the results of each individual CV, grouped by type: eclipsing systems (Section 5.3), non-eclipsing systems in quiescence (Section 5.4); non-eclipsing CVs in outburst (Section 5.5), and

---

[1] formerly LCOGT

CVs for which no period could be determined (Section 5.6). Section 5.7 contains a summary of the data and discussion of the results.

5.2 Observations

Most photometric observations presented in this chapter were obtained at the SAAO site in Sutherland. Differential photometry was performed using the Sutherland High-speed Optical Camera (SHOC; see Gulbis et al. 2011; Coppejans et al. 2013) mounted on the 74- and 40-in reflector telescopes of the SAAO. Additional observations were obtained with SHOC mounted on the SAAO's new 1-m telescope, Lesedi (Worters et al., prep). Making use of a frame-transfer, thermoelectrically-cooled, back-illuminated CCD, SHOC allows for high-quality, high-speed photometry. This makes SHOC an ideal instrument to use in the search of short periods in brighter objects. This includes searching for Dwarf Nova Oscillations (DNOs, with a range of 5 - 40s), longer period DNOs (lpDNOs, with approximately 3 - 5 times the period of DNOs) and Quasi-Periodic Oscillations (QPOs, with a range of 50 -1000s) during outburst (Warner & Woudt, 2004). Observations were taken with 1 MHz readout, in conventional mode, with exposure times ranging from 1 to 120 seconds.

No filters were used and data were calibrated using PSF_r magnitudes[2] from either SkyMapper (Keller et al., 2007) or PANSTARRS (Kaiser et al., 2002)), unless stated otherwise. The catalogue magnitudes used to calibrate each system are given in Table 5.1. As found by Coppejans et al. (2014), r-band is a close approximation to white light (WL - no or clear filter) for bluer sources ($g - r$ = 0.2 to 1.0). Since CVs are typically blue sources, we can use the r magnitude as an estimate of the WL magnitude; this calibration is good to $\sim$ 0.1 mag. The data were reduced using standard IRAF packages (such as the `phot` and `mkapfile` commands) to perform aperture-corrected photometry. Frequency spectrum analysis of the data was done using EAGLE, a program written by Darragh O'Donoghue for time-series analysis of unevenly spaced data containing large data gaps. For MLS 0720+17, photometric observations were taken with an Andor camera on the 1.3m telescope at MDM Observatory on Kitt Peak, Arizona. The MDM observations were taken

---

[2] consistent with SDSS r

with a GG420 filter, which suppresses light with wavelengths < 4200 Å. A log of all observations is presented in Table 5.1. Only the first 10 lines are shown here, with the full version available online.

For two sources, ASASSN-15kw and MLS 0720+17, we include time-series spectroscopy from the 2.4m Hiltner telescope at MDM Observatory on Kitt Peak, Arizona, USA. We used the 'modspec' spectrograph.[3]. For ASASSN-15kw, the CCD covered from 4340 to 7500 Å at 3.5 Å resolution FWHM, with severe vignetting toward the red end of the range. For MLS 0720+17, a 2048 × 2048 SITe CCD that covered 4210 to 7500 Å with 3.6 Å resolution was used. MLS 0720+17 set early in the night, limiting the observable hour angle range. The calibration, reduction, and analysis protocols followed the same steps described by Thorstensen et al. (2016) and Thorstensen & Halpern (2013). Table 5.2 gives a journal of these observations.

5.3 Eclipsing systems

This section contains the details of the eclipsing systems presented in this chapter. These systems are listed in alphabetical order and our average light curves, except for ASASSN-14ka, are shown in Figure 5.1. Eclipsing systems play an important role in the study of CV evolution through the modeling of eclipse profiles (Hardy et al., 2017). With the exception of ASASSN-14ka and ASASSN-15fm which has shallow eclipses, the eclipsing systems in this chapter show narrow eclipses, ranging from 0.2 to 2 mag in depth. A table listing eclipse times for the well defined eclipses presented in this chapter is available online.

5.3.1 ASASSN-14hq

ASASSN-14hq shows evidence of previous outbursts, as well as eclipses, in the CRTS data. It was identified as a CV candidate by the ASAS-SN survey on 2014 September 24, when it went into outburst reaching $V = 13.97$ mag (Shappee et al., 2014). ASASSN-14hq shows a characteristic light curve of an eclipsing dwarf nova in quiescence. Our average light curve is shown in Figure 5.1, and shows deep, narrow eclipses of more than 1 mag in depth during quiescence. ASASSN-14hq

---

[3] http://mdm.kpno.noao.edu/Manuals/ModSpec/modspec_man.html

Table 5.1: Observing log. Only the first 10 lines are shown here. The full version is available online.

Object	Type	Run	Telescope	Date of obs. (start of night)	HJD of start of run (+2450000)	Length (hrs)	t_{in} (s)	r (mag)
ASASSN-14eq	SU	S8508	74-in	2014/11/19	6981.3886	2.58	60	15.6- 18.5[1]
		S8515	74-in	2014/11/23	6985.3277	2.83	30	
		S8516	74-in	2014/11/24	6986.3093	1.00	10	
		S8517	74-in	2014/11/25	6987.2580	3.72	10	
		S8733	40-in	2015/08/05	7240.4354	6.21	10	
		S8735	40-in	2015/08/06	7241.4772	5.13	10	
		S8737	40-in	2015/08/07	7242.4807	5.14	10	
		S8739	40-in	2015/08/08	7243.4939	4.79	10	
		S8741	40-in	2015/08/09	7244.4304	1.05	10	
ASASSN-14hq	DN	S8496	74-in	2014/11/13	6975.5570	0.97	20	18.8 - 21.7[1]

Notes: t_{in}: integration time; DN: dwarf nova; SU: SU Ursae Majoris; IP: intermediate polar; *: system was in outburst; r: r magnitude of the system in quiescence; [1] makes use of the SkyMapper catalogue (Wolf et al., 2018) for magnitude calibration; [2] makes use of PANSTARRS (Flewelling et al., 2016) for magnitude calibration; [3] uses another calibrated run on the same night for magnitude calibration.

Table 5.2: Spectroscopic Journal for ASASSN-15kw and MLS 0720+17.

Object	Type	Date of obs. (start of night)	HJD of start of run (+2450000)	Length (hrs)	t_{in} (s)
ASASSN-15kw	DN	2017/04/01	7845.0411	0.5	600
		2017/04/02	7845.8097	3.0	600
		2017/04/03	7846.8028	0.5	600
MLS 0720+17	SW Sex	2015/04/28	7140.6566	1.0	900
		2015/04/29	7141.6448	1.5	900
		2015/04/30	7142.6388	1.5	900

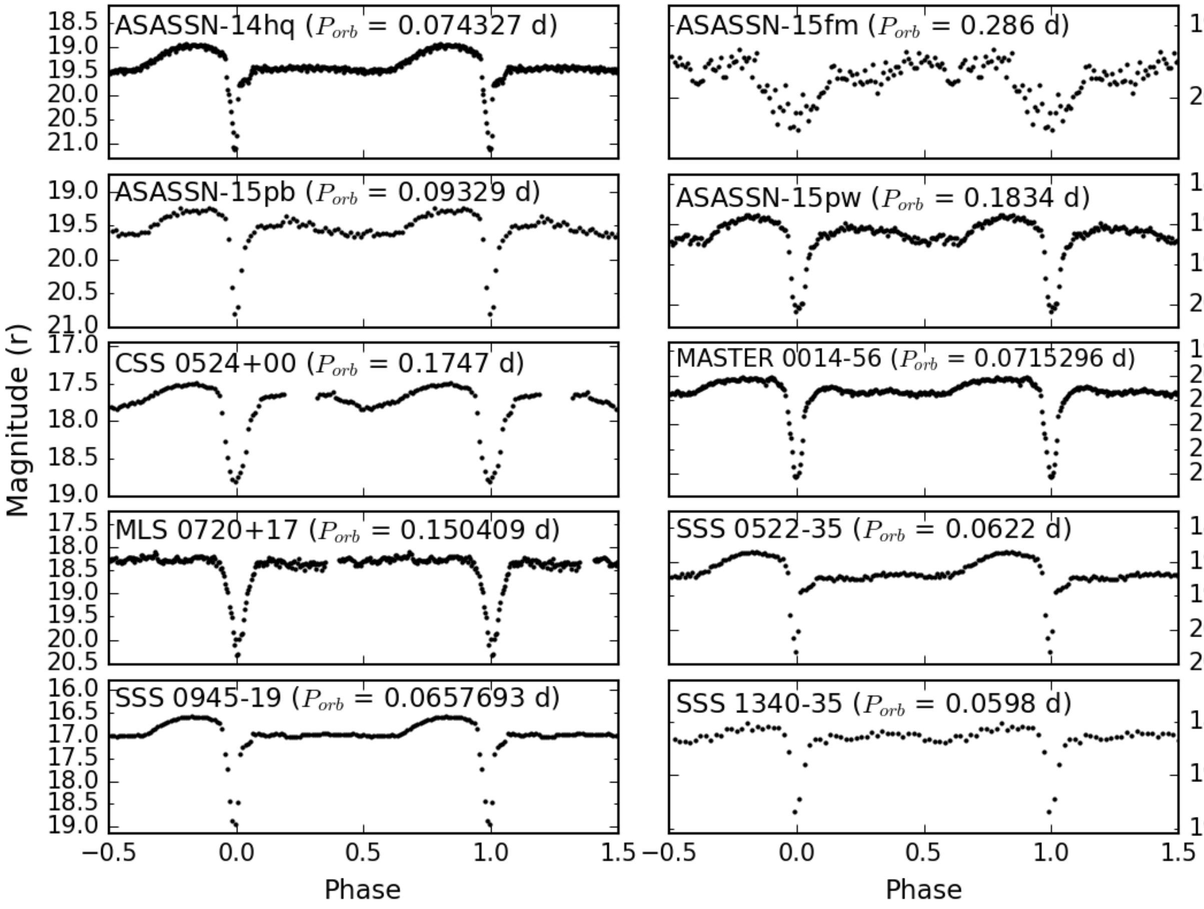

Figure 5.1: Our average light curves of eclipsing systems presented in this chapter, duplicated over 2 orbital cycles. The system's name and orbital period is shown in the plot. For ASASSN-14hq, runs S8825 and S8831 are excluded due to bad weather, and the target being in a brighter state (possibly on the rise of a normal outburst) respectively. Due to lack of data, phase 0.19-0.3 is not plotted for CSS 0524+00. Due to lack of data, phase 0.35-0.4 is not plotted for MLS 0720+17 and only runs obtained in Sutherland, denoted with run names containing 'S', are included. Many of these systems show strong orbital humps in their light curves.

has an orbital period of 0.074327(±9) d and the eclipse ephemeris is

$$\mathrm{HJD}_{\mathrm{min}} = 2456975.5971(\pm 2) + 0.074327(\pm 9)\ E \tag{5.1}$$

With an orbital period below the period gap, we expect this system to have superoutbursts. Although the archival data of CRTS does show outbursts, there is inadequate coverage to determine whether these are normal outbursts, or in fact superoutbursts. Archival data from ASAS-SN however, show evidence of regularly occuring normal outbursts and superoutbursts.

5.3.2 ASASSN-14ka

ASASSN-14ka, was announced as a CV candidate by the ASAS-SN survey on 2014 September 15, when it underwent an outburst peaking at $V = 15.06$ mag (Shappee et al., 2014)). It was also reported by the Gaia Photometric Science Alerts (Wyrzykowski et al., 2012) in 2017 as Gaia17anx. Archival data from the ASAS-SN survey team (Shappee et al., 2014), displayed in Figure 5.2, show regular outbursts occurring approximately once a month. Our SHOC light curves obtained are displayed in Figure 5.2, each being vertically offset for display purposes. During runs S8495, S8498, S8501 and S8503, the system was still in a brightened state, with a resulting eclipse minimum of 18.4 mag. During the three later runs (S8549, S8551 and S8592), the system had returned to quiescence and showed a slightly deeper eclipse minimum of 18.7 mag. ASASSN-14ka has an orbital period of 0.17716(±1) d and the eclipse ephemeris is

$$\mathrm{HJD}_{\mathrm{min}} = 2456975.3845(\pm 2) + 0.17716(\pm 1)\ E \tag{5.2}$$

Evidence of a modulation with an amplitude of 0.6 magnitude at half the orbital period can be seen in the bottom right panel of Figure 5.2. While ASASSN-14ka shows flickering on the order of 0.2 mag, no evidence of other periods was found.

5.3.3 ASASSN-15fm

ASASSN-15fm, was announced as a CV candidate by the ASAS-SN survey on 2015 March 15, when it went into outburst with a peak magnitude of $V = 16.26$ mag (Shappee et al., 2014)). The Fourier

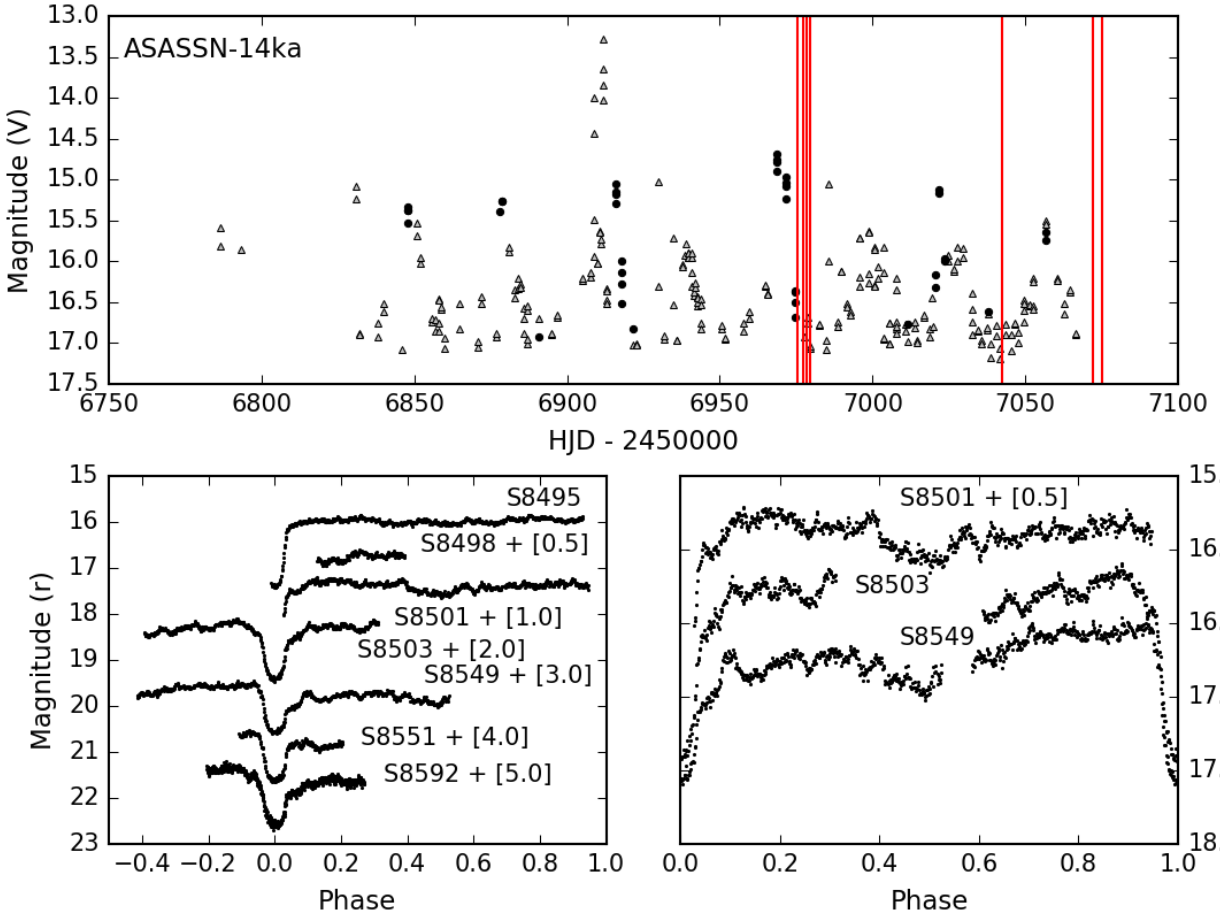

Figure 5.2: Top: Long term light curve of ASASSN-14ka obtained from the ASAS-SN survey team. The grey triangle indicate upper limits, while the red lines show when the observation presented in this cahpter where taken. Bottom left: Individual light curves of ASASSN-14ka. The light curve for run S8495 is displayed at the correct brightness; the vertical offset for each light curve thereafter, is given in brackets. The figure clearly shows the structure present in quiescence, as well as the changing eclipse profile as the system was declining from outburst. Bottom right: Individual light curves from runs S8501, S8503 and S8549, folded on the ephemeris given in equation 5.2. Run S8501 vertically offset by 0.5 mag for display purposes. This plot highlights the modulation seen in ASASSN-14ka at half the orbital period.

Transform (FT) of the three longest runs, the displayed in Figure 5.3, shows that ASASSN-15fm is a probable intermediate polar (IP). The highest peak in the FT is most likely the orbital period (represented by Ω), while the spin of the white dwarf, along with the interaction between these two periods, appears as the two smaller peaks highlighted by the dashed lines. The two smaller periods at 18.57($\pm$1) and 20.37($\pm$1) mins are separated by twice the orbital frequency, but the duration of our data is insufficient to distinguish which is the spin period of the white dwarf. A more detailed study at higher cadence is needed to determine the spin period of the white dwarf. Our average

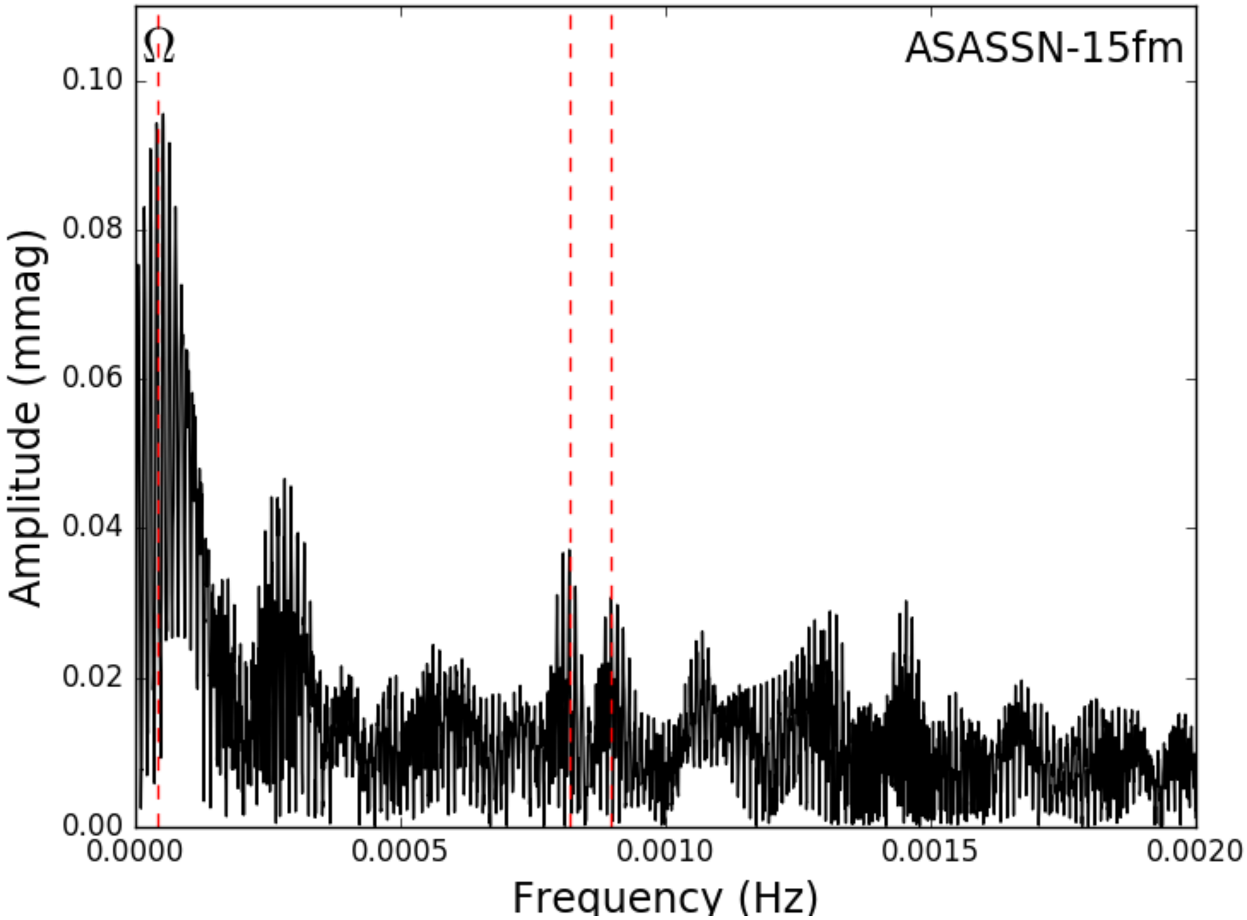

Figure 5.3: FT of three longest runs (S8638, S8640, S8643) for ASASSN-15fm. The dashed lines show the orbital period (Ω), the spin of the white dwarf, and a 2nd side band.

light curve is shown in Figure 5.1. The orbital ephemeris for minimum light is

$$\mathrm{HJD_{min}} = 2457134.7530(\pm 5) + 0.286(\pm 1)\ E \tag{5.3}$$

5.3.4 ASASSN-15pb

The CRTS light curve provides no evidence of previous outbursts or eclipses for ASASSN-15pb due to sparse coverage. ASASSN-15pb was listed as a CV candidate by the ASAS-SN survey on 2015 September 1, when it went into outburst with $V = 16.48$ mag (Shappee et al., 2014). Our average light curve is shown in Figure 5.1, and shows eclipse depths of more than 1.5 mag in quiescence. ASASSN-15pb has an orbital period of 0.09329(±2) d, just above the period gap minimum of

2.15(±0.03) hrs (Knigge et al., 2011), and the eclipse ephemeris is

$$\mathrm{HJD_{min}} = 2457312.349(\pm1) + 0.09329(\pm2)\ E \tag{5.4}$$

5.3.5 ASASSN-15pw

ASASSN-15pw shows evidence of previous outbursts, but no eclipses, within the CRTS data. It was listed as a CV candidate by the ASAS-SN survey on 2015 September 22, when it went into outburst with $V = 16.07$ mag (Shappee et al., 2014). Our average light curve is shown in Figure 5.1, and shows eclipses with a depth of around 1 mag. ASASSN-15pw has an orbital period of 0.1834(±3) d and the eclipse ephemeris is

$$\mathrm{HJD_{min}} = 2457316.585(\pm1) + 0.1834(\pm3)\ E \tag{5.5}$$

5.3.6 CSS 0524+00 (CSS131106:052412+004148)

Since the discovery of CSS 0524+00 by CRTS (Drake et al., 2009) on 2013 Nov 6, ample coverage shows evidence of multiple eclipses and outbursts. With evidence of eclipses, Hardy et al. (2017) observed CSS 0524+00, finding a period of 0.17466647(2) d. We find a period of 0.1747(±3) d, in agreement with that found by Hardy et al. (2017). Our average light curve, folded on the ephemeris $\mathrm{HJD_{min}} = 2456651.4304(\pm3) + 0.1747(\pm3)\ E$, is shown in Figure 5.1; and shows eclipse depths of around 1.2 mag.

5.3.7 MASTER 0014–56 (MASTER OT J001400.25–561735.0)

CRTS data of MASTER 0014–56 show evidence of eclipses, along with a possible outburst. MASTER 0014–56 was discovered by MASTER-SAAO when it went into outburst with an amplitude of more than 3.7 mag (Gress et al., 2015). Our average light curve is shown in Figure 5.1, and shows deep, narrow eclipses of ~ 2 mag depth in quiescence. MASTER 0014–56 has an orbital period of 0.0715296(±6) d and the eclipse ephemeris is

$$\mathrm{HJD_{min}} = 2457245.5456(\pm1) + 0.0715296(\pm6)\ E \tag{5.6}$$

5.3.8 MLS 0720+17 (MLS101226:072033+172437)

After the discovery of MLS 0720+17 by CRTS, Drake et al. (2009) interpreted the variability seen in the light curve as eclipses. Hardy et al. (2017) confirmed the presence of eclipses when they obtained a short observation, in which they observed part of an eclipse. Oliveira et al. (2017) later obtained a spectrum of MLS 0720+17. They concluded that the spectrum was typical of a polar, with the eclipse seen by Hardy et al. (2017) being a modulation due to cyclotron emission, and the narrow emission lines seen in the spectrum inconsistent with an eclipsing disc system. Our individual light curves and time-resolved spectroscopy are shown in Figure 5.4 and Figure 5.5 respectively, while our average light curve is shown in Figure 5.1. Our observations confirm MLS0720+17 as an eclipsing system. From the four eclipses in the 2015 SAAO light curves, we found a preliminary period of 0.1504 d, which we constrained further using the 2013 eclipse from SAAO and the October and January eclipses from MDM. The eclipse ephemeris is

$$\mathrm{HJD}_{\mathrm{min}} = 2457072.2582(\pm 7) + 0.150409(\pm 7)\ E \tag{5.7}$$

The radial velocities, determined using the convolution method described by Schneider & Young (1980), do not independently determine the period due to the limited time span, but they do show a strong modulation consistent with the known period. We fit the velocities with a sinusoid of the form

$$v(t) = \gamma + K \sin(2\pi(t - t_0)/P) \tag{5.8}$$

using linear least squares, with the period P fixed at the value derived from the eclipses. This yielded $t_0 = \mathrm{HJD}_0 = 2457141.698(\pm 0.003)$, $K = 299 \pm 23$ km s^{-1}, and $\gamma = 88 \pm 19$ km s^{-1}. The radial velocities, folded on the eclipse ephemeris, are shown in Figure 5.5 with the sinusoidal fit superposed. There is a phase difference between the radial velocity fit and eclipse phase of 0.175 ± 0.031 cycles, a hallmark of a subclass of CVs, the SW Sextantis (SW Sex) stars. First classified by Thorstensen et al. (1991). These are nova-like CV stars that exhibit a suite of properties as follows: (1) Absorption in the Balmer and HeI lines appears near orbital phase 0.5; (2) An S-wave absorption feature in the emission of H_α is often observed; (3) In cases in which the true orbital phase is known from eclipses, the zero phase of the radial velocities lag behind the eclipses if they were to trace the white dwarf's motion; in other words, at eclipse, the Balmer line velocities have not yet decreased to their mean value; (4) The orbital periods of SW Sex stars are clustered from the 3 hour upper limit of the period gap up to about 4 hours (Rodríguez-Gil et al., 2009).

In many SW Sex stars, the HeI and Balmer absorption features appear around phase 0.5, opposite the eclipse. This is not apparent in the present data, most likely due to low signal-to-noise. Further studies are necessary to determine whether the absorption feature appears. The spectrum seems to show 2 additional traits of SW Sex stars: signs of a HeII 4686 + Bowen blend, and singly peaked emission lines. The bottom panel of Figure 5.5 shows a grey-scale representation of the H_α line as a function of phase. The velocity shifts are readily apparent. There is an artificial brightening of the intensity of the H_α line during eclipse (phase 0 and 1) because the line is normalized to the continuum, boosting the line when the continuum is eclipsed. SW Sex stars' eclipses are often deeper in the continuum than in the lines (Dhillon, 1998). Groot et al. (2001) showed that this effect is a result of the emission lines forming above the disc.

5.3.9 SSS 0522–35 (SSS111126:052210–350530)

SSS 0522–35 was discovered by CRTS (Drake et al., 2009) on Nov 11, 2011 with a peak outburst amplitude of 2.53 mag. CRTS data show evidence of high variability and outbursts roughly 5-6 months apart. Our average light curve is shown in Figure 5.1, and shows eclipse depths of around 1.5 mag. SSS 0522–35 has an orbital period of 0.0622(±5) d and the eclipse ephemeris is

$$\mathrm{HJD_{min}} = 2455913.4374(\pm 2) + 0.0622(\pm 5)\ E \tag{5.9}$$

5.3.10 SSS 0945–19 (SSS130413:094551–194402)

Suspected as a variable by Kukarkin et al. (1981) (known as NSV4618), the CRTS light curve of SSS 0945–19 shows evidence of deep eclipses, as well as previous outbursts. Eclipses and an orbital period of 0.065769264(2) d was reported by Kato, T. through the *vsnet* collaboration (vsnet-alert 15615). Hardy et al. (2017) observed a single eclipse, showing it to have clear white dwarf and bright spot features. Our average light curve is shown in Figure 5.1. SSS 0945–19 has an orbital period of 0.0657693(±3) d, in agreement with the period reported by Kato, T., and the eclipse

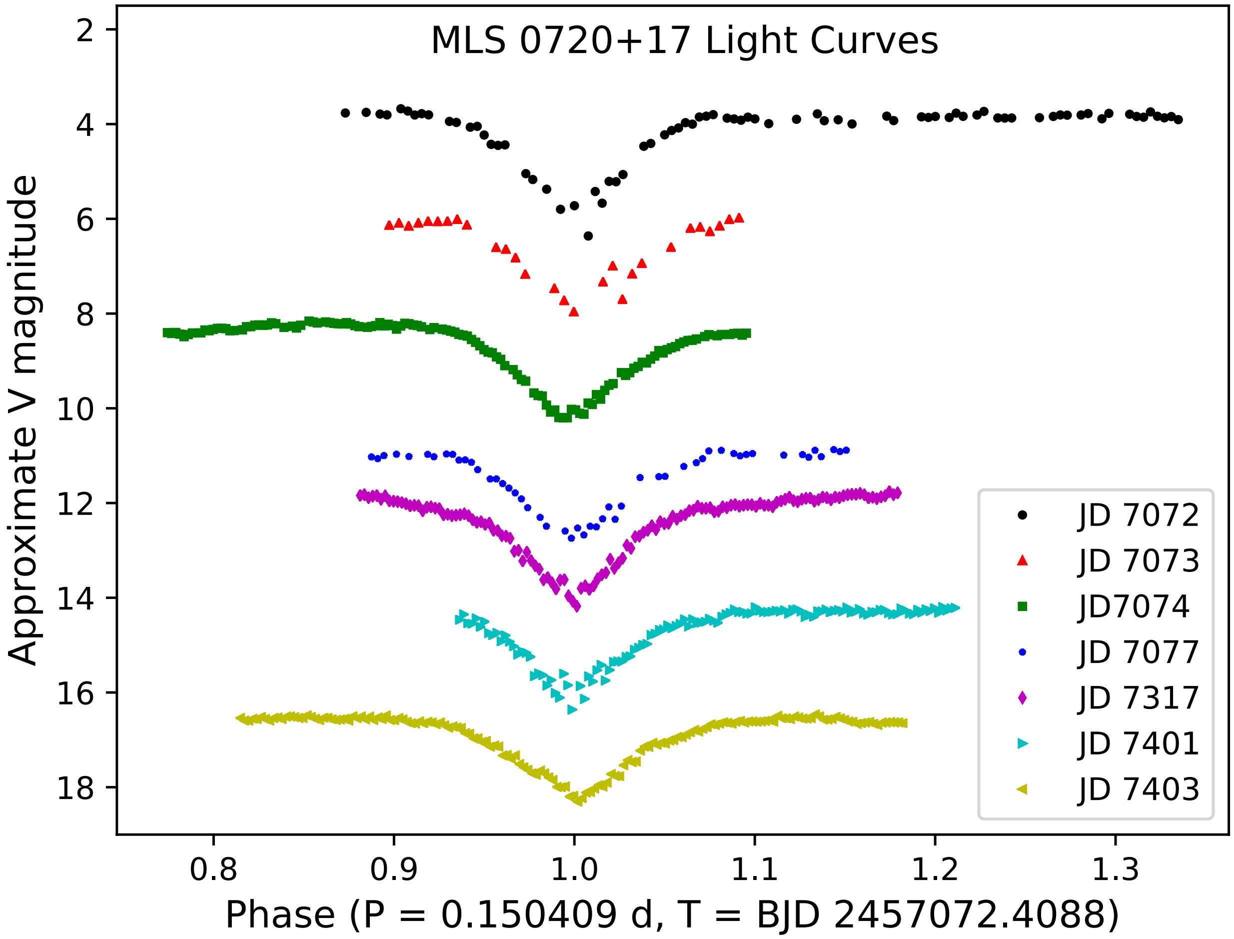

Figure 5.4: Differential photometry in V (approximated by the shift in white light by the comparison star) of MLS 0720+17 as a function of orbital phase. Each light curve is offset by $\Delta V = 3$ respectively. The first four nights' data were taken with SHOC without a filter. The V-shaped eclipse is another trait of SW Sex stars.

ephemeris is

$$\mathrm{HJD_{min}} = 2456421.3612(\pm 1) + 0.0657693(\pm 3)\ E \tag{5.10}$$

5.3.11 SSS 1340–35 (SSS120402:134015–350512)

After its discovery by CRTS (Drake et al., 2009), and first observed by Coppejans et al. (2014), SSS 1340–35 was found to be eclipsing with an orbital period of 0.059(±1) d. With our new observations, the orbital period has been refined to be 0.0598(±1) d. Our average light curve is shown in Figure 5.1. The eclipse ephemeris is

$$\mathrm{HJD_{min}} = 2457073.5421(\pm 8) + 0.0598(\pm 1)\ E \tag{5.11}$$

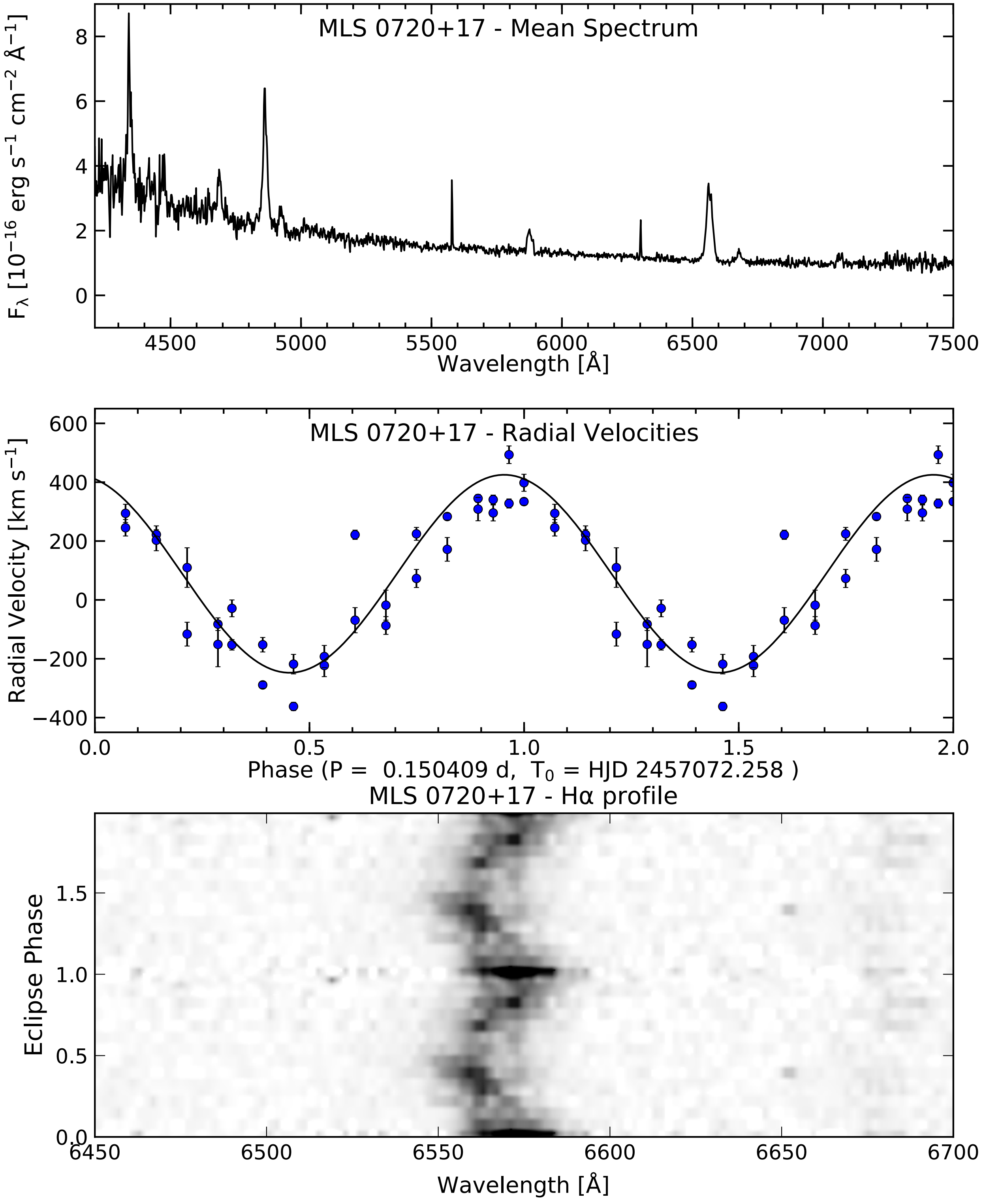

Figure 5.5: (Upper) Mean spectrum of MLS 0720+17 from MDM data taken April 2017. (Mid) H_α radial velocities folded on the eclipse ephemeris given in equation 5.7. There is an apparent 0.175± 0.031 cycle phase shift. (Lower) H_α plotted as a function of phase.

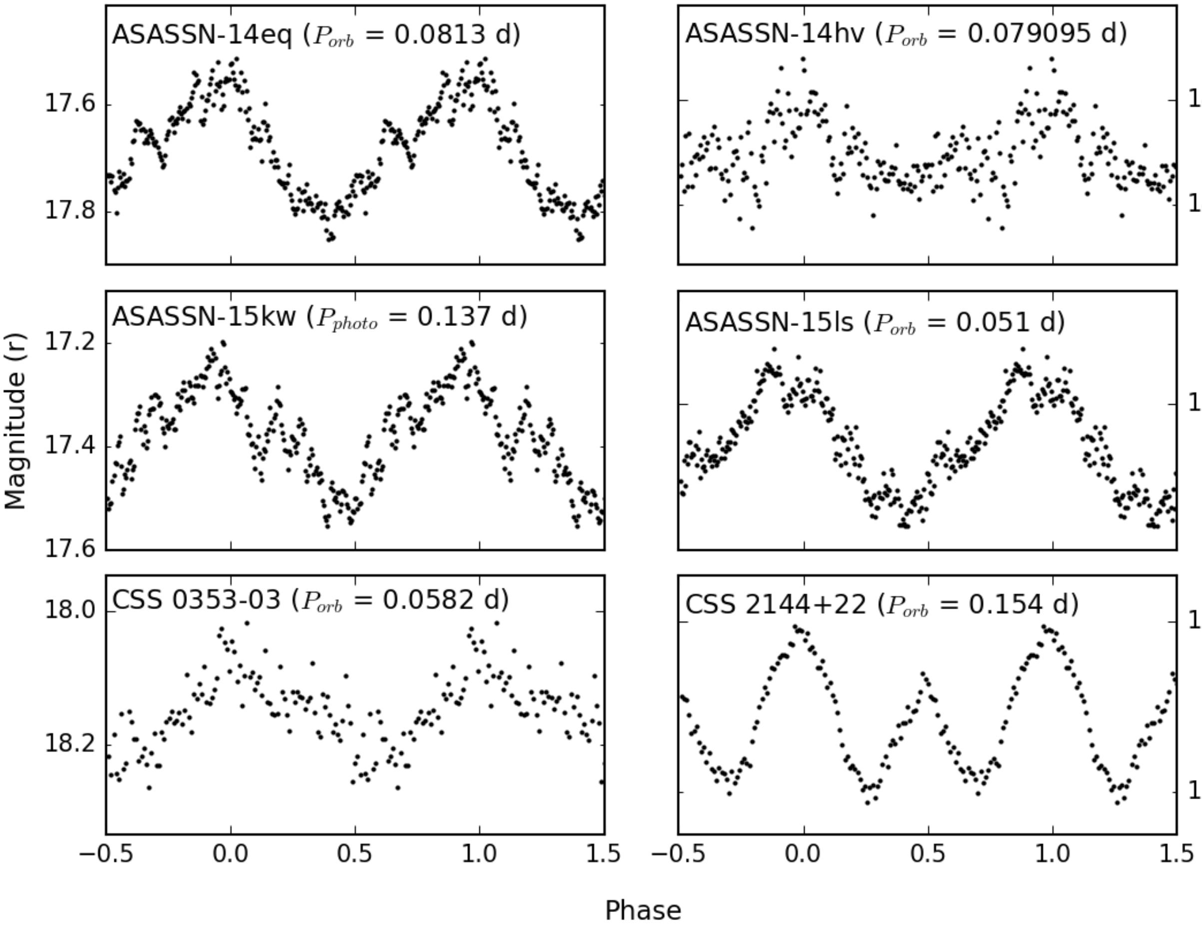

Figure 5.6: Our average light curves of non-eclipsing systems in quiescence presented in this chapter, duplicated over 2 orbital cycles. The system name and orbital period are shown in the plot. Only the later five runs (S8533 - S8545) are shown for ASASSN-14eq.

5.4 Non-eclipsing systems in quiescence

This section contains the details of individual non-eclipsing systems, for which orbital periods were found. These systems are listed in alphabetical order and our average light curves are shown in Figure 5.6.

5.4.1 ASASSN-14eq

ASASSN-14eq appears in both the CRTS (Drake et al., 2009), as well as the All Sky Automated Survey release 3 (ASAS-3; Pojmanski & Maciejewski 2004). The combined survey light curves show evidence of previous outbursts, some of which resemble superoutbursts. It was announced as a CV candidate by the ASAS-SN survey on 2014 July 28, when it underwent an outburst reaching a of $V = 13.53$ mag (Shappee et al., 2014). Our average light curve is shown in Figure 5.6. The observations presented in this chapter were taken: 1) nearly 4 months (S8508 - S8517); and 2) over a year (S8533 - S8545), after the outburst recorded by Kato et al. (2015). The system was in quiescence during all of these observations. Kato et al. (2015) found a superhump period of 0.079467 d. Observations of ASASSN-14eq show an orbital period of 0.0813(±3) d. This results in a negative superhump excess of –0.02, consistent with the expected value for such an orbital period (Hellier 2001, Figure 6.19). The orbital ephemeris for maximum light is

$$\mathrm{HJD}_{\mathrm{max}} = 2457240.5088(\pm1) + 0.0813(\pm3)\ E \tag{5.12}$$

ASASSN-14eq shows flickering on the order of 0.1 mag, with no evidence of other periods found.

5.4.2 ASASSN-14hv

ASASSN-14hv was announced as a CV candidate by the ASAS-SN survey on 2014 September 27, when it underwent an outburst with a peak of $V = 14.16$ mag (Shappee et al., 2014), and shows outbursts, including superoutbursts, approximately once every 2 months. Our observations, excluding runs S8846 and S8847 in which the system appear to be declining from outburst, were taken when the system was in quiescence. From run S8847, we determine a superhump period of 0.082(±2) days. Our average light curve in quiescence is shown in Figure 5.6. With an orbital period of 0.079095(±7) d, ASASSN-14hv shows a superhump excess of 0.04 consistent with the expected value (Hellier, 2001). The FT of the earlier runs (from Nov 2014) and the later runs (from May 2017) are shown in Figure 5.7. The orbital period and its harmonic can be seen in the FTs, but with the power changing between the orbital period and the harmonic. The orbital ephemeris for maximum light is

$$\mathrm{HJD}_{\mathrm{max}} = 2456981.6068(\pm7) + 0.079095(\pm7)\ E \tag{5.13}$$

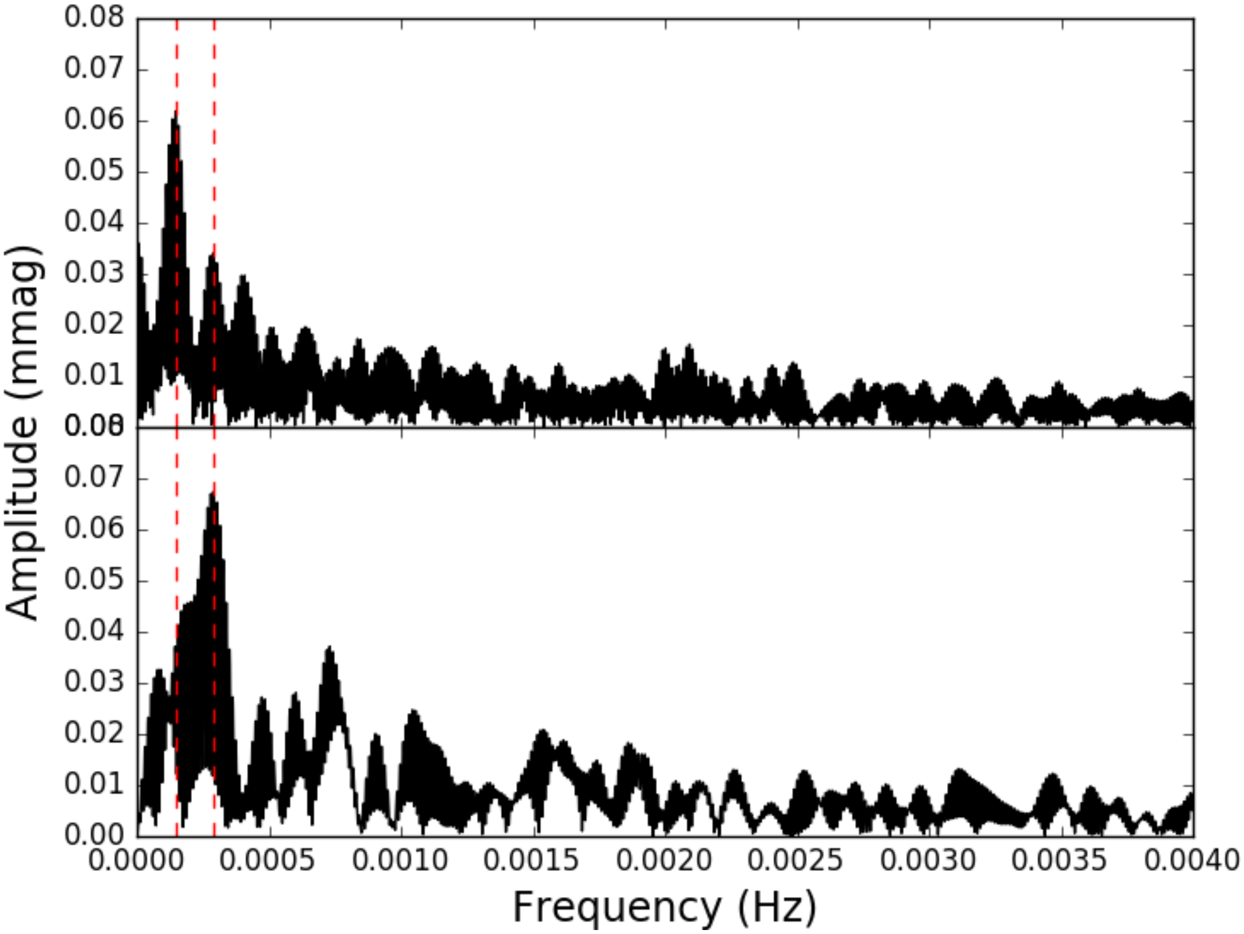

Figure 5.7: Above: FT of runs S8509, S8511, S8513 and S8514. Below: FT of runs S8851 and S8854. The dashed lines show the orbital period and the first harmonic. It is interesting to note the shifting of power between the orbital period and the harmonic. The reason for this is unclear.

5.4.3 ASASSN-15kw

With a possible outburst in the CRTS, ASASSN-15kw was announced as a CV candidate by the ASAS-SN survey on 2015 June 10, when it went into outburst with a peak magnitude of $V = 14.44$ mag (Shappee et al., 2014). Campbell et al. (2015) obtained a spectrum of ASASSN-15kw, confirming its classification as a CV. Our average light curve is shown in Figure 5.6. Individual light curves show flickering with an amplitude on the order of 0.3 mag. The ephemeris for maximum light is

$$\mathrm{HJD_{max}} = 2457217.3939(\pm 1) + 0.137(\pm 6)\ E \tag{5.14}$$

Our mean spectrum, shown in Figure 5.8, is typical of dwarf novae at minimum light. The emission lines are almost double-peaked, with typical FWHM near 2000 km s^{-1}; the emission equivalent widths of Hβ and Hα are respectively –80 and –115 Å. The Hα radial velocities show a significant modulation at an umbiguously-determined period of 0.05924(±10) d, or 85.3 min; a sinusoidal fit in the form of equation 5.8 gives $t_0 = 2457845.891(\pm 1)$ BJD, $\gamma = -36(\pm 6)$ km s^{-1}, and $K = 75(\pm 9)$ km s^{-1} at this period.

It is likely that the 85-min period is $P_{\rm orb}$, and the 3.28-hour photometric period arises from some other phenomenon. We do not have a ready explanation for these two periods, but note that Woudt & Warner (2002) found a similar discrepancy in another short-period dwarf nova, GW Lib; its orbital period is 1.28 h, but they found a significant photometric modulation at 2.09 h, and they note similar discrepant periodicities in FS Aur and V2051 Oph.

5.4.4 ASASSN-15ls

ASASSN-15ls, not covered by the CRTS, was announced as a CV candidate by the ASAS-SN survey on 2015 June 19, when it went into outburst with a peak magnitude of $V = 16.33$ mag (Shappee et al., 2014). Our average light curve is shown in Figure 5.6. The orbital ephemeris for maximum light is

$$\mathrm{HJD_{max}} = 2457240.2242(\pm 1) + 0.051(\pm 8)\ E \tag{5.15}$$

5.4.5 CSS 0353-03 (CSS111231:035318-034847)

After its discovery on 2011 Dec 31, (Drake et al., 2009), Szkody et al. (2014) obtained a spectra of CSS 0353-03 during the 2013 Jan outburst. The spectrum showed a flat blue continuum. CRTS data show evidence of outbursts occurring roughly once a year. Our average light curve is shown in Figure 5.6. The orbital ephemeris for maximum light is

$$\mathrm{HJD_{max}} = 2456247.5218(\pm 2) + 0.0582(\pm 1)\ E \tag{5.16}$$

5.4.6 CSS 214426+22 (CSS100520:214426+222024)

CSS 214426+22 was discovered by CRTS on 2010 May 20, (Drake et al., 2009) with a peak outburst amplitude of 2.41 mag. The CRTS light curve shows evidence of previous outbursts, as well as a possible superoutburst. Hardy et al. (2017) observed CSS 214426+22, confirming no eclipses. Our

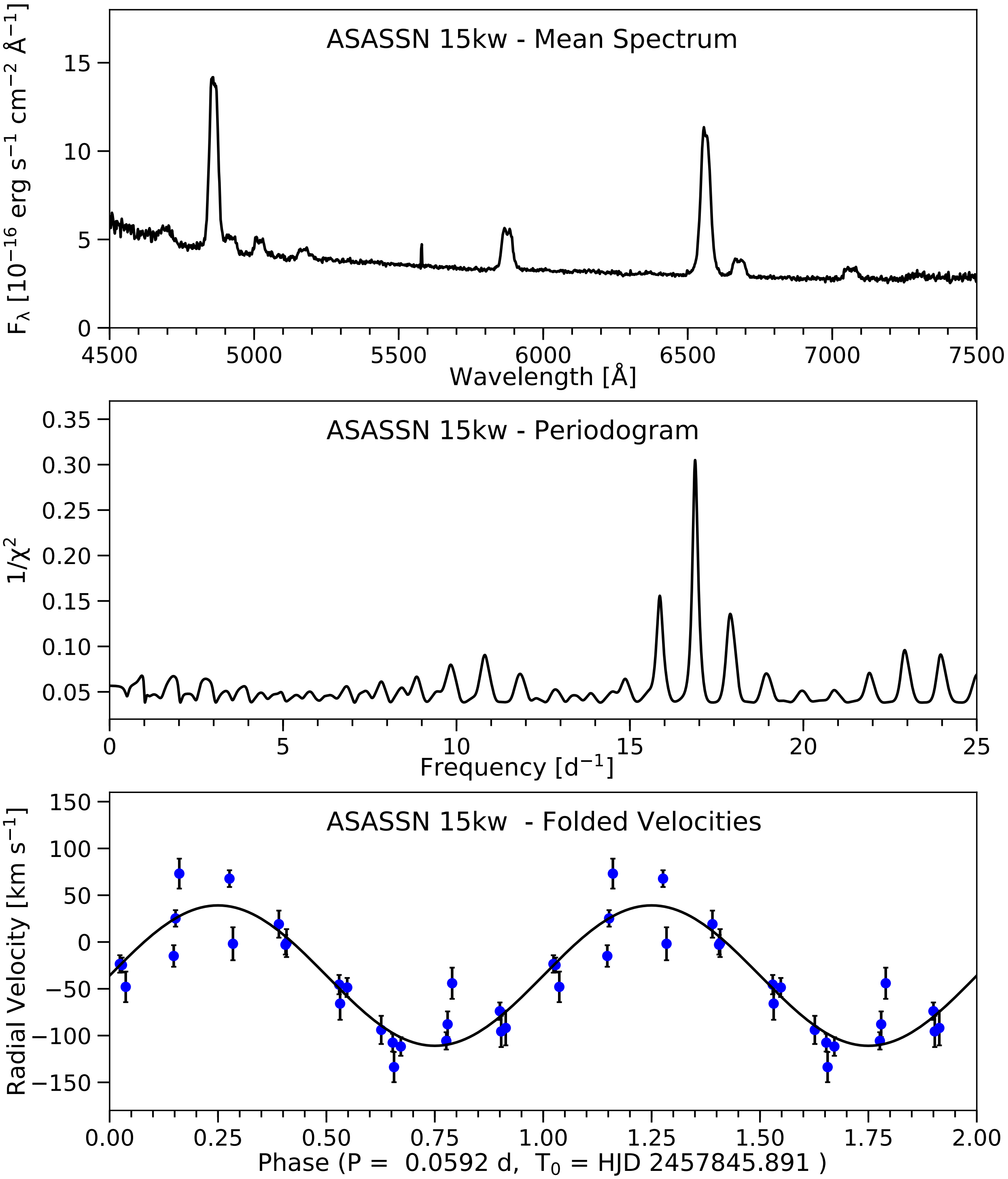

Figure 5.8: (Upper) Mean spectrum of ASASSN-15kw from MDM data taken April 2017. (Mid) Periodogram of the Hα emission velocities. The peaks flanking the main peak are aliases caused by the sampling. (Lower) Radial velocities of Hα, plotted across 2 phases, folded on the best-fitting spectroscopic ephemeris, with the best-fit sinusoid superposed. Uncertainties shown are derived from counting statistics.

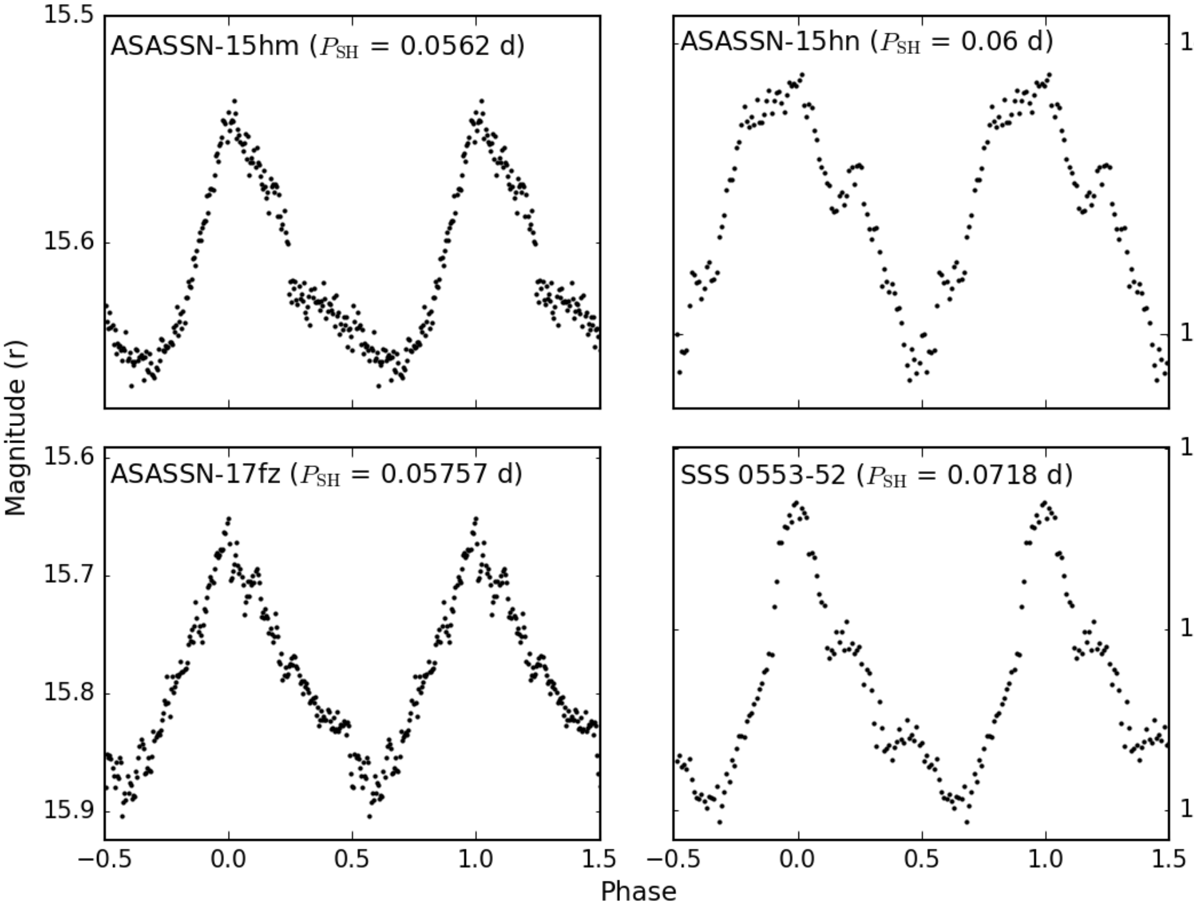

Figure 5.9: Our average light curves of systems in outburst presented in this chapter duplicated over 2 orbital cycles. The system name and superhump period is shown in the plot. Only the longest two runs (S8649 and S8651) are shown for ASASSN-15hm.

average light curve is shown in Figure 5.6. The orbital ephemeris for maximum light is

$$\mathrm{HJD_{max}} = 2456564.3701(\pm 3) + 0.154(\pm 1)\ E \tag{5.17}$$

5.5 Non-eclipsing systems in outburst

This section contains the details of individual systems which were observed during outburst, and for which superhump periods were found. Our average light curves are shown in Figure 5.9. Our observations for ASASSN-17fz are shown in Figure 5.10, to show the overall shape of the observed outburst.

5.5.1 ASASSN-15hm

ASASSN-15hm was observed during outburst after it was announced as a CV candidate by the ASAS-SN survey on 2015 April 18, (Shappee et al., 2014). ASASSN-15hm was also detected a month later by Gaia Photometric Science Alerts (Wyrzykowski et al., 2012) as Gaia15aeu. Campbell et al. (2015) obtained a spectrum of ASASSN-15hm, but classified it as a stellar object due to its redness and strong, narrow NaD absorption. Kato et al. (2016) reported a superhump period of 0.056219 d. Using the two longest runs (as these were the cleanest with multiple orbital cycles) presented in this chapter (S8649 and S8651), a superhump period of 0.0562(±1) d was found. This period agrees with the superhump period found by Kato et al. (2016). Our average light curve of run S8653, folded on the ephemeris $\mathrm{HJD}_{\mathrm{max}} = 2457145.22513(\pm 1) + 0.0562(\pm 1)\ E$, is shown in Figure 5.9.

5.5.2 ASASSN-15hn

ASASSN-15hn was observed during outburst after it was announced as a CV candidate by the ASAS-SN survey on 2015 April 18, (Shappee et al., 2014). We obtained 4 runs, the later three runs (S8647, S8653 and S8657) overlap with the data presented by Kato et al. (2016). These runs provided limited coverage, and a superhump period of 0.06(1) was found using them. Kato et al. (2016) reported a superhump period of 0.06189 d. Our average light curve of run S8653, folded on the ephemeris $\mathrm{HJD}_{\mathrm{max}} = 2457147.20394(\pm 1) + 0.06(\pm 1)\ E$, is shown in Figure 5.9.

5.5.3 ASASSN-17fz

ASASSN-17fz was observed during a superoutburst after it was announced as a CV candidate by the ASAS-SN survey on 2017 May 5, (Shappee et al., 2014). Our observations of ASASSN-17fz are shown in Figure 5.10. A single observation obtained by D. L. Holdsworth on the SAAO 1-m with SHOC on 12 Dec 2017 placed an upper limit of 21 mag on the brightness of the system. With a quiescent magnitude of >21, the amplitude of the observed superoutburst is more than six magnitudes. The superoutburst also showed a slow decline of ~ 0.13 mag per day for the duration of the observing period, classifying ASASSN-17fz as a WZ Sge-type star. Our average light curve is shown in Figure 5.9. A superhump period of 0.05757(±5) d was found during the outburst with

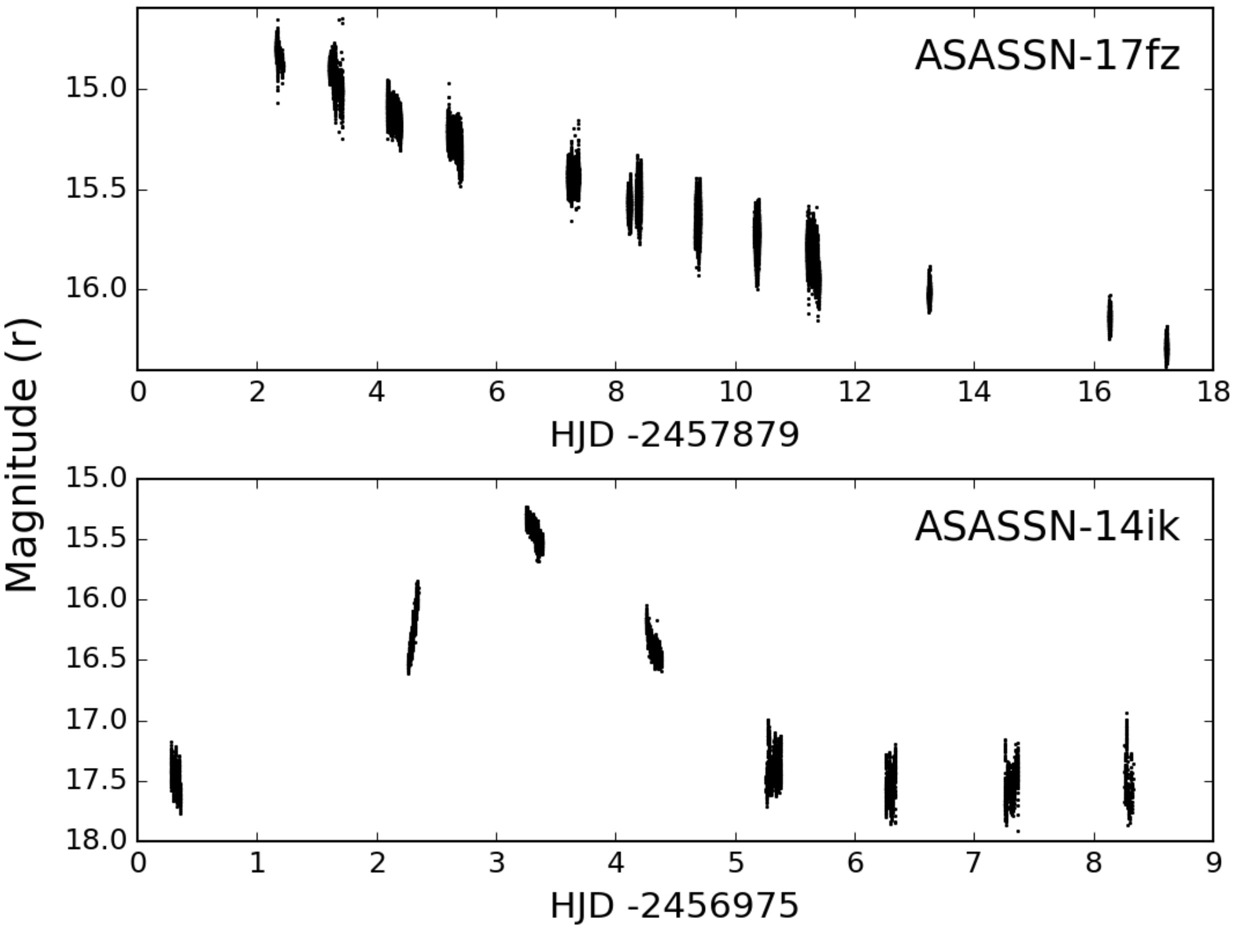

Figure 5.10: Multiple runs showing the magnitude of systems observed in outburst. Top: All observations of ASASSN-17fz presented in this chapter. Bottom: Observations of ASASSN-14ik showing the general shape of the Nov 2014 outburst.

an ephemeris for maximum light during outburst given by

$$\mathrm{HJD}_{\mathrm{max}} = 2457888.40859(\pm1) + 0.05757(\pm5)\ E \tag{5.18}$$

5.5.4 SSS 0553-52 (SSS111213:055349-525045)

Since its discovery by CRTS (Drake et al., 2009) on 2011 Dec 13, there has been sparse coverage of SSS 0553-52 within CRTS. Our average light curve is shown in Figure 5.10. The orbital ephemeris for maximum light is

$$\mathrm{HJD}_{\mathrm{max}} = 2455910.4994(\pm1) + 0.0718(\pm2)\ E \tag{5.19}$$

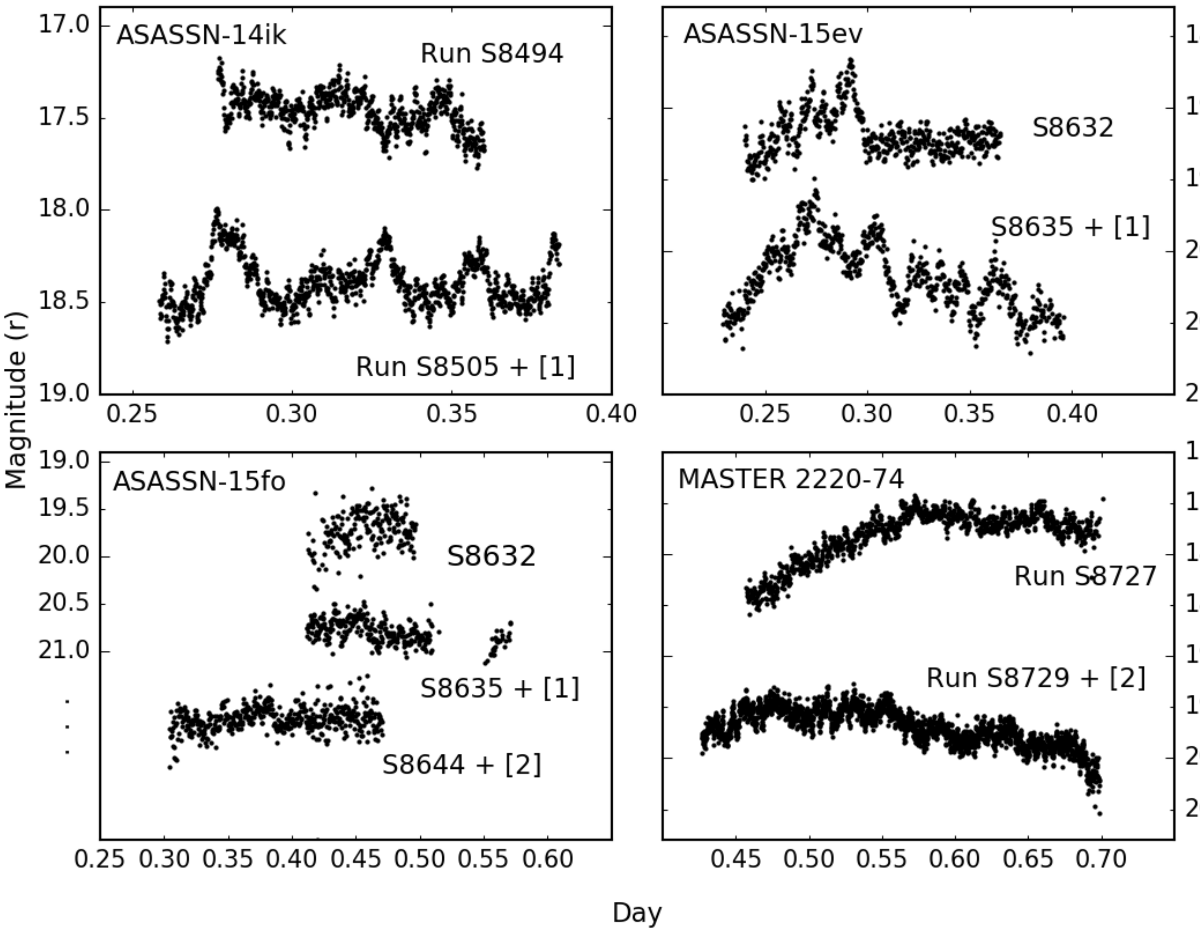

Figure 5.11: Light curves of systems where for which periods could not be determined. Top left: Individual light curves of ASASSN-14ik (run S8494 and S8505), plotted on the same scale for comparison. Flickering with an amplitude on the order of 0.1 mag is seen both before and after the outburst, while flaring with an amplitude on the order of 0.6 mag is only seen after the outburst. Top right: Individual light curves of the long two runs on ASASSN-15ev. The light curve for run S8632 is displayed at the correct brightness; the vertical offset for S8635 is given in brackets. Bottom left: Individual light curves of ASASSN-15fo. The light curve for run S8630 is displayed at the correct brightness; the vertical offset for each light curve thereafter, is given in brackets. Bottom right: Individual light curves of the two longest runs of MASTER OT J222049.51-740240.9. These runs show evidence of an orbital period longer than the individual runs presented in this chapter.

5.6 CVs for which no periodicity could be determined

This section contains the details of individual systems in for which no persistent periods were found. Some of the individual light curves for these systems are shown in Figure 5.11. Our observations of the 2014 Nov outburst of ASASSN-14ik are displayed in Figure 5.10, to show the overall shape of the observed outburst.

5.6.1 ASASSN-14ik

CRTS data of ASASSN-14ik show evidence of previous outbursts, possible superoutbursts, and high variability during quiescence. ASASSN-14ik was announced as a CV candidate by the ASAS-SN survey on 2014 October 1, when it underwent an outburst reaching $V = 14.15$ mag (Shappee et al., 2014), and has shown regular outbursts, occurring approximately once a month, since its discovery. Our observations in November, 2014 saw ASASSN-14ik undergoing a normal outburst, with a 2 mag amplitude and duration of 5 days. The shape of the outburst is shown in Figure 5.10. No DNOs or QPOs were found during the outburst. Our individual light curves of two long runs (S8494, taken just before the Nov 2014 outburst, and S8505, taken after the outburst) are shown in Figure 5.11. ASASSN-14ik shows flickering with an amplitude of ~ 0.1 mag, as well as large flaring with an amplitude of ~ 0.5 mag which is seen most clearly after the outburst. However, no persistent period was found in the data. A longer term study while the system is in quiescence is needed to confirm the presence or absence of any persistent periods.

5.6.2 ASASSN-15ev

ASASSN-15ev was announced as a CV candidate by the ASAS-SN survey on 2015 March 16, when it went into outburst with a peak magnitude of $V = 14.71$ mag (Shappee et al., 2014). The individual light curves of the longest two runs (S8632 and S8635) are displayed in Figure 5.11, each being vertically offset for display purposes, and shows flaring of ~ 0.5 mag. Matches to GALEX (Bianchi et al., 2018) and Swift (Evans et al., 2013) show the presence of UV and X-ray emission from ASASSN-15ev. The observations presented in this chapter were taken over a month after the outburst recorded by Kato et al. (2016), once the system was in quiescence. Using the relation between superhump period and orbital period of $P_{orb} = 0.9162(52)P_{SH} + 5.39(52)$ mins, found by Gänsicke et al. (2009), an estimate of the orbital period can be made using the superhump period found by Kato et al. (2016). With a reported superhump period of 0.057961 d, we predict an orbital period of around 0.056847 d. No evidence of the predicted orbital period, or any other periods, was found during quiescence.

5.6.3 ASASSN-15fo

ASASSN-15fo was announced as a CV candidate by the ASAS-SN survey on 2015 March 20, when it went into outburst with a peak magnitude of $V = 14.57$ mag. The individual light curves are displayed in Figure 5.11, each being vertically offset for display purposes. The observations presented in this chapter were taken a month after the outburst recorded by Kato et al. (2016), once the system was in quiescence. Using the relation between superhump period and orbital period found by Gänsicke et al. (2009), we predict an orbital period of around 0.058991 days from the superhump period of 0.060301 d report by Kato et al. (2016). No evidence of the predicted orbital period, or any other periods, was found during quiescence.

5.6.4 MASTER OT J2220–74 (MASTER OT J222049.51–740240.9)

MASTER OT J2220–74 was discovered by MASTER-SAAO when it went into outburst with an amplitude of more than 3.5 mag (Shumkov et al., 2015). Archival data from CRTS show evidence of variability. Our individual light curves of the two longest runs are shown in Figure 5.11. MASTER OT J2220–74 shows flickering with an amplitude on the order of 0.4 mag and a possible suggestion of a very long orbital period of over 9 hrs.

5.7 Discussion and Conclusions

We observed 25 CVs with the aim of classifying them, determining their orbital periods, searching for sub-orbital periodicities and highlighting interesting targets for possible in-depth studies. This sample consists of 15 CVs detected by ASAS-SN, 2 by MASTER and 8 by CRTS. A summary of the results are shown in Table 5.3.

Eleven of the systems (ASASSN-14hq, ASASSN-14ka, ASASSN-15fm, ASASSN-15pb, ASASSN-15pw, CSS 0524+00, MASTER J0014–56, MLS 0720+17, SSS 0522–35, SSS 0945–19, SSS 1340–35) were found to be eclipsing, most with eclipse depths ≥ 1 mag. Systems with clearly defined eclipse components (bright spot, accretion disc, white dwarf and donor star) can be modelled to accurately determine the systems parameters, such as masses and radii of the stellar components. This information contributes towards completing the sample distribution of CV parameters (such as orbital period distribution or white dwarf mass distribution) and plays an important role in understanding their evolution (Hardy et al., 2017). ASASSN-14ik and ASASSN-14ka have outburst periods of ∼ 1 month, while ASASSN-14hv has outbursts approximately every 2 months, along with superoutbursts,.

The light curve and periodogram of ASASSN-15fm indicate that this system is likely an IP, but further observations are needed to confirm the spin period of the white dwarf. With an orbital period within the period range of known SW Sex CVs, and a radial velocity phase shift of 0.175 ± 0.031 cycles with respect to the orbital phase, it is likely that MLS 0720+17 is a SW Sex-type CV. Although S-waves are not visible in our spectra, this is most likely due to low signal-to-noise. Higher S/N observations are also needed to confirm the presence of tthe phase 0.5 absorption feature seen in most SW Sex CVs. ASASSN-15kw was found to have different photometric and spectroscopic periods, similar to GW Lib and 3 other dwarf novae. The cause of this phenomenon is still unknown, but the addition of ASASSN-15kw has increased the number of the systems showing this phenomenon to 5.

Out of the 5 systems that were previously observed in outburst, we were able to confirm the superhump period for 2 of the systems and obtained an orbital period for a third system while in quiescence (ASASSN-14eq). With a superoutburst amplitude of more than 6 mag, and a superoutburst duration ≥ 46 days (assuming a constant decline of 0.13 mag per day and an upper limit of 21 mag for quiescence), ASASSN-17fz is classified as a WZ Sge-type star (see Kato 2015 for a review). Superoutburst are rare in WZ Sge-type stars, with recurrence times on the order of 1000's of days. Although a period could not be determined for MASTER OT J222049.51–740240.9, a suggestion of a very long orbital period, ≥ 9 hrs, is seen in the light curves. Long-term observations are needed to determine the orbital period.

In the final paper of this series on high speed photometry of faint cataclysmic variables we reflect briefly on nearly two decades of this survey. In the nine survey papers we have presented high speed photometry of 124 CVs, with an initial focus on faint southern nova remnants and a later focus on faint CVs discovered in optical transient surveys, probing the underlying orbital period distribution of CVs. In the last three papers alone (Woudt et al. 2012; Coppejans et al. 2014, and this paper) we presented photometry of 65 CVs resulting in 43 new photometric periods. Highlights from the survey include the discovery of a fair number of new AM CVn systems including the 10-min binary ES Ceti (Warner & Woudt, 2002), and new insights in the nature of dwarf nova oscillations and quasi-periodic oscillations in CVs (Warner, 2004).

Table 5.3: Summary of results.

Object	Type	P_{orb}	P_{SH}	r	Remarks
ASASSN-14eq	SU	0.0813(±3)	0.079467^c	$15.6 - 18.5^a$	Negative superhump excess
ASASSN-14hq	DN	0.074327(±9)	-	$18.8 - 21.7^a$	Eclipsing
ASASSN-14hv	SU	0.079095(±8)	0.082(±2)	$17.7 - 18.5^a$	Outburst ∼ once every two months
ASASSN-14ik	DN	-	-	$17.0 - 18.1^a$	Outburst ∼ once a month
ASASSN-14ka	DN	0.17716(±1)	-	$16.3 - 17.8^a$	Eclipsing; outburst ∼ once a month
ASASSN-15ev	SU	-	0.057961^d	$18.0 - 20.3^a$	
ASASSN-15fm	IP	0.286(±1)	-	$19.4 - 20.4^a$	Intermediate polar
ASASSN-15fo	SU	-	0.060301^d	$18.7 - 23.0^a$	
ASASSN-15hm	SU	-	0.0562(±1), 0.056219^d	14.7^b	
ASASSN-15hn	SU	-	0.06(±1)	14.3^b	
ASASSN-15kw	DN	0.05924(±10)	-	$16.8 - 17.8^a$	Longer photometric period present alongside spectroscopic orbital period.
ASASSN-15ls	DN	0.051(±8)	-	$16.6 - 17.7^a$	
ASASSN-15pb	DN	0.09329(±2)	-	$18.2 - 21.1^a$	Eclipsing
ASASSN-15pw	DN	0.1834(±3)	-	$16.8 - 20.3^a$	Eclipsing
ASASSN-17fz	WZ Sge	-	0.05757(±5)	21^a, 14.7^b	Superoutburst of ≥ 6 mag, slow decline
CSS 0353-03	DN	0.0582(±1)	-	$17.7 - 18.9^a$	
CSS 0524+00	DN	0.1747(±3)	-	$17.4 - 18.9^a$	Eclipsing
CSS 2144+22	SU	0.154(±1)	-	$16.4 - 17.3^a$	
MASTER J0014-56	DN	0.0715296(±6)	-	$19.1 - 22.9^a$	Eclipsing
MASTER J2220-74	DN	0.39277(±6)	-	$16.9 - 18.7^a$	
MLS 0720+17	SW Sex	0.150409(±7)	-	$17.9 - 21.1^a$	Eclipsing
SSS 0522-35	DN	0.0622(±5)	-	$17.9 - 20.7^a$	
SSS 0553-52	DN	0.0718(±2)	-	$16.9 - 17.4^a$	
SSS 0945-19	SU	0.0657693(±3)	-	$16.43 - 19.41^a$	Eclipsing
SSS 1340-35	DN	0. 0598(±1)	-	$18.42 - 19.57^a$	Eclipsing

Notes: DN: dwarf nova; SU: SU Ursae Majoris; IP: intermediate polar; ^{a}: quiescent magnitude range (including eclipses); ^{b}:peak outburst magnitude; ^{c}: period determined by Kato et al. (2015); ^{d}: period determined by Kato et al. (2016); r: r magnitude of the system in quiescence. This magnitude is an estimate and is accurate to 0.1 mag.

Chapter 6

Conclusion

In this thesis, the development, implementation and testing of the data processing pipeline for MeerLICHT are presented, including extracting variables from the MeerLICHT data and the high-speed photometric study of 25 CVs. MeerLICHT is a fully robotic, wide-field optical telescope situated at the South African Astronomical Observatory (SAAO) site in Sutherland. Linked to MeerKAT in real-time, MeerLICHT will provide simultaneous observations of the transient night sky together with the ThunderKAT and MeerTRAP projects on MeerKAT. MeerLICHT will provide real-time alerts of transients in the optical, as well as providing a wealth of data on variable sources.

6.1 Pipeline

Although further production is still underway to optimize the MeerLICHT pipeline, the pipeline is complete and able to process data in real-time. The pipeline started with the adaption of the SkyMapper Transient Search pipeline. Developments to solving the astrometric solution and the implementation of proper image subtraction using the ZOGY algorithm led to vast improvements to the performance of the pipeline for MeerLICHT. Future development for the pipeline includes testing the combination of the pipeline, database and website; and the training and implementation of a neural network machine learning algorithm for the real-bogus determination.

In its current state, the pipeline shows promising results on its performance and ability to produce reliable measurements. Comparison of the astrometry to GAIA showed a median difference in position of 0.051 arcsec in RA and 0.040 arcsec in Dec, with standard deviations of 0.246 arcsec and 0.251 arcsec for RA and Dec respectively. These measurements used 2MASS index files to create the astrometric solution. As testing was underway, the pipeline was updated to use GAIA index files to create the astrometric solution, showing preliminary results of 0.005 arcsec median difference in both RA and Dec and a standard deviation of 0.024 arcsec and 0.035 arcsec in Dec. The saturation limits and magnitudes at which a SNR of 5 is reached are within 0.1 mag of the expected values for a given seeing, providing a clear indication that MeerLICHT and BlackGEM will achieve the predicted photometry in optimal conditions. Adding fake transients to images, the pipeline was able to recover up to 100% for transients with SNR above 11. The pipeline is able to process an image from start to finish in $\sim$ 10 minutes. As multiple images can be processed in parallel, the 10 minutes introduces a delay between ingestion and output for each image but will not accumulate if a sufficient number of cores is available. Thus, the pipeline can provide real-time processing, with a 10 minute delay. Work is under way to further reduce this time, by looking into parallelizing the processing for a single image. Even with several factors limiting the accuracy of the data, the timescale of variability and amplitude recovered from an known variable shows promising results for the reliability of the light curves and future operation. Detection of variability with amplitudes on the order of 10 mmag is possible.

6.2 Science

From the commissioning data, 3 potential new variables, with variability ranging from 21.9 to 29.5 mins, were found in 3 different fields, while the amplitude and period of a known variable, OGLE-BLAP014, was successfully recovered. High-speed photometry of 25 CVs from multiple other telescopes resulted in the determination of 16 new orbital periods, 10 of which are eclipsing, and 1 new superhump period; a probable intermediate polar; a SW Sex-type star; a WZ Sge-type star; and increase the sample of systems showing different photometric and spectroscopic periods to 5. Systems with clearly defined eclipse components (bright spot, accretion disc, white dwarf and donor star) play an important role in understanding their evolution, as they can be modeled accurately to determine the systems parameters, such as masses and radii.

6.3 Future

MeerLICHT shows great potential for future operations. As seen in Chapters 3 and 4 and discussed above, initial tests with commissioning data show promising results. Although the pipeline shows promising results, some improvements can be made and are planned as future projects. Firstly, the addition of a real-bogus machine learning algorithm will have the biggest impact on the efficiency of the pipeline. The addition of a real-bogus component, trained on MeerLICHT data, will significantly increase the reliability of the transient detections and reduce the need for human intervention. Other components of the pipeline currently under development and testing which will improve the usability of MeerLICHT as a whole but not discussed in detail are the database and web interface for visualization. Another improvement which can be implemented is the multi-processing of a single image to reduce the delay from image ingestion to outputs. The reduction of this time will allow for quicker transient alerts, allowing the rapid follow-up of interesting sources by the community.

Commissioning of MeerLICHT is nearly complete and supervised observations are being conducted. Once commissioning is complete and normal operations begin, we can expect many transients alerts from MeerLICHT and the pipeline. MeerKAT was officially inauguration in July 2018, and has began taking data of the radio sky. After MeerLICHT commissioning is complete, testing can begun of the real-time link between MeerLICHT and MeerKAT, and the MeerLICHT scheduling. Once completely operational, MeerLICHT and MeerKAT will be able to provide a wealth of information about the variable sky in both optical and radio. MeerLICHT, along with MeerKAT, will contribute greatly to the field of time-domain astronomy, especially in the areas of providing rapid response to unusual transients, to optical counterparts of radio transients such as fast radio bursts, and to study the relative delays between optical and radio emission in astrophysical transients.

MeerLICHT has also provided invaluable experience regarding the design, commissioning, operations, and transient detection for the BlackGEM project. With the 3 BlackGEM telescopes currently under constructing and testing, the installation and commissioning of these telescopes in

Chile will be a much smoother process due to the efforts of the MeerLICHT team. Implementation of the pipeline for BlackGEM will also be much easier thanks to the work contributed by MeerLICHT collaborators. With the next LIGO run planned for early next year, it will be imperative for the BlackGEM project to be up and running before then in order to provide rapid detection of GW counterparts.

MeerLICHT and BlackGEM provide good case studies for future large surveys such as LSST. With the large number of transients detected each night with LSST, it will be of vital importance for the community to learn how to handle such large numbers of alerts. Being able to distinguish between known transients and exotic, rare events will be important for filtering the large number of transients for selected follow up. MeerLICHT and BlackGEM will be able to contribute towards this goal, by providing a snapshot of the data sample LSST will provide.

Acknowledgements

In connection with the submitted paper, Paterson et al. described in Chapter 5: KP acknowledges funding by the National Astrophysics and Space Science Programme (NASSP), the National Research Foundation of South Africa (NRF) through a South African Radio Astronomy Observatory (SARAO) bursary, and University of Cape Town (UCT). PW and BW acknowledge support from the NRF and UCT. JT and CG acknowledge support from NSF grant AST1008217; and would like to thank Dartmouth undergraduates Mackenzie Carlson, Edrei Chua, Robert Cueva, Natalia Drozdoff, John French, Emma Garcia, Zoe Guttendorf, Rachel McKee, Krystyna Miles, Jack Neustadt, Sam Rosen, Marie Schwalbe, and Nick Scwhartz, all of whom helped acquire the SAAO data for MLS 0720+17 as part of a foreign study program, Dartmouth graduate students Erek Alper and Mackenzie Jones who contributed as teaching assistants to the success of the observing; as well as Prof. Brian Chaboyer for his contributions to the foreign study program. This research uses observations made at the SAAO and MDM Observatory. We acknowledge additional observations taken by D. L. Holdsworth. We acknowledge the use of the ASAS-SN, MASTER and CRTS databases. We acknowledge ESA Gaia, DPAC and the Photometric Science Alerts Team (http://gaia.ac.uk/selected-gaia-science-alerts). The national facility capability for SkyMapper has been funded through ARC LIEF grant LE130100104 from the Australian Research Council, awarded to the University of Sydney, the Australian National University, Swinburne University of Technology, the University of Queensland, the University of Western Australia, the University of Melbourne, Curtin University of Technology, Monash University and the Australian Astronomical Observatory. SkyMapper is owned and operated by The Australian National University's Research School of Astronomy and Astrophysics. The survey data were processed and provided by the SkyMapper Team at ANU. The SkyMapper node of the All-Sky Virtual Observatory (ASVO) is hosted at the National Computational Infrastructure (NCI). Development and support the SkyMapper node of the ASVO has been funded in part by Astronomy Australia Limited (AAL) and the Australian Government through the Commonwealth's Education Investment Fund (EIF) and National Collaborative Research Infrastructure Strategy (NCRIS), particularly the National eResearch Collaboration Tools and Resources (NeCTAR) and the Australian National Data Service Projects (ANDS). The Pan-STARRS1 Surveys (PS1) and the PS1 public science archive have been made possible through contributions by the Institute for Astronomy, the University of Hawaii, the Pan-STARRS Project Office, the Max-Planck Society and its participating institutes, the Max Planck Institute for Astronomy, Heidelberg and the Max Planck Institute for Extraterrestrial Physics, Garching, The Johns Hopkins University, Durham University, the University of Edinburgh, the Queen's University Belfast, the Harvard-Smithsonian Center for Astrophysics, the Las Cumbres Observatory Global Telescope Network Incorporated, the National Central University of Taiwan, the Space Telescope Science Institute, the National Aeronautics and Space Administration under Grant No. NNX08AR22G issued through the Planetary Science Division of the NASA Science Mission Directorate, the National Science Foundation Grant No. AST-1238877, the University of Maryland, Eotvos Lorand University (ELTE), the Los Alamos National Laboratory, and the Gordon and Betty Moore Foundation. Some of the data presented in the paper were obtained from the Mikulski Archive for Space Telescopes (MAST). STScI is operated by the Association of Universities for Research in Astronomy, Inc., under NASA contract NAS5-26555.

Bibliography

Abbott B. P., et al., 2016, Phys. Rev.~Lett., 116, 061102

Abbott B. P., et al., 2017, Phys. Rev.~Lett., 119, 161101

Acernese F., et al., 2015, Classical and Quantum Gravity, 32, 024001

Alard C., 1999, preprint, pp astro–ph/9903111

Alard C., Lupton R. H., 1998, ApJ, 503, 325

Althaus L. G., Córsico A. H., Isern J., García-Berro E., 2010, Astronomy and Astrophysics Review, 18, 471

Atwood B., et al., 2012, in Ground-based and Airborne Instrumentation for Astronomy IV. id, 84466G, doi:10.1117/12.925383

Bailes M., et al., 2016, in Proceedings of MeerKAT Science: On the Pathway to the SKA. 25-27 May. id, 11

Becker A., 2015, HOTPANTS: High Order Transform of PSF ANd Template Subtraction, Astrophysics Source Code Library (ascl:1504.004)

Bellm E., 2014, in Wozniak P. R., Graham M. J., Mahabal A. A., Seaman R., eds, The Third Hot-wiring the Transient Universe Workshop. (`arXiv:1410.8185`)

Bertin E., 2010, SWarp: Resampling and Co-adding FITS Images Together, Astrophysics Source Code Library (ascl:1010.068)

Bertin E., 2013, PSFEx: Point Spread Function Extractor, Astrophysics Source Code Library (ascl:1301.001)

Bertin E., Arnouts S., 2010, SExtractor: Source Extractor, Astrophysics Source Code Library (ascl:1010.064)

Bessell M., Bloxham G., Schmidt B., Keller S., Tisserand P., Francis P., 2011, PASP, 123, 789

Bhardwaj A., et al., 2017, A&A, 605, A100

Bianchi L., de la Vega A., Shiao B., Bohlin R., 2018, Ap&SS, 363, 56

Bildsten L., Shen K. J., Weinberg N. N., Nelemans G., 2007, ApJ, 662, L95

Blanton M. R., Roweis S., 2007, AJ, 133, 734

Bloemen S., Groot P., Nelemans G., Klein-Wolt M., 2015, in Living Together: Planets, Host Stars and Binaries.

Bloemen S., et al., 2016, in Ground-based and Airborne Telescopes VI. id, 990664, doi:10.1117/12.2232522

Blyth S., et al., 2016, in Proceedings of MeerKAT Science: On the Pathway to the SKA. 25-27 May. id, 4

Bode M. F., Evans A., 2008, Classical Novae

Booth R. S., Jonas J. L., 2012, African Skies, 16, 101

Bourke T. L., et al., eds, 2015, Proceedings, Advancing Astrophysics with the Square Kilometre Array (AASKA14) Vol. AASKA14. SISSA, `http://pos.sissa.it/cgi-bin/reader/conf.cgi?confid=215`

Bredthauer R., Boggs K., Bredthauer G., Lesser M., 2012, in High Energy, Optical, and Infrared Detectors for Astronomy V. id, 84531M, doi:10.1117/12.925750

Breedt E., 2015, in The Golden Age of Cataclysmic Variables and Related Objects - III (Golden2015). id, 25

Breger M., 1979, PASP, 91, 5

Breger M., Montgomery M., eds, 2000, Delta Scuti and Related Stars Vol. 210

Cai R.-G., Cao Z., Guo Z.-K., Wang S.-J., Yang T., 2017, National Science Review, 4, 687

Campbell H., Wevers T., Fraser M., Jonker P. G., Wyrzykowski L., Hodgkin S., Blagorodnova N., 2015, The Astronomer's Telegram, 7641, 1

Capaccioli M., Schipani P., 2011, The Messenger, 146, 2

Carter P. J., et al., 2013, MNRAS, 429, 2143

Catelan M., Smith H. A., 2015, Pulsating Stars. Wiley-VCH

Chambers K. C., Pan-STARRS Team 2016, in American Astronomical Society Meeting Abstracts #227. id, 324.07

Chandrasekhar S., 1931, ApJ, 74, 81

Coppejans R., et al., 2013, PASP, 125, 976

Coppejans D. L., et al., 2014, MNRAS, 437, 510

Coppejans D. L., Körding E. G., Knigge C., Pretorius M. L., Woudt P. A., Groot P. J., Van Eck C. L., Drake A. J., 2016, MNRAS, 456, 4441

Crause L. A., et al., 2016, in Ground-based and Airborne Instrumentation for Astronomy VI. id, 990827, doi:10.1117/12.2230818

De Blok W. J. G., et al., 2016, in Proceedings of MeerKAT Science: On the Pathway to the SKA. 25-27 May. id, 7

Dhillon V., 1998, in Wild Stars in the Old West. (`arXiv:astro-ph/9711163`)

Díaz M. C., et al., 2016, ApJ, 828, L16

Djorgovski S. G., et al., 2011, in Mihara T., Kawai N., eds, The First Year of MAXI: Monitoring Variable X-ray Sources. (`arXiv:1102.5004`)

Dong S., et al., 2016, Science, 351, 257

Drake A. J., et al., 2009, ApJ, 696, 870

Drake A. J., et al., 2014, ApJS, 213, 9

Drake A. J., Djorgovski S. G., Mahabal A. A., Graham M. J., Stern D., Catelan M., Christensen E., Larson S. M., 2016, The Astronomer's Telegram, 9319, 1

Drew J. E., et al., 2014, MNRAS, 440, 2036

Dubus G., Otulakowska-Hypka M., Lasota J.-P., 2018, A&A, 617, A26

Einstein A., 1905, Annalen der Physik, 322, 132

Einstein A., 1916, Annalen der Physik, 354, 769

Erasmus N., et al., 2019, ApJS, A Taxonomic Study of Asteriod Families from KMTNET-SAAO Multi-Band Photometry

Evans P. A., et al., 2013, VizieR Online Data Catalog, p. IX/43

Eyer L., Mowlavi N., 2008, in Journal of Physics Conference Series. id, 012010 (`arXiv:0712.3797`), doi:10.1088/1742-6596/118/1/012010

Flewelling H. A., et al., 2016, preprint, p. arXiv:1612.05243 (`arXiv:1612.05243`)

Freyhammer L. M., Andersen M. I., Arentoft T., Sterken C., Nørregaard P., 2001, Experimental Astronomy, 12, 147

GAIA Collaboration et al., 2016, A&A, 595, A1

Gänsicke B. T., et al., 2009, MNRAS, 397, 2170

Ghosh S., Bloemen S., Nelemans G., Groot P. J., Price L. R., 2016, A&A, 592, A82

Gieseke F., et al., 2017, MNRAS, 472, 3101

Graham M. J., Drake A. J., Djorgovski S. G., Mahabal A. A., Donalek C., Duan V., Maker A., 2013, MNRAS, 434, 3423

Grainge K., et al., 2017, Astronomy Reports, 61, 288

Green M. J., et al., 2018, MNRAS, 477, 5646

Greisen E. W., Calabretta M. R., 2002, A&A, 395, 1061

Gress O., et al., 2015, The Astronomer's Telegram, 7860, 1

Groot P. J., Rutten R. G. M., van Paradijs J., 2001, A&A, 368, 183

Groot P. J., et al., 2003, MNRAS, 339, 427

Gulbis A. A. S., et al., 2011, PASP, 123, 461

Gupta N., et al., 2016, in Proceedings of MeerKAT Science: On the Pathway to the SKA. 25-27 May. id, 14

Hardy L. K., et al., 2017, MNRAS, 465, 4968

Hartman J. D., Bakos G. Á., 2016, Astronomy and Computing, 17, 1

Hayes D. S., 1985, in Calibration of Fundamental Stellar Quantities.

Hayes D. S., Latham D. W., 1975, ApJ, 197, 593

Hellier C., 2001, Cataclysmic Variable Stars. Springer

Henden A., Munari U., 2014, Contributions of the Astronomical Observatory Skalnate Pleso, 43, 518

Hillebrandt W., Niemeyer J. C., 2000, ARA&A, 38, 191

Hobbs D., et al., 2018, Technical report, Gaia DR2 documentation Chapter 3: Astrometry

Holoien T. W. S., et al., 2016, MNRAS, 463, 3813

Horne K., 1986, PASP, 98, 609

Howell S. B., ed. 1992, Astronomical CCD observing and reduction techniques Vol. 23

Howell S. B., Ellis R., Huchra J., Kahn S., Rieke G., Stetson P. B., 2006, Handbook of CCD Astronomy

Jarvis M., et al., 2016, in Proceedings of MeerKAT Science: On the Pathway to the SKA. 25-27 May. id, 6

Jenness T., et al., 2016, in Software and Cyberinfrastructure for Astronomy IV. id, 99130G, doi:10.1117/12.2231313

Jonas J., et al., 2016, in Proceedings of MeerKAT Science: On the Pathway to the SKA. 25-27 May. id, 1

Jonker P. G., et al., 2011, ApJS, 194, 18

Jordi K., Grebel E. K., Ammon K., 2006, A&A, 460, 339

Kaiser N., et al., 2002, in Tyson J. A., Wolff S., eds, Vol. 4836, Survey and Other Telescope Technologies and Discoveries. , doi:10.1117/12.457365

Kato T., 2015, PASJ, 67, 108

Kato M., Hachisu I., 2012, BASI, 40, 393

Kato T., et al., 2015, PASJ, 67, 105

Kato T., et al., 2016, PASJ, 68, 65

Keller S. C., et al., 2007, PASA, 24, 1

Kim S.-L., et al., 2016, Journal of Korean Astronomical Society, 49, 37

Knigge C., Baraffe I., Patterson J., 2011, ApJS, 194, 28

Koen C., O'Donoghue D., Stobie R. S., Kilkenny D., Ashley R., 1995, MNRAS, 277, 913

Krolik J., Piran T., Svirski G., Cheng R. M., 2016, ApJ, 827, 127

Kuijken K., 2011, The Messenger, 146, 8

Kukarkin B. V., et al., 1981, Catalogue of suspected variable stars. Moscow, p. 0

Kupfer T., et al., 2017, ApJ, 851, 28

Kupfer T., et al., 2018, MNRAS, 480, 302

LSST Science Collaboration et al., 2009, preprint, p. arXiv:0912.0201 (`arXiv:0912.0201`)

Lang D., Hogg D. W., Mierle K., Blanton M., Roweis S., 2010, AJ, 139, 1782

Levitan D., et al., 2013, MNRAS, 430, 996

Lipunov V., et al., 2010, Advances in Astronomy, 2010, 349171

Lomb N. R., 1976, Ap&SS, 39, 447

Lorimer D. R., 2008, Living Reviews in Relativity, 11, 8

Macfarlane S. A., Toma R., Ramsay G., Groot P. J., Woudt P. A., Drew J. E., Barentsen G., Eislöffel J., 2015, MNRAS, 454, 507

Macfarlane S. A., et al., 2017, MNRAS, 470, 732

Marsh T. R., Nelemans G., Steeghs D., 2004, MNRAS, 350, 113

Mighell K. J., 1999, in Astronomical Data Analysis Software and Systems VIII.

Mighell K. J., 2005, MNRAS, 361, 861

Morales-Rueda L., Groot P. J., Augusteijn T., Nelemans G., Vreeswijk P. M., van den Besselaar E. J. M., 2006, doi:10.1111/j.1365-2966.2006.10792.x, 371, 1681

Naylor T., 1998, MNRAS, 296, 339

Nelemans G., 2013, in Auger G., Binétruy P., Plagnol E., eds, Vol. 467, 9th LISA Symposium. (`arXiv:1302.0138`)

Nelemans G., Yungelson L. R., Portegies Zwart S. F., 2001, A&A, 375, 890

Oke J. B., 1974, ApJS, 27, 21

Oliveira A. S., Rodrigues C. V., Cieslinski D., Jablonski F. J., Silva K. M. G., Almeida L. A., Rodríguez-Ardila A., Palhares M. S., 2017, AJ, 153, 144

Osaki Y., 1996, PASP, 108, 39

Paczynski B., 1986, ApJ, 301, 503

Petersen J. O., Christensen-Dalsgaard J., 1999, A&A, 352, 547

Pietrukowicz P., et al., 2017, Nature Astronomy, 1, 0166

Pojmanski G., 2002, Acta Astron., 52, 397

Pojmanski G., Maciejewski G., 2004, Acta Astron., 54, 153

Ramsay G., et al., 2014, MNRAS, 437, 132

Ramsay G., et al., 2018, preprint, p. arXiv:1810.06548 (`arXiv:1810.06548`)

Rau A., et al., 2009, PASP, 121, 1334

Rodríguez-Gil P., Martínez-Pais I. G., de la Cruz Rodríguez J., 2009, MNRAS, 395, 973

Rodríguez E., Rolland A., López de Coca P., Martín S., 1996, A&A, 307, 539

Scalzo R. A., et al., 2017, PASA, 34, e030

Scargle J. D., 1982, ApJ, 263, 835

Schaffenroth V., Barlow B. N., Drechsel H., Dunlap B. H., 2015, A&A, 576, A123

Schneider D. P., Young P., 1980, ApJ, 238, 946

Schneider P., Ehlers J., Falco E. E., 1992, Gravitational Lenses, doi:10.1007/978-3-662-03758-4.

Schwarzenberg-Czerny A., 1989, MNRAS, 241, 153

Serra P., et al., 2016, in Proceedings of MeerKAT Science: On the Pathway to the SKA. 25-27 May. id, 8

Shappee B., et al., 2014, in American Astronomical Society Meeting Abstracts 223. id, 236.03

Shumkov V., et al., 2015, The Astronomer's Telegram, 7521, 1

Shupe D. L., Laher R. R., Storrie-Lombardi L., Surace J., Grillmair C., Levitan D., Sesar B., 2012, in Software and Cyberinfrastructure for Astronomy II. id, 84511M, doi:10.1117/12.925460

Singer L. P., et al., 2014, ApJ, 795, 105

Skrutskie M. F., et al., 2006, AJ, 131, 1163

Solheim J. E., 2010, PASP, 122, 1133

Sooknunan K., et al., 2019, MNRAS, Classification of Multiwavelength Transients with Machine Learning

Stappers B., 2016, in Proceedings of MeerKAT Science: On the Pathway to the SKA. 25-27 May. id, 10

Stappers B., Kramer M., 2016, in Proceedings of MeerKAT Science: On the Pathway to the SKA. 25-27 May. id, 9

Stetson P. B., 1996, PASP, 108, 851

Szkody P., et al., 2002, AJ, 123, 430

Szkody P., et al., 2003, AJ, 126, 1499

Szkody P., Everett M. E., Howell S. B., Landolt A. U., Bond H. E., Silva D. R., Vasquez-Soltero S., 2014, AJ, 148, 63

Tamuz O., Mazeh T., North P., 2006, MNRAS, 367, 1521

Taylor R., Camilo F., Leeuw L., Moodley K., eds, 2018, Proceedings, MeerKAT Science: On the Pathway to the SKA (MeerKAT2016) Vol. MeerKAT2016. SISSA, `https://pos.sissa.it/277/`

Ter Horst R., Kragt J., Lesman D., Navarro R., 2016, in Advances in Optical and Mechanical Technologies for Telescopes and Instrumentation II. id, 99121J, doi:10.1117/12.2232348

Thorstensen J. R., Halpern J., 2013, AJ, 146, 107

Thorstensen J. R., Ringwald F. A., Wade R. A., Schmidt G. D., Norsworthy J. E., 1991, AJ, 102, 272

Thorstensen J. R., Alper E. H., Weil K. E., 2016, AJ, 152, 226

Tody D., 1986, in Instrumentation in astronomy VI. , doi:10.1117/12.968154

Toma R., et al., 2016, MNRAS, 463, 1099

Van Dokkum P. G., Bloom J., Tewes M., 2012, L.A.Cosmic: Laplacian Cosmic Ray Identification, Astrophysics Source Code Library (ascl:1207.005)

Verbeek K., et al., 2012, MNRAS, 420, 1115

Warner B., 1995, Cambridge Astrophysics Series, 28

Warner B., 2004, PASP, 116, 115

Warner B., Woudt P. A., 2002, PASP, 114, 129

Warner B., Woudt P. A., 2004, in IAU Colloq. 193: Variable Stars in the Local Group. (`arXiv:astro-ph/0310072`)

Watson C. L., Henden A. A., Price A., 2006, Society for Astronomical Sciences Annual Symposium, 25, 47

Wickramasinghe D., 2014, in European Physical Journal Web of Conferences. id, 03001, doi:10.1051/epjconf/20136403001

Winget D. E., Kepler S. O., 2008, ARA&A, 46, 157

Wolf C., et al., 2018, PASA, 35, e010

Worters H., et al., 2019 in prep.

Woudt P. A., Warner B., 2002, Ap&SS, 282, 433

Woudt P. A., et al., 2009, ApJ, 706, 738

Woudt P. A., Warner B., de Budé D., Macfarlane S., Schurch M. P. E., Zietsman E., 2012, MNRAS, 421, 2414

Woudt P. A., et al., 2016, in Proceedings of MeerKAT Science: On the Pathway to the SKA. 25-27 May. id, 13

Wyrzykowski Ł., Hodgkin S., Blogorodnova N., Koposov S., Burgon R., 2012, in 2nd Gaia Follow-up Network for Solar System Objects. (`arXiv:1210.5007`)

Zacharias N., Monet D. G., Levine S. E., Urban S. E., Gaume R., Wycoff G. L., 2005, VizieR Online Data Catalog, p. I/297

Zackay B., Ofek E. O., 2017, ApJ, 836, 187

Zackay B., Ofek E. O., Gal-Yam A., 2016, ApJ, 830, 27

van Roestel J., et al., 2019, MNRAS, 484, 4507

Appendix A

MeerLICHT/BlackGEM Pipeline User Guide

K Paterson

July 9, 2018

Version 1.0

A.1 Introduction

The MeerLICHT/BlackGEM pipeline is written in python and was developed for real time reduction and analysis of optical photometric data from MeerLICHT and BlackGEM. It has been written as a generalized pipeline, allowing the reduction of any optical photometric data, provided a setting file specific to the telescope is provided to the pipeline. The image subtraction component of the pipeline, '**subpipe**', was adapted from the SkyMapper Transient pipeline. The pipeline has been developed to run on a cloud based environment for multi-processing of images. Each subsection below describes an aspect of the pipeline in more details.

A.2 Installation

The pipeline will be publicly available on Github at `https://github.com/sbloemen/BGreduce`. Included on the Github is an INSTALL file which describes what packages are needed as well as other dependencies. The **test_pipeline.py** script can be used to test if all the needed python packages are installed. Subpipe is contained separately on Github at `https://github.com/sbloemen/subpipe`. Subpipe requires multiple external programs to run, including: SExtractor, PSFex, and `Astrometry.net`. These details are described in the INSTALL file. The use of containers, which creates a virtual machine with a specified environment and programs, enable reproducibility for the pipeline across different hardware and software. There are a number of container solutions available for use. An image, which creates the pipeline environment, will be made available on the Docker Hub for such purposes. This image will reproduce the version of the pipeline currently in use on MeerLICHT/BlackGEM. This image can be installed using Docker[1], or imported by Singularity[2].

A.3 Licence

Please see LICENSE file on Github for details.

A.4 Running

Running the pipeline is done through the terminal by calling the pipeline through python e.g. **python pipeline.py**. The pipeline allows users to provide parameters using a double dash i.e. **- -**, to define variables based on the telescope and local environment. A detailed description of each parameter is provided below, along with a summary of each parameter's function in Table **A.1**. Only one parameter is needed for the pipeline to run, the **telescope** (see **A.4.1**) parameter. Thus, in order to run the pipeline, the minimum command needed is **python pipeline.py - - telescope 'telescope'**, where **'telescope'** is the name of the pipeline setting file.

A.4.1 telescope

telescope is the only parameter needed by the pipeline in order to run. This parameter needs to be set by the user and allows the pipeline to load a setting file with the same name. This setting file is a python script containing the details unique to each telescope, see **A.5** for more details. The setting file must be in the same directory as the pipeline script and is called without the extension

---

[1] `https://www.docker.com`
[2] `https://singularity.lbl.gov`

i.e. the setting file **meerlicht.py** would be called as the telescope parameter with **- - telescope meerlicht**. The default for **telescope** is **None** and if no parameter is given by the user, the pipeline will exit with the error: `No telescope given, please give telescope and re-run`. If a **telescope** parameter is provided but the setting file does not exist or is not in the same directory as the pipeline, the pipeline with exit with the error: `No such telescope file, please check that the file is in the same directory as the pipeline`. Currently available setting files include **kmtnet**, for reduction of data taken with the Korean Micro-lensing Telescope Network (KMTNet) situated in Sutherland, and **meerlicht**.

A.4.2 mode

The **mode** parameter defines how the pipeline will run. There are two options available to the user. The **day** mode processes and create the calibration files needed for basic image corrections, while the **night** mode processes science files for real-time processing (see **A.4.3** for more options within the **night** mode of the pipeline). A more detailed description of the dataflow for each mode is given in section **A.6**. The default for **mode** is **day**. If anything other than **day** or **night** is provided, the pipeline will exit with the error: `Mode not understood, exiting`.

A.4.3 night_start

The **night_start** parameter is an option within the **night** mode of the pipeline and defines how the pipeline handles waiting science files in the real-time processing. There are two options available to the user. The **correct** option processes any waiting files first before continuing to wait for new files, processing them in real time, while the **late** option begins real-time processing of files immediately, catching up on any files present at the start of the pipeline after the scheduled exit time has been reached (see **A.5** for more details). A more detailed description of the dataflow for each option is given in section **A.6**. The default for **night_start** is **late**. If anything other than **correct** or **late** is provided, the pipeline will exit with the error: `Night_start option not understood, please choose between late and correct, exiting pipeline`.

A.4.4 date

The **date** parameter defines which data the pipeline will process. The inputted **date** needs to be in any of the following forms: **yyyy/mm/dd**, **yyyy-mm-dd**, **yyyy.mm.dd**, or **yyyymmdd**. If no **date** is provided, the pipeline will automatically select the date. For the **day** mode, this equates to the previous day's date. For the **night** mode, the pipeline will set the date to the start of the current night's date i.e. starting the pipeline after 12 UTC, but before 0 UTC, **date** is set to the current day's date; while starting the pipeline after 0 UTC, and before 12 UTC, **date** is set to the previous day's date. The **date** parameter is used to define read, write and work paths within the pipeline, see section **A.6** for more details.

A.4.5 cpu

The **cpu** parameter defines how many CPUs is used by the pipeline for multiprocessing. Setting **cpu** >1 allows the pipeline to process multiple files at once. When creating the master bias, a **cpu** >1 allows multiple extensions to be processed simultaneously. When processing flat files, a **cpu** >1 allows multiple files to reduced simultaneously. When processing science files, a **cpu** >1 allows multiple files to processed simultaneously. If the number of CPUs set by the user is greater than the number of CPUs available on the system, the pipeline will set **cpu** to the maximum number of CPUs available.

A.4.6 process_bias

The **process_bias** parameter sets whether the pipeline will process or ignore bias files within the **day** mode of the pipeline. If set to **True**, the pipeline will attempt to create a master bias with all available bias files. If set to **False**, the pipeline will ignore bias files and will load a previously created master bias, searching the reference directory specified by the **write_path** parameter and the **bias_path** set in the setting file. The pipeline will not use a master bias that was created with data that is a year older that the current date being processed. If no suitable master bias is found, the pipeline is exited with the error: `No suitable master bias present for reduction, exiting pipeline`. The default for **process_bias** is **True**.

A.4.7 process_flat

The **process_flat** parameter sets whether the pipeline will process or ignore flat files within the **day** mode of the pipeline. If set to **True**, the pipeline will reduce flat files and create a master flat for each filter. If set to **False**, the pipeline will ignore flat files. The default for **process_flat** is **True**.

A.4.8 reduce_science

The **reduce_science** parameter sets whether the pipeline will reduce science files. If set to **True**, the pipeline will reduce science files by performing basic reductions such as: the crosstalk correction, the gain correction, applying the master bias, applying the master flat, constructing the data into a single image (via stitching multiple extensions/trimming), and cleaning cosmic rays. The pipeline will also prepare the science files for submission to subpipe by updating the header with the required keywords, and creating a mask file (see section **A.7** for more details). If set to **False**, the pipeline will not reduce science files. This option is used for cases when the user wishes to submit already reduced files to subpipe through the pipeline. The default for **reduce_science** is **True**.

A.4.9 submit_subpipe

The **submit_subpipe** parameter sets whether the pipeline will submit files to subpipe. If set to **True**, the pipeline will submit science files to subpipe for analysis. If set to **False**, the pipeline will not submit the science files to subpipe and will save the reduced files to the appropriate path specified by the **write_path** parameter and the **red_path** set in the setting file. The default for **submit_subpipe** is **True**.

A.4.10 read_path

The **read_path** parameter defines where the pipeline will look for the raw data. The user should input the full raw data path, should it differ from the default. The default for **read_path** is set in the setting file.

A.4.11 write_path

The **write_path** parameters defines where the pipeline will save the outputs. The user should input the full output path, should it differ from the default. The default for **write_path** is set in the setting file.

A.4.12 file_name

The **file_name** parameter defines what pattern the pipeline uses to glob (a python function used to get a list of files) the raw files. The user should input a pattern containing the general characteristics of the raw file names in combination with the wildcard character e.g. ***.fits**, should it differ from the default. The default for **file_name** is set in the setting file.

A.4.13 crosstalk_file

The **crosstalk_file** parameter defines the name of the file containing the crosstalk correction. The user should input the full path of the crosstalk correction file, should it differ from the default. The default for **crosstalk_file** is set in the setting file.

A.4.14 nonlin_file

The **nonlin_file** parameter defines the name of the file containing the non-linearity correction. The user should input the full path of the crosstalk correction file, should it differ from the default. The default for **nonlin_file** is set in the setting file.

A.4.15 bad_pixel_mask

The **bad_pixel_mask** parameter defines the name of the file containing the bad pixel mask. The user should input the full path of the bad pixel mask file, should it differ from the default. The default for **bad_pixel_mask** is set in the setting file.

A.4.16 work_path

The **work_path** parameter defines where the pipeline stores temporary files during processing. The user should input the full work path, should it differ from the default. The default for **work_path** is set in the setting file.

A.4.17 log_path

The **log_path** parameter defines where the pipeline log files will be stored. The path provided is a relative path and is used in conjunction with the **write_path** parameter i.e. **write_path+log_path**. The default for **log_path** is set in the setting file.

A.4.18 fpack

The **fpack** parameter sets whether the pipeline will compress output files via fpack. If set to **True**, the pipeline will compress all output fits files via fpack. If set to **False**, the pipeline will not compress the output files. The default for **fpack** is **True**.

A.4.19 verbose

The **verbose** parameter sets whether the pipeline will provide extra information during subpipe. If set to **True**, the pipeline will print extra running information to the terminal during subpipe. This extra information is useful during testing and is not included in the logs. If set to **False**, the pipeline will not print this extra information to the terminal. The default for **verbose** is **False**.

A.4.20 slack

The **slack** parameter sets whether the pipeline will upload log messages to slack during the **night** mode of the pipeline. If set to **True**, the pipeline will upload all logged messages to slack. If the pipeline cannot connect to slack, the error: `Connection error: failed to connect to slack. Above message not uploaded.` will be added to the log file. If set to **False**, the pipeline will not upload any of the logged messages to slack. The default for **slack** is **True**.

A.5 Setting file

The setting file contains the unique settings and functions for each telescope and is loaded by the pipeline using the **telescope** parameter. A description of each function is described below.

Table A.1: Summary of pipeline parameters.

Parameter	Allowed	Default	Description
telescope	file name	None	Name of the pipeline setting file per telescope.
mode	**day**, **night**	**day**	Mode of the pipeline, defining the dataflow.
night_start	**correct** **late**	**late**	Option with the **night** mode of the pipeline, defining how the pipeline handles waiting files.
date	**yyyy/mm/dd** **yyyy-mm-dd** **yyyy.mm.dd** **yyyymmdd**	**day**: previous day's date **night**: start of night for current day's date	Date of data to be processed.
cpu	int	1	Number of CPUs available to the pipeline for multiprocessing.
process_bias	**True** **False**	**True**	Option to process bias files and create master bias.
process_flat	**True** **False**	**True**	Option to process flat files and create master flats.
reduce_science	**True** **False**	**True**	Option to reduce science files.
submit_subpipe	**True** **False**	**True**	Option to submit science files to subpipe for image subtraction and analysis.
read_path	directory name	set in the setting file	Full directory where pipeline reads raw data.
write_path	directory name	set in the setting file	Full directory where pipeline write outputs.
file_name	pattern	set in the setting file	Raw file name pattern used to glob files.
crosstalk_file	file name	set in the setting file	Name of file containing crosstalk correction.
nonlin_file	file name	set in the setting file	Name of file containing non-linearity correction.
bad_pixel_mask	file name	set in the setting file	Name of bad pixel mask.
work_path	directory name	set in the setting file	Relative working directory of pipeline.
log_path	directory name	set in the setting file	Relative directory where log files are written to.
fpack	**True** **False**	**True**	Option to compress files via fpack.
verbose	**True** **False**	**False**	Option to print extra information during subpipe.
slack	**True** **False**	**True**	Option to upload logs to slack during **night** mode.

A.5.1 read_path

The **read_path** function returns the absolute path `[str]` where the raw data is stored. This function is called by the pipeline if no user input is given to the **read_path** parameter.

A.5.2 write_path

The **write_path** function returns the absolute path `[str]` where outputted files from the pipeline is written to. This function is called by the pipeline if no user input is given to the **write_path** parameter.

A.5.3 work_path

The **work_path** function returns the absolute path `[str]` of the temporary working directory of the pipeline. This function is called by the pipeline if no user input is given to the **work_path** parameter.

A.5.4 log_path

The **log_path** function returns the relative path `[str]` where the pipeline log files are written to. This function is used in combination with **write_path** to obtain the absolute path i.e. the absolute path where pipeline log files are written to is the concatenated combination of **write_path+log_path**. This function is called by the pipeline if no user input is given to the **log_path** parameter.

A.5.5 bias_path

The **bias_path** function returns the relative path `[str]` where master bias files are written to. This function is used in combination with **write_path** to obtain the absolute path i.e. the absolute path where master bias files are written to is the concatenated combination of **write_path+bias_path**.

A.5.6 flat_path

The **flat_path** function returns the relative path `[str]` where master flat files are written to. This function is used in combination with **write_path** to obtain the absolute path i.e. the absolute path where master flat files are written to is the concatenated combination of **write_path+flat_path**.

A.5.7 red_path

The **red_path** function returns the relative path `[str]` where all science outputs from the pipeline are written to. This function is used in combination with **write_path** to obtain the absolute path i.e. the absolute path where all science outputs from the pipeline are written to is the concatenated combination of **write_path+red_path**.

A.5.8 file_name

The **file_name** function returns the filename pattern `[str]` used by the pipeline to glob raw files. This function is called by the pipeline if no user input is given to the **file_name** parameter.

A.5.9 crosstalk_file

The **crosstalk_file** function returns the absolute path `[str]` of the crosstalk correction file. This function is called by the pipeline if no user input is given to the **crosstalk_file** parameter.

A.5.10 nonlin_file

The **nonlin_file** function returns the absolute path `[str]` of the non-linearity correction file. This function is called by the pipeline if no user input is given to the **nonlin_file** parameter.

A.5.11 bad_pixel_mask

The **bad_pixel_mask** function returns the absolute path `[str]` of the file containing the bad pixel bad for the telescope. This function is called by the pipeline if no user input is given to the **bad_pixel_mask** parameter.

A.5.12 fieldID

The **fieldID** function returns the field ID of a file `[str]`. This function requires the header of the file. Depending on the telescope, this function can either read the field ID from the header, load in the field ID from a file, or manually set the field ID. If this fails, the pipeline will set the field ID to 0000. A field ID of 0000 only affects **subpipe**, indicating a error with the WCS.

A.5.13 subframe

The **subframe** function returns the number of sub-images present in each file `[list of integers]`.

A.5.14 ext_num

The **ext_num** function returns the number of data extensions `[int]` present in the file. This is used to access all the data extensions when dealing with MEF files.

A.5.15 img_num

The **img_num** function returns the number of extensions `[int]` per image. This is used to construct each image when dealing with MEF files containing sub-images.

A.5.16 channels

The **channels** function returns the number of channels `[int]` per file. This is used when dealing with channel based corrections e.g. crosstalk, gain etc.

A.5.17 filters

The **filters** function returns the filters available from the telescope `[list of strings]`. This is used to sort files by filter, and create the master flat files for each filter.

A.5.18 ccd_sec

The **ccd_sec** function returns the size of each channel `[tuple of integers]`.

A.5.19 data_sec

The **data_sec** function returns the sections of the fits file that contains the image data. The form depends on the telescope e.g. `[list of lists]/[str]`. This is used to define where the image data is in the fits file data.

A.5.20 bias_sec

The **bias_sec** function returns the section of the fits file that contains the bias data. The form depends on the telescope e.g. `[list of lists]/[str]`. This is used to define where the bias data is in the fits file data.

A.5.21 overscan_sec

The **overscan_sec** function returns the section of the fits file that contains the overscan data. The form depends on the telescope e.g. `[list of lists]/[str]`. This is used if the overscan region differs from the bias region and defines where the overscan data is in the fits file data.

A.5.22 update_keywords

The **update_keywords** function updates the header of a science file with any missing keywords needed for **subpipe**, as well as deleting any non-standard keywords. This function requires the header and field ID of the file, the pipeline version, and the name of the log file.

A.5.23 add_wcs_keywords

The **add_wcs_keywords** function updates the primary header with the WCS keywords. This function requires the primary header and the data header of the file. This is used if the WCS keywords are present in the data header, instead of the primary header.

A.5.24 bias_minmax_clip

The **bias_minmax_clip** function returns whether the pipeline will apply `minmax clipping` during the creation of the master bias `[True/False]`.

A.5.25 bias_min_clip

The **bias_min_clip** function returns the value of `min` used during the `minmax clipping` function `[int]`.

A.5.26 bias_max_clip

The **bias_max_clip** function returns the value of `max` used during the `minmax clipping` function `[int]`.

A.5.27 master_bias

The **master_bias** function create a master bias. This function requires a list of bias files to be used, and the extension of the fits file being combined. The function performs the gain correction, creates the master bias using the `ccdproc.combine` function, calculates the median level and the readnoise of the bias section. The function then returns: the extension, the master bias, the median bias level, the readnoise.

A.5.28 bias_quality

The **bias_quality** function returns the optimal noise, in electrons, for a master bias. This is used to assess the quality of the master bias created `[float]`.

A.5.29 debias

The **debias** function applies the master bias correction to files. This function requires the raw file to be corrected (either the name of the file, or a list containing the file data) and the master bias. An optional `file` argument, set to `True/False`, is used when the inputted raw file is a file name. The function performs the gain correction, determines the readnoise, subtracts the bias using the `ccdproc.subtract_bias` function, performs the overscan correction either with the `ccdproc.correct_overscan` function or the **overscan** function in the setting file, and trims the data if from a MEF file. The function then returns: the debiased file, the readnoise for each channel.

A.5.30 append_mbias_bias

The **append_mbias_bias** function updates the header of the master bias with the median bias level for each channel (as well as the mean of these values depending on the telescope). This function requires the header of the master bias file, the extension, and the median bias level.

A.5.31 append_mbias_rdnoise

The **append_mbias_rdnoise** function updates the header of the master bias with the readnoise for each channel (as well as the mean of these values depending on the telescope). This function requires the header of the master bias file, the extension, and the readnoise.

A.5.32 flat_minmax_clip

The **flat_minmax_clip** function returns whether the pipeline will apply the `minmax clipping` during the creation of the master flat `[True/False]`.

A.5.33 flat_min_clip

The **flat_min_clip** function returns the value of `min` used during the `minmax clipping` function `[int]`.

A.5.34 flat_max_clip

The **flat_max_clip** function returns the value of `max` used during the `minmax clipping` function `[int]`.

A.5.35 flat_sigma_clip

The **flat_sigma_clip** function returns whether the pipeline will apply the `sigma clipping` during the creation of the master flat `[True/False]`.

A.5.36 flat_quality

The **flat_quality** function returns the optimal noise, in electrons, for a master flat for each filter `[float]`. This is used to assess the quality of the master flat created.

A.5.37 flat_std

The **flat_std** function returns the maximum number of pixels allowed to deviate from the master flat median by 3 standard deviations `[float]`. This ensures the master flat is smooth and does not contain stars.

A.5.38 mask_bad_pixels

The **mask_bad_pixels** function returns the bad pixel mask `[array]`. This function requires the name of the bad pixel mask file, determined by the **bad_pixel_mask** parameter, to load the bad pixel mask from file.

A.5.39 saturation

The **saturation** function returns the value of saturation for the telescope in electrons `[float]`.

A.5.40 binning

The **binning** function returns the value used to bin the science files when masking the satellite trails `[int]`.

A.5.41 construct

The **construct** function returns the data constructed as a single array `[array]`. This function requires the data in a list. The function constructs the data from a list into a single array, only containing the image data.

A.5.42 bias_min

The **bias_min** function returns the minimum number of bias files needed to create a master bias `[int]`.

A.5.43 flat_min

The **flat_min** function returns the minimum number of flat files needed to create a master flat `[int]`.

A.5.44 gain

The **gain** function returns the gains for each channel `[list of floats]`.

A.5.45 gain_correct

The **gain_correct** function applies the gain correction to the data. This function requires the data to be corrected. The function applies the gain correction and then returns the corrected data.

A.5.46 overscan

The **overscan** function applies a defined overscan correction if the usual `ccdproc.correct_overscan` function could not be used. This function requires the data to be corrected. The overscan correction to be applied is defined within this function. The function applies the overscan correction and then returns the corrected data.

A.5.47 norm_sec

The **norm_sec** function returns the section of the image used to normalize flat files `[list of lists]`.

A.5.48 log_file

The **log_file** function returns a unique name for the pipeline log file, determined using the current time `[str]`.

A.5.49 slack_client

The **slack_client** function returns the slack channel ID as a slack client object. This function loads the slack channel ID from file and returns the slack client object made with this channel ID.

A.5.50 MyLogger

The **MyLogger** class controls all messages from the pipeline to be logged. Logging is divided into 3 classes: **INFO** - normal successful running of the pipeline; **ERROR** - expected errors that do not affect the running of the pipeline; **CRITICAL** - critical/unexpected errors that affect the running of the pipeline. This class also controls the uploading of messages to slack during the **night** mode of the pipeline.

A.5.51 scheduled_exit

The **scheduled_exit** function returns whether the pipeline should exit `[True/False]`. This function requires the current UTC time, and defines between which UTC times the **night** mode of the pipeline will automatically exit at. The function compares the current time with the scheduled exit times; if the current time is between these times, the function returns `True`, else it returns `False`.

A.5.52 crosstalk_correction

The **crosstalk_correction** function applies the crosstalk correction. This function requires the file to be corrected, and the name of the crosstalk correction file (set by the **crosstalk_file** parameter). The function applies the crosstalk correction and then returns the corrected data.

A.5.53 nonlin_correction

The **nonlin_correction** function applies the non-linearity correction. This function requires the file to be corrected, and the name of the non-linearity correction file (set by the **nonlin_file** parameter). This function is currently not implemented, and forms a part of the future development (see **A.9**), and thus returns the data as inputted.

A.5.54 dithering

The **dithering** function returns the dithering option used during compression with fpack `[str]`.

A.5.55 quantized

The **quantized** function returns the quantization value used during compression with fpack `[str]`.

A.5.56 filter_keyword

The **filter_keyword** function returns the header keyword used to describe the filter of the image `[str]`.

A.5.57 mask_edge_pixels

The **mask_edge_pixels** function is used to mask edge pixels. This function requires the data to be masked, and the mask containing the edge pixels. The function masks the edge pixels by setting them to zero, and then returns the masked data.

A.5.58 mask_bp

The **mask_bp** function returns if bad pixels are included in the mask `T/F`.

A.5.59 mask_cr

The **mask_cr** function returns if cosmic ray are included in the mask `T/F`.

A.5.60 mask_sp

The **mask_sp** function returns if saturated pixels are included in the mask `T/F`.

A.5.61 mask_scp

The **mask_scp** function returns if saturated-connected pixels included in the mask `T/F`.

A.5.62 mask_sat

The **mask_sat** function returns if satellite trails are included in the mask `T/F`.

A.5.63 mask_ep

The **mask_ep** function returns if edge pixels are included in the mask `T/F`.

A.5.64 xtalk

The **xtalk** function returns if a crosstalk correction was applied `T/F`.

A.5.65 nonlin

The **nonlin** function returns if a non-linearity correction was applied `T/F`.

A.5.66 gain_apply

The **gain_apply** function returns if a gain correction was applied `T/F`.

A.5.67 mbias

The **mbias** function returns if a bias correction was applied `T/F`.

A.5.68 mflat

The **mflat** function returns if a flat correction was applied `T/F`.

A.5.69 cosmic

The **cosmic** function returns if cosmic ray were corrected `T/F`.

A.5.70 sat

The **sat** function returns if the image was processed for satellite trails `T/F`.

A.6 Dataflow

The data flow within the pipeline depends on the mode in which the pipeline is running. The **day** mode of the pipeline processes all files at once: creating the master bias and master flat files, and processing all available science files; while the **night** mode of the pipeline processes science files in real-time, watching a directory and processing science files as they appear. Figure A.1 summarizes how the data flows during the different modes. Each function is described in more details in **A.7**, with the description of **subpipe** in **A.8**.

The data is read, saved and worked from/to/in directories relating to the date which the data was taken on i.e. **date**. These directories are in the format of **yyyy/mm/dd/** and are used in conjunction with **read_path**, **write_path** and **work_path** e.g. *ML/raw/2017/10/12/*, *ML/red/2017/10/12/*, *ML/tmp/2017/10/12/*.

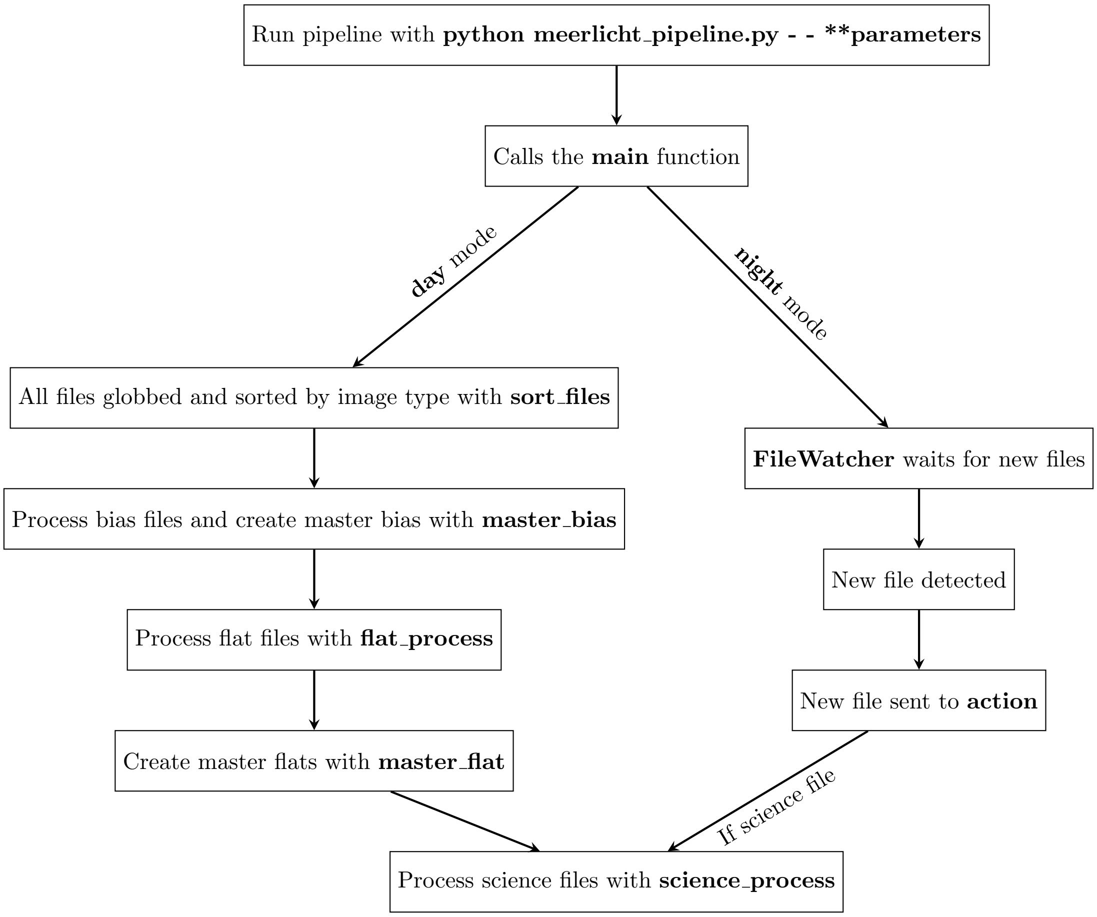

Figure A.1: Basic data flow of pipeline.

A.7 Pipeline functions

This section describes the functions within the pipeline in more details. When running the pipeline, the **main** function within in the **pipeline.py** script is called automatically.

A.7.1 header_ext

The **header_ext** function returns the extension in which the primary header is keep in the fits file. The extension depends on whether the file is compressed via fpack and the number of extensions present in the fits file.

A.7.2 sort_files

The **sort_files** function globs all raw files in **read_path** and sorts them by image type. This function requires **read_path**, **date**, **file_name**, and **filters**. The function uses the IMAGETYPE header keyword to sort the raw files, then returns a list of bias files, flat files, and science files.

A.7.3 append_median

The **append_median** function updates a header with the median bias level in the bias section for each channel. This function requires the header of the file to be updated and a list of channel bias levels.

A.7.4 append_rdnoise

The **append_rdnoise** function updates a header with the mean readnoise across all the channels, as well as the readnoise per channel. This function requires the header of the file to be updated and a list of channel readnoises.

A.7.5 append_gain

The **append_gain** function updates a header with the effective gain (in e-/ADU), as well as the gain that was applied to each channel. This function requires the header of the file to be updated.

A.7.6 date_obs_get

The **date_obs_get** function reads the observation date from a header and returns it in the format require for the pipeline. This function requires the header of the file. The function then reads the observation date from the DATE-OBS keyword and returns it in the form **yyyymmdd_hhmmss**.

A.7.7 load_bias

The **load_bias** function loads a previously created master bias. This function requires **date**, **write_path**, and **bias_path**. The function looks for a master bias in the **write_path+bias_path** directory, and loads the master bias created with the closest date (starting with the current date being processed and looking back to previous dates) to the date currently being processed. The pipeline will not use a master bias that is older than a year to the current date being processed. Should no suitable master bias be present, the function will exit the pipeline with the error: `No suitable master bias present for reduction, exiting pipeline`. Should a suitable master bias be found, the name of the master bias will be added the header of the processed file with the `MBIAS` keyword. The function returns the loaded master bias and the date which it was loaded from.

A.7.8 check_bias

The **check_bias** function checks the quality of a newly created master bias. This function requires the HDU object of the master bias. If the noise in the newly created master bias is larger than 10% of the optimal value, set in the setting file by **bias_quality**, the function will not write this newly created master bias to file. This check ensures that the master bias was created correctly, with the needed signal. If the noise is within the allowed value, the master bias is written to file.

A.7.9 check_flat

The **check_flat** function checks the quality of a newly created master flat. This function requires the HDU object of the master flat, the filter of the master flat, and the number of pixels in the master flat 3 standard deviations above the median level. If the median level of the newly created master flat is greater than the expected value (the expected value is 1 as a master flat is normalized to 1), the noise larger than 10% of the optimal value, set in the setting file by **flat_quality**, or the number of pixels within the master flat which have a value greater than 3 standard deviations above the median is greater than the minimum number allowed, set in the setting file by **flat_std**, the function will not write this newly created master flat to file. These checks ensure that the master flat was created correctly, and behaving as expected. If these values are within the allowed value, the master flat will be written to file. The function returns whether the master flat passed the checks `[True/False]`.

A.7.10 flat_process

The **flat_process** function processes all flat files, applying basic corrections such as gain correction and bias subtraction. This function requires the name of the flat file, **write_path**, and the name of the pipeline log file. The function updates the header of the flat with the master bias used, subtracts the master bias using **debias** from the setting file, updates the header with the readnoise using **append_rdnoise** and the gain used using **append_gain**, and constructs the data into a single array for writing to the temporary working directory. The function returns the success, or failure, of the flat reduction to add to pipeline log.

A.7.11 master_flat

The **master_flat** function creates a master flat with the reduced flat files. This function requires a list of flat files, the HDU object for the master flat, the filter of the master flat being created, the sub-image of the master flat being created, **date**, **write_path**, and **flat_path**. The function creates the master flat using **ccdproc.combine** (using the median of the flat as a weight, and 1/(the median of the **norm_sec**) as a scaling relation), updates with the master flat header with the median level and noise across the entire master flat and within the **norm_sec**, and checks the quality of the master flat using **check_flat** before writing to file. The function then returns the name of the master flat file, as well the success or failure of **flat_check**.

A.7.12 science_process

The **science_process** function processes science files; including the reduction, mask creation, and submission to **subpipe**. This function requires the name of the science file, **telescope**, **date**,

write_path, **mode**, the name of the log file, **reduce_science**, **submit_subpipe**, **fpack**, **verbose**, **crosstalk_file**, **work_path**, **nonlin_file**. If **reduce_science** is **True**: the function applies the crosstalk correction using **crosstalk_correction** and updates the header with the name of the crosstalk correction file; applies the non-linearity correction using **nonlin_correction** and updates the header with the name of the non-linearity correction file; subtracts the master bias using **debias**; updates the header with the read noise, gain used and any missing keywords using **update_keywords** and **add_wcs_keywords**; constructs the data into a single array using **construct**; loads in a master flat and performs the flat correction using **ccdproc.flat_correct**; cleans the data of cosmic rays using **astroscrappy.detect_cosmics**, creates a cosmic ray mask and updates the mask header with the number of pixels affected by cosmic rays; creates a saturation star mask using **astroscrappy.update_mask** and updates the mask header with the number of pixels affected by saturated pixels and stars; determines satellite trails using **acstools.satdet.detsat** and updates the mask header with the number of pixels affected by satellite trails; loads in the bad pixel mask and updates the mask header with the number of pixels affect by bad and edge pixels; combines all masks, updating the mask header with the flags; writes the mask to file; and writes the reduced science data to file. If the reduction of the science file and the creation of the mask is successfully completed, the function sets the local variable **analyse** to **True**. If the reduction of the science file and the creation of the mask fails, the function will report this, adding it to the pipeline log file, and skip the rest of the processing for this science file. If **submit_subpipe** is **True**, while **reduce_science** is **False**: the function submits the science file to **subpipe.main** with the **process** parameter set to **False**. This option is used for submitting already reduced science files to **subpipe** through the pipeline. Next, if **submit_subpipe** is **True** and **analyse** is **True**: the function submits the reduced science files to **subpipe** with the **process** parameter set to **True**. The success of **subpipe**, as well as any expected error occurring in **subpipe**, is reported back to the function and added to the pipeline log file. If a critical or uncaught error occurs in **subpipe**, causing the pipeline to fail, the function will move the pipeline log file to the correct end path before exiting the pipeline. If **submit_subpipe** is **False**: the function will clean up, compressing output fits files using fpack (if **fpack** is set to **True**) and moving all kept files to the correct paths.

A.7.13 copying

The **copying** function implements a block on the pipeline until a new file is finished copying. This function requires the name of the new file. The function checks the size of the file every second, implementing a block until the size of the file is stable and no longer copying. The function returns **True** once the size of the file no longer changes.

A.7.14 action

The **action** function checks the image type of a new file and submits new science files to **science_process**. This function requires a list containing: the event picked up by **FileWatcher** or name of a file, **telescope**, **date**, **write_path**, **mode**, the name of the pipeline log file, **reduce_science**, **submit_subpipe**, **fpack**, **verbose**, and **work_path**. The function loads the parameters from the list, checks that an event reported by **FileWatcher** is a fits file, checks the image type using the `IMAGETYP` header keyword, submits the file to **science_process** if it is a science file, and ignores the files if it is not a science file.

A.7.15 FileWatcher

The **FileWatcher** class monitors a directory and reports newly created files. This class requires a list containing: a queue, **telescope**, **date**, **write_path**, **mode**, the name of the pipeline log file, **reduce_science**, **submit_subpipe**, **fpack**, and **verbose**; and the path to watch given by **read_path+date**. When a file is created within the watched path, the class adds the event to the queue.

A.7.16 main

The **main** function controls the main data flow of the pipeline. This function requires all the input parameters and is automatically called when running the pipeline. The function first sets all pipeline parameters, either from user inputs or loads the defaults from the setting file. The function then loads all global parameters from the setting file, creating any directories not present. The log file and logging system is then set up using the standard python logging through **MyLogger**. Logging is set to the INFO level and messages have the format: **yyyy-mmdd hh:mm:ss LEVEL**

log entry. The data flow through the rest of the function then depends on the **mode** of the pipeline. For the **day mode**: all files are globbed and sort by image type using **sort_files**; the number of each file type is added to the pipeline log. If **process_bias** is **True**: a header for the master bias is created containing the names of the files used during creation and the name of the pipeline log file; the master bias is created using **master_bias**, multiprocessing multiple extensions at a time; the master bias header is updated with the median bias levels, the readnoise and the gain used using **append_mbias_biasmed**, **append_mbais_rdnoise** and **append_gain**; and the quality of the master bias is checked with **check_bias**. Should an error occur, the master bias was not with quality standards, or **process_bias** is **False**; a previously created master bias is loaded using **load_bias**. If **process_flat** is **True**: flat files are processed using **flat_process**, multiprocessing multiple flat files at once. After processing all flat files: a header for each master flat is created containing the names of the files used during creation and the name of the pipeline log file; and the master flat is created using **master_flat**. The function then submits all science files to **process_science**. For the **night mode**: a previously created master bias is loaded, an observer using **FileWatcher** is created, and all files already present are globbed. If **night_start** is **corrrect**: the function submits the already present files to the queue and starts the observer. The function then continues checking the time using **scheduled_exit**, stopping the observer and moving the pipeline log file to the correct path once the scheduled exit time is reached. If **night_start** is **late**: the function starts the observer to begin processing incoming files. The function then continues checking the time using **scheduled_exit**; stopping the observer, submitting the files that were present at the start of the pipeline to the queue, waiting until all these files have been processed, and moving the pipeline log file to the correct directory once the scheduled exit time is reached. If an OS or System error occurs during the pipeline, the error will be added to the pipeline log file, the log file moved to the correct directory, and the pipeline exited.

A.8 Subpipe

Subpipe is contained separately from the main pipeline and is not required to run the pipeline. Subpipe was adapted from the SkyMapper Transient pipeline for use with the MeerLICHT/BlackGEM pipeline. Subpipe can still be run as an independent component or called through another python script, as is done in the pipeline. Subpipe is responsible for the science analysis of science images. Subpipe controls the flow of images, such as finding a reference image and cleaning up, while the main science analysis is handled by ZOGY (a Python implementation written by Paul Vreeswijk of proper image subtraction: Zackay et al. 2016). The science analysis performed by ZOGY includes: solving the astrometry; performing optimal photometry, including calculating the zero points for photometric calibration; transient detection; and creating the catalogues, metadata and thumbnails for the database.

A.9 Future developments

Minor future improvements for MeerLICHT/BlackGEM include: higher order crosstalk correction and including non linearity correction. Major additions to the pipeline planned for the future include: implementation of multiprocessing over a single image i.e. a single image processed across multiple CPUs, instead of the single image per CPU, to decrease processing time per image; and implementation of a reference building job for science images i.e. the creation of a deep science image per field to use as a reference instead of the single image currently used.

Appendix B

Observation table

The full observation log presented in Table 5.1.

Table B.1: Full observing log for chapter 5.

Object	Type	Run	Telescope	Date of obs. (start of night)	HJD of start of run (+2450000)	Length (hrs)	t_{in} (s)	r (mag)
ASASSN-14eq	SU	S8508	74-in	2014/11/19	6981.3886	2.58	60	15.6- 18.5[1]
		S8515	74-in	2014/11/23	6985.3277	2.83	30	
		S8516	74-in	2014/11/24	6986.3093	1.00	10	
		S8517	74-in	2014/11/25	6987.2580	3.72	10	
		S8733	40-in	2015/08/05	7240.4354	6.21	10	
		S8735	40-in	2015/08/06	7241.4772	5.13	10	
		S8737	40-in	2015/08/07	7242.4807	5.14	10	
		S8739	40-in	2015/08/08	7243.4939	4.79	10	
		S8741	40-in	2015/08/09	7244.4304	1.05	10	
ASASSN-14hq	DN	S8496	74-in	2014/11/13	6975.5570	0.97	20	18.8 - 21.7[1]
		S8504	74-in	2014/11/17	6979.5378	1.64	40	
		S8506	74-in	2014/11/18	6980.4205	4.55	20	
		S8518	74-in	2014/11/25	6987.5430	1.67	20	
		S8554	40-in	2015/02/19	7073.2663	2.50	25	
		S8558	40-in	2015/02/20	7074.3849	0.83, 2.00	35, 40	
		S8570	40-in	2015/02/25	7079.3357	1.00	30	
		S8599	74-in	2015/02/23	7077.3606	1.88	7.5	
		S8825	40-in	2017/02/09	7794.3970	1.93	30	
		S8831	40-in	2017/02/14	7799.2681	2.50	30	
ASASSN-14hv	SU	S8509	74-in	2014/11/19	6981.5354	1.50	30	17.7 - 18.5[1]
		S8511	74-in	2014/11/20	6982.4422	4.00	60	
		S8513	74-in	2014/11/21	6983.4585	3.50	60	
		S8514	74-in	2014/11/22	6984.4592	1.65	60	

Table B.1: - *continued*

Object	Type	Run	Telescope	Date of obs. (start of night)	HJD of start of run (+2450000)	Length (hrs)	t_{in} (s)	r (mag)
		S8625	74-in	2015/04/02	7115.3556	2.58	10	
		S8628	74-in	2015/04/06	7119.2220	3.54	20	
		S8846*	40-in	2017/05/03	7877.2021	3.18	5, 5, 10	Outburst?
		S8847*	40-in	2017/05/04	7878.2001	3.50	20	Outburst?
		S8851	40-in	2017/05/06	7880.2080	3.83	30	
		S8854	40-in	2017/05/07	7881.1972	3.00	30	
ASASSN-14ik	DN	S8494	74-in	2014/11/13	6975.2767	2.00	10	17.0 - 18.1[1]
		S8497*	74-in	2014/11/15	6977.2636	2.00	10	
		S8499*	74-in	2014/11/16	6978.2549	2.32	2	
		S8500*	74-in	2014/11/16	6978.3573	0.79	10	
		S8502*	74-in	2014/11/17	6979.2559	3.00	5	
		S8505	74-in	2014/11/18	6980.2585	3.00	10	
		S8507	74-in	2014/11/19	6981.2573	2.49	10	
		S8510	74-in	2014/11/20	6982.2539	4.14	10	
		S8512	74-in	2014/11/21	6983.2590	2.86	10	
		S8711	40-in	2015/07/10	7214.4305	2.74	20	
		S8715	40-in	2015/07/12	7216.3813	3.43	20	
ASASSN-14ka	DN	S8495	74-in	2014/11/13	6975.3827	4.00	20	16.3 - 17.8[1,3]
		S8498	74-in	2014/11/15	6977.3560	1.13	20	
		S8501	74-in	2014/11/16	6978.4010	3.92	20	
		S8503	74-in	2014/11/17	6979.3897	3.00	20	
		S8549	74-in	2014/11/19	7042.2775	4.00	20	
		S8551	40-in	2014/11/18	7072.2721	1.33	20	

Table B.1: - *continued*

Object	Type	Run	Telescope	Date of obs. (start of night)	HJD of start of run (+2450000)	Length (hrs)	t_{in} (s)	r (mag)
		S8592	74-in	2014/11/21	7075.2666	0.13, 1.85	7.5, 10	
ASASSN-15ev	SU	S8632	74-in	2015/04/23	2457136.2398	3.00	20	18.0 - 20.3^{2,3}
		S8635	74-in	2015/04/24	2457137.2293	4.00	20	
		S8644	74-in	2015/04/28	2457141.2241	0.80	20	
		S8868	40-in	2017/05/13	2457887.2584	2.00	60	
		S8870	40-in	2017/05/14	2457888.1995	0.36, 2.50	60	
		S8873	40-in	2017/05/15	2457889.1986	3.00	60	
ASASSN-15fm	IP	S8631	74-in	2015/04/22	2457134.5099	0.77	40	19.4 - 20.4^{2}
		S8634	74-in	2015/04/23	2457135.6397	1.06	40	
		S8638	74-in	2015/04/25	2457138.5002	4.28	40	
		S8640	74-in	2015/04/26	2457139.4764	3.52, 1.37	40, 60	
		S8643	74-in	2015/04/27	2457140.4784	4.83	40	
ASASSN-15fo	SU	S8630	74-in	2015/04/22	7135.4126	2.00	30	18.7 - 23.0^{2,3}
		S8636	74-in	2015/04/24	7137.4114	2.74	30	
		S8642	74-in	2015/04/27	7140.3040	4.00	30	
ASASSN-15hm	SU	S8633*	74-in	2015/04/23	7136.4114	0.59	1	Outburst^{2}
		S8639*	74-in	2015/04/26	7139.4157	1.00	1	
		S8648*	40-in	2015/05/01	7144.3002	2.03	10	
		S8649*	40-in	2015/05/02	7145.1973	6.25	5	
		S8651*	40-in	2015/05/03	7146.1940	6.00	5	
		S8656*	40-in	2015/05/05	7148.1957	2.33	5	
ASASSN-15hn	SU	S8629*	74-in	2015/04/22	7135.2157	4.00	1	Outburst^{2}
		S8647*	40-in	2015/05/01	7144.2103	0.42	5	

Table B.1: - *continued*

Object	Type	Run	Telescope	Date of obs. (start of night)	HJD of start of run (+2450000)	Length (hrs)	t_{in} (s)	r (mag)
		S8653*	40-in	2015/05/04	7147.1918	2.00	2	
		S8657*	40-in	2015/05/05	7148.3059	0.45	2	
ASASSN-15kw	DN	S8717	40-in	2015/07/13	7217.2700	0.39, 1.08, 2.03	5, 40 , 20	16.8 - 17.8[2]
		S8720	40-in	2015/07/14	7218.2580	6.00	5	
		S8722	40-in	2015/07/22	7226.2276	1.17, 1.97	5, 20	
		S8723	40-in	2015/07/24	7228.2392	0.74	20	
		S8724	40-in	2015/07/25	7229.2319	0.67	5	
		S8726	40-in	2015/07/26	7230.3236	3.00	5	
		S8728	40-in	2015/07/27	7231.21148	5.00	5	
		S8730	40-in	2015/07/28	7232.2075	4.00, 2.00	5, 10	
		S8745	40-in	2015/08/11	7246.2401	2.00	5	
ASASSN-15ls	DN	S8732	40-in	2015/08/05	7240.2241	4.57	10	16.6 - 17.7[1]
		S8734	40-in	2015/08/06	7241.2188	6.00	10	
		S8736	40-in	2015/08/07	7242.2239	6.00	10	
		S8738	40-in	2015/08/08	7243.2110	6.00	10	
		S8740	40-in	2015/08/09	7244.2230	4.00	20	
		S8742	40-in	2015/08/10	7245.2096	3.00	10	
		S8746	40-in	2015/08/11	7246.3272	1.50	10	
ASASSN-15pb	DN	S8760	40-in	2015/10/16	7312.2406	4.50	60	18.2 - 21.1[1]
		S8763	40-in	2015/10/17	7313.2537	4.25	90	
		S8766	40-in	2015/10/19	7315.2451	2.50	90	
		S8770	40-in	2015/10/20	7316.2391	1.50	90	
		S8784	40-in	2015/10/24	7351.2796	2.00	90	

Table B.1: - *continued*

Object	Type	Run	Telescope	Date of obs. (start of night)	HJD of start of run (+2450000)	Length (hrs)	t_{in} (s)	r (mag)
ASASSN-15pw	DN	S8765	40-in	2015/10/17	7313.5410	2.18	30	16.8 - 20.3[1,3]
		S8772	40-in	2015/10/20	7316.4138	5.17	30	
		S8774	74-in	2015/11/18	7345.4241	4.50	30	
		S8778	74-in	2015/11/21	7348.4210	4.50	60	
		S8780	74-in	2015/11/22	7349.4718	3.25	60	
		S8783	74-in	2015/11/23	7350.4769	3.02	60	
ASASSN-17fz	WZ Sge	S8855*	40-in	2017/05/07	7881.3269	2.47	1, 5	Outburst[1]
		S8858*	40-in	2017/05/08	7882.2184	3.89	1, 1, 1, 5, 5, 5	
		S8861*	40-in	2017/05/09	7883.1865	5.25	1	
		S8864*	40-in	2017/05/10	7884.1938	5.25	1	
		S8866*	40-in	2017/05/12	7886.2023	3.61	1, 1, 2, 5, 2	
		S8867*	40-in	2017/05/13	7887.2096	2.50	1	
		S8871*	40-in	2017/05/14	7888.3373	1.85	1	
		S8874*	40-in	2017/05/15	7889.3252	1.68	1	
		S8877*	40-in	2017/05/16	7890.2018	4.65	1, 5, 1, 1, 1, 1, 2	
		S8881*	Lesedi	2017/05/18	7892.2363	0.50	1.5	
		S8882*	Lesedi	2017/05/21	7895.2546	0.50	2.5	
		S8883*	Lesedi	2017/05/22	7896.2080	0.50	2.5	
CSS 0353-03	DN	S8236	40-in	2012/11/15	6247.4404	0.61	20	17.7 - 18.9
		S8240	40-in	2012/11/16	6248.4540	2.70	30	
		S8249	40-in	2012/11/21	6253.4396	3.98	60	
		S8250	40-in	2012/11/22	6254.4321	3.98	60	
		S8251	40-in	2012/11/23	6255.4362	3.11	60	

Table B.1: - *continued*

Object	Type	Run	Telescope	Date of obs. (start of night)	HJD of start of run (+2450000)	Length (hrs)	t_{in} (s)	r (mag)
CSS 0524+00	DN	S8345	74-in	2013/12/24	6651.3116	4.00	30	17.4 - 18.9[2]
		S8347	74-in	2013/12/25	6652.3715	3.40	20	
		S8351	74-in	2013/12/27	6654.2980	3.00	20	
CSS 2144+22	SU	S8326	40-in	2013/09/28	6564.3363	3.74	30	16.4 - 17.3
		S8328	40-in	2013/09/29	6565.3045	4.49	30	
		S8330	40-in	2013/09/30	6566.3009	3.44	40	
MASTER 0014-56	DN	S8744	40-in	2015/08/10	7245.4707	0.04, 5.32	5, 30	19.1 - 22.9[2,3]
		S8747	40-in	2015/08/11	7246.3960	1.94	10	
		S8759	40-in	2015/10/15	7311.2959	0.26, 0.34, 7.35	5, 10, 30	
		S8761	40-in	2015/10/16	7312.4396	2.00	10	
		S8771	40-in	2015/10/20	7316.3203	0.19, 1.79	10, 15	
		S8781	74-in	2015/11/23	7350.2861	1.50	10	
		S8793	40-in	2016/05/13	7583.6235	1.67	10	
MASTER 2220-74	DN	S8718	40-in	2015/07/13	7217.5127	0.28	30	16.9 - 18.7[1]
		S8721	40-in	2015/07/14	7218.5154	4.45	10	
		S8725	40-in	2015/07/25	7229.4758	4.58	10	
		S8727	40-in	2015/07/26	7230.4571	5.86	20	
		S8729	40-in	2015/07/27	7231.4265	6.53	10	
		S8731	40-in	2015/07/28	7232.4655	3.44	20	
		S8743	40-in	2015/08/10	7245.3544	2.00	10	
MLS 0720+17	SW Sex	S8352	74-in	2013/12/27	6654.4291	4.00	60	17.9 - 21.1[2]
		S8552/JD7072	40-in	2015/02/18	7072.3897	2.38	50	
		S8555/JD7073	40-in	2015/02/19	7073.4462	2.43	70	

Table B.1: - *continued*

Object	Type	Run	Telescope	Date of obs. (start of night)	HJD of start of run (+2450000)	Length (hrs)	t_{in} (s)	r (mag)
		S8587/JD7074	74-in	2015/02/20	7074.3301	2.67	30	
		S8567/JD7077	40-in	2015/02/23	7077.3553	1.13	45	
		JD7317	MDM	2015/10/22	7317.8577	1.08	30	
		JD7401	MDM	2016/01/14	7401.9444	1.00	30	
		JD7403	MDM	2016/01/16	7403.8814	1.33	30	
SSS 0522-35	DN	S8138	74-in	2011/12/17	5913.3897	4.72	20	18.3 - 21.0^1
		S8140	74-in	2011/12/19	5915.3823	1.59	20	
		S8142	74-in	2011/12/20	5916.4017	4.30	20	
SSS 0553-52	DN	S8131	74-in	2011/12/14	5910.4922	2.08	15	17.2 - 17.8^1
		S8133	74-in	2011/12/15	5911.3900	4.65	10	
		S8135	74-in	2011/12/16	5912.3878	2.78	10	
SSS 0945-19	SU	S8312	74-in	2013/05/08	6421.3071	2.14	5	16.43 - 19.41^2
		S8313	74-in	2013/05/09	6422.2031	3.00	5	
		S8315	74-in	2013/05/10	6423.2094	4.98	5	
		S8348	74-in	2013/12/25	6652.5231	0.50	10	
		S8571	40-in	2015/02/25	7079.3869	3.67	20	
		S8572	40-in	2015/02/26	7080.2839	0.77	20	
		S8577	40-in	2015/02/28	7082.4593	0.66	20	
SSS 1340-35	DN	S8556	40-in	2015/02/19	7073.4942	2.20	70	18.42 - 19.57^2
		S8562	40-in	2015/02/21	7075.4655	1.17	120	
		S8564	40-in	2015/02/22	7076.4499	1.48	70	
		S8575	40-in	2015/02/27	7081.5141	1.47	90	

Notes: t_{in}: integration time; DN: dwarf nova; SU: SU Ursae Majoris; IP: intermediate polar; *: system was in outburst; r: r magnitude of the system in quiescence. ^{1} makes use of the SkyMapper catalogue (Wolf et al., 2018) for magnitude calibration; ^{2} makes use of PANSTARRS (Flewelling et al., 2016) for magnitude calibration; ^{3} uses another calibrated run on the same night for magnitude calibration.